ADVANCED STAMP GEOMETRIES AND ADHESIVELESS TRANSFER PRINTING MODALITIES FOR USE IN DETERMINISTIC MATERIALS ASSEMBLY

BY

ANDREW CARLSON

DISSERTATION

Submitted in partial fulfillment of the requirements
for the degree of Doctor of Philosophy in Materials Science and Engineering
in the Graduate College of the
University of Illinois at Urbana-Champaign, 2012

Urbana, Illinois

Doctoral Committee:

Professor John A. Rogers, Chair
Professor Paul V. Braun
Professor Placid M. Ferreira
Professor Nancy R. Sottos

ABSTRACT

Transfer printing has become a robust technique for assembling disparate classes of micro-and nanomaterials into spatially organized, functional arrangements in two and three-dimensional layouts. Such capabilities have made this assembly process invaluable in realizing novel or unusual forms of many high-performance systems, such as flexible electronics, three-dimensional optoelectronics, and bio-compatible or bio-integrated electronic devices. The focus of this thesis is to develop a collection of advanced transfer printing modalities that enable expansion in breadth and diversity of materials and formats that serve as either ink or substrate layers during assembly. Targeted modulation of adhesion at the stamp/nanomaterial interface provides a direct route for enhancing printing efficacy, particularly in 'dry' or adhesiveless systems where intimate contact between the substrate and transferred material is desired. This body of work progresses from several simple, passive techniques that demonstrate either strong or weak levels of stamp adhesion for retrieval and printing, respectively, to more active methods that utilize first dynamic adhesion switching and then ultimately fine control over stamp adhesive strength through the use of targeted mechanical loading. Several examples of assembled devices are discussed to demonstrate the broad utility of these protocols, as well as integration strategies for high throughput, massively parallel printing paradigms.

ACKNOWLEDGEMENTS

Throughout my time at the University of Illinois, I've been extremely fortunate to have been surrounded with a large network of supportive and brilliant people who have taught and inspired me to continually strive for success and have been very generous with their time and patience.

I am not sure I will ever be able to adequately express my gratitude to my advisor, Professor John Rogers for all that he has done for me over the years. John took a chance when hiring me, someone who had never worked with traditionally 'soft' materials before, and let me jump in with both feet in the lab and research group as a whole. Much of the work presented in the following chapters would not have been successful without the insight and resources he has provided. John has also been an excellent role model, not only as a model scientist, but also as a leader and visionary in his field. Rarely do you get to work with someone who has the scientific acumen, business savvy, and entrepreneurial spirit that John possesses. I count myself fortunate to have witnessed and participated in this first-hand; I could not have asked for a better advisor and research experience.

I am also exceedingly grateful to professors Placid Ferreira and Yonggang Huang. Professor Ferreira has been like an unofficial co-advisor in many ways and always provides provocative insights into the work and how to adapt them to transfer printing. Professor Huang and his students, likewise, have been instrumental in developing much of the theoretical framework for the various projects comprising the chapters of this dissertation. He consistently makes the complex understandable and has always been willing to lend us his talents; our work is much stronger for his contributions.

The diverse collaborations afforded during my doctoral studies have enabled me to appreciate the unique and collegial atmosphere at the University of Illinois. Not only was this an excellent venue for interesting science, but I also gained valuable relationships that will last a lifetime. Paulius Elvikis was one of the best collaborators that I have ever had the opportunity to work with. He provided incredible amounts of insight into implementing transfer printing into large-scale, automated machines and started me onto the path of developing techniques that could be implemented in these toolbits. Even after he had graduated, Paulius was still gracious enough to field calls from me at all hours regarding a detail of the printing tool or how to implement a technique in the existing setup. Beyond that, Paulius was a friend and made the long hours spent working side-by-side pass all the more quickly. Audrey Bowen has been an amazing resource for all things related to materials chemistry. She has seen or heard about even the most obscure printing techniques and is truly an expert in soft lithography; she can always point you in the right direction on any topic. Audrey is also one of the hardest working people I know (quite impressive from such a group of hard working people) and is always willing to lend an ear or aid. I know she will be immensely successful in all that she strives to do. Both Numair Ahmed and Steve Elgan have been instrumental in developing new printing tools and keeping the existing ones operational. They have been cornerstones of the transfer printing hardware and excellent resources for ideas and implementations of even the most outlandish designs. Steve has also shown that one can have an excellent family life (and a life in general) outside of the lab. Finally, Aaron Jackson has been a constant friend since our early days in the department. During times of success and tumult, Aaron has always been a source of humor and a realization that everything is manageable. We've been in the trenches together and will always remain friends because of that.

Being part of such a large research group has been a truly wonderful resource over the years. I have learned something from every member of the Rogers research group and working beside some of the brightest graduate students and postdocs has been an enriching experience. Seok Kim is an expert in synthetic biomimetic adhesives and microscale adhesion testing; much of our success in this field can be traced to early discussions we had when he joined the group as a postdoc. Since then, I have enjoyed our collaborations and I am always amazed by his scientific intuition – he will be an excellent professor at UIUC. Sang Yoon Yang has been another fantastic source of support. I have enjoyed our conversations on rate-dependent adhesives, nanomembrane printing, and life as a postdoc. Sang has been instrumental in several important projects and a reliable colleague during tough deadlines. Shuodao Wang has been my collaborator-in-arms on several projects and a constant source of insight for mechanics questions; he will make an excellent postdoc and professor. I've also been extremely fortunate to work with two undergrads, Matt Sykes and Kaile Chen. I was amazed at how quickly both learn, inside the lab and out, as well as their drive to succeed. Never did they baulk when I asked them to stay late, come in early, or work weekends to finish up a project. It has been extraordinarily rewarding to watch them grow and become successful scientists in their own right.

Last, but in no means least, it is impossible to enumerate the countless things my parents, Ken and Charlotte Carlson, have taught and continue to teach me. They have always supported my endeavors, provided helpful advice whenever needed, and shared equally in good times and bad. My parents have made it a priority to make their children's lives easier so that we could focus on our goals and be successful; for that I am extremely grateful. My brother, Nicholas, and sister, Erica, have likewise always been supportive of my choices and continually remind me

how fortunate I am to have such a family. And finally, without Andrea, my life in Illinois would not have been nearly as memorable or colorful. She has been a constant source of strength, perseverance, and love, challenging me to strive for the best in every aspect of life.

TABLE OF CONTENTS

CHAPTER 1

INTRODUCTION

1.1. Micro/Nanofabrication

Tools and protocols for micro/nanofabrication and assembly are essential to every field of nanoscience and are at the heart of modern high-performance devices.[1-10] From the perspective of research and development, micro- and particularly nanoscale fabrication processes involve use of specialized techniques to fabricate small collections of devices or device components, in a form resembling craftsmanship. Discoveries that emerge from such work, however, only yield valuable technologies when they can be implemented with techniques that can be scaled for cost effective manufacturing – approaches that offer low cost of operation, high throughputs, and precise repeatability. In some cases, these techniques might rely on adaptation of methods with industrial origins. For example, photolithography and e-beam lithography are some of the most important fabrication processes in the microelectronics industry, providing efficient mass produced high resolution pattern replication for manufacturing devices.[6, 11, 12] Since its codification in 1965, Moore's Law, an extrapolated prediction of the achievable resolution trends over time, expressed most often by the number of transistors that can be economically placed on an integrated circuit [13, 14], has been a closely followed industry standard. This benchmark, which predicts that the number of transistors will double every two years, has been achieved often through advanced capabilities of the 2D lithography toolsets used in device manufacture (e.g. new, short-wavelength exposure sources, optimized photoresist chemistries, geometric design rules of the intended pattern, etc). [4, 11, 15, 16] Recently however, Intel introduced a new 22 nm resolution 3D transistor technology (Tri-Gate Ivy Bridge)

utilizing vertical gating technology as opposed to the traditional planar (2D) gates. This 3D geometry is predicted to improve performance significantly (by up to 37% as compared to 32 nm resolution 2D transistors) by allowing more transistors to be packed in a given areal layout.[17] While increasing resolution has long been considered a key metric of a particular fabrication process, the advent of industrial technologies such as Ivy Bridge represent a shift in device design priorities. The interest in multidimensional architectures such as these is appealing not only for the enhancement of performance, but also as a means for enabling applications in many branching fields such advanced microelectricalmechanical systems (MEMS), photonics, optics, and unconventional electronic systems.

Other forms of emergent technologies require fabrication and assembly processes beyond the current competencies of industrial techniques, either in manipulation of unusual materials, fabrication over unusual surfaces (flexible, curvilinear), or to enable challenging feature sizes and structure geometries.[5, 18, 19] While there are many viable techniques to meet these requirements, some of the most widely adopted and commercially successful are based on soft lithography.[10, 19-24] Soft lithographic fabrication processes typically rely on some form of mass transfer using physical contact of a stamp, 'inked' with the material to be transferred ('printed'), and a receiving substrate. One of the earliest and quintessential applications of this process was demonstrated in micro-contact printing where a monolayer of alkanethiols was delivered onto a gold coated substrate from the surface of a patterned elastomeric stamp.[25, 26] The assembled molecular patterns provided a number of functionalities, such as etch resist for patterning the underlying metallic film. These and similar techniques have proven to be highly adaptable and demonstrated deployment of traditionally soft materials (polymers,[27] functional molecular arrangements,[8, 28] elastomers[20, 29, 30] and others) over large areas and non-

planar surfaces.[30] Inspired by the scalability and cost advantage of this approach to materials fabrication and assembly,[10, 19, 23, 31] sophisticated variants of soft lithographic protocols have been developed to manipulate a wider range of material classes. Transfer printing has emerged as one of the most robust and well-established techniques to evolve from soft lithography and the development of novel printing modalities, particularly those exploiting 'dry' or adhesiveless schemes, to complement traditional device fabrication processes will be a unifying focus for this thesis.

1.2. Transfer Printing-Based Microcomponent Assembly

Transfer printing techniques represent a potentially transformational approach to materials assembly and micro-/nanofabrication with far ranging fields of use. At the heart of the method is the use of highly parallel protocols to print 'inks', here defined as a diversity of material classes with a wide range of geometries and configurations having broadly adaptable levels of functional integration, into the precise architectures required by devices. Recent rapid progress in the field has expanded the competencies of transfer printing, in terms of both the range of materials for patterning and scope of applications enabled. As demonstrated in the literature, essentially any class of material can be developed in the form of an ink appropriate for transfer printing-based fabrication schemes – from complex molecular scale materials (self-assembled monolayers (SAMs),[10, 19, 23, 31] nanotubes and graphene,[32-35] functional polymers,[36-38] DNA,[39-41] photoresists,[27] etc.), to high performance hard materials (single-crystalline inorganic semiconductors,[42-46] metals,[47-50] oxide thin films,[51, 52] etc.), to fully integrated device structures (thin film transistors (TFTs),[42, 53-56] light emitting

diodes (LEDs),[57, 58] complementary metal oxide semiconductor (CMOS) circuits,[59-61] sensing arrays,[62, 63] solar cells,[64, 65] etc.). Elegant demonstrations of unique material constructs and devices created by advanced forms of transfer printing appear in Figures 1.1a-f. These examples illustrate functional integration and demonstrate how the myriad capabilities inherent to transfer printing can enable new fabrication routes such as multidimensional assembly (Figure 1.1a),[66] large-area deployment of nanostructured materials (Figure 1.1b),[67] and manufacture of passive (Figure 1.1c-d)[68, 69] and active (Figure 1.1e-f)[70-72] devices in lightweight, flexible, and curvilinear formats.

While the demonstrations in Figure 1.1 represent the diversity of materials and configurations that can be realized with transfer printing, inorganic semiconductors are one of the most well-developed materials classes for use with this technique and provide straightforward pathways for fabrication of high performance unconventional electronic systems.[46, 53, 73] In this context, the general form of transfer printing, utilizes an elastomeric stamp element to mediate physical mass transfer between a host or 'donor' wafer and a secondary, receiving or target substrate ('receiver'). Starting with a wafer-based source material, simple wafer level processing can be performed to define microstructures or devices which are lightly tethered to the host. For the case of inorganic materials, this usually requires chemical undercutting (or anisotropic etching), but not full release from the substrate.[74] When properly designed, these microstructures define the ink layer. Next, deterministic contact and lifting of the structure from the source wafer (generally referred to as 'inking' or retrieval) with the stamp element followed by contact with a dissimilar receiver substrate enables registered placement of the inks for printing. This strategy is particularly valuable, in part, because it dramatically expands the materials possibilities in fabrication by separating growth and processing of the inks

from the donor and the receiving substrates, allowing access to final formats which might not be stable to the thermal and chemical requirements of processing and fabrication.

Kinetically controlled transfer printing is a specialized, yet robust form of transfer assembly which utilizes the rate-dependent adhesion of a soft, elastomeric stamp element to enable particularly interesting forms of adhesiveless printing.[66, 75-77] This process, shown schematically in Figure 1.2, follows the general form of transfer printing, but relies on the delamination velocity of the stamp to determine whether retrieval or printing will occur, with larger velocities yielding proportionally larger stamp adhesion. A more detailed discussion of the mechanics of this process will be presented in subsequent sections. This technique is particularly powerful due to its natural compatibility with high performance, single crystalline semiconductor materials (such as Si, GaAs, GaN, InP, etc.)[42, 44, 46, 75, 78] in micro- or nanostructured forms. Transfer printing such materials enables their deterministic assembly onto nearly any type of substrate, at room temperature, with high yields in rapid, parallel fashion. When repeated, this process provides a high resolution, scalable assembly technique, with capabilities in two or three dimensional layouts and in heterogeneous levels of materials integration, all of which lie beyond the competency of any other method.[19, 23, 31]

A key advantage of the procedure outlined in Figure 1.2 is that it enables rapid delivery of materials in sparse or dense layouts over large substrate areas, specifically via multiple stamp inking and printing cycles. Several variants of sequential inking and printing can be used: in the first method, delineated ink structures on a donor wafer can be translated directly to a receiver, either by use of a stamp with a flat surface or one in which the surface relief pattern is directly matched to the format of the donor ink. Final layouts for the donor are determined during

processing of the ink and can exploit precise positioning and size control available to the lithographic fabrication steps used to construct the ink.[79, 80] A second method utilizes molded relief embossed on a stamp surface to determine pitch, layout, and critical dimensions of the printed inks, independent of the configuration on the donor substrate. Figures 1.3a-c demonstrate a case of area expansion in which densely packed thin plates of compound semiconductor (here in the form of epitaxial stacks of materials designed for light emitting diodes) on the donor are selectively retrieved with a microstructured stamp and printed, with expanded pitch, across a sparsely populated area on the target.[57] Printing in this manner enables transformation of the donor wafer geometry upon translation to the receiver, as demonstrated in Figures 1.3b-c where the pitch of the inks is expanded by ~7 times from the donor to the target array. This capability has several advantages, including efficient use of ink materials, precise control of ink spacing and density, and access to final layouts that are not restricted by the substrate size limitations of traditional lithography tools. Figures 1.3d-e show optical images of small 250 μm × 250 μm × 2.5 μm plates sparsely assembled over transparent substrates. Figure 1.3d presents an image of ~1600 such structures printed onto a plastic sheet that is subsequently wrapped around a glass cylinder. Figure 1.3e illustrates the same type of devices printed onto a glass substrate that rests above a sheet of paper with lettering and logos to demonstrate transparency and relative size scales.[57]

The generalized protocol[26] for fabrication of structured elastomeric stamps such as those demonstrated in Figures 1.2 and 1.3a follow well-establish casting and curing techniques. The process begins with patterning of a master template typically fabricated by photolithography or rigid surface micromachining. The master provides a rigorously controlled reusable topographical template from which polymeric materials are molded and formed into embossed

stamps.[19, 23] The master is usually subject to a surface modification treatment, such as deposition of a fluoroalkyl trichlorosilane which acts as an anti-adhesion release layer. Liquid prepolymer is finally cast onto the surface of the master and allowed to cure before careful demolding from the template reveals corresponding relief patterns on the stamp surface. A common, commercially available elastomer used extensively as a stamp material in this body work is poly(dimethylsiloxane) (PDMS), Dow Corning Sylgard 184. Specific formulations of PDMS used and template geometries molded for stamps will be discussed in the various chapters of this thesis. PDMS has many attributes that lend the material to quite broad utility, specifically: good thermal stability in air over a wide range of temperatures (-100°C to 180°C), low modulus (~1-10 MPa), high gas/vapor permeability, low chemical reactivity, low surface free energy (~20-25 mN/m), and optical transparency down to λ=230 nm.[5, 19, 81-84] An extremely useful property of PDMS that is routinely exploited in transfer printing is its ability to form a reversible conformal contact with nearly any surface, even ones with surface roughness or asperities. The reversibility in sealing occurs as a result of the low interfacial free energy and the nearly ideal van der Waals adhesion that occurs upon contact between the stamp and substrate surface.[26, 85] Such aspects make the material suitable for the high resolution molding necessary in the most advanced forms of transfer printing as will be demonstrated.

1.3. Mechanics of Adhesiveless Printing

Effective transfer printing, relies, fundamentally, on control of adhesion and fracture mechanics at the critical interfaces between the ink/donor, the ink/stamp and the ink/receiver. A first consideration is the chemistry and generalized adhesion forces at these interfaces. In a

broad sense, the only interface that should bond permanently is the one between the ink and the receiver substrates; all others should be reversible and, preferably, switchable in a passive or active mode. For efficient transfer printing, release at the interface between the ink/donor must occur. This release can involve cohesive fracture in the ink, in some other class of material that temporarily bonds the ink to the donor (adhesive-assisted printing), or between the ink and the donor itself (adhesiveless printing). In most cases, this ink/donor interface can be engineered to enable release onto unmodified surfaces of elastomeric stamps that are capable of soft, conformal contact. The delivery part of the printing process requires a difference in work of adhesion between the stamp/ink and ink/receiver.

Physical effects in the stamps can strongly enhance the efficiency of transfer, in a way that can complement strategies based on interfacial materials designs. One powerful and widely used such strategy exploits rate-dependent effects with viscoelastic stamps, such as those made with PDMS[42, 44-46, 51, 53, 54, 56, 64, 74-77, 79, 80, 86-90] where the velocity of separation of the stamp from a surface influences the adhesive strength.[75] Ink retrieval and delivery can, therefore, occur efficiently at velocities on the order of 10 cm/s or greater and a few mm/s or less, respectively.[75] This process can be modeled as the initiation and propagation of interfacial cracks,[77, 91] with each interface providing a competing fracture pathway that has a characteristic steady-state energy release rate G defined as:

$$G = \frac{F}{w} \tag{1.1}$$

where F is the force applied to the stamp in the normal direction and w is the stamp width. While G is a measure of the interfacial adhesive strength between the stamp and its contacting

substrate, it differs from the work of adhesion since it accounts for both interfacial bond breaking and viscoelastic energy dissipation surrounding the crack tip. [75, 92-95] Separation at either the stamp/ink or ink/substrate interface corresponds to a critical value of the energy release rates, $G_c^{stamp/ink}$ and $G_c^{ink/sub}$, respectively and comparison of these values provides criteria for predicting retrieval or printing:[5, 77]

$$G_c^{stamp/ink} < G_c^{ink/sub} \quad \text{for printing} \tag{1.2a}$$

$$G_c^{stamp/ink} > G_c^{ink/sub} \quad \text{for retrieval} \tag{1.2b}$$

The elastic nature of both the rigid ink and substrate implies that $G_c^{ink/sub}$ is constant, to first approximation, with no dependence of interfacial strength on velocity. By contrast, the viscoelasticity of the stamp leads to a velocity dependent $G_c^{stamp/ink}$, i.e. $G_c^{stamp/ink} = G_c^{stamp/ink}(v)$.[77, 92-95] At a critical velocity v_c, the energy release rates for both interfaces are equal, leading to the condition:

$$G_c^{stamp/ink}(v) = G_c^{ink/sub} \tag{1.3}$$

marking the transition from a retrieval to printing regime, as shown in Figure 1.4. A general power-law relationship, predicted by Gent and others, fits the rate-dependence, according to (1.4):[77, 93, 94, 96]

$$G_c^{stamp/ink}(v) = G_0[1 + (\tfrac{v}{v_0})^n] \tag{1.4}$$

where G_0 is the zero-velocity energy release rate similar to a fatigue limit fracture energy, v is the separation velocity, v_o a reference velocity associated with G_0, and n the scaling parameter.[75,

77, 97] Rearranging equation (1.4) provides an analytical expression for the critical separation velocity:

$$v_c = v_0[\frac{G_c^{stamp/ink} - G_0}{G_0}]^{1/n} \quad (1.5)$$

Kinetically controlled printing can be influenced in complex ways by the ambient environment and temperature. Discussion of these effects, while outside the scope of this dissertation, are available in the literature.[77, 93, 94, 97-100]

1.4. Automated Transfer Printing Tools

1.4.1. Automated Transfer Printing

We next turn to a brief discussion of advanced toolbits which enable rapid, massively parallel printing modalities which can deploy materials over large areas at throughputs that approach millions of objects per hour.[66, 101] These tools are nominally comprised of *x*-, *y*-, and *z*-axis linear stages with additional tilt- and rotation staging to enable controlled and reproducible manipulation of a stamp element independent of a host or receiving substrate. Integrated optics and high precision load cells provide alignment monitoring and force-feedback sensing to determine contact between a stamp and substrate on length scales ranging from microns up to centimeters or longer. Micron scale registration and positioning accuracy across stamp/substrate contact and a repeatable overlay accuracy (the ability to automatically return to the same location on a substrate) of less than 500 nm are characteristic staging requirements.

Figure 1.5a provides an optical image view of one such tool built at the University of Illinois with critical components labeled.

1.4.2. Custom Microscale Adhesion Setup

The flexibility and high precision afforded by tools like the one demonstrated in Figure 1.5a can be configured for additional functionality beyond simple automated printing. Figure 1.5b shows a magnified optical micrograph of a custom adhesion setup which integrates a precision load cell (Transducer Techniques, GSO-10) and additional tip/tilt plate (ThorLabs, GNO-10) onto the automated *x*-, *y*- staging platform of the toolbit. The elastomeric stamps are mounted on an independent vertical (*z*-) stage (Aerotech, PRO165) that allows contact with a target substrate (traditionally a piece of silicon wafer) connected to the load cell at controlled speeds and forces. The separate optics system provides monitoring capabilities complementary to the load cell, enabling direct visual observation and evaluation of contact and printing events. In general, stamp surfaces compressed against the surface in this manner are allowed a set relaxation time before retraction in the vertical direction. For some specific printing modalities (e.g. shear-based printing), lateral stage displacement can be incorporated into the adhesion test protocols prior to stamp delamination. During retraction of the stamp, the load cell monitors the change in vertical direction forces, providing force-time or force-displacement curves. Figure 1.6a shows a representative curve for a 100 × 100 × 50 μm post molded on the surface of a 1 mm thick piece of PDMS (5:1 monomer:crosslinking agent). The stamp was loaded to 1.5 mN, allowed to relax for 5 seconds, and then delaminated at 10 μm/s. The maximum tensile force during retraction (sharp negative feature) defines the strength of adhesion. Measuring that

change in pull-off force for different retraction velocities provides a characterization of the rate-dependent adhesion of the stamp.[66] The full pull-off force vs. delamination velocity curve for this stamp (velocities ranging 1 – 1000 μm/s) are shown in Figure 1.6b.[102] Modifications to these protocols, where appropriate for testing different stamp geometries, are described in the ensuing chapters.

1.5. Overview of Work

This thesis describes a suite of advanced transfer printing protocols that enable expansion in breadth and diversity of materials and formats that serve as either ink or substrate layers during assembly. Targeted control of adhesion at the stamp/ink interface provides a direct route for enhancing printing efficacy, particularly in adhesiveless systems. This body of work progresses from several simple techniques that are passive nature demonstrating either strong or weak levels of adhesion to a stamp for retrieval and printing, respectively, to more active methods that utilize first adhesion switchability and then ultimately fine control over stamp adhesive strength through the use of targeted mechanical loading. We end by looking at how these and related techniques can be used to assemble multilayer stacks of heterogeneous materials as a route for novel device platforms in silicon nanomembranes.

Chapter 2 describes three techniques designed to affect different levels of adhesion during transfer printing based on the geometry of embossed microstructures on the stamp surface. Systematic studies utilizing stamps with simple line-and-space grating structures on the surface are used to derive a scaling relationship between stamp contact area and overall

adhesion, leading to enhanced printing for fabricating interesting types silicon-on-glass (SOG) transistors. An alternative geometry, which mimics the naturally occurring pedestal geometry of gecko toe pads, is used to demonstrate an extreme adhesive state which may be beneficial for certain ink retrieval scenarios. This geometry, when coupled with a technique for release, can effectively transfer a variety of fully functional devices or their constitutive components. A final set of studies explores the change in adhesive strength that occurs with different forms of PDMS elastomer, particularly low-modulus variants. A new analytical model is developed which accounts for variations in the measured energy release rate curves for this very soft material compared to other stamp material tested.

Chapter 3 presents a more advanced printing protocol, active in nature, which uses hierarchical structures of pyramidal relief on the surface of a stamp to switch between high adhesion states (adhesion-on) to low adhesion states (adhesion-off). Here, mechanical loading of a stamp in the vertical direction controllably alters the contact between a stamp and ink during retrieval and printing, which when coupled with viscoelastic effects of the stamp demonstrates adhesion switching over three orders of magnitude. This remarkable capability is used to deploy silicon platelets over increasingly difficult substrates and in complex, multilayer configurations. Mechanics contact models are developed to explain the adhesive characteristics, optimum surface geometry and dimensions, and minimum contact during release states.

Chapters 4 and 5 extend the previously developed protocols relying on mechanical loading to enhance release from a stamp surface. Chapter 4 demonstrates how targeted shearing of a simple rectangular protrusion from a stamp surface can lead to reversible modulation of stamp adhesion to levels well below those obtained in the slow peel limit of rate-dependent

adhesives. An analytical model to describe the interfacial mechanics responsible for this unprecedented level of control is developed and verified with finite element analysis. Transfer printing yield studies coupled with examples of printed structures reveal interesting capabilities for emerging forms of printed MEMS. Chapter 5 provides a final stamp geometry which incorporates microchannels and reservoirs connected to external pressurization sources to modulate adhesion strength through local inflation of the stamp surface. Critical design parameters reveal that these stamps can achieve near maximal adhesion to an ink through viscoelastic effects of the material as well as the tunable adhesive control of other techniques. We demonstrate how these ideas can be scaled up to multi-reservoir stamps that provide programmable functionality for transfer printing.

Chapter 6 describes how the protocols developed in previous chapters and similar schemes can be used to fabricate interesting device platforms from large area (mm × mm) silicon nanomembranes. We present ideas for fabricating multilayer structures using these materials with early demonstration of a 'print-and-pattern' scheme for aligned, passive light guiding devices. Extension of these concepts to more complex structures such optical phase arrays (OPA) will be discussed.

1.6. References

[1] Y. Chen, A. Pepin, *Electrophoresis* **2001**, *22*, 187.
[2] W.M. Moreau, *Semiconductor lithography*. 1988, New York: Plenum Publishing Co.
[3] J.D. Plummer, M. Deal, P.D. Griffin, *Silicon VLSI technology: fundamentals, practice, and modeling*. 2000, Upper Saddle River: Prentice Hall.

[4] P. Rai-Choudhury, *Handbook of microlithography, micromachining, and microfabrication, Volume 1: Microlithography*. 1997, Stevenage: The Institution of Electrical Engineers.
[5] J.A. Rogers, H.H. Lee, *Unconventional nanopatterning techniques and applications*. 2008, Hoboken: John Wiley & Sons, Inc. 598.
[6] L.F. Thompson, C.O. Willson, M.J. Bowden, *Introduction to microlithography*. 1983, Washington, D.C.: American Chemical Society.
[7] E. Kim, Y. Xia, G.M. Whitesides, *J. Am. Chem. Soc.* **1996**, *118*, 5722.
[8] J.L. Wilbur, A. Kumar, H.A. Biebuyck, E. Kim, G.M. Whitesides, *Nanotechnology* **1996**, *7*, 452.
[9] Y. Xia, E. Kim, G.M. Whitesides, *Chem. Mater.* **1996**, *8*, 1558.
[10] Y. Xia, G.M. Whitesides, *Annu. Rev. Mater. Sci.* **1998**, *28*, 153.
[11] S. Okazaki, *J. Vac. Sci. Technol. B* **1991**, *9*(2829).
[12] D. Brambley, B. Martin, P.D. Prewett, *Adv. Mater. Opt. Electron.* **1994**, *4*, 55.
[13] D.C. Brock, *Understanding Moore's law: four decades of innovation*. 2006, Philadelphia: Chemical Heritage Foundation.
[14] G.E. Moore, *Proc. SPIE* **1995**, 2438.
[15] A.K. Wong, *Resolution enhancement techniques in optical lithography*. 2001, Bellingham: SPIE.
[16] D.P. Sanders, *Chem. Rev.* **2010**, *110*, 321.
[17] Release (May, 2011) *Intel Reinvents Transistors Using New 3-D Structure*. http://newsroom.intel.com/community/intel_newsroom/blog/2011/05/04/intel-reinvents-transistors-using-new-3-d-structure.
[18] M. Geissler, Y. Xia, *Adv. Mater.* **2004**, *16*, 1249.
[19] Y. Xia, G.M. Whitesides, *Angew. Chem. Int. Ed.* **1998**, *37*, 551.
[20] W.R. Childs, R.G. Nuzzo, *J. Am. Chem. Soc.* **2002**, *124*, 13583.
[21] P. Kim, K.W. Kwon, M.C. Park, S.H. Lee, S.M. Kim, K.Y. Suh, *Biochip J.* **2008**, *2*, 1.
[22] H. Schmid, B. Michel, *Macromolecules* **2000**, *33*, 3042.
[23] J.A. Rogers, R.G. Nuzzo, *Mater. Today* **2005**, *8*, 50.
[24] D.B. Weibel, W.R. DiLuzio, G.M. Whitesides, *Nat. Rev. Microbiol.* **2007**, *5*, 209.
[25] A. Kumar, G.M. Whitesides, *Appl. Phys. Lett.* **1993**, *63*, 2002.
[26] B. Michel, A. Bernard, A. Bietsch, E. Delamarche, M. Geissler, D. Juncker, H. Kind, J.-P. Renault, H. Rothuizen, H. Schmid, P. Schmidt-Winkel, R. Stutz, H. Wolf, *IBM J. Res. & Dev.* **2001**, *45*, 697.
[27] J. Yeom, M.A. Shannon, *Adv. Func. Mater.* **2010**, *20*, 289.
[28] C. Thibault, V. LeBerre, S. Casimirius, E. Trevisiol, J. Francois, C. Vieu, *J. Nanobiotechnology* **2005**, *3*, 7.
[29] M. Kim, Y.S. Kim, *J. Am. Chem. Soc.* **2007**, *129*, 11304.
[30] A.M. Bowen, R.G. Nuzzo, *Adv. Func. Mater.* **2009**, *19*, 3243.
[31] E. Menard, M.A. Meitl, Y. Sun, J.-U. Park, D.J. Shir, Y.-S. Nam, S. Jeon, J.A. Rogers, *Chem. Rev.* **2007**, *107*, 1117.
[32] R.H. Baughman, A.A. Zakhidov, W.A. deHeer, *Science* **2002**, *297*, 787.
[33] Q. Cao, J.A. Rogers, *Adv. Mater.* **2009**, *21*, 29.
[34] T. Dürkop, S.A. Getty, E. Cobas, M.S. Fuhrer, *Nano Lett.* **2004**, *4*, 35.

[35] J. Kong, N.R. Franklin, C. Zhou, M.G. Chapline, S. Peng, K. Cho, H. Dai, *Science* **2000**, *287*, 622.
[36] G. Malliaras, R. Friend, *Phys. Today* **2005**, *58*, 53.
[37] T.W. Kelley, P.F. Baude, C. Gerlach, D.E. Ender, D. Muyres, M.A. Haase, D.E. Vogel, S.D. Theiss, *Chem. Rev.* **2004**, *16*, 4413.
[38] J.M.J. Frechet, *Science* **1994**, *263*, 1710.
[39] P. Bjork, S. Holmstrom, O. Inganas, *Small* **2006**, *2*, 1068.
[40] H. Nakao, M. Gad, S. Sugiyama, K. Otobe, T. Ohtani, *J. Am. Chem. Soc.* **2003**, *125*, 7162.
[41] A.A. Yu, F. Stellacci, *J. Mater. Chem.* **2006**, *16*, 2868.
[42] E. Menard, K.J. Lee, D.-Y. Khang, R.G. Nuzzo, J.A. Rogers, *Appl. Phys. Lett.* **2004**, *84*, 5398.
[43] K.J. Lee, J. Lee, H. Hwang, Z.J. Reitmeier, R.F. Davis, J.A. Rogers, R.G. Nuzzo, *Small* **2005**, *1*, 1164.
[44] Y. Sun, J.A. Rogers, *Adv. Mater.* **2007**, *19*, 1897.
[45] Y. Sun, H.-S. Kim, E. Menard, S. Kim, I. Adesida, J.A. Rogers, *Small* **2006**, *2*, 1330.
[46] A.J. Baca, J.-H. Ahn, Y. Sun, M.A. Meitl, E. Menard, H.-S. Kim, W.M. Choi, D.-H. Kim, Y. Huang, J.A. Rogers, *Angew. Chem. Int. Ed.* **2008**, *47*, 5524.
[47] Y.-L. Loo, R.L. Willett, K.W. Baldwin, J.A. Rogers, *J. Am. Chem. Soc.* **2002**, *124*, 7654.
[48] E.J. Smythe, M.D. Dickey, G.M. Whitesides, F. Capasso, *ACS Nano* **2009**, *3*, 59.
[49] K. Felmet, Y.-L. Loo, Y. Sun, *Appl. Phys. Lett.* **2004**, *85*, 3316.
[50] H. Schmid, H. Wolf, R. Allenspach, H. Riel, S. Karg, B. Michel, E. Delamarche, *Adv. Func. Mater.* **2003**, *13*, 145.
[51] T.-H. Kim, W.M. Choi, D.-H. Kim, M.A. Meitl, E. Menard, H. Jiang, J.A. Carlisle, J.A. Rogers, *Adv. Mater.* **2008**, *20*, 2171.
[52] A. Kawahara, H. Katsuki, M. Egashira, *Sens. Actuator, B* **1998**, *49*, 273.
[53] J.-H. Ahn, H.-S. Kim, K.J. Lee, Z. Zhu, E. Menard, R.G. Nuzzo, J.A. Rogers, *IEEE Electron Device Lett.* **2006**, *27*, 460.
[54] S. Mack, M.A. Meitl, A.J. Baca, Z.-T. Zhu, J.A. Rogers, *Appl. Phys. Lett.* **2006**, *88*, 213101.
[55] K.J. Lee, M.A. Meitl, J.-H. Ahn, J.A. Rogers, R.G. Nuzzo, V. Kumar, I. Adesida, *J. Appl. Phys.* **2006**, *100*, 124507.
[56] E. Menard, R.G. Nuzzo, J.A. Rogers, *Appl. Phys. Lett.* **2005**, *86*, 093507.
[57] S.-I. Park, Y. Xiong, R.-H. Kim, P. Elvikis, M. Meitl, D.-H. Kim, J. Wu, J. Yoon, C.-J. Yu, Z. Liu, Y. Huang, K.-C. Hwang, P. Ferreira, X. Li, K. Choquette, J.A. Rogers, *Science* **2009**, *325*, 977.
[58] J.-H. Choi, K.-H. Kim, S.-J. Choi, H.H. Lee, *Nanotechnology* **2006**, *17*, 2246.
[59] D.-H. Kim, Y.-S. Kim, J. Wu, Z. Liu, J. Song, H.-S. Kim, Y.Y. Huang, K.-C. Hwang, J.A. Rogers, *Adv. Mater.* **2009**, *21*, 3703.
[60] D.-H. Kim, J.-H. Ahn, H.-S. Kim, K.J. Lee, T.-H. Kim, C.-J. Yu, R.G. Nuzzo, J.A. Rogers, *IEEE Electron Device Lett.* **2008**, *29*, 73.
[61] J.-H. Ahn, H.-S. Kim, K.J. Lee, S. Jeon, S.J. Kang, Y. Sun, R.G. Nuzzo, J.A. Rogers, *Science* **2006**, *314*, 1754.
[62] I. Jung, G. Shin, V. Malyarchuk, J.S. Ha, J.A. Rogers, *Appl. Phys. Lett.* **2010**, *96*, 021110.

[63] H.C. Ko, M.P. Stoykovich, J. Song, V. Malyarchuk, W.M. Choi, C.-J. Yu, J.B.G. III, J. Xiao, S. Wang, Y. Huang, J.A. Rogers, *Nature* **2008**, *454*, 748.
[64] J. Yoon, A.J. Baca, S.-I. Park, P. Elvikis, J.B.G. III, L. Li, R.H. Kim, J. Xiao, S. Wang, T.-H. Kim, M.J. Motala, B.Y. Ahn, E.B. Duoss, J.A. Lewis, R.G. Nuzzo, P.M. Ferreira, Y. Huang, A. Rockett, J.A. Rogers, *Nat. Mater.* **2008**, *7*, 907.
[65] A.J. Baca, K.J. Yu, J. Xiao, S. Wang, J. Yoon, J.H. Ryu, D. Stevenson, R.G. Nuzzo, A.A. Rockett, Y. Huang, J.A. Rogers, *Energy Environ. Sci.* **2010**, *3*, 208.
[66] S. Kim, J. Wu, A. Carlson, S.H. Jin, A. Kovalsky, P. Glass, Z. Liu, N. Ahmed, S.L. Elgan, W. Chen, P.M. Ferreira, M. Sitti, Y. Huang, J.A. Rogers, *P. Natl. Acad. Sci. U.S.A.* **2010**, *107*, 17095.
[67] D. Chanda, K. Shigeta, S. Gupta, T. can, A. Carlson, A. Mihi, A.J. Baca, G.R. Bogart, P. Braun, J.A. Rogers, *Nat. Nanotechnol.* **2011**, *6*, 402.
[68] D.-H. Kim, N. Lu, R. Ma, Y.-S. Kim, R.-H. Kim, S. Wang, J. Wu, S.M. Won, H. Tao, A. Islam, K.J. Yu, T.-I. Kim, R. Chowdhury, M. Ying, L. Xu, M. Li, H.-J. Chung, H. Keum, M. McCormick, P. Liu, Y.-W. Zhang, F.G. Omenetto, Y. Huang, T. Coleman, J.A. Rogers, *Science* **2011**, *333*, 838.
[69] H. Kim, E. Brueckner, J. Song, Y. Li, S. Kim, C. Lu, J. sulking, K. Choquette, Y. Huang, R.G. Nuzzo, J.A. Rogers, *Proc. Natl. Acad. Sci. U.S.A.* **2011**, *108*(25), 10072.
[70] T.-H. Kim, K.-S. Cho, E.K. Lee, S.J. Lee, J. Chae, J.W. Kim, D.H. Kim, J.-Y. Kwon, S.Y. Lee, B.L. Choi, Y. Kuk, J.M. Kim, K. Kim, *submitted* **2010**.
[71] Q. Cao, H.-S. Kim, N. Pimparkar, J.P. Kulkarni, C. Wang, M. Shim, K. Roy, M.A. Alam, J.A. Rogers, *Nature* **2008**, *454*, 495.
[72] Q. Cao, J.A. Rogers, *Nano Res.* **2008**, *1*, 259.
[73] K.J. Lee, H. Ahn, M.J. Motala, R.G. Nuzzo, E. Menard, J.A. Rogers, *J. Micromech. Microeng.* **2010**, *20*, 075018.
[74] H.C. Ko, A.J. Baca, J.A. Rogers, *Nano Lett.* **2006**, *6*, 2318.
[75] M.A. Meitl, Z.-T. Zhu, V. Kumar, K.J. Lee, X. Feng, Y.Y. Huang, I. Adesida, R.G. Nuzzo, J.A. Rogers, *Nat. Mater.* **2006**, *5*, 33.
[76] T.-H. Kim, A. Carlson, J.-H. Ahn, S.M. Won, S. Wang, Y. Huang, J.A. Rogers, *Appl. Phys. Lett.* **2009**, *94*, 113502.
[77] X. Feng, M.A. Meitl, A.M. Bowen, Y. Huang, R.G. Nuzzo, J.A. Rogers, *Langmuir* **2007**, *23*, 12555.
[78] Y. Sun, S. Kim, I. Adesida, J.A. Rogers, *Appl. Phys. Lett.* **2005**, *87*, 083501.
[79] A.J. Baca, M.A. Meitl, H.C. Ko, S. Mack, H.-S. Kim, J. Dong, P.M. Ferreira, J.A. Rogers, *Adv. Func. Mater.* **2007**, *17*, 3051.
[80] K.J. Lee, M.J. Motala, M.A. Meitl, W.R. Childs, E. Menard, A.K. Shim, J.A. Rogers, R.G. Nuzzo, *Adv. Mater.* **2005**, *17*, 2332.
[81] B.D. Gates, Q. Xu, M. Stewart, D. Ryan, C.G. Willson, G.M. Whitesides, *Chem. Rev.* **2005**, *105*, 1171.
[82] G.C. Randall, P.S. Doyle, *Proc. Natl. Acad. Sci. U.S.A.* **2005**, *102*, 10813.
[83] B.D. Gates, Q. Xu, J.C. Love, D.B. Wolfe, G.M. Whitesides, *Annu. Rev. Mater. Res.* **2004**, *34*, 339.
[84] F. Hua, Y. Sun, A. Gaur, M.A. Meitl, L. Bilhaut, L. Rotkina, J. Wang, P. Geil, M. Shim, J.A. Rogers, *Nano Lett.* **2004**, *4*, 2467.
[85] A. Bietsch, B. Michel, *J. Appl. Phys.* **2000**, *88*, 4310.

[86] J.-H. Ahn, H.-S. Kim, E. Menard, K.J. Lee, Z. Zhu, D.-H. Kim, R.G. Nuzzo, J.A. Rogers, I. Amlani, V. Kushner, S.G. Thomas, T. Duenas, *Appl. Phys. Lett.* **2007**, *90*, 2135011.
[87] Y. Sun, E. Menard, J.A. Rogers, H.-S. Kim, S. Kim, G. Chen, I. Adesida, R. Dettmer, R. Cortez, A. Tewksbury, *Appl. Phys. Lett.* **2006**, *88*, 183509.
[88] Y. Sun, D.-Y. Khang, F. Hua, K. Hurley, R.G. Nuzzo, J.A. Rogers, *Adv. Func. Mater.* **2005**, *15*, 30.
[89] Y. Sun, J.A. Rogers, *Nano Lett.* **2004**, *4*, 1953.
[90] H.-C. Yuan, J. Shin, G. Qin, L. Sun, P. Bhattacharya, M.G. Lagally, G.K. Celler, Z. Ma, *Appl. Phys. Lett.* **2009**, *94*, 013102.
[91] T.L. Anderson, *Fracture mechanics: fundamentals and applications*. 2nd. ed. 1995, Boca Raton: CRC Press.
[92] K.H. Tsai, K.S. Kim, *Int. J. Solids. Struct.* **1993**, *30*, 1789.
[93] A.N. Gent, *J. Polym. Sci. B: Polym. Phys.* **1994**, *32*, 1543.
[94] A.N. Gent, *Langmuir* **1996**, *12*, 4492.
[95] K.S. Kim, J. Kim, *J. Eng. Mater. Technol.* **1988**, *110*, 266.
[96] F. Saulnier, T. Ondarcuhu, A. Aradia, E. Raphael, *Macromolecules* **2004**, *37*, 1067.
[97] K. Shull, D. Ahn, W.-L. Chem, C.M. Flanigan, A. Crosby, *Macromol. Chem. Phys.* **1998**, *199*, 489.
[98] M.L. Williams, R.F. Landel, J.D. Ferry, *J. Am. Chem. Soc.* **1955**, *77*, 3701.
[99] I.M. Ward, J. Sweeney, *The Mechanical Properties of Solid Polymers*. 2nd ed. 2004, West Sussex: John Wiley & Sons, Ltd.
[100] H.K. Mueller, W.G. Knauss, *J. Appl. Mech.* **1971**, *38*, 483.
[101] S. Burroughs, R. Conner, B. Furman, E. Menard, A. Gray, M. Meitl, S. Bonafede, D. Kneeburg, K. Ghosal, R. Bukovnic, W. Wagner, S. Seel, M. Sullivan, *A new approach for a low cost CPV module design utilizing micro-transfer printing technology*, in *CPV-6*. 2010: Freiburg, Germany.
[102] A. Carlson, H.-J. Kim-Lee, J. Wu, P. Elvikis, H. Cheng, A. Kovalsky, S. Elgan, Q. Yu, P.M. Ferreira, Y. Huang, K.T. Turner, J.A. Rogers, *Appl. Phys. Lett.* **2011**, *98*, 264104.

1.7. Figures

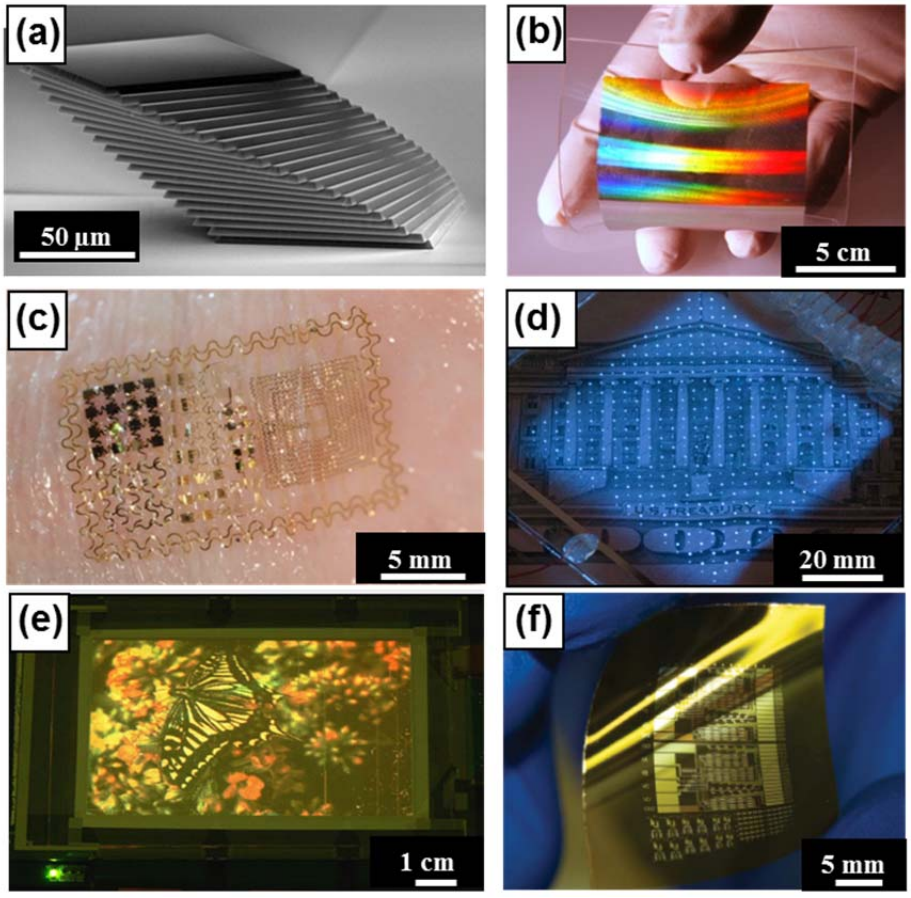

Figure 1.1. Representative examples of unusual constructs, devices and integrated systems enabled by the techniques of transfer printing. (a) SEM image of a printed multilayer stack of silicon platelets. (b) Photograph of a large area (10 cm x 10 cm) negative index metamaterial (NIM) comprised of alternating layers of Ag and MgF_2 in a fishnet pattern printed onto flexible substrate. (c) Photograph of an 'epidermal' electronic device, conformally laminated onto the surface of the skin. The key components of the system, from radio frequency antennae, inductive coils, inductors, capacitors, silicon diodes, strain gauges, light emitting diodes (LEDs), temperature sensors, electrophysiological sensors and field effect transistors, are all fabricated by transfer printing. (d) Image of a partially transparent array of ultrathin, microscale, blue LEDs printed from a source wafer onto a thin strip of plastic. (e) Picture of a 4-inch, full-color quantum dot (QD) LED display that uses printed collections of QDs in an active matrix configuration of 320 × 240 pixels. (f) Photograph of a flexible integrated circuit (four-bit decoder composed of 88 transistors) that uses printed networks of single walled carbon nanotubes for the semiconductor.

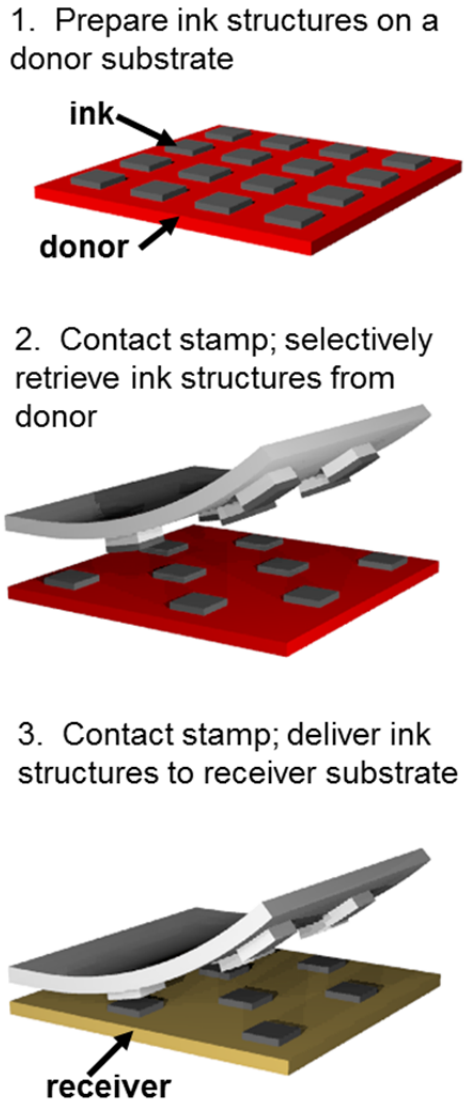

Figure 1.2. Protocols for kinetically controlled transfer printing via an elastomeric stamp. The stamp makes contact with a donor substrate that supports pre-fabricated micro or nanostructures. Peeling the stamp away leads to removal of selected structures from the donor substrate. Printing onto a receiving substrate completes the process. Here, chemical, thermal and/or mechanical strategies facilitate the inking and printing processes, to enable high yield, efficient operation.

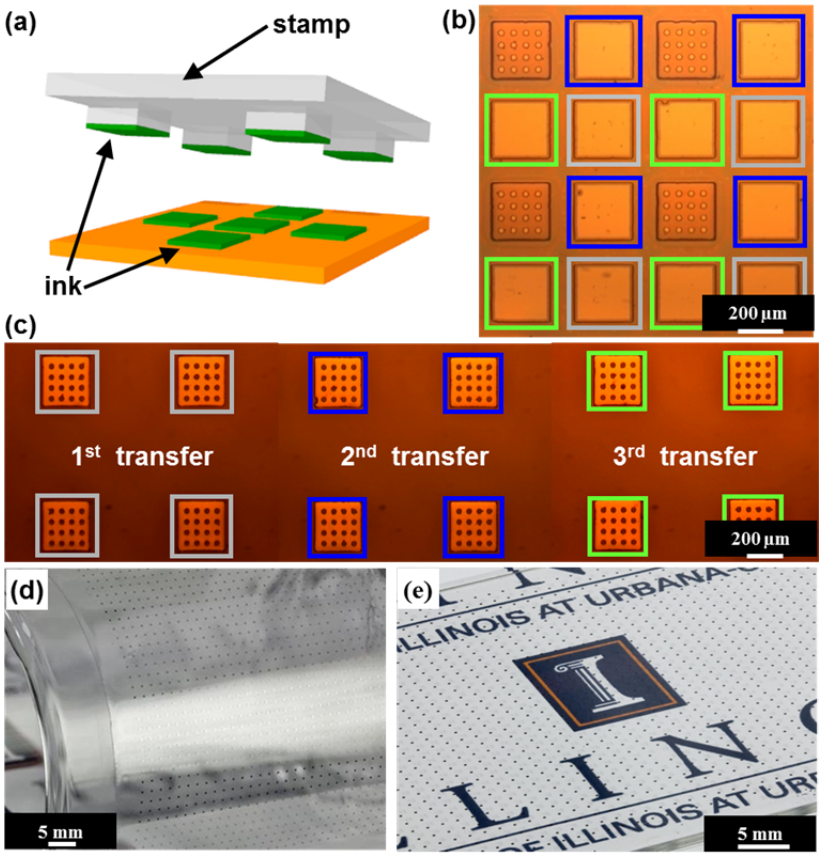

Figure 1.3. (a) Schematic illustration of retrieving and printing selected sets of microstructures (platelets designed to yield AlInGaP LEDs) with a stamp. (b) Optical micrograph of a donor substrate after three cycles of printing. Each colored box (gray, blue, green) highlights different sets of platelets retrieved in sequential cycles of printing. (c) Micrograph of a receiving substrate after printing from the donor substrate of (b), illustrating the concept of area expansion, in which dense arrays of microstructures are distributed into sparse configurations. The gray, blue and green boxes show platelets that correspond to those highlighted in a similar manner in (b). (d) Large-scale collection of structures (~1600 in a square array with pitch of 1.4 mm) printed onto a thin, flexible sheet of plastic, shown here wrapped onto a cylindrical glass substrate. (e) Similar collection of structures printed onto a plate of glass.

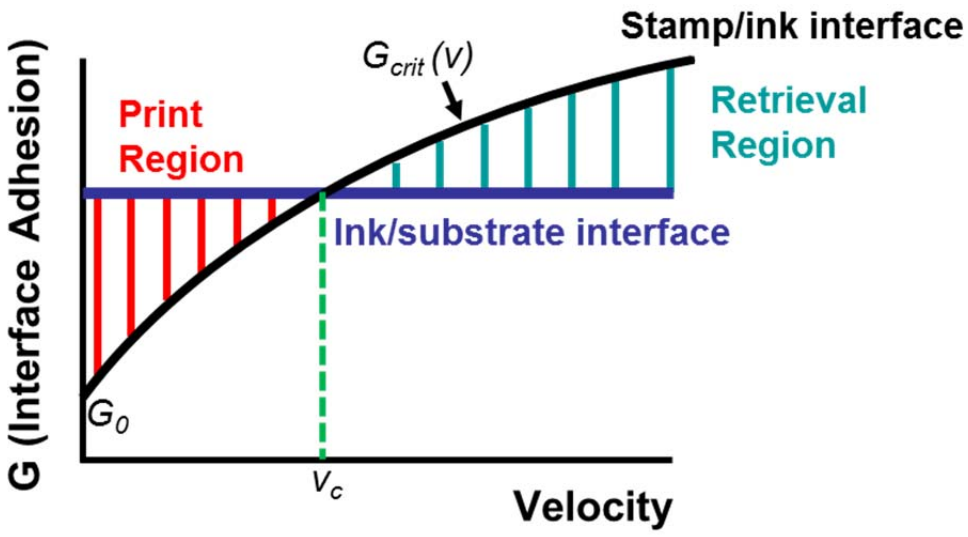

Figure 1.4. Energy release rates for stamp/ink and ink/substrate interface. Intersection of the curves determines the critical velocity, v_c, and defines the printing and pick-up regimes.

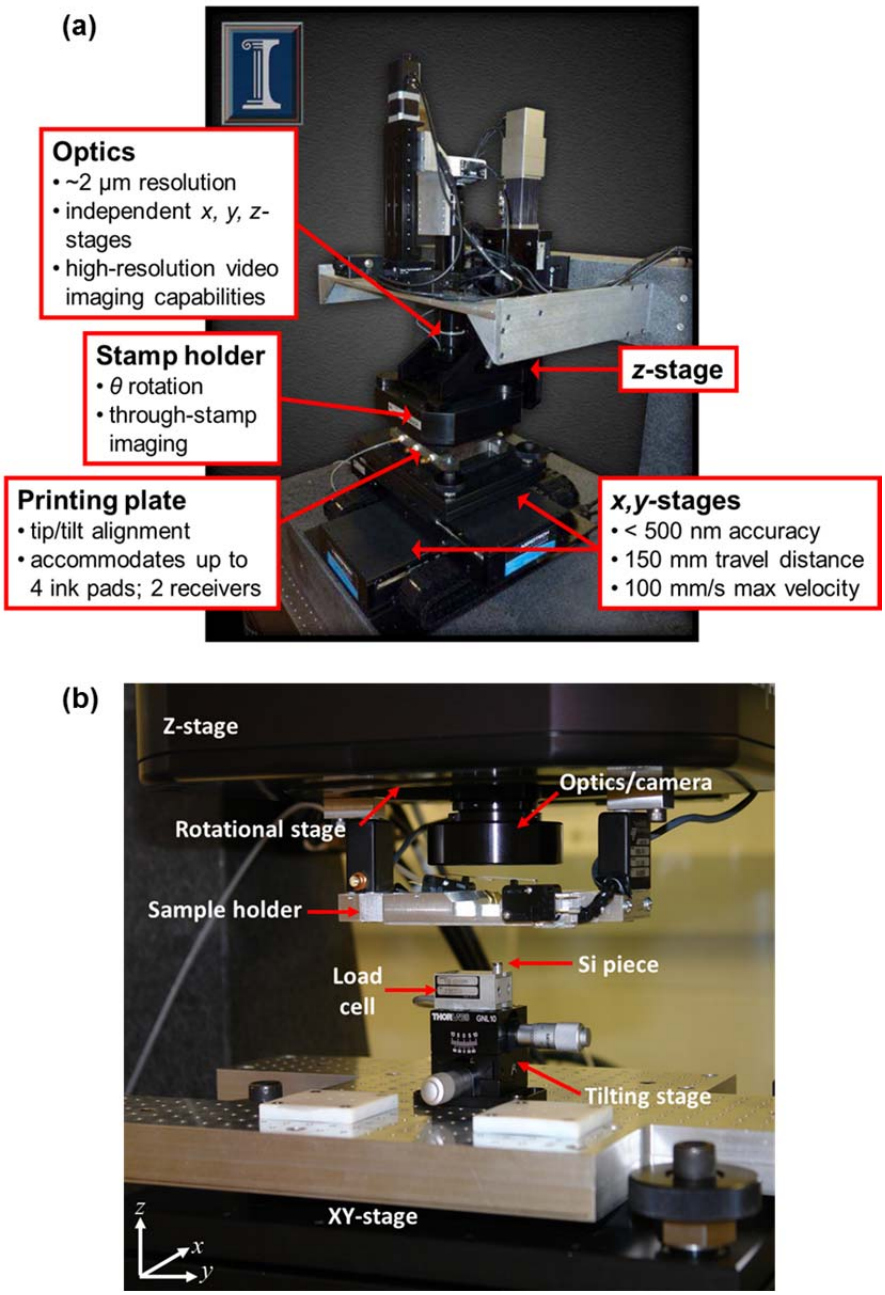

Figure 1.5. (a) Picture of a high-throughput automated tool for transfer printing developed at the University of Illinois with key components labeled. (b) Custom adhesion setup integrated into the automated tool in (a).

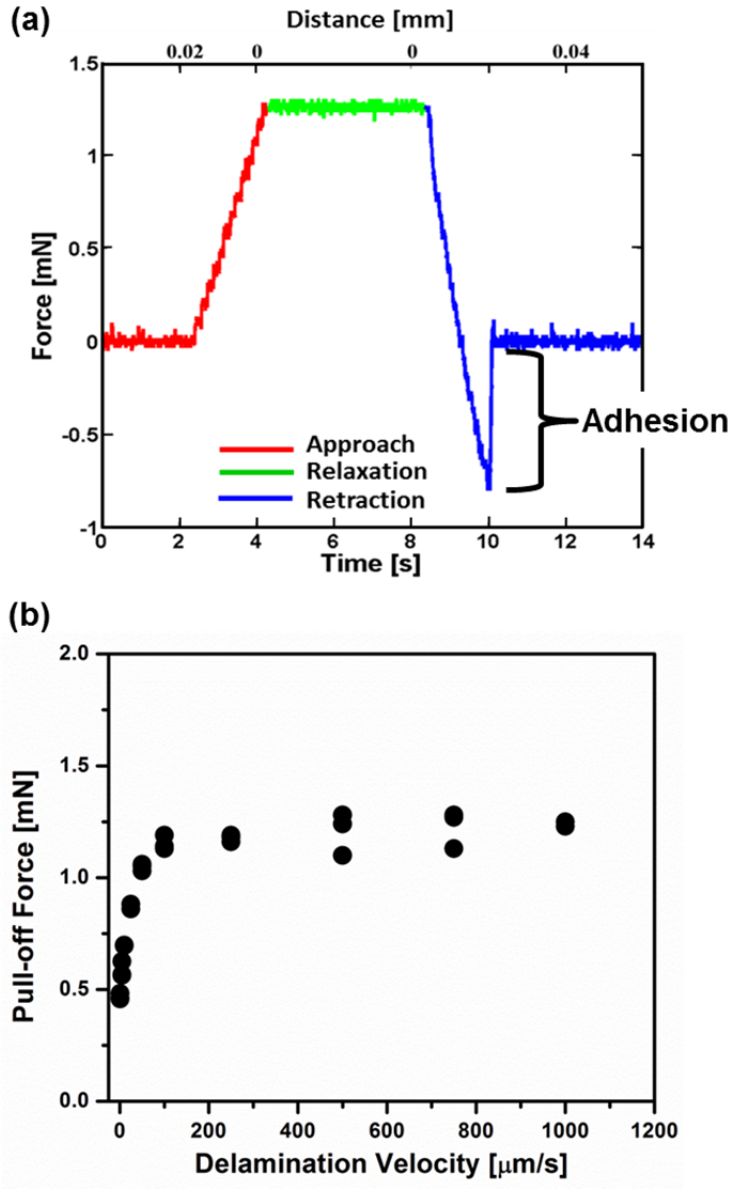

Figure 1.6. (a) A representative force-time, force-distance curve as recorded by the load cell during stamp approach, relaxation, and vertical retraction. The sharp negative feature (blue) shows maximum tensile force, a measure of the stamp adhesive strength. (b) Representative force-velocity plot for a 100 × 100 × 50 μm single-post molded PDMS stamp showing the rate-dependent behavior of the material.

CHAPTER 2

PASSIVE MECHANISMS FOR ADHESION MODULATION IN KINETICALLY CONTROLLED ADHESIVELESS TRANSFER PRINTING: TECHNIQUES BASED ON CONTACT AREA MODULATION, PEDESTAL SURFACE RELIEF, AND FINITE DEFORMATION MECHANICS[1,2,3]

2.1. Abstract

This chapter describes a collection of transfer protocols designed to complement the current capabilities of adhesiveless or 'dry' transfer printing schemes based on the kinetic-variability of elastomeric stamps. The developed techniques are passive in nature, relying on optimized microstructures of surface relief or modulation of the mechanical and material properties of the stamp to alter the adhesive behavior of a poly(dimethylsiloxane) (PDMS) stamp. Alteration occurs in a variety of modes: decreased adhesion during printing (adhesion-off state) demonstrated via contact area modulation at the ink/stamp interface; increased adhesive forces during retrieval (adhesion-on state) demonstrated through use of relief features having re-entrant pedestal geometries; and alteration of the steady-state critical energy release rate for a low-modulus PDMS stamp. Experimental measurement of velocity-dependent adhesive strength reveals key scaling properties and provides a means for comparison to developed theoretical expectations. For low-modulus stamp materials, a new analytical expression for the energy release rate is obtained and used to determine the critical delamination velocity in terms of the critical energy release rates and the tensile stiffness of the stamp. The capabilities of these

[1] Reprinted, with permission from T.-H. Kim, A. Carlson, J.-H. Ahn, S.M. Won, S. Wang, Y. Huang, J.A. Rogers, "Kinetically Controlled, Adhesiveless Transfer Printing Using Microstructured Stamps," *App. Phys. Lett.* **94**, 113502 (2009). Copyright: 2009 American Institute of Physics.

[2] Reprinted, with permission from S. Kim, A. Carlson, H. Cheng, S. Lee, J.-K. Park, Y. Huang, J.A. Rogers, "Enhanced Adhesion with Pedestal-Shaped Elastomeric Stamps for Transfer Printing," *submitted*.

[3] Reprinted, with permission from X. Feng, A.M. Bowen, A. Carlson, Y. Huang, R.G. Nuzzo, J.A. Rogers, "An Experimental and Theoretical Study of Finite-Deformation Mechanics in Kinetically Controlled Transfer Printing With Soft Stamps," *submitted*.

techniques are demonstrated through several examples of heterogeneous assembly including transfer of fully fabricated microscale light-emitting diodes (μ-ILEDS) and formation of transistor devices that use nanoribbons of silicon transfer printed directly onto glass substrates without adhesive layers for high-performance (mobilities >325 cm^2/Vs, on/off ratios $>10^5$) single crystal silicon on glass (SOG) technology.

2.2. Introduction

Elastomeric materials such as polydimethylsiloxane (PDMS) have been widely used as stamps for transfer printing, a patterning process which transfers solid objects (e.g. 'inks' - semiconducting nanomaterials,[1-5] single walled carbon nanotubes,[6-9] microdevices,[10-13] and others) from surfaces on which they are fabricated ('donor') to foreign substrates ('receiver' or 'target') such as semiconductor wafers, glass plates, plastic sheets and rubber slabs.[14-17] The ability to separate the fabrication of these inks, which often require high temperatures and harsh chemical processing environments, from the receiving substrate presents a range of benefits. First, it allows use of a greatly expanded range of receiver materials, including those with limited thermal and chemical stability. Second by allowing essentially any solid material to be printed on any surface, this type of process provides a facile means for fabrication of complex heterogeneous devices made up of a wide range of distinct materials.[13, 14, 18] Furthermore, through choice of appropriate protocols, transfer printing represents a massively parallel assembly technique to deploy the diversity of ink materials across a desired substrate in a deterministic manner, with full implemented control over pitch, alignment, and configuration.[10]

In the most robust version of the transfer printing process, adhesion to the stamp arises from nonspecific, van der Waals interactions,[19, 20] while that to the target substrate is mediated by an adhesive, such as a photocurable polymer[13, 21] or functional molecular patterns such as self-assembled monolayers.[22, 23] A more interesting and valuable transfer process exploits the viscoelastic nature of the stamps to control adhesion through peeling rate, whereby inking and printing can be accomplished at high and low peel rates, respectively, without any adhesives.[16, 20] This operation is contingent upon two conditions: first, that the adhesive strength of the stamp is sufficiently large to overcome the tethering forces that anchor the ink to a donor substrate during retrieval and, second, the strength of ink adhesion to the target substrate is sufficiently large to overcome the van der Waals adhesion to the stamp, even in the limit of a slow peel print. Such printing often presents a practical challenge in part due to the reduced contact areas between many inks and target substrates compared to contact between inks and flat, soft, conformable stamps.

Embossed relief features are often incorporated into the surface of a stamp, as described in Chapter 1, to effect selective retrieval and printing of ink materials. The surface microstructures, however, can also provide a viable mechanism for altering the stamp adhesive strength through optimized geometry and arrangement. Additionally, exploiting well-established casting and curing methods of soft lithography,[22, 24, 25] a diversity of relief features can be formed based on the myriad pattern geometries afforded by photolithography. The influence of surface microstructure on interfacial adhesion is evidenced extensively by studies on synthetic 'dry' adhesives which mimic naturally occurring systems.[26-30] Two important geometries recently explored in the past decade are those based on rectangular or circular punches[31] (simulating e.g. hairy fibers) and spatulated fibers[29, 32] (simulating e.g. gecko foot hairs). In

both systems, optimized geometry is a critical factor for determining the exhibited adhesive characteristics. For example, flat punch shaped fibers demonstrate an inverse relationship with size of the adhesive system, requiring greater numbers of small, highly specialized structures to support larger loads;[26] without the scaling, the microstructured surfaces provide equivalent or potentially inferior adhesive strength compared to a flat surface.

Alternatively, spatulated fibers which have a narrow central post connected to a terminal flat plate at the contact surface, have demonstrated a variety of adhesion enhancements in both vertical and direction-dependent delamination modalities.[27, 29, 32, 33] Systematic studies have shown that factors such as tip shape and size, angle of contact, and backing layer thickness, all have significant effects on adhesive characteristics.[29, 33-35] One seemingly critical aspect of this optimized design is the ability to deform (due to flexibility of the central post) to maximize contact with a surface (such as non-planar or rough substrates) while ultilizing flat plates to provide interesting mechanical effects during interfacial sepation.[32] Such designs have been explored for applications requiring reversible, anti-fouling synthetic systems and can be important when fabricating stamps for adhesiveless printing.

In this chapter, we borrow patterning concepts similar to those developed for dry adhesives to introduce two stamp geometries which demonstrate modulated adhesion during delivery and retrieval of solid ink layers. The first utilizes a simple line-and-space grating structure embossed into the surface of thin strips of PDMS elastomer to controllably tune the interfacial contact area to two model ink materials, flat thin films of gold and collections of single crystal silicon nanoribbons. Scaling of the adhesion strength with contact area is demonstrated through high yield printing studies of the nanoribbons onto glass substrates for use in high performance silicon on glass (SOG) transistors.[36, 37] The second geometry mimics the

naturally occurring pedestal shape to provide adhesion enhancement during retrieval. Experimental adhesion tests and finite element analysis for stamps with systematically variant geometries demonstrate large adhesion enhancements stemming primarily from reducing stress concentrations surrounding the stamp contact perimeter. Delivery of fully functional microscale light-emitting diodes (μ-ILEDs) and silicon chips onto a bare silicon substrate demonstrate the printing capability of these designs.

Finally, in a related concept, instead of modulating stamp adhesion strength through microstructured relief, alteration of the stamp mechanical and material properties (e.g. stiffness, elastic modulus, etc) can provide pathways for adhesion enhancement. We discuss one such technique utilizing soft, low-modulus variants of PDMS and their impact on determining a critical velocity separating the retrieval and printing regimes. An analytical expression is derived for this critical velocity in terms of the material properties and mechanical energy stored in the system. Experimental measurements of the critical velocity are presented to verify the developed model in the context of rate and modulus-dependent peel data.

2.3. Results and Discussion

2.3.1. Enhanced Ink Release via Line-and-Space Surface Relief

Simple line-and-space grating structures embossed into the surface of a PDMS stamp (10:1 monomer:crosslinking agent) were used to evaluate the effect of contact area modulation on transfer printing efficacy. Figure 2.1(a) presents a schematic illustration of the adhesiveless transfer process using a stamp containing representative relief geometry. Such features were comprised of rectangular ridges having varying widths and pitch arrayed perpendicular to the

direction of stamp delamination, as indicated in the schematic. Here, the ink consists of thin ribbons of silicon with lengths much larger than the width of the stamp relief structures. After contacting the stamp against the ink, the nanoribbons are separated from the donor substrate by removing the stamp with a high peeling rate.[16, 20] Placing the inked stamp in contact with a flat target substrate, and then removing at low peeling rate affects transfer and completes the process. The reduced contact area associated with the relief structure facilitates release to achieve overall yields that are greater than possible with flat stamps. Surface and cross-sectional scanning electron microscope (SEM) images of a representative structured stamp made by this procedure appear in Figures 2.1b, c, respectively. By varying the geometry of the surface relief, particularly through ridge dimension and spacing, stamps with nearly any ratio of raised to recessed regions can be produced. In well-designed systems only the raised regions make contact with the ink and this contact area, as defined by the coverage of raised regions, is a critical parameter that controls the strength of adhesion between the stamp and the ink.

For high yield printing of nanoribbons, the relative adhesive strength of the ink to the stamp must be less than that to the substrate layer.[20] The former quantity can be evaluated explicitly by determining the energy released during separation of the ribbons from the stamp at a steady-state velocity.[16, 20, 38-40] In a simple tape peel test, this energy release rate, G, is related to the stamp width, w, and the applied force, F, by $G = F/w$. Due to stamp viscoelasticity, the energy release rate at the ink/stamp interface is strongly velocity-dependent, i.e. $G^{ink/stamp}(v)$.[20, 41-43] Thus, to print, this energy release rate must be less than the corresponding G-value between the nanoribbons and the target substrate, $G^{ink/stamp}(v) < G^{ink/target}$. For most cases where the ink and target are non-viscoelastic, $G^{ink/target}$ is constant.[16, 20] In a similar analysis to Feng, *et al.*, who studied non-continuous contacting ink/stamp layers (i.e.

segmented inks or patterned stamps), the average energy release rate, in the absence of contact between substrate and stamp, will be related to the fractional contact area *f* at the stamp/ink interface, $G_{pr\,\mathrm{int}} = fG^{ink/stamp}(v)$.[20] This suggests that the adhesive strength for the stamp/nanoribbon/substrate system should scale proportionally with the contact area.

Ninety degree peel tests[20, 39, 41] were conducted to determine quantitatively the stamp adhesive strength as a function of contact area with a continuous ink layer. Patterned PDMS stamps 1 mm thick were cleaned with ethanol, dried under nitrogen, and laminated against a 1 mm thick glass slide (Fisher Scientific) coated with gold (100 nm). Applying constant loads to one end of the stamp initiated delamination from the gold film. The distance travelled by the delamination front, the point of separation between the stamp and ink layer, and time were obtained by video recordings of each peeling event. From the resulting displacement-time profiles, steady-state separation velocities were determined for each applied load with the corresponding energy release rates calculated from the load and stamp width. Figure 2.2(a) illustrates the velocity-dependent energy release rate for a flat stamp (100% contact) and for structured stamps having 60% contact area (lines, 30 μm widths, 20 μm spaces, 15 μm depth) and 40% contact area (lines, 20 μm widths, 30 μm spaces, 15 μm depth). Qualitatively, decreasing the contact area leads to a corresponding decrease in the adhesive strength. Removing contact area effects by dividing the velocity-dependent energy release rates by *f* reveals a common master adhesion curve, as shown in Figure 2.2(b). The results, while validating a basic prediction of the theory, may not exhibit the same level of quantitative agreement for all relief geometries and peel directions. However, the general trend toward lower adhesion for lower contact area should remain valid for relief features of a given type.

Adhesion reduction through contact area can be used to advantage for printing, as demonstrated in Figure 2.3 with stamps having different relief patterns. The left panels of Figures 2.3a-c show optical micrographs of arrays of 300 nm-thick single crystal Si nanoribbons (20 μm width, 100 μm length) printed onto glass substrates by the stamps imaged in the corresponding right panels. For the flat stamp of Figure 2.3a (control, 100% contact area) the transfer printing yield is 20%. However, for the patterned regions of Figure 2.3b (lines, 1 μm widths, 0.7 μm spaces; 1.5 μm depth, 60% contact area) and Figure 2.3c (lines, 1 μm widths, 1.3 μm spaces, 1.5 μm depth, 44% contact area) the printing yield is 46% and 85%, respectively. In all cases, as for the tape peel tests, delamination occurred perpendicular to the relief features on the stamp and yields were limited by printing, rather than the inking part of the process. Additional measurements of this type, shown in Figure 2.3d, provide a more complete relationship between the yield (%) and contact area (%).

Interfacial contact area also influences the efficacy of both the inking and printing steps in the total transfer printing process. For efficient inking, f must be greater than $f_{\min} = G^{ink/donor} / G(v_{\max})$, a system-dependent minimum contact area necessary for ink retrieval. $G^{ink/donor}$ and $G(v_{\max})$ are the energy release rates at the ink/donor interface and at maximum peeling velocity, v_{max}, respectively. For the grating structures examined here, complete retrieval of ribbons (i.e. inking) occurred with stamps having at least 40% contact area; below this threshold, adhesion to the stamp was not sufficiently strong. In a similar manner, the contact area for printing structures must be smaller than $f_{\max} = G^{ink/target} / G_0$ where G_0 is an empirical zero-velocity critical energy release rate;[20, 41, 42] values of f greater than this maximum result in incomplete release from the stamp. In the case of the 1 μm-line width/1.5 μm-space stamp

(40% contact area), the yield for the full process (i.e. inking and printing) was maximized at 92.4%. This value does not represent an upper limit, but rather an optimal case for the particular stamp and nanoribbon geometry examined here. For example, larger or interconnected ribbons can have process yields which are much higher (> 99% as shown in Figure 2.4a).

To demonstrate the practical value of this approach, transistors were fabricated using single crystal Si printed onto glass via an optimized structured stamp. Figure 2.4(a) shows an example of a printed n-doped Si nanomembrane, in which the regular array of shaded patterns corresponds to the phosphorus-doped regions. Figure 2.4b shows transistor devices formed with a gate dielectric of SiO_2 (100 nm thickness). The resulting thin film transistors (TFTs) show accumulation mode n-channel transistor behavior, as indicated by the current-voltage characteristics in Figure 2.4c. The channel length and width of the demonstrated device are 25 μm and 200 μm, respectively. The transfer characteristics presented in Figure 2.4c indicate a threshold voltage of ~0 V, an effective mobility of 325 $cm^2/V\cdot s$, and device on/off ratios typically $>10^5$. These results could be relevant to the development of an unusual type of SOG technology. The same approaches can also be valuable for printing other classes of materials (e.g. GaAs, GaN, etc) onto other classes of substrates (e.g. semiconductor wafers, plastic sheets, etc), a process of particular utility for systems that demand intimate contact between the printed materials and the underlying substrate without intervening adhesive layers.

2.3.2. Biomimetic Pedestal Geometries for Enhanced Stamp Adhesion

Like the microstructure surface relief described in Section 2.3.1, rectangular posts, in either singular or arrayed configurations, represent one of the most common geometries of relief

molded onto a stamp surface to affect selective retrieval and printing. Although this structure can offer efficient transfer printing for many materials and applications, improved strength of adhesion in the adhesion-on state is often a necessity for advanced printing protocols or for expanded breadth of 'printable' materials. Whereas the previously discussed surface relief enabled adhesive modulation through decrease of the adhesion-off state, adhesion-on conditions still rely on the rate-dependent effects of the viscoelastic stamp. One method to enhance adhesive strength in the adhesion-on state is through modification of the basic rectangular relief geometry (i.e. flat punch) to one which mimics the shape of a pedestal, using concepts adapted from fibrillar dry adhesives, inspired by the spatula form of gecko foot- hairs.[11, 27-29, 33, 44] Here, a hierarchical stamp design is presented of this general type for enhanced adhesion strength in stamps for transfer printing. Measured contact forces show enhancement in adhesion of more than 15x with appropriate pedestal designs, as guided and validated by quantitative modeling of the mechanics.

Figure 2.5a schematically illustrates transfer printing with an optimized pedestal stamp. The advantage of the pedestal design is that it offers enhanced adhesion to the ink, by comparison to a flat punch with similar contact area. As investigated theoretically elsewhere,[27] the origin of this enhanced adhesion is the different debonding mechanisms which describe the various contact geometries. For the case of a flat punch (e.g. fiber or rectangular post), when subjected to uniform vertical loads, delamination occurs due to cracks that initiate at the external perimeter and propagate toward the center. The location of crack initiation points is due primarily to large stress concentrations which arise from the sharp interface surrounding the punch perimeter or to surface defects and asperities along the perimeter. For a pedestal, crack formation is completely inhibited at the edge and instead initiates mostly due to internal

interfacial defects at the inner region, usually co-located with the center of the supporting post as shown in Figure 2.5b. For sufficiently clean surfaces, enhanced adhesion is therefore anticipated with a pedestal design due to retarded crack formation and delamination, compared to a simple flat post stamp. To explore this system experimentally for transfer printing, we designed and fabricated pedestal features with four different geometries, and characterized their adhesion strength to a flat surface.

Pedestal stamps were fabricated by combining and bonding two separate pieces, a thin square pad and a narrow rectangular post on a backing layer, both of which were made of PDMS (Dow Corning Sylgard 184, 5:1 monomer:crosslinking agent). The bulk of the stamp, comprising the post and backing layer, was formed by molding PDMS against a suitable template structure fabricated by photolithographically patterning a layer of epoxy (SU8 50, MicroChem) on a silicon wafer.[45] For the pedestal pads, an additional template with square trenches (100 μm × 100 μm, 15 μm thick) was created in a similar manner. Here, the PDMS precursor was poured on the template and then scraped away using a razor blade ('doctor blading') to eliminate material everywhere outside of the recessed square regions[44]. Next, precision translational, rotational stages and optics brought the prefabricated rectangular post and backing into contact with the PDMS precursor in these recesses, in co-centered alignment. The combined structure was then cured at 70 ˚C for 3 hours, yielding strong bonding between the post and the pad. Peeling the bonded structured away from the template completed the fabrication. Figure 2.5b, c provide SEM images of the fabricated pedestal stamps with 50 μm and 40 μm thick posts, respectively. In Figure 2.5c, the pedestal stamp holds a 100 × 100 × 10 μm silicon chip retrieved from a donor substrate.

The geometries of both the central post and pad have significant influence on the mechanics and resulting adhesive behavior. To quantify the adhesive differences for various pedestal designs, a custom setup, described in Chapter 1 [16, 45] was used to measure pull-off forces of the stamp from a flat silicon surface, under vertical loads. For each of the pedestal geometries considered, the contact pad dimensions were fixed (100 μm × 100 μm × 15 μm) while the rectangular post region linking the pad to the backing layer (Figure 2.6a) varied in lateral dimensions from 50 μm to 100 μm. Fixing the contact pad dimensions ensured the same contact surface for all stamps. The results, then, provide insight into the role of the post in concentrating stresses away from the perimeter of pad contact.

The protocols used to evaluate pedestal stamp adhesive behavior are similar to the generic methods described in the last chapter. Initially, a pedestal stamp was brought into contact with a piece of silicon wafer (~3 mm × 3 mm), connected to the load cell, to a desired preload force. The stamp was allowed to relax for 5 seconds while maintaining the preload and then retracted at a fixed velocity. From the recorded force-displacement curves, a maximum pull-off force could be determined, corresponding to maximum adhesion of the stamp for a particular delamination velocity. Figure 2.6b, c show the velocity-dependent behavior of the pull-off forces for stamps having several different central post lateral dimensions. In the case of posts having widths of 60, 80, and 100 μm, there is a monotonic increase in pull-off force with delamination velocity, consistent with viscoelastic behavior reported for stamps having rectangular surface relief.[16, 46] The similar behaviors in these cases suggest that separation between the stamp and silicon surface is dominated by non-specific van der Waals forces, typical of rate-dependent adhesives like PDMS. Visualization of the stamp at separation with a high-speed camera shows that peeling initiates along one edge of the contact pad and propagates

across the stamp/Si interface, consistent with stamps that do not incorporate the pedestal design (e.g. rectangular posts in direct contact with silicon). The results indicate that the central posts in these types of stamps do not sufficiently localize pull-off forces to the center of the contact pad, a condition necessary to initiate interior crack formation at the stamp/substrate interface.

For pedestal stamp geometry having a central post width of 50 μm, the pull-off behaviors are qualitatively different than those with larger posts. In this case, the stamp shows strong pull-off forces at low delamination velocities, coming to a maximum peak around 5 μm/s, and then slowly declining to an approximately constant value. Visualization of the stamp under these slower unloading conditions indicates that peeling initiates at the center of the contact pad underneath the region of the central post and propagates outward towards the perimeter, terminating ultimately with complete separation of the stamp and substrate. During the retraction process, the contact pad and central post undergo extensive deformation before separation occurs. Measurement of the post elongation using an optical microscope and controlled stage displacements indicate engineering strains exceeding 150% are routinely exhibited, at lower velocities, prior to debonding. These large deformations are consistent with the remarkable adhesive enhancements enabled by these designs, corresponding to a 15x increase in pull-off force compared to flat punch geometry (e.g. 100 μm × 100 μm). For some geometries, the low-velocity adhesive forces are so large that they lead to fracture fat the point where the central post meets the backing layer, prior to any separation at the contact btween the pedestal pad and the substrate. This result indicates that the designs presented here could be limited ultimately by the fracture strength of the PDMS, representing an upper limit to the adhesive strength provided by this material.

Figure 2.6b shows a magnified region of the measured pull-off forces at low velocities for the four different post widths. Since material and fabrication methods are the same, the extreme values and different nature of the rate-dependent adhesion are due exclusively to differences in crack initiation and interface separation. By carefully designing the pedestal geometry, stresses can be concentrated to the center of the contact pad, providing a means to drastically increase stamp adhesion without use of complicated surface relief or mechanical loading parameters. We note that the rate-dependent adhesive response of the pedestal geometry with a post width of 50 μm follows trends that are different than those for the flat punch designs and for other related cases. We speculated that is behavior arises from a complex interaction between the viscoelastic properties of the stamp and the physio-mechanical effects associated with crack initiation in an enclosed region. Further work is needed to establish models that can capture this physics.

The static differences can, on the other hand, be readily understood through three dimensional finite element analysis (3D-FEA) with conditions matched to those used in experiments: pad lateral dimensions of 100 μm × 100 μm, a fixed post height of 50 μm, and an applied normal direction pull-off force, F, of 8 mN. The simulations also used a radius of curvature (~1 μm) around the perimeter edge of the contact pad, consistent with experimental observations. Figures 2.7a, b show the distribution of normal stresses (along the pull-off direction) at the interface between the contact pad and silicon surface for post widths of 50 μm and 60 μm, respectively. The maximum interfacial stress for the 50 μm post is reached at the central region of the contact pad. In contrast, the 60 μm post exhibits large stress concentration at the perimeter edges of the pad. These different locations of peak stress suggest that crack initiation and propagation would start at the center of the interface between the contact pad and

silicon for the 50 μm post and at the edge for the 60 μm post. The transition from internal to edge cracks occurs between 50 and 60 μm. This result is further validated by FEA for a 2 μm internal interfacial crack at the center of the pad/silicon contact, and by FEA for edge cracks of the same length. Figure 2.7c provides a plot of the calculated interfacial crack tip energy release rates G versus the post width, where G is normalized by $F^2/\left(EL_{\text{pad}}^3\right)$, with E as the Young's modulus of the stamp and L_{pad} as the width of contact pad. The internal crack has higher energy release rates for post widths of 50 μm and smaller, whereas the opposite holds for post widths greater than 60 μm. These results confirm the experimentally observed differences in delamination behavior, indicating that internal and edge crack initiation (and propagation) are responsible for the adhesive strengths of pedestal stamp with narrow (≤50 μm) and wide (≥60 μm) posts, respectively, with a transition that occurs between the two behaviors at ~58 μm (Figure 2.7c).

Figure 2.8 provides a demonstration of the adhesiveless transfer capabilities of pedestal designed stamps and their suitability for heterogeneous integration strategies. Due to the extreme adhesive strength of these stamps, for release, we exploited techniques that actively reduce the interfacial adhesion. In particular, we used laser pulses to induce heating and, by differential thermal expansion between the stamp and the ink, delamination and release.[47] An infrared (805 nm) laser beam (pulsed at a repetition rate of 0.2 Hz, with 2.3 ms pulse widths, and peak powers of 38 mW) was focused on the pad of a pedestal stamp with an ink on its surface. For the purpose of this demonstration, a 2 × 2 array of silicon chips[48] and InGaN microscale inorganic light emitting diodes[11] (μ-ILEDs) with lateral dimensions of 100 μm × 100 μm and thicknesses of 3 μm (silicon) and 5 μm (InGaN) were printed onto a bare silicon wafer. Figure 2.8a shows an SEM image of the results (the μ-ILEDs have square contact pads in opposite

corners). To demonstrate that retrieval and printing with a pedestal stamp does not affect performance of the μ-ILED, a probe station was used to operate and characterize a representative device. Figure 2.8b provides a representative optical image while Figure 2.8c shows the recorded current-voltage (*I-V)* characteristics before and after printing. The observed current densities are similar to those of devices tested prior to printing and from similar devices described in the literature.[11]

2.3.3. Finite Deformation of Soft Elastomeric Stamps

In the previous sections, we utilized PDMS stamps having well-established mixing ratios between the monomer and crosslinking agent (10:1 and 5:1 by weight) primarily as a route to elucidate the effects of various relief geometry on the adhesive strength of a stamp. However, in some instances, direct modification of stamp material properties, through aging effects or leaching of unreacted mobile oligomers from a stamp bulk, have demonstrated significant effects on transfer printing efficacy. Here we explore a different, but related methodology in which we modulate stamp adhesion by systematically varying elastic modulus of the PDMS. First we develop a modified model of the energy release rate for soft, low-modulus stamps followed by comparison to tape peel tests of flat specimens having modulus values of 0.03 MPa, 0.3 MPa, and 1.7 MPa.

2.3.3.1. Model for Finite Deformation

As described in Chapter 1, an analytic mechanics model was recently developed to relate the steady-state energy release rate, *G*, to applied external forces and the stamp geometry,

$G = F/w$.[16, 20, 39, 41] While this simple expression for the energy release rate is able to quantify many variables that describe kinetically controlled transfer printing,[20] it requires the simplifying assumptions that:

(1) the incremental elastic energy $\left(F^2/(2EA)\right)v_p\,dt$ in the peeling arm (the length of stamp that has already separated from the film) is negligible compared to the energy dissipation $Gwv_d dt$ due to the delamination of film/substrate interfaces, where the tensile stiffness of the peeling arm (EA) is equal to Ewh, E is the stamp modulus, h is the stamp thickness, v_p is the peeling velocity and v_d is delamination velocity, and

(2) the peeling velocity v_p is equal to the film/substrate delamination velocity v_d.

As dictated by these assumptions, when v_p=v_d the expression $Gwv_d dt >> \left(F^2/(2EA)\right)v_p\,dt$ can be reduced to $Eh>>G/2$.[49, 50] This assumption holds for normal PDMS stamps, which have a modulus of around 1.7MPa, but for very compliant stamps (e.g. PDMS with a Young's modulus less than 1 MPa) one can no longer assume that $Eh>>G/2$, and $G = F/w$ cannot be used to analyze printing dynamics in such cases. A new expression was derived for the steady-state energy release rate that no longer requires the simplifying assumption that $Eh>>G/2$, but still provides the ability to quantify the important variables associated with kinetically controlled transfer printing.

The stamp (or peeling arm in a tape peel test) being peeled away from the substrate is modeled as a beam subjected to large rotation (a constant 90^0 angle is maintained throughout entire peeling motion). For steady-state delamination at the ink/substrate interface over the time increment dt, the external work is given by $Fv_p dt$. The energy dissipation due to delamination at

the film/substrate interface is $Gwv_d dt$, while the change of elastic energy in the peeling arm is $\left(F^2/(2EA)\right)v_d\, dt$. Using these terms, the energy balance can be presented as: $Fv_p = Gwv_d + \left(F^2/(2EA)\right)v_d$, and a relationship between the peeling and delamination velocities established to be: $v_p = v_d\left(1 + F/(EA)\right)$. The steady-state energy release rate can be expressed as:

$$G = \frac{F}{w} + \frac{F^2}{2wEA}, \tag{2.1}$$

where the contribution from $F^2/(2wEA)$ becomes significant for compliant stamps with low tensile stiffness EA, as a result of finite deformation due to axial stretching of the peeling arm. The complete derivations associated with this work are beyond the scope of this thesis, but can be found in manuscripts.

2.3.3.2. Peeling with a Low Modulus Stamp

To measure the influence of finite deformation on energy release rate, as given in Eq. (2.1), tape peel tests were performed with PDMS (Sylgard 184, Dow Corning) stamps of varying stiffness on gold films (100 nm thick) supported on glass. The PDMS stamp modulus was controlled by modifying the relative amount of crosslinking agent mixed into the prepolymer solution. Dynamic Mechanical Analysis was used to measure the modulus of stamps made with prepolymer to crosslinker mix ratios of 50:1, 25:1, and 10:1, by weight. The resulting stamp modulus values obtained from static stress-strain tests were 0.03 MPa, 0.3 MPa, and 1.7 MPa, respectively. For low prepolymer:crosslinker mix ratios (0.03 MPa and 0.3 MPa), the surfaces of the resulting stamps were sticky due to the large amount of unpolymerized PDMS oligomers

present in the bulk material.[51] A 25 μm thick capping layer of 10:1 PDMS was incorporated onto one surface of each low modulus stamp in order to produce a consistent interface for the peeling experiments. The tensile stiffness for the composite PDMS stamps is given by the expression:

$$\overline{EA} = \left(E_{stamp} h_{stamp} + E_{capping} h_{capping} \right) w \tag{2.2}$$

Figure 2.9 compares experimentally obtained data for the energy release rate calculated via the new Eq. (2.1) and the simple expression $G=F/w$ as a function of the delamination velocity v_d for a 1 mm thick PDMS stamp peeled away from a 100 nm thick Au film. As shown in Figure 2.9, the energy release rate calculated by Eq. (2.1) and $G=F/w$ are essentially the same for stamps with Young's modulus of $E_{stamp} = 1.7MPa$ and $0.3MPa$. However, for stamps with lower Young's modulus (in this case $E_{stamp} = 0.03MPa$) the effects of finite deformation result in large differences in the energy release rates calculated by the two equations, especially at larger v_d values. The energy release rate curves in Figure 2.9 can be represented by the power-law relation $G = 2.16\left[1+\left(v/v_0\right)^n\right] J/m^2$, where $v_0 = 1.9423$, 0.2644 and $0.1895\, cm/s$, and n=0.66, 0.7404 and 1.084 for PDMS with Young's modulus $E_{stamp} = 1.7$, 0.3 and $0.03MPa$, respectively.

The steady-state energy release rate for retrieval, $G^{film/substrate}$, is obtained from Eq. (2.1) using the equivalent stiffness of the composite stamp and the gold film, represented by $\overline{EA} + E_{film} h_{film} w$, where $E_{film} = 150GPa$, such that $G^{film/substrate} = \frac{F_{pick-up}}{w}\left(1+\frac{F_{pick-up}}{2\left(\overline{EA}+E_{film}h_{film}w\right)}\right)$.

The critical peeling force for retrieval is then determined by the relationship

$G^{film/substrate} = \frac{F_{pick-up}}{w}\left(1+\frac{F_{pick-up}}{2\left(\overline{EA}+E_{film}h_{film}w\right)}\right) = G_{crit}^{film/substrate}$, which is rearranged to form the expression:

$$F_{pick-up} = \left(\overline{EA}+E_{film}h_{film}w\right)\left[\sqrt{1+\frac{2G_{crit}^{film/substrate}w}{\overline{EA}+E_{film}h_{film}w}}-1\right], \tag{2.3}$$

where $G_{crit}^{film/substrate}$ is the critical energy rate for separation of the film/substrate interface. Similarly, the steady-state energy release rate for printing, $G^{stamp/film}$, is obtained from Eq. (2.1) with the tensile stiffness in Eq. (2.1), which, together with $G^{stamp/film} = G_{crit}^{stamp/film}\left(v_d\right)$ for delamination of stamp/film interface, give the critical peeling force for printing

$$F_{printing} = \overline{EA}\left[\sqrt{1+\frac{2G_{crit}^{stamp/film}\left(v_d\right)w}{\overline{EA}}}-1\right], \tag{2.4}$$

where the critical energy rate for delamination of stamp/film interface $G_{crit}^{stamp/film}\left(v_d\right)$ depends on the delamination velocity v_d. The criterion for retrieval and printing is obtained by comparing the corresponding critical peeling forces determined by Eqs. (2.3) and (2.4), i.e., $F_{retrieval} < F_{printing}$ for retrieval and $F_{retrieval} > F_{printing}$ for printing.

Figure 2.10 shows the predicted critical peeling forces (normalized by the stamp width *w*) for retrieval and printing, versus the delamination velocity v_d for a model PDMS/Au/glass system where $E_{stamp} = E_{capping} = 1.7MPa$, $h_{stamp} = 1mm$, $h_{capping} = 25\mu m$, $E_{film} = 150GPa$ and $h_{film} = 100nm$. The critical energy release rates are $G_{crit}^{film/substrate} = 12\,J/m^2$ for the Au/glass interface[52] and $G = 2.16\left[1+\left(v/1.9423cm/s\right)^{0.66}\right]J/m^2$ for the PDMS/Au interface (as

determined by experimentally obtained data). The intercept of the curves in Figure 2.10 gives the critical delamination velocity v_c that separates printing from retrieval. Setting $F_{pick-up} = F_{printing}$ (from Equations 2.3 and 2.4) provides a mathematical approach to determining the velocity dependent critical energy release rate of the stamp/film interface:

$$G_{crit}^{stamp/\,film}\left(v_c\right) = \frac{\overline{EA}}{2w}\left[\left(\sqrt{1+\frac{2G_{crit}^{film/substrate}w}{\overline{EA}+E_{film}h_{film}w}}\,\frac{\overline{EA}+E_{film}h_{film}w}{\overline{EA}} - \frac{E_{film}h_{film}w}{\overline{EA}}\right)^2 - 1\right] \qquad (2.5)$$

which simplifies to $G_{crit}^{stamp\,/\,film}\left(v_c\right) = G_{crit}^{film\,/\,substrate}$ for small $G_{crit}^{film/substrate}$ values.[52] From Eq. (2.5) it is evident that the critical delamination velocity depends on the tensile stiffness of the composite stamp modulus ($\overline{EA}$) and the tensile stiffness of the film to be picked up ($E_{film}h_{film}w$).

The top panel of Figure 2.11 presents critical peeling force per unit width (F/w) as a function of the tensile stiffness of the stamp per unit width ($\overline{EA}/w$) for a model PDMS/Au/glass system in which the tensile stiffness of the stamp is varied (by adjusting either the stamp modulus or thickness), but the tensile stiffness of the gold film is held constant. The solid horizontal line represents the critical force separating pickup and printing as predicted by the model. It is important to note that the critical energy release rate at the film/substrate interface ($G_{crit}^{film/substrate}$) is a constant value. We therefore expect that regardless of stamp stiffness, the film should peel at the same G, in this case ~ 12 J/m^2 (as determined previously).[20] Experimental peel tests were conducted for an array of stamps with varying stiffness; the force at which the gold film was peeled from the substrate using each of these stamps (black squares on plot) was compared with the predicted critical peeling force. The predicted and experimental values for critical peeling force agree within experimental error. Critical force was chosen in place of

critical velocity as a benchmark for this comparison because it is extremely difficult to accurately measure the critical delamination velocity.

The lower panel of Figure 2.11 shows the predicted critical velocity trends for stamps with $E_{stamp} = 1.7$, 0.3 and $0.03MPa$ over a variety of tensile stamp stiffnesses (in this case achieved by varying h_{stamp} and holding E_{stamp} constant for each curve). Even for gold films with thicknesses that differ by two orders of magnitude, in this case $h_{film} = 100nm$ or $10\mu m$, the calculated critical velocities are identical, illustrating that v_c is independent of the thickness and Young's modulus of the ink, in this case. This trend is consistent among all of the varieties of PDMS examined and is due to the large difference in tensile stiffness between the Au films and PDMS stamps. Such a difference gives rise to a simplification of Eq. (2.5):

$$G_{crit}^{stamp/\,film}\left(v_c\right) \approx G_{crit}^{film/substrate} + \frac{\left(G_{crit}^{film/substrate}\right)^2 w}{2\overline{EA}}, \tag{2.6}$$

where the last term represents the contribution from finite deformation due to stretching in the peel arm. For stamps of large tensile stiffness, the above equation degenerates to $G_{crit}^{stamp/\,film}\left(v_c\right) \approx G_{crit}^{film/substrate}$ as finite deformation effects become negligible.[20] The large relative differences between the critical velocity curves, presented in Figure 2.11, result from the difference in stamp modulus which leads to a difference in critical energy release rate ($G_{crit}^{stamp/\,film}\left(v_c\right)$) between the stamps, as described in Eq. (2.6) for stamps with small $\overline{EA}$. The asymptotic behavior observed for each curve indicates that for small values of stamp stiffness ($\overline{EA}$), in this case achieved by decreasing the thickness of a constant modulus stamp, contributions from finite deformation in the peeling arm are not as dramatic as for larger stamp

stiffness values. Thicker stamps (larger $\overline{EA}$) provide more material and higher surface areas in the peel arm capable of absorbing energy during stretching and, in turn, more effectively contribute to finite deformation than thinner stamps of the same modulus. The plot indicates that, in accordance with this idea, for a given stamp modulus, there is a threshold stiffness below which the critical velocity dramatically increases; the model predicts that this threshold stiffness will occur around 100 N/m. Experiments determined that stamps with stiffnesses below 100 N/m are also extremely difficult to fabricate due to the fragile nature of very thin low modulus materials. For these reasons, we do not report data in the stamp stiffness regime below 100 N/m. This limitation does not, however, affect the utility of this theory for practical application, as lower critical velocity values are most desirable for enhanced ink retrieval at reduced peeling velocity.

2.4. Conclusions

Three simple techniques have been described for modulating the adhesive strength of PDMS stamps used in adhesiveless transfer printing. Of these passive methods, two rely on surface embossed microstructures to control adhesive strength in either the adhesion-off or adhesion-on state. In the former, simple line-and-space grating patterns were used to vary the contact area of the stamp with an ink layer to demonstrate enhanced release during printing. Modeling and tape peel tests provided key insights into how adhesion physics scales with the interfacial contact area and model SOG systems were developed. In the latter, we demonstrated a complex hierarchical stamp surface mimicking the pedestal geometry found in naturally occurring adhesive systems. Rate-dependent adhesion tests show that for optimized designs,

adhesion can be enhanced by 15X in the adhesion-on state, which is advantageous for expanding the breadth of printable classes of materials. Comprehensive modeling of this system indicates that enhancement is due to localization of stresses and crack initiation at the interior of the microstructure geometry, away from sharp edges of contact. Printing utility was demonstrated through transfer of fully functional μ-ILEDs to a bare silicon wafer.

In the third technique described in this chapter, low-modulus flat stamps were developed and characterized as a potential materials-modification approach to adhesion engineering. Analysis of relationships determined through experiments and theoretical modeling reveal that critical velocity separating the retrieval from printing regimes in rate-dependent adhesion is affected by the stiffness of low modulus stamps. Specifically, critical velocity decreases as stamp modulus decreases, indicating that film retrieval occurs at lower peeling velocities for softer stamps, a trend that is potentially useful for transfer printing inks that have low retrieval efficiencies or are otherwise impossible to retrieve with a traditional PDMS stamp (E_{stamp} = 1.7 MPa). Most importantly, this ability to retrieve structures that are more strongly bound to the donor substrate allows for less rigorous design of the anchoring schemes[53] (which are typically carefully engineered to tether an ink in place, but still allow for efficient retrieval with a PDMS stamp in a deterministic manner), and potentially the ability to retrieve inks that cannot be fully undercut or released (i.e. nanoparticles, quantum dots, etc.). In turn, this mode of pick up can potentially eliminate the need for post-patterning cleaning steps typically necessary for removing residual anchors on the ink or residual material at fracture sites that result from poor release schemes. By eliminating this cleaning step, multi-layer heterogeneous integration becomes simpler, as materials that are not robust to such cleaning processes can now be integrated into the final device in any sequence without special considerations to avoid damage of previously

printed layers. In addition to enhanced retrieval, inked low modulus PDMS stamps also have the potential to be integrated directly into a number of advanced applications that require substrates with enhanced stretching properties. The use of low modulus bilayer PDMS stamps discussed in this work, however, have the potential to support higher strains than normal 10:1 PDMS, yet maintain the same local and surface properties of the higher modulus material. Such low modulus PDMS stamps are potentially useful as biocompatible substrates for flexible skin-mimicking electronics, bio-implantable diagnostic and structural health monitoring systems that conformally stretch across topographically complex organs that routinely undergo large deformations in order to function.[54-59] Such applications of the theory developed in this paper bring to light the potential for expanding the stamps used in transfer printing beyond traditional PDMS formulations, and in that way expand the range of materials types and geometries able to be printed.

2.5. Experimental

2.5.1. Enhanced Ink Release via Line-and-Space Surface Relief

Fabrication of molding template: Bare silicon (100) wafers (WRS Materials) were degreased with acetone, isopropyl alcohol, and deionized water and dried under nitrogen prior to exposure to a UV/ozone environment for 5 minutes. A thin layer of negative tone photoactive epoxy (SU8-10, MicroChem; 15 μm thick) was spin-cast onto the wafer and then baked at 120˚C on a hotplate for 5 minutes to remove residual solvent. Exposure to UV radiation (λ=365 nm) through a quartz mask (90 mJ cm^{-2} dose) defined the desired line-and-space patterns in the epoxy. A second annealing step on a hotplate at 120˚C for 5 minutes selectively cross-linked the

exposed portions of the film. Development resulted in a patterned structure for direct molding of PDMS. Prior to molding, the surface of the template was treated (tridecafluoro-1,1,2,2-tetrahydrooctyl) trichlorosilane (FOTCS, Gelest) via vapor deposition in an evacuated chamber for 1 hour.

Molded stamps: PDMS (Sylgard 184, 10:1 monomer:crosslinking agent) pre-polymer was poured into a petri dish, degassed at 50 mTorr in an evacuated chamber for 1 hour and then poured onto the lithographic template. The template was positioned between two flat polycarbonate plates separated by precision 1 mm spacers; small holes along the plate perimeter allowed access for the liquid PDMS to infill the patterned feature geometry. The entire setup was cured in an oven at 70˚C for 4 hours. After curing and demolding from the template, a scalpel was used to cut out the PDMS into the desired stamp shape and size. Prior to testing the stamps were cleaned with commercial pressure sensitive adhesives (e.g, Scotch™ tape).

Sample preparation: Glass slides (Fisher Scientific) were cleaned in a Piranha solution (3:1 H_2SO_4/H_2O_2) for 30 min, rinsed thoroughly with deionized (Milli-Q) water, and dried under a stream of nitrogen. The cleaned slides were treated with hexamethyldisilazane (HMDS) to create an intermediate adhesive strength interface[20] by exposing to HMDS vapor in a bell jar for 5 minutes. The samples were then immediately loaded into a Temescal electron beam evaporator for deposition of 100 nm of Au.

Peel test and separation velocity measurement: Tape peel tests were performed to measure the adhesion against an established interface (gold thin film). Clean PDMS stamps were laminated onto the gold coated side of a prepared substrate and left in conformal contact with the surface for 3 minutes. Inverting the stamp/slide (stamp side down) and attaching controlled loads to one end of the stamp initiated peeling from the slide which was captured via a high

resolution video camera. Analysis of the recordings enabled calculation of the delamination velocity by measuring the position and corresponding time interval of the delamination front.

Silicon nanoribbon fabrication: Nanoribbons were derived from Silicon-on-Insulator (SOI) source material (Shin-Etsu) with a 300 nm thick top silicon layer. E-beam lithography was used to pattern the ribbon geometry and dry, reactive ion etching (RIE, PlasmaTherm) transferred the resist pattern to the top device layer. Rinsing with acetone removed the residual resist on the surface. Next, bathing the samples in buffered oxide etch solution for 30 minutes preferentially removed the buried oxide (BOx) layers and released the nanomembranes for retrieval.

Si nanoribbon transistor fabrication: Phosphorous-doped nanoribbons were retrieved with an optimized microstructured stamp and transfer printed onto a degreased glass substrate without the use of adhesive layers. A gate dielectric of SiO_2 (100 nm thick) was deposited via plasma-enhanced chemical vapor deposition (PECVD) with SiH_4 and N_2O at 250˚C. Drain, source, and gate electrodes of Cr/Au (3/100 nm) were formed by lift-off lithography of electron beam (Temescal BJD1800) evaporated metal of the metal layers.

2.5.2. Biomimetic Pedestal Geometries for Enhanced Stamp Adhesion

Silicon chip fabrication: Silicon chips were derived from SOI wafers with 3 μm thick device layers (top silicon), 1.1 μm thick BOx and 450 μm thick handle substrates (supporting wafer). Plates with lateral dimensions of 100 × 100 μm were defined by a layer of photoresist (AZ 5214E, AZ Electronic Materials) that served as a resist for dry etching (RIE, PlasmaTherm RIE) of the top silicon. The chips were then dipped in concentrated hydrofluoric acid (HF, 49%) for 55 seconds to remove the exposed BOx and partially undercut the silicon plates, resulting in narrow (~1.1 μm) trenches along the perimeter. The substrate was cleaned in Piranha solution

(3:1 H_2SO_4/H_2O_2) for 3 minutes, rinsed, and coated with a 1.5 μm layer of photoresist (AZ 5214E). Flood exposing the photoresist in a mask aligner (Karl Suss MJB3) with a 150 mJ cm^{-2} dose of UV radiation (λ=365 nm), exposed all of the photoresist except in the partially undercut regions along the plates. Developing for 45 seconds in basic solution (AZ Electronic Materials, MIF 327) removed the exposed photoresist. The plates were then undercut etched in concentrated HF for 4.5 hours to remove the remaining BOx. These procedures left the plates tethered to the handle by the narrow rim of photoresist that remained along their perimeters.[48]

InGaN μ-ILED fabrication: A GaN/Si(111) wafer (Azzurro Semiconductor) with layers of GaN:Mg (110 nm), five repeats of InGaN/GaN:Si (3 nm:10 nm), GaN:Si (1,700 nm), AlN:Si/GaN:Si (1,900 nm), GaN (750 nm), and AlN/AlGaN (300 nm) served as the starting material. Multiple metal layers (Ti:15 nm/Al:60 nm/Mo:20 nm/Au:100 nm) are deposited via e-beam evaporator on regions of n-GaN exposed by ICP-RIE etching and annealed at 860 °C for 30 s in N_2 ambient to form n-type ohmic contact to GaN:Si layer. For p-type ohmic contact to GaN:Mg layer, metal layers (Ni:10 nm/Au:10 nm) are deposited via e-beam evaporator and annealed at 500 °C for 10 min in air ambient. Next, opaque contact pads are formed by e-beam evaporation (Ti:10 nm/Au:120 nm). As a resist for KOH attack on ohmic contacts, a 300 nm layer of silicon nitride was deposited by plasma enhanced chemical vapor deposition. The geometry of the device array was photo-lithographically defined by patterning a metal etch mask of metal (Ti:50 nm/Ni:450 nm) by photoresist lift-off process then removing the exposed silicon nitride by RIE with SF_6. An ICP-RIE step provided the mesa etch, to generate an isolated array of devices. Anisotropic undercut etching of the silicon was performed by complete immersion in a solution of KOH (PSE-200, Transene) at 100˚C (hot plate temperature).[11]

2.5.3. Finite Deformation of Soft Elastomeric Stamps

Composite stamps: Composite stamps (25 μm thick capping layer of 10:1 PDMS on low modulus backing) were fabricated by spin coating a thin film of 10:1 PDMS onto a FOTCS-treated silicon wafer and partially curing on a hotplate at 70˚C for 7 minutes. After partial cure, a degassed mix of PDMS prepolymer (either 25:1 or 50:1 mix ratio) was applied to the top of the film. Molding the PDMS between two flat polycarbonate plates held at variable distances set the desired stamp thickness. After curing at 70°C in an oven for 3 hours, a scalpel was used to cut the stamps from the sheet with desired lateral dimensions.

2.6. References

[1] E. Menard, K.J. Lee, D.-Y. Khang, R.G. Nuzzo, J.A. Rogers, *Appl. Phys. Lett.* **2004**, *84*, 5398.

[2] K.J. Lee, J. Lee, H. Hwang, Z.J. Reitmeier, R.F. Davis, J.A. Rogers, R.G. Nuzzo, *Small* **2005**, *1*, 1164.

[3] Y. Sun, J.A. Rogers, *Adv. Mater.* **2007**, *19*, 1897.

[4] Y. Sun, H.-S. Kim, E. Menard, S. Kim, I. Adesida, J.A. Rogers, *Small* **2006**, *2*, 1330.

[5] A.J. Baca, M.A. Meitl, H.C. Ko, S. Mack, H.-S. Kim, J. Dong, P.M. Ferreira, J.A. Rogers, *Adv. Func. Mater.* **2007**, *17*, 3051.

[6] Q. Cao, J.A. Rogers, *Adv. Mater.* **2009**, *21*, 29.

[7] Q. Cao, Z.-T. Zhu, M.G. Lemaitre, M.-G. Xia, M. Shim, J.A. Rogers, *Appl. Phys. Lett.* **2006**, *88*, 113511.

[8] D.R. Hines, S. Mezhenny, M. Breban, E.D. Williams, V.W. Ballarotto, G. Esen, A. Southard, M.S. Fuhrer, *Appl. Phys. Lett.* **2005**, *86*, 163101.

[9] S.J. Kang, C. Kocabas, H.-S. Kim, Q. Cao, M.A. Meitl, D.-Y. Khang, J.A. Rogers, *Nano Lett.* **2007**, *7*, 3343.

[10] S.-I. Park, Y. Xiong, R.-H. Kim, P. Elvikis, M. Meitl, D.-H. Kim, J. Wu, J. Yoon, C.-J. Yu, Z. Liu, Y. Huang, K.-C. Hwang, P. Ferreira, X. Li, K. Choquette, J.A. Rogers, *Science* **2009**, *325*, 977.

[11] H. Kim, E. Brueckner, J. Song, Y. Li, S. Kim, C. Lu, J. sulking, K. Choquette, Y. Huang, R.G. Nuzzo, J.A. Rogers, *Proc. Natl. Acad. Sci. U.S.A.* **2011**, *108*(25), 10072.

[12] J. Yoon, S. Jo, I.S. Chun, I. Jung, H.-S. Kim, M. Meitl, E. Menard, X. Li, J.J. Coleman, U. Paik, J.A. Rogers, *Nature* **2010**, *465*, 329.

[13] J. Yoon, A.J. Baca, S.-I. Park, P. Elvikis, J.B.G. III, L. Li, R.H. Kim, J. Xiao, S. Wang, T.-H. Kim, M.J. Motala, B.Y. Ahn, E.B. Duoss, J.A. Lewis, R.G. Nuzzo, P.M. Ferreira, Y. Huang, A. Rockett, J.A. Rogers, *Nat. Mater.* **2008**, *7*, 907.

[14] J.-H. Ahn, H.-S. Kim, K.J. Lee, S. Jeon, S.J. Kang, Y. Sun, R.G. Nuzzo, J.A. Rogers, *Science* **2006**, *314*, 1754.
[15] S.-H. Hur, D.-Y. Khang, C. Kocabas, J.A. Rogers, *Appl. Phys. Lett.* **2004**, *85*, 5730.
[16] M.A. Meitl, Z.-T. Zhu, V. Kumar, K.J. Lee, X. Feng, Y.Y. Huang, I. Adesida, R.G. Nuzzo, J.A. Rogers, *Nat. Mater.* **2006**, *5*, 33.
[17] T.-H. Kim, W.M. Choi, D.-H. Kim, M.A. Meitl, E. Menard, H. Jiang, J.A. Carlisle, J.A. Rogers, *Adv. Mater.* **2008**, *20*, 2171.
[18] A. Javey, S. Nam, R.S. Friedman, H. Yan, C.M. Lieber, *Nano Lett.* **2007**, *7*, 773.
[19] J. Israelachvili, *Intermolecular and Surface Forces*. 1991, Boston: Academic Press.
[20] X. Feng, M.A. Meitl, A.M. Bowen, Y. Huang, R.G. Nuzzo, J.A. Rogers, *Langmuir* **2007**, *23*, 12555.
[21] E. Menard, R.G. Nuzzo, J.A. Rogers, *Appl. Phys. Lett.* **2005**, *86*, 093507.
[22] Y. Xia, G.M. Whitesides, *Angew. Chem. Int. Ed.* **1998**, *37*, 551.
[23] J.A. Rogers, R.G. Nuzzo, *Mater. Today* **2005**, *8*, 50.
[24] Y. Xia, G.M. Whitesides, *Annu. Rev. Mater. Sci.* **1998**, *28*, 153.
[25] P. Kim, K.W. Kwon, M.C. Park, S.H. Lee, S.M. Kim, K.Y. Suh, *Biochip J.* **2008**, *2*, 1.
[26] E. Artz, S. Gorb, R. Spolenak, *Proc. Natl. Acad. Sci. U.S.A.* **2003**, *100*, 10603.
[27] G. Carbone, E. Pierro, S.N. Gorb, *Soft Matter* **2011**, *7*, 5545.
[28] S. Gorb, M. Varenberg, A. Peressadko, J. Tuma, *J. R. Soc. Interface* **2007**, *4*, 271.
[29] S. Kim, M. Sitti, *Appl. Phys. Lett.* **2006**, *89*(261911).
[30] K. Autumn, M. Sitti, Y.A. Liang, A.M. Peattie, W.R. Hansen, S. Sponberg, T.W. Kenny, R. Fearing, J.N. Israelachvili, *Proc. Natl. Acad. Sci. U.S.A.* **2002**, *99*, 12252.
[31] J. Gao, J. Yao, *Proc. Natl. Acad. Sci. U.S.A.* **2004**, *101*, 7851.
[32] A.K. Geim, S.V. Dubonos, I.V. Grigorieva, K.S. Novoselov, A.A. Zhokov, S.Y. Shapoval, *Nat. Mater.* **2003**, *2*, 461.
[33] M.P. Murphy, B. Aksak, M. Sitti, *Small* **2009**, *5*, 170.
[34] S. Kim, M. Sitti, C.-Y. Hui, R. Long, A. Jagota, *Appl. Phys. Lett.* **2007**, *91*, 161905.
[35] S. Kim, B. Aksak, M. Sitti, *Appl. Phys. Lett.* **2007**, *91*, 221913.
[36] K.P. Larsen, J.T. Ravnkilde, O. Hansen, *TRANSDUCERS, Solid-State Sensors, Actuators and Microsystems, 12th International Conference on* **2003**, 1655.
[37] J. Chae, H. Kulah, K. Najafi, *J. Micromech. Microeng.* **2005**, *15*, 336.
[38] A. Majumder, A. Ghatak, A. Sharma, *Science* **2007**, *318*, 258.
[39] A.N. Gent, *J. Polym. Sci. B: Polym. Phys.* **1994**, *32*, 1543.
[40] T.L. Anderson, *Fracture mechanics: fundamentals and applications*. 2nd. ed. 1995, Boca Raton: CRC Press.
[41] A.N. Gent, *Langmuir* **1996**, *12*, 4492.
[42] K. Kendall, *Science* **1992**, *263*, 1720.
[43] K.S. Kim, J. Kim, *J. Eng. Mater. Technol.* **1988**, *110*, 266.
[44] M.J. Kim, J. Yoon, S.-I. Park, J.A. Rogers, *Appl. Phys. Lett.* **2009**, *95*, 214101.
[45] A. Carlson, H.-J. Kim-Lee, J. Wu, P. Elvikis, H. Cheng, A. Kovalsky, S. Elgan, Q. Yu, P.M. Ferreira, Y. Huang, K.T. Turner, J.A. Rogers, *Appl. Phys. Lett.* **2011**, *98*, 264104.
[46] T.-H. Kim, A. Carlson, J.-H. Ahn, S.M. Won, S. Wang, Y. Huang, J.A. Rogers, *Appl. Phys. Lett.* **2009**, *94*, 113502.
[47] R. Saeidpourazar, R. Li, Y. Li, M.D. Sangid, S. Kim, C. Lu, H.-S. Kim, J. Song, Y. Huang, J.A. Rogers, P.M. Ferreira, *J Microelectromech S* **2011**, *submitted*.

[48] Y. Yang, Y. Hwang, H.A. Cho, J.-H. Song, S.-J. Park, J.A. Rogers, H.C. Ko, *Small* **2011**, *7*, 484.
[49] K.-S. Kim, N. Aravas, *Int. J. Solids Struc.* **1988**, *24*, 417.
[50] K.-S. Kim, J. Kim, *J. Eng. Mater. Technol.* **1988**, *110*, 266.
[51] J.N. Lee, C. Park, G.M. Whitesides, *Anal. Chem.* **2003**, *75*, 6544.
[52] X. Feng, M.A. Meitl, A.M. Bowen, Y. Huang, J.A. Rogers, R.G. Nuzzo, *Langmuir* **2007**, *23*, 12555.
[53] M.A. Meitl, X. Feng, J. Dong, E. Menard, P.M. Ferreira, Y. Huang, J.A. Rogers, *Appl. Phys. Lett.* **2007**, *90*, 083110.
[54] J. Viventi, D.-H. Kim, J.D. Moss, Y.-S. Kim, J.A. Blanco, N. Annetta, A. Hicks, J. Xiao, Y. Huang, D.J. Callans, J.A. Rogers, B. Litt, *Sci. Transl. Med.* **2010**, *2*, 24ra22.
[55] R.-H. Kim, D.-H. Kim, J. Xiao, B.H. Kim, S.-I. Park, B. Panilaitis, R. Ghaffari, J. Yao, M. Li, Z. Liu, V. Malyarchuk, D.G. Kim, A.-P. Le, R.G. Nuzzo, D.L. Kaplan, F.G. Omenetto, Y. Huang, Z. Kang, J.A. Rogers, *Nat. Mater.* **2010**, *9*, 929.
[56] D.-H. Kim, N. Lu, R. Ghaffari, Y.-S. Kim, S.P. Lee, L. Xu, J. Wu, R.-H. Kim, J. Song, Z. liu, J. Viventi, B.d. Graff, B. Elolampi, M. Mansour, M.J. Slepian, S. Hwang, J.D. Moss, S.-M. Won, Y. Huang, B. Litt, J.A. Rogers, *Nat. Mater.* **2011**, *10*, 316.
[57] J. Viventi, D.-H. Kim, L. Vigeland, E.S. Frechette, J.A. Blanco, Y.-S. Kim, A.E. Avrin, V.R. Tiruvadi, S.-W. Hwang, A.C. Vanleer, D.F. Wulsin, K. Davis, C.E. Gelber, L. Palmer, J.V.d. Spiegel, J. Wu, J. Xiao, Y. Huang, D. Contreras, J.A. Rogers, B. Litt, *Nat. Neurosci.* **2011**, *14*, 1599.
[58] D.-H. Kim, J. Viventi, J.J. Amsden, J. Xiao, L. Vigeland, Y.-S. Kim, J.A. Blanco, B. Panilaitis, E.S. Frechette, D. Contreras, D.L. Kaplan, F.G. Omenetto, Y. Huang, K.-C. Hwang, M.R. Zakin, B. Litt, J.A. Rogers, *Nat. Mater.* **2010**, *9*, 511.
[59] D.-H. Kim, N. Lu, R. Ma, Y.-S. Kim, R.-H. Kim, S. Wang, J. Wu, S.M. Won, H. Tao, A. Islam, K.J. Yu, T.-I. Kim, R. Chowdhury, M. Ying, L. Xu, M. Li, H.-J. Chung, H. Keum, M. McCormick, P. Liu, Y.-W. Zhang, F.G. Omenetto, Y. Huang, T. Coleman, J.A. Rogers, *Science* **2011**, *333*, 838.

2.7. Figures

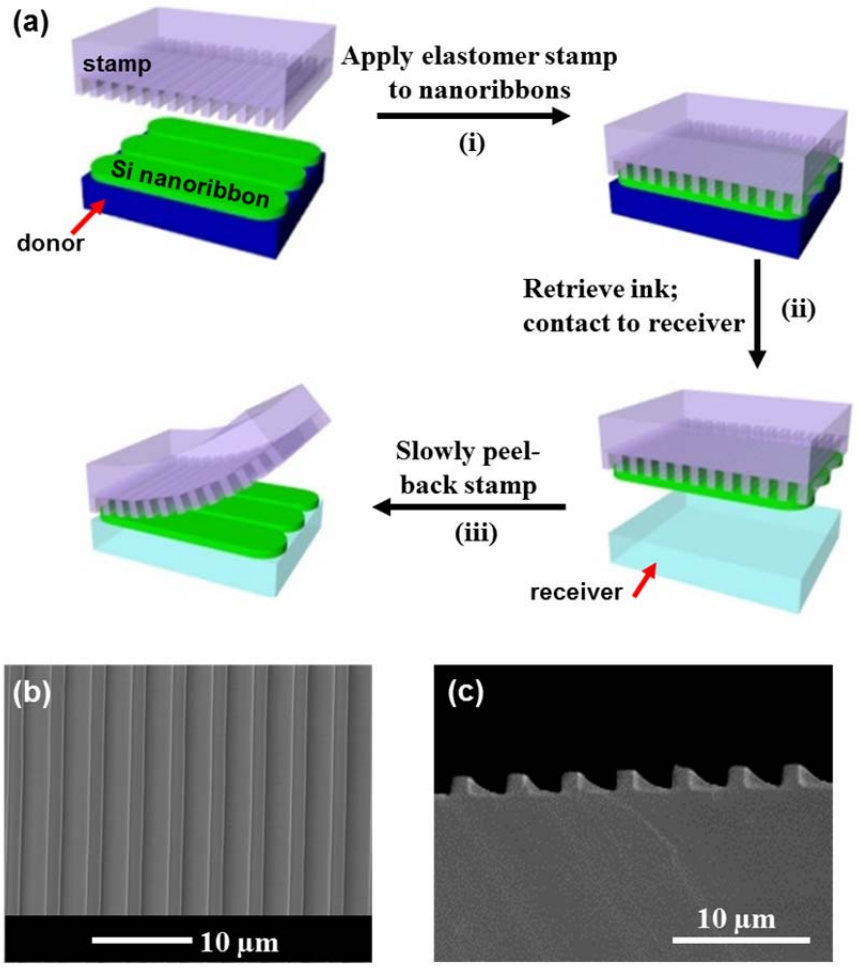

Figure 2.1. (a) Schematic illustration of the transfer printing process using a structured stamp. (b) Top view SEM image of a representative stamp of this type. (c) Cross-sectional SEM image of the stamp.

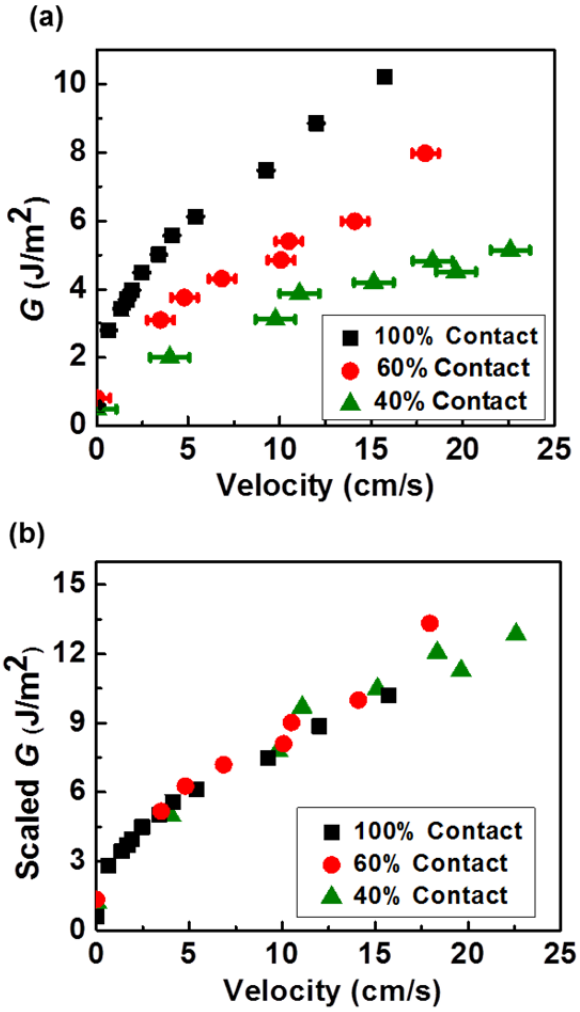

Figure 2.2. Velocity-dependent adhesive strength of structured PDMS stamps with different contact areas. (a) Three curves representing the cases of 100% (squares; flat stamp), 60% (circles; line and space stamp), and 40% (triangles; line and space stamp) contact areas. The peel direction in all cases was perpendicular to the surface relief structures. Error bars represent the standard deviation in delamination velocity for each applied load. (b) Common adhesion curve for all stamps measured.

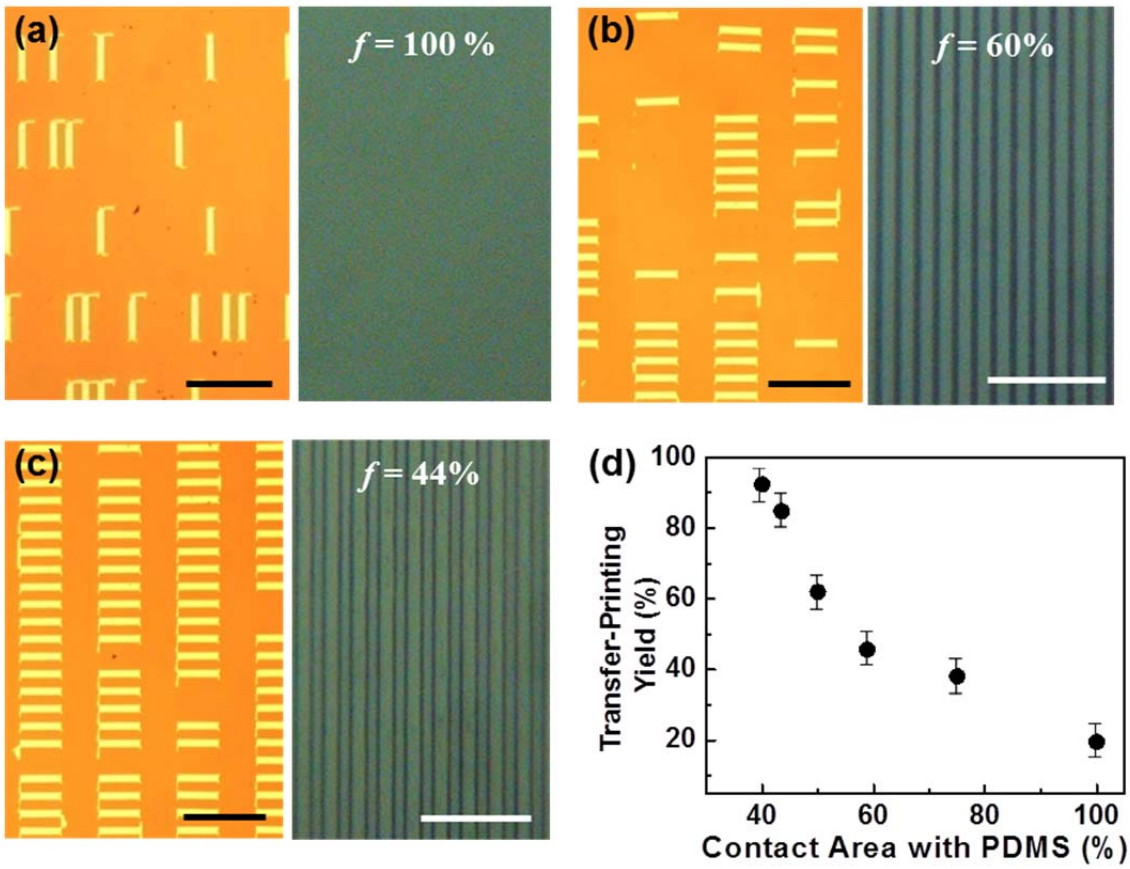

Figure 2.3. (a)-(c) Left Panel: top view optical images of arrays of 300 nm-thick Si ribbons transfer printed onto a glass substrate by the PDMS stamps shown in the right panels. Contact areas, *f*, for the stamps are: (a) 100% (flat surface), (b) 60% (line/space relief), and (c) 44% (line/space relief). Scale bars for all ribbon array images is 200 μm and for stamp images is 10 μm. (d) Printing yield as a function of the contact area between structured PDMS stamps and Si ribbons

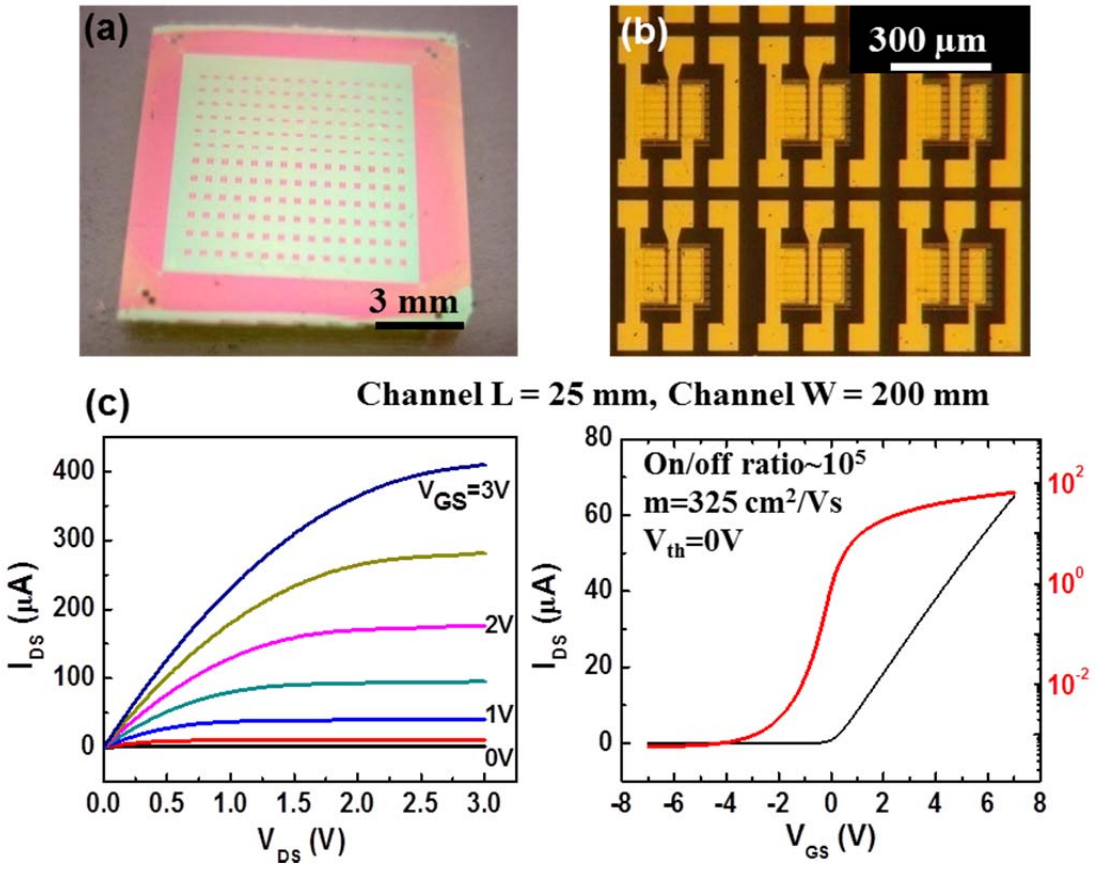

Figure 2.4. (a) Photograph of a 300 nm-thick phosphorus-doped silicon membrane printed onto a glass substrate without an adhesion layer. (b) Optical images of an array of single-crystal silicon TFTs fabricated on this membrane with a SiO_2 gate dielectric layer (100 nm thick) and source, drain and gate electrodes of Cr/Au (3/100 nm). (c) Full current–voltage and transfer (source/drain bias = 0.1 V) characteristics of devices with channel lengths and widths of 25 µm and 200 µm, respectively.

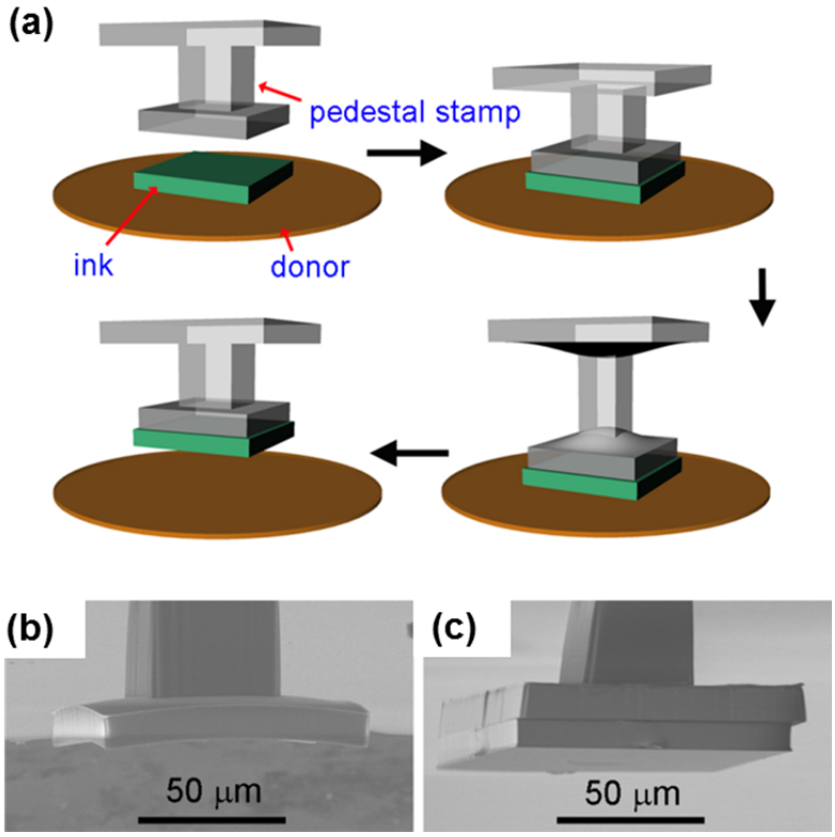

Figure 2.5. (a) Schematic illustration of the procedure for transfer printing with a pedestal stamp. Scanning electron microscope (SEM) images of such as stamp, with a 50 μm wide post (b) and a 40 μm wide post (c). The latter stamp has a 100 × 100 μm, 10 μm thick silicon chip on its surface.

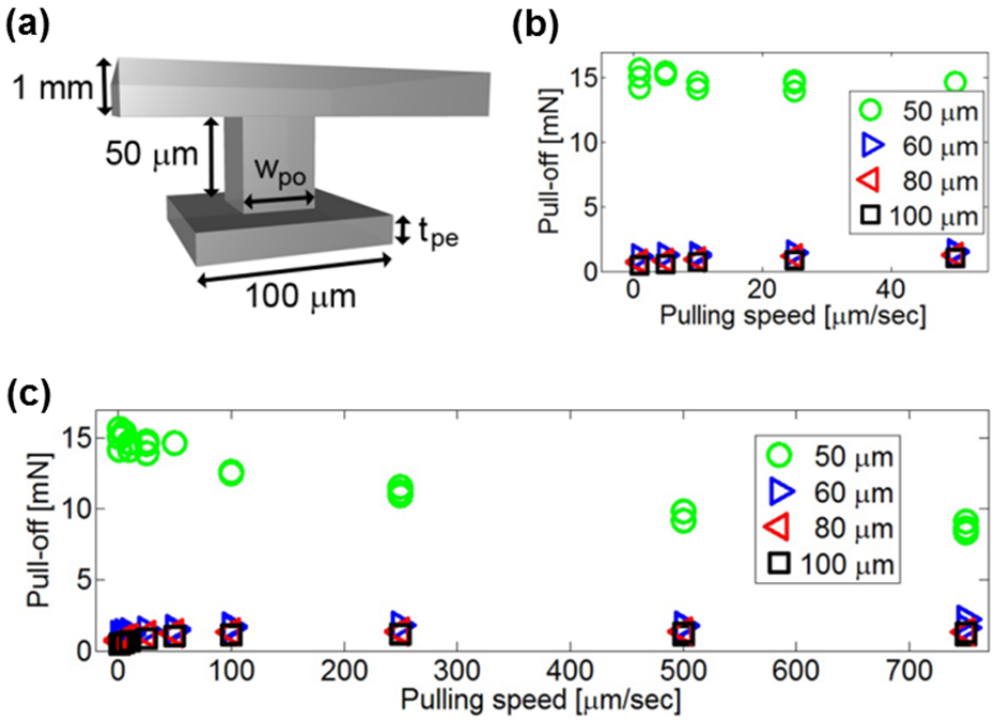

Figure 2.6. (a) Illustration of a pedestal stamp, with key dimensions indicated. (b, c) Pull-off force measured using pedestal stamps with four different post widths after full contact with a clean silicon wafer, as a function of pulling speed; magnified region at low velocities (b) and for the full range of velocities (c).

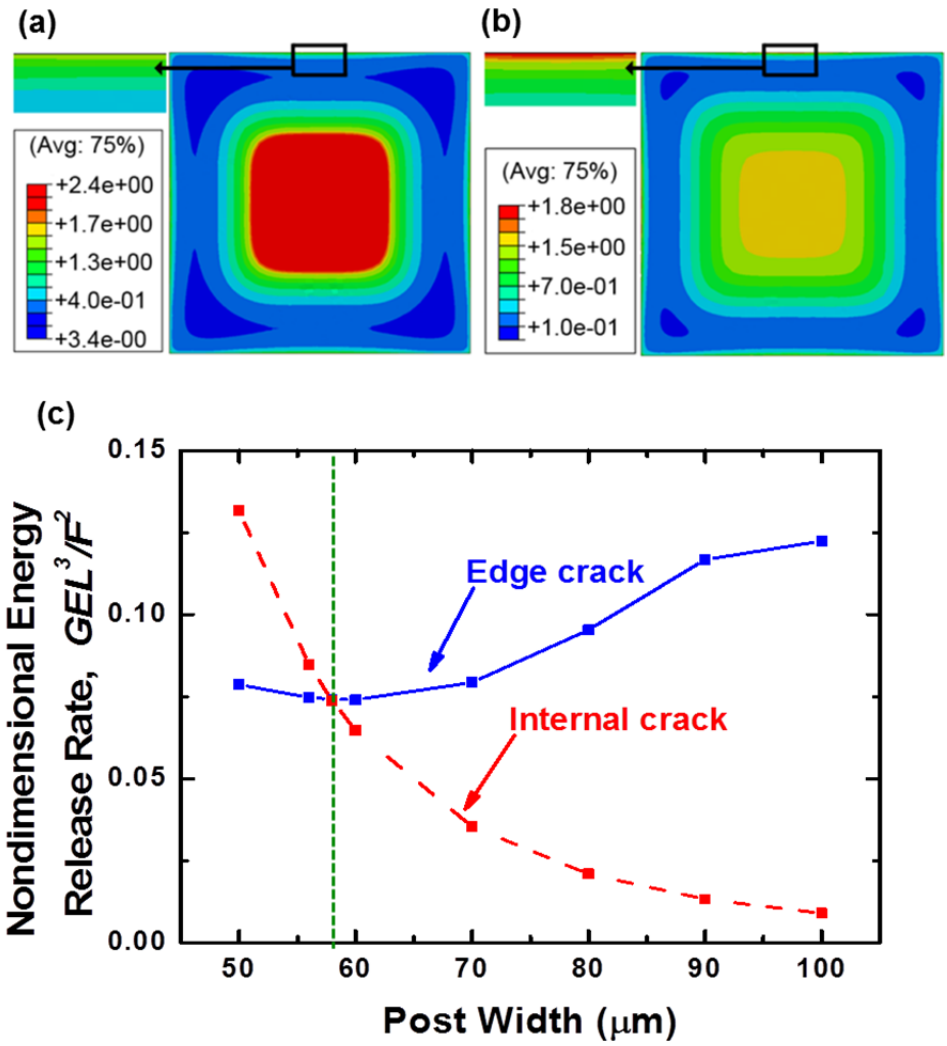

Figure 2.7. Distribution of normal stress (along the pull-off direction) at the interface between the contact pad and a silicon surface for post widths of 50 μm (a) and 60 μm (b). (c) Interfacial crack tip energy release rates *G* versus the post width.

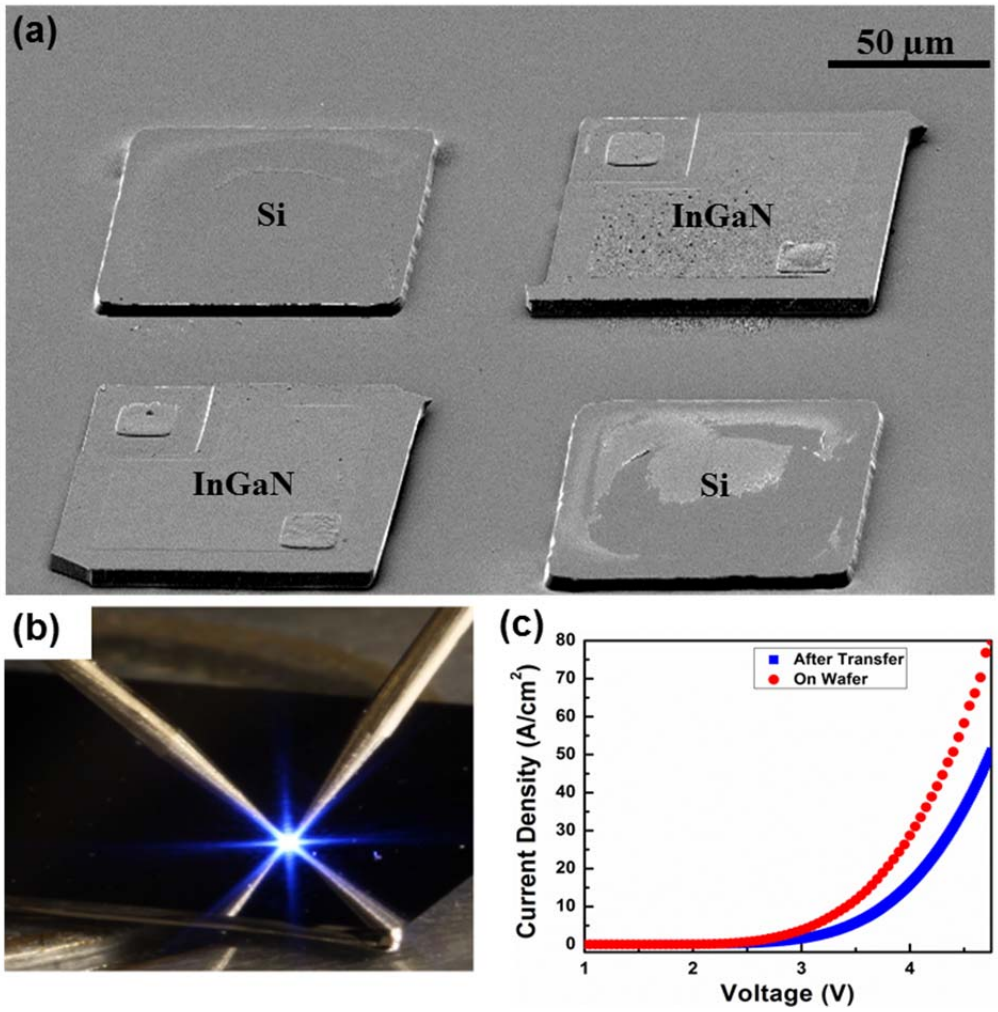

Figure 2.8. SEM image of printed Si chips and InGaN µ-ILEDs (a), representative optical image of an operating device (b) and the recorded *I-V* characteristics before and after transfer.

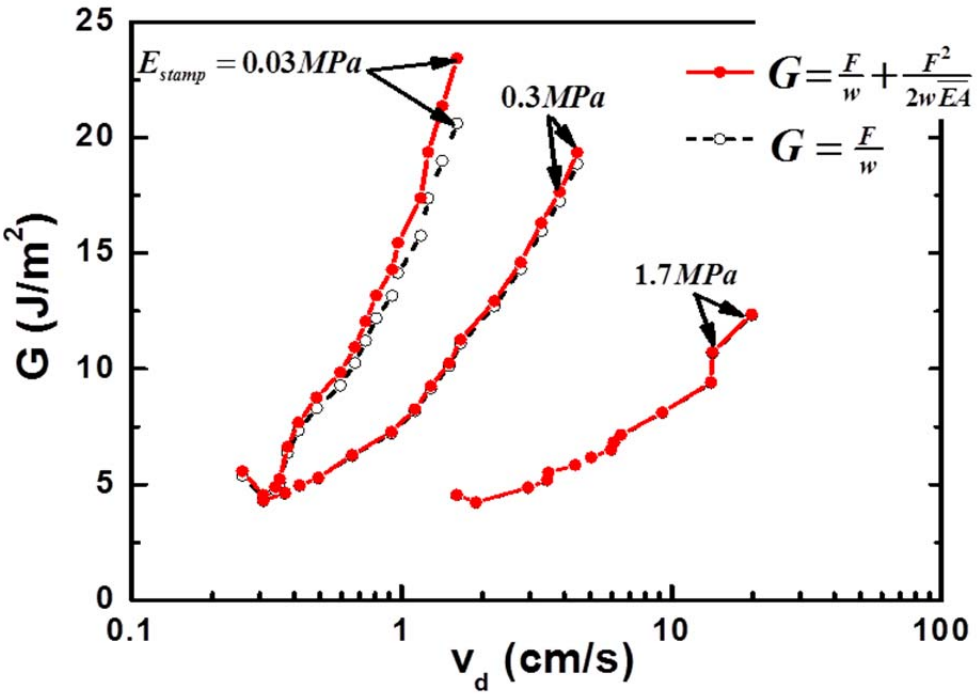

Figure 2.9. Comparison of energy release rates calculated using Eq. (2.1) and the simple expression $G = F/w$ versus the delamination velocity v_d. The experimental data (v_d values and peeling force used to calculate G) was obtained using three PDMS stamps of same thickness but different Young's modulus, 1.7, 0.3 and 0.03 *MPa*.

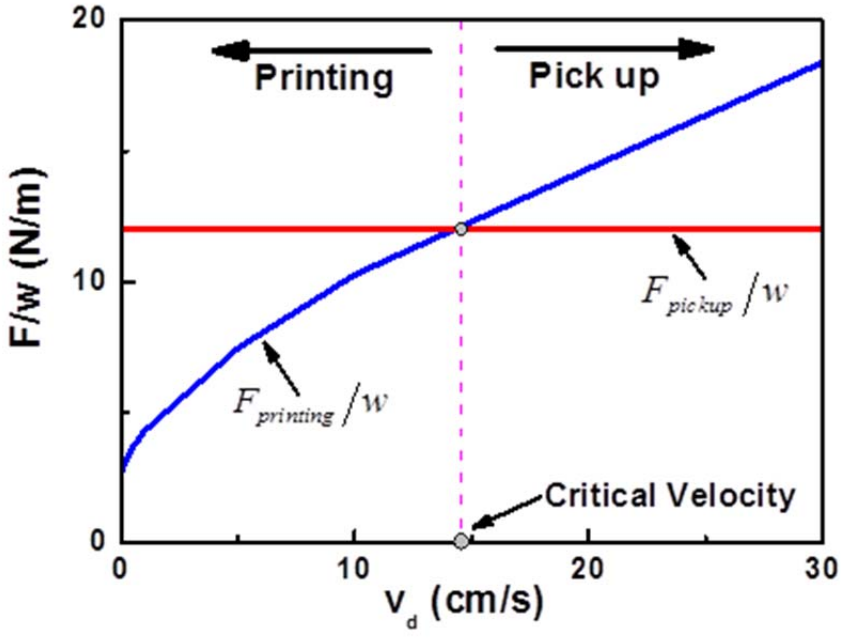

Figure 2.10. The calculated forces (per unit width) *F/w* for retrieval (delamination of Au/glass interface) and for printing (delamination of PDMS/Au interface) versus the delamination velocity v_d for a system with $E_{stamp} = 1.7MPa$, h_{stamp}=1 *mm*, $E_{film} = 150GPa$, and $h_{film} = 100nm$. The intercept of the two curves provides the critical delamination velocity for kinetically controlled transfer printing.

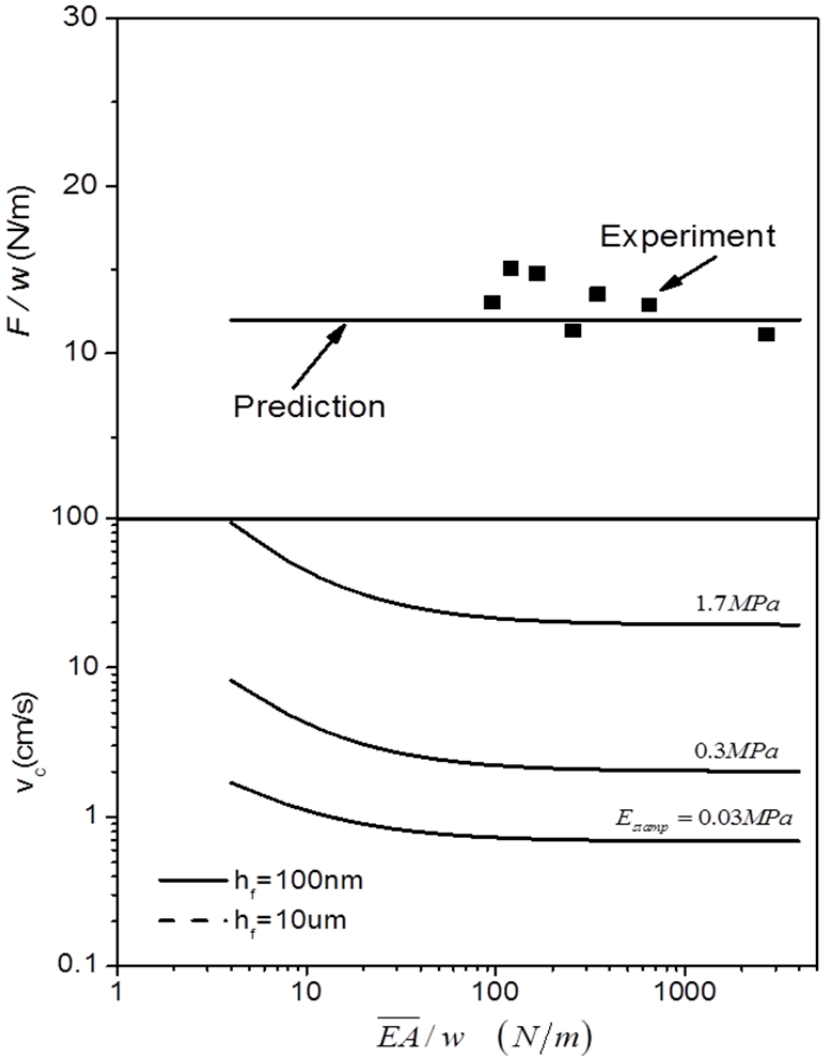

Figure 2.11. The critical force per unit width (*F/w*) and the critical delamination velocity v_c separating retrieval and printing versus the tensile stiffness of the stamp per unit width ($\overline{EA}$) for stamps of varying Young's modulus (1.7, 0.3, and 0.03 *MPa*) used to retrieval gold films of thickness $h_{film} = 100nm$ and $10\mu m$.

CHAPTER 3

MICROSTRUCTURED ELASTOMERIC SURFACE WITH REVERSIBLE ADHESION AND EXAMPLES OF THEIR USE IN DETERMINISTIC ASSEMBLY BY TRANSFER PRINTING[1]

3.1. Abstract

Reversible control of adhesion is an important feature of many desired, existing and potential systems, including climbing robots, medical tapes, and stamps for transfer printing. We present experimental and theoretical studies of an active mode of pressure modulated adhesion between flat, stiff objects and elastomeric stamps with sharp features of surface relief in optimized geometries. Here, the strength of non-specific adhesion can be switched by more than three orders of magnitude, from strong to weak, in a reversible fashion. Implementing these concepts in advanced stamps for transfer printing enables versatile modes for deterministic assembly of solid materials in micro/nanostructured forms. Demonstrations in printed two and three dimensional collections of silicon platelets and membranes illustrate some capabilities.

3.2. Introduction

Modes of adhesion observed in insects and small animals such as geckos are repeatable, robust, and power efficient. In fact, certain features such as the ability to adhere to a wide variety of surfaces, to rapidly and reversibly change adhesion strength between strong and weak modes and to self-clean contaminants significantly exceed those available in conventional

[1] Reprinted, with permission from S. Kim, J. Wu, A. Carlson, S.H. Jin, A. Kovalsky, P. Glass, Z. Liu, N. Ahmed, S.L. Elgan, W. Chen, P.M. Ferreira, M. Sitti, Y. Huang, J.A. Rogers, "Microstructured Elastomeric Surfaces with Reversible Adhesion and Examples of Their Use in Deterministic Assembly by Transfer Printing," *Proc. Natl. Acad. Sci. U.S.A.* **107**, 17095 (2010) Copyright: 2010 National Academy of Science.

pressure sensitive tapes or structural adhesives. Many of these creatures have micro and nanoscale structures with varying levels of complexity on foot or toe-pads.[1] Some of these beneficial aspects can be reproduced in synthetic materials to yield dry adhesives[2-4] that offer, for example, switchability in adhesion through changes in thermal and/or mechanical conditions.[3-5] Although most reports focus on fibrillar structures found on the feet of gecko lizards, attachment mechanisms that emulate adhesion organs or pads of common insects might provide attractive alternatives. For example, when adhering to or releasing from a smooth surface, aphid adhesion organs (*pulvilli*) are everted by increased blood pressure or withdrawn by contraction of tibial muscles,[6] respectively. This pressure driven mechanical sagging or retraction of the *pulvilli* enlarges or diminishes the contacting areas, in a reversible fashion that induces corresponding changes in adhesion strength. This and related biological strategies provide opportunities for controlled adhesion in engineered systems, with one area of possible utility in methods for deterministic assembly of micro/nanomaterials by transfer printing.[7, 8] Here we introduce a switchable adhesive surface inspired by the aphid in which pressure induced sagging of a microstructured elastomeric surface provides extreme, reversible levels of switchability in non-specific, generalized adhesion, with strong to weak adhesion ratios higher than 1000. The designs, which we refer to as microtip surfaces, are robust, reusable and can be easily cleaned with commercial pressure sensitive adhesives like Scotch™ tape. Experimental and theoretical studies provide insights into the basic mechanisms of adhesion. We exploit these ideas in advanced stamps for printing-based assembly of silicon nanomembranes and platelets on a variety of surfaces, in two and three dimensional layouts that would be difficult or impossible to accommodate using other methods.

The adhesives reported here have potential uses in many applications. Our principal motivation is for advanced capabilities in the manipulation of stiff, solid micro/nano-objects via their selective transfer from one substrate (i.e. donor substrate) to another substrate (i.e. receiver substrate) using soft, elastomeric stamps. This transfer printing process[7, 9-11] enables massively parallel assembly of diverse materials (i.e. Si,[12, 13] GaN,[14, 15] GaAs,[16, 17] mica,[7] graphene,[18, 19] silica,[7] and others) in various structural forms (i.e. wires, membranes, plates, with dimensions from a few nanometers to macroscopic scales), with throughputs that correspond to millions of objects per hour. A rapidly growing number of applications in micro and nanotechnology benefit from or are enabled by this type of approach[9, 20-22]. The yields in transfer depend critically on the ability to switch from strong to weak adhesion for retrieval (i.e. 'inking') and delivery (i.e. 'printing'), respectively. To maximize the versatility, control must be accomplished without specialized surface chemistries or adhesives. Kinetic approaches that exploit viscoelastic effects in the stamps[7] are useful, but the low contrast in adhesion switching (i.e. ~3) limits their broad utility. The experimental results and associated theoretical models presented here provide alternative design strategies, with significantly enhanced capabilities for printing based assembly, and the potential for other areas of use

3.3. Results and Discussion

Figure 3.1a illustrates a representative elastomeric microtip surface, with key dimensions labeled. The geometry consists of four features of pyramidal relief on the surfaces of square posts in a square array placed on a ~1 mm thick backing layer of the same material, configured to allow collapse of the regions of each post between the pyramids when subjected to sufficient

applied force. This design enables extremely high levels of switching in adhesion, with a physics that involves a complex interaction between the pressure-controlled contact area, similar the considerations in Chapter 2, and aspects of soft adhesion inherent in the viscoelastic nature of the elastomer, as revealed through the presented systematic studies. We begin with a qualitative description of the process for use in transfer printing (Figure 3.1b), and then outline some aspects of design, supported by quantitative measurements and theory. During retrieval, downward force mechanically collapses the regions between the microtips, thereby maximizing the contact area and, as a result, the strength of generalized adhesion, typically dominated by van der Waals interactions,[8, 23] between the object to be transferred (green platelet in Figure 3.1b) and the stamp. For sufficiently low strengths of adhesion to the donor substrate, retracting at high speeds retrieves the platelet, in a way that simultaneously maximizes its adhesion to the stamp through viscoelastic effects. Immediately after retraction, elastic restoring forces bring the relief back to its original geometry, leaving contact only at the sharp points of the microtips. To affect printing, the stamp, 'inked' in this manner, presses against a receiver surface such that the platelet comes into complete contact on its bottom surface, but the relief on the stamp does not collapse. Slow retraction minimizes the adhesion strength associated with viscoelastic effects, thereby facilitating release and completing the adhesiveless transfer printing assembly process.

A custom measurement setup provides the ability to quantify the adhesion (see, for example Chapter 1, 2). The system consists of motorized x, y stages and a manual tilting stage (ThorLabs, GNO-10) that supports a precision load cell (Transducer Techniques, GSO-10). Microtip surfaces, similar to the one illustrated in Figure 3.1 are mounted on an independent vertical stage (Aerotech, PRO165) that allows contact with a target substrate (i.e. silicon wafer for the results presented here) at controlled speeds and forces. For the work presented here, we

formed these surfaces with the elastomer poly(dimethylsiloxane) (PDMS), using casting and curing procedures of soft lithography with appropriate templates.[24, 25] The molding procedure is described in Figure 3.2a. PDMS is a transparent elastomer with well known, attractive properties for this application, such as linear elastic response to elongations of 100% or more, high physical toughness and excellent fatigue characteristics.[25] Figure 3.3a-d provide scanning electron microscope (SEM) images of a structure in the design of Figure 3.1 without and with an adhering silicon platelet and a schematic illustration for the latter case. Figure 3.3e, f show an advanced configuration that involves the addition of a large microtip in the center, for purposes described subsequently. Figure 3.4a, b present typical force-time plots for a single post having the four-tipped design, with distance scales indicated on the top axes, collected at an approach speed of 5 μm/s, terminated at a specified load for 5 seconds, and then retracted at 1 mm/s. The maximum tensile force during retraction defines the strength of adhesion (i.e. pull-off). Figure 3.4a shows data for a representative case of full mechanical collapse under a preload of 1 mN, with a retraction speed of 1 mm/s. Two slopes are evident in the approaching curve (red line), indicating an increase in stiffness when the region between the microtips collapses and contacts the substrate. The slope in the first region defines an effective spring constant associated with compression of the microtips, with a minor contribution from deformation of the post. The second region includes the elasticity of the post itself, and its thicker elastomeric support. The sharp, negative feature in the curve collected during retraction (blue line) corresponds to rapid release from the contacting surface; its magnitude defines the adhesion force (i.e. pull-off). Figure 3.4b summarizes the corresponding case without collapse, at 0.2 mN preload and 1 mm/s retraction. Here, the adhesion force is too small to measure with the load cell. Images collected with an inverted optical microscope and an SEM (Figures 3.3 and 3.5)

suggest effective contact areas in the collapsed and uncollapsed states that correspond to ~80% and ~0.07% of the projected area of the post and the microtips, respectively. The ratio of these areas suggests an expected difference in adhesion of more than 1000 times. This value, however, underestimates the actual difference that can be achieved because it ignores viscoelastic effects, as observed clearly in the data of Figure 3.4c. In particular, with preloads sufficient to induce mechanical collapse (i.e. 1.5 mN and 3 mN), the adhesion force depends strongly on retraction speed. This functional dependence, which is evident also in data for the corresponding flat surfaces (Figure 3.4d), arises from the viscoelastic nature of the PDMS, as reported previously.[7] We did not observe any significant changes in these adhesion behaviors even on repeated cycling tests (Figure 3.6).

These combined geometric and material effects offer exceptionally high levels of switching in adhesion, for unmatched capabilities in transfer printing, without the need for surface chemistries or separate adhesives to guide transfer. For purposes of demonstration, we use platelets of silicon (100 × 100 μm; thicknesses of 260 nm or 3 μm) fabricated by removing the buried oxide layer from a silicon-on-insulator (SOI) wafer, as illustrated in Figure 3.2b. Figure 3.7a shows such platelets printed onto an array of islands (7 x 7 μm squares, separated by 13 μm with square packing arrangement). The ability to transfer at high yields without adhesives, particularly on structured surfaces where contact areas with the receiver are much smaller than the areas of the platelets themselves, clearly illustrates the utility of the microtip design; these capabilities are unavailable to methods that rely solely on viscoelastic effects for control[7]. As a more challenging example, Figure 3.7b shows the results of printing onto the rough surface of a film of ultrananocrystalline diamond (2 μm thick, root mean square (rms) roughness >70 nm with sharp facet edges; see inset), where we estimate the contact area to be

less than 1% of the platelet area. Stamps with five microtips (Figure 3.3e, f, Figure 3.8) were needed for successful printing of 260 nm thick platelets, where adhesion in the printing mode can be quite small, due to contact only at the single, central post in the final stages of release. Even freely suspended geometries are possible. Figure 3.7c, d show printed platelets (3 μm and 260 nm thicknesses) that span the gaps between pairs of silicon bars on receiver substrates. The high yield and versatility of this process also enable the formation of complex, three dimensional assemblies. Figure 3.7e, f provide images of multilayer configurations of 3 μm thick silicon platelets in single and multiple stacks with translational and rotational increments. These examples demonstrate a construction capability for 3D micro/nanostructures that approaches those of macro-scale fabrication methods based on assembly of building blocks, e.g. *LEGO*® with silicon.

The pyramid geometry has certain practical advantages: (1) it is easy to fabricate in a well-controlled, lithographic manner using techniques of anisotropic etching in silicon and (2) the radius of curvature of the tip can be extremely small, and it is decoupled from the overall height of the relief feature (i.e. the pyramid). The underlying mechanics principles can be used with other shapes.

Data analysis guided by theoretical mechanics modeling reveals the underlying physics of adhesion in surfaces of the type described previously, and identifies the key parameters for optimization. We first consider the strength of the low adhesion state, where the adhesion energy per unit area in the limit of zero peel rate multiplied by the area of contact at the ends of the microtips is important. Figure 3.3a, c show a representative case, where the stamp, made of PDMS, incorporates anisotropically etched pits in silicon (100), to yield microtips with radii of curvature, $R_{microtip}$, less than ~100 nm (Figure 3.2a). Contact with the silicon causes the

microtips to deform, to maintain equilibrium between attraction from surface adhesion and elastic repulsion. These deformations lead to contact areas that are considerably larger than those that might be inferred based only on the geometry of the stamp. Classical models of contact mechanics[26] can be adapted to give analytically the contact radius $R_{contact}$ (Figure 3.3d, Appendix A)

$$\frac{R_{contact}}{\gamma/\overline{E}} = s\left(\frac{R_{microtip}}{\gamma/\overline{E}}, \theta\right) \tag{3.1}$$

where s is a non-dimensional function of the microtip cone angle θ (Figure 3.3d) and $R_{microtip}$. Finite element analysis yields similar results (Appendix A). The value of $R_{contact}$ scales linearly with the work of adhesion γ between the PDMS and the contacting surface, and inversely with the plane-strain modulus $\overline{E} = E/(1-\nu^2)$ of PDMS (E --Young's modulus, υ~0.5 --Poisson's ratio). Analysis shows that $R_{contact}$ decreases with $R_{microtip}$, but reaches an asymptotic value for $R_{microtip} \rightarrow 0$ (Figure 3.9) given by

$$R_{contact}^{\min} = \frac{32\gamma}{\pi\overline{E}} \tan^2 \frac{\theta}{2} \tag{3.2}$$

We note that the above analytical models assume symmetric deformations, without any bending or buckling. The SEM and FEM results of Figure 3.3 support the validity of this assumption.

For the case of a PDMS stamp and a silicon surface, where E=1.8 MPa [27] and γ = 155 mJ/m^2, [28, 29] $R_{contact}$ is approximately the same as $R_{contact}^{\min}$ when $R_{microtip}$ is less than ~100 nm. When $\theta = 90^o$ between two opposite edges of pyramid ($w_{microtip} = \sqrt{2}h_{microtip}$ in experiments, Figure 3.1a), $R_{contact}^{\min}$ is ~680 nm, comparable to 750 nm evident from Figure 3.3c, and 732 nm

given by the finite element method (Appendix A). The conclusion, then, is that existing methods for producing elastomer surfaces in a material like PDMS can already achieve values of $R_{microtip}$ well below the value needed to realize minimal contact area. Advanced microtip layouts can, however, reduce the contact area below that provided by the four tip design. Figure 3.3e, f shows an example. During release, separation occurs first at the microtips at the corners, followed last by the one at the center, thereby reducing the contact area immediately before complete release to the minimum possible value dictated by the physics described above (Figure 3.8), and four times lower than that associated with Figure 3.3c. Further reductions might be possible by increasing E, with other silicones, or decreasing γ, with related elastomers such as perfluoropolyethers,[30] or decreasing the microtip cone angle θ.

The heights of the microtips and their nearest neighbor separations represent other critical parameters. The designs must enable unstable collapse, with near full area contact in the compressed state. For a given separation, there exists a minimum height of the microtip, h_{min}, below which the elastic restoring force is too small to bring the relief back to its original geometry after pressure induced collapse. This minimum height can be determined by equating the strain energy in the compressed PDMS and microtips to the adhesion energy between the contacting surfaces, which gives for the four tip design

$$h_{\min} = \sqrt{\frac{w_{stamp}\gamma}{\overline{E}}\left[3.04\ln\left(\frac{w_{stamp}\overline{E}}{\gamma\tan^2\frac{\theta}{2}}\right)-11.5\right]} \tag{3.3}$$

where w_{stamp} is the width of the post of the stamp. For w_{stamp} = 100 μm (E=1.8 MPa, γ = 155 mJ/m^2 and $\theta = 90^o$), the above expression gives h_{min} = 8.44 μm, which agrees well with the

minimum height of ~8.5 μm observed systematically in experiments (see Figure 3.9, Appendix A). There also exists a maximum height, h_{max}, above which the elastic restoring force associated with compression of the microtips is so large that the stamp rapidly delaminates from the platelet after the pull-off force is applied, thereby preventing large contact areas for efficient removal of an object (e.g. platelet, as illustrated in Figure 3.1) from a donor substrate. The value of h_{max} can be determined analytically by equating the energy release rate to the work of adhesion between the PDMS stamp and the silicon platelet. The result is (see Appendix A)

$$h_{\max} = w_{stamp} f\left(\frac{P}{w_{stamp}^2 \overline{E}}, \frac{w_{microtip}}{w_{stamp}}, \frac{\gamma}{w_{stamp} \overline{E}} \right) \tag{3.4}$$

where f is a non-dimensional function of the applied force P, the microtip width ($w_{microtip}$, Figure 3.1a), and the work of adhesion γ. The full expression is given in Appendix A. For an applied force of 1 mN and $w_{microtip} = \sqrt{2} h_{microtip}$ (other material and geometry parameters the same as before), the maximum height is h_{max} = 13.3 μm, which agrees reasonably well with the maximum height of ~12.7 μm from experiments (see Figure 3.9c, d and Appendix A for details). These minimum and maximum values elucidate criteria that define three possible energy states of the stamp and the platelet: (i) platelet retrieval with relief collapsed, (ii) platelet retrieval with relief delaminated, (iii) failure in platelet retrieval. The microtip sizes were optimized to obtain the second state for representative preload forces (> 1 mN) and retrieval velocities (> 200 μm/s). Experiments with different microtips showed that when h is ~20% smaller or larger than this optimal value, states (i) (platelet retrieval with relief collapsed) or (iii) (failure in platelet retrieval) with the same preloads and velocities could be achieved, respectively.

The rate dependence observed in the microtip structures is identical, to within experimental uncertainties, to that in flat post stamps. The latter effects were explored previously, in the case

of transfer printing,[7] and in the more general context of adhesion between viscoelastic and non-viscoelastic materials.[8, 28, 31]

For operation in the retrieval mode, the stamp must be retracted sufficiently quickly that the fracture of the interface between the platelets and their donor substrate occurs before the viscoelastic fracture of the stamp/platelet interface. During fast retraction the compressed microtips do not have time to relax back to their original shapes; their heights remain small and the overall contact area remains high, such that the energy release rate is lower than the work of adhesion. An analytical viscoelastic model, with creep compliance data for PDMS from the literature,[32] gives a relaxation time of 0.052 seconds (for pulling speed 460 μm/s), at which the collapsed stamp starts to debond from the substrate (Appendix A). For fast retraction (pulling speed > 200 μm/s), this timescale is roughly consistent with experimental observation because the time for complete separation of the stamp/substrate interface is about the same as the time for initial debonding. Additionally, this viscoelastic analysis predicts a pull-off force that is in quantitative agreement with the experiments at pulling speeds > 200 μm/s, as shown in Figure 3.4c. For pulling speeds < 200 μm/s, the analysis gives a larger pull-off force than the experiments because the debonding may gradually propagate along the stamp/substrate interface due to slow retraction, but the model does not account for crack propagation along the interface. Improved analysis and comparison to experiment will require accurate measurements of creep compliance in PDMS of this structure and direct visualization of the interface using high speed imaging techniques. These topics are the focus of future work.

The force-distance curves and other behaviors of Figure 3.4 can also be captured by mechanics modeling. For the case of Figure 3.4a, modeling predicts two slopes, as observed in

experiment: $k_{microtip}$ when contact occurs only at the microtips, and k_{post} for contact at both the microtips and the intervening regions. In particular, analysis yields (Appendix A)

$$\frac{1}{k_{microtip}} = \frac{1}{k_{post}} + \frac{1}{Ew_{microtip}}\left[\frac{3h_{microtip}}{4w_{microtip}} + \frac{1}{\pi}\left(\frac{w_{microtip}}{w_{stamp}} - 2\frac{w_{microtip}^3}{w_{stamp}^3}\right)\ln\left(\frac{w_{stamp}^2}{2w_{microtip}^2} - 1\right)\right] \tag{3.5}$$

For $k_{microtip}$ = 30 N/m and k_{post} = 90 N/m extracted from Figure 3.4a, and $h_{microtip}$ = 10.6 μm and width $w_{microtip} = \sqrt{2}h_{microtip}$ = 15 μm from experiments, the left- and right-hand sides of Eq. (3.5) give 0.033m/N and 0.036m/N, respectively. This excellent level of agreement validates the modeling, and its further use in examining the differences between Figures 3.4c, d to gain insights into the adhesion mechanics. In the collapsed state, the microtips provide forces that add to the externally applied force needed to cause delamination. This effect can be explored through calculation. In particular, the mechanics models described previously yield analytical forms for the restoring force, F, associated with the compressed microtips. The result takes the form (Appendix A)

$$F = w_{stamp}^2 \overline{E}\, g\left(\frac{P}{w_{stamp}^2 \overline{E}}, \frac{w_{microtip}}{w_{stamp}}, \frac{h_{microtip}}{w_{stamp}}\right) \tag{3.6}$$

where g is a non-dimensional function of the applied force P, microtip width $w_{microtip}$ and height $h_{microtip}$, and is given in Appendix A. This force, as shown in Figure 3.10a, is the same as the preload when only microtips contact the platelet. The sudden increase in the restoring force corresponds to the collapse of post between microtips. This force then increases linearly with the preload (post contact in Figure 3.10a), but with reduced slope due the elasticity of the post. This dependence is followed by a nonlinear increase, at a reduced rate because the contact area also increases (zipping of interface in Figure 3.10a). For an applied force of 1.5 mN, the total restoring force is 0.63 mN for the collective effect of four microtips with height $h_{microtip}$ = 10.6

μm and width $w_{microtip} = \sqrt{2}h_{microtip}$ = 15 μm (other material and geometry parameters are the same as above). Note that this restoring force is larger than the preload 0.39 mN needed to cause collapse of the regions between the microtips (i.e. position in the red curve of Figure 3.4a that occurs at the point where the linear slope changes) because the microtips continue to be compressed after the intervening regions collapse (see Figure 3.10a). Figure 3.10b presents a master plot obtained by shifting the data of Figure 3.4b downward along the y-axis by an amount equal to the total restoring force evaluated by modeling, and plotting the results together with the data of Figure 3.4c. The overlap of the resulting curves, to within experimental uncertainty, supports the modeling and the associated interpretation of the underlying physics.

3.4. Conclusions

This chapter reports a new and versatile method for deterministic assembly of solid micro/nanoscale parts into two and three dimensional configurations, and some theoretical foundation for understanding key design parameters. The work presented here provides experimental data and theoretical models on the use of microstructures of relief on elastomeric surfaces to achieve pressure induced switching in adhesion strength. Theoretically guided design optimization yields high levels of control, with more than three orders of magnitude difference between the forces measured in strong and weak adhesive states. These characteristics enable transfer printing reliably and repeatedly with very high yield (almost 100%) in new modes, with important consequences for applications. Future opportunities include exploring other uses, and pursuing strategies for increasing the adhesion over the corresponding flat surface by incorporating techniques discussed in previous chapters or developing new designs such as those using vacuum effects or notched features on the sidewalls of the posts. These and other

structural designs can be further enhanced through the introduction of new materials, using guidance from mechanical models similar to those presented here and the future viscoelastic effect model on elastomeric microtip surface adhesion during high speed retrieval.

3.5. Experimental

Fabrication of elastomeric surfaces with microtips. Fabricating microtip stamps (Figure 3.2a) involved casting and curing the elastomer polydimethylsiloxane (PDMS, Sylgard 184, Dow Corning; 5:1 monomer:crosslinking agent) against a Si (100) wafer (Addison Engineering) with a pattern of photodefined epoxy (SU-8 50; MicroChem Corp.; 100 μm thick) and an array of pyramidal pits (15 x 15 μm squares, 10.6 μm deep, separated by 70 μm with square packing arrangement) formed by anisotropic etching with KOH through a photolithographically patterned hard mask of SiN (100 nm thick, formed using PECVD, PlasmaTherm). The epoxy layer provided square openings (100 x 100 μm) with corners aligned to the sets of pits. Casting the PDMS prepolymer against the anti-adhesion functionalized (FOTCS, United Chemical Technology) surface of this wafer, thermally curing the PDMS (70˚C for 2 hours) and then demolding from the template yielded the desired elastomeric surfaces with microtips.

Fabrication of silicon platelets for printing. The printed structures consisted, in all cases, of flat plates of silicon (100) derived from silicon-on-insulator (SOI) wafers (Shin-Etsu Chemical Co., Ltd. and Soitec), with thicknesses of 3 μm or 260 nm. These plates were defined by patterning a layer of photoresist (AZ5214, 1.5 μm thick) in a square geometry (100 x 100 μm, square packing arrangement, 300 μm separation) and then etching the exposed top Si by SF_6 reactive ion etching (RIE, PlasmaTherm). Next, wet etching with HF through a mask of photoresist removed the buried oxide everywhere except for 110 x 110 μm squares co-centered

with the squares of silicon. A final pattern of photoresist (AZ5214) defined mechanical anchor features (15 x 45 μm rectangles, 1.5 μm thick) to tether the silicon squares to the underlying wafer at each of their four corners. Undercut etching of the remaining oxide with HF for 4 hours completed the process. Figure 3.2b summarizes the steps.

Transfer Printing. Precision translation and rotational stages controlled the positions of the stamps during the various steps in printing, as illustrated in Figure 3.1. After each complete sequence of printing, the structures were annealed at 200-900˚C depending on receiver substrates in air for 3 minutes (TMC Services, Inc., Micristar Model 828) to eliminate residual photoresist and to increase the interfacial strength of adhesion between layers.

3.6. References

[1] E. Artz, S. Gorb, R. Spolenak, *Proc. Natl. Acad. Sci. U.S.A.* **2003**, *100*, 10603.
[2] A.K. Geim, S.V. Dubonos, I.V. Grigorieva, K.S. Novoselov, A.A. Zhokov, S.Y. Shapoval, *Nat. Mater.* **2003**, *2*, 461.
[3] M.P. Murphy, B. Aksak, M. Sitti, *Small* **2009**, *5*, 170.
[4] S. Kim, M. Sitti, T. Xia, X. Xiao, *Soft Matter* **2009**, *5*, 3689.
[5] A. Carlson, H.-J. Kim-Lee, J. Wu, P. Elvikis, H. Cheng, A. Kovalsky, S. Elgan, Q. Yu, P.M. Ferreira, Y. Huang, K.T. Turner, J.A. Rogers, *Appl. Phys. Lett.* **2011**, *98*, 264104.
[6] A.D. Lees, J. Hardie, *J. Exp. Biol.* **1987**(136), 209.
[7] M.A. Meitl, Z.-T. Zhu, V. Kumar, K.J. Lee, X. Feng, Y.Y. Huang, I. Adesida, R.G. Nuzzo, J.A. Rogers, *Nat. Mater.* **2006**, *5*, 33.
[8] X. Feng, M.A. Meitl, A.M. Bowen, Y. Huang, R.G. Nuzzo, J.A. Rogers, *Langmuir* **2007**, *23*, 12555.
[9] D.H. Kim, J.-H. Ahn, W.-M. Choi, H.-S. Kim, T.-H. Kim, J. Song, Y. Huang, L. Zhuangjian, L. Chun, J.A. Rogers, *Science* **2008**, *320*, 507.
[10] Z. Fan, J.C. Ho, Z.A. Jacobson, H. Razavi, A. Javey, *Proc. Natl. Acad. Sci. U.S.A.* **2008**, *105*, 11066.
[11] J. Yu, V. Bulovic, *Appl. Phys. Lett.* **2007**, *91*, 043102.
[12] E. Menard, K.J. Lee, D.-Y. Khang, R.G. Nuzzo, J.A. Rogers, *Appl. Phys. Lett.* **2004**, *84*, 5398.
[13] A.J. Baca, M.A. Meitl, H.C. Ko, S. Mack, H.-S. Kim, J. Dong, P.M. Ferreira, J.A. Rogers, *Adv. Func. Mater.* **2007**, *17*, 3051.
[14] K.J. Lee, M.A. Meitl, J.-H. Ahn, J.A. Rogers, R.G. Nuzzo, V. Kumar, I. Adesida, *J. Appl. Phys.* **2006**, *100*, 124507.
[15] H. Kim, E. Brueckner, J. Song, Y. Li, S. Kim, C. Lu, J. sulking, K. Choquette, Y. Huang, R.G. Nuzzo, J.A. Rogers, *Proc. Natl. Acad. Sci. U.S.A.* **2011**, *108*(25), 10072.

[16] Y. Sun, H.-S. Kim, E. Menard, S. Kim, I. Adesida, J.A. Rogers, *Small* **2006**, *2*, 1330.
[17] J. Yoon, S. Jo, I.S. Chun, I. Jung, H.-S. Kim, M. Meitl, E. Menard, X. Li, J.J. Coleman, U. Paik, J.A. Rogers, *Nature* **2010**, *465*, 329.
[18] X. Liang, Z. Fu, S.Y. Chou, *Nano Lett.* **2007**, *7*, 3840.
[19] X. Li, Y. Zhu, W. Cai, M. Borysiak, B. Han, D. Chen, R.D. Piner, L. Colombo, R.S. Ruoff, *Nano Lett.* **2009**, *9*, 4359.
[20] D.-H. Kim, N. Lu, R. Ma, Y.-S. Kim, R.-H. Kim, S. Wang, J. Wu, S.M. Won, H. Tao, A. Islam, K.J. Yu, T.-I. Kim, R. Chowdhury, M. Ying, L. Xu, M. Li, H.-J. Chung, H. Keum, M. McCormick, P. Liu, Y.-W. Zhang, F.G. Omenetto, Y. Huang, T. Coleman, J.A. Rogers, *Science* **2011**, *333*, 838.
[21] J. Yoon, A.J. Baca, S.-I. Park, P. Elvikis, J.B.G. III, L. Li, R.H. Kim, J. Xiao, S. Wang, T.-H. Kim, M.J. Motala, B.Y. Ahn, E.B. Duoss, J.A. Lewis, R.G. Nuzzo, P.M. Ferreira, Y. Huang, A. Rockett, J.A. Rogers, *Nat. Mater.* **2008**, *7*, 907.
[22] Y. Qi, J. Kim, T.D. Nguyen, B. Lisko, P.K. Purohit, M.C. McAlpine, *Nano Lett.* **2011**, *11*, 1331.
[23] T.-H. Kim, A. Carlson, J.-H. Ahn, S.M. Won, S. Wang, Y. Huang, J.A. Rogers, *Appl. Phys. Lett.* **2009**, *94*, 113502.
[24] J.A. Rogers, R.G. Nuzzo, *Mater. Today* **2005**, *8*, 50.
[25] Y. Xia, G.M. Whitesides, *Angew. Chem. Int. Ed.* **1998**, *37*, 551.
[26] D. Maugis, *Langmuir* **1995**, *11*, 679.
[27] K.H. Kim, Z. Liu, Y.S. Kim, J. wu, J. Song, H.S. Kim, Y. Huang, K.C. Hwang, Y. Zhang, J.A. Rogers, *Small* **2009**, *5*, 2841.
[28] M.K. Chaudhury, G.M. Whitesides, *Langmuir* **1991**, *7*, 1013.
[29] Y.Y. Huang, W. Zhou, K.J. Hsia, E. Menard, J.-U. Park, J.A. Rogers, A.G. Alleyne, *Langmuir* **2005**, *21*, 8058.
[30] T.T. Truong, R. Lin, S. Jeon, H.H. Lee, J. Maria, A. Gaur, F. Hua, I. Meinel, J.A. Rogers, *Langmuir* **2007**, *23*, 2898.
[31] A.N. Gent, *Langmuir* **1996**, *12*, 4492.
[32] Z. Xu, K. Kim, Q. Zou, P. Shrotriya, *Appl. Phys. Lett.* **2008**, *93*, 133103.

3.7. Figures

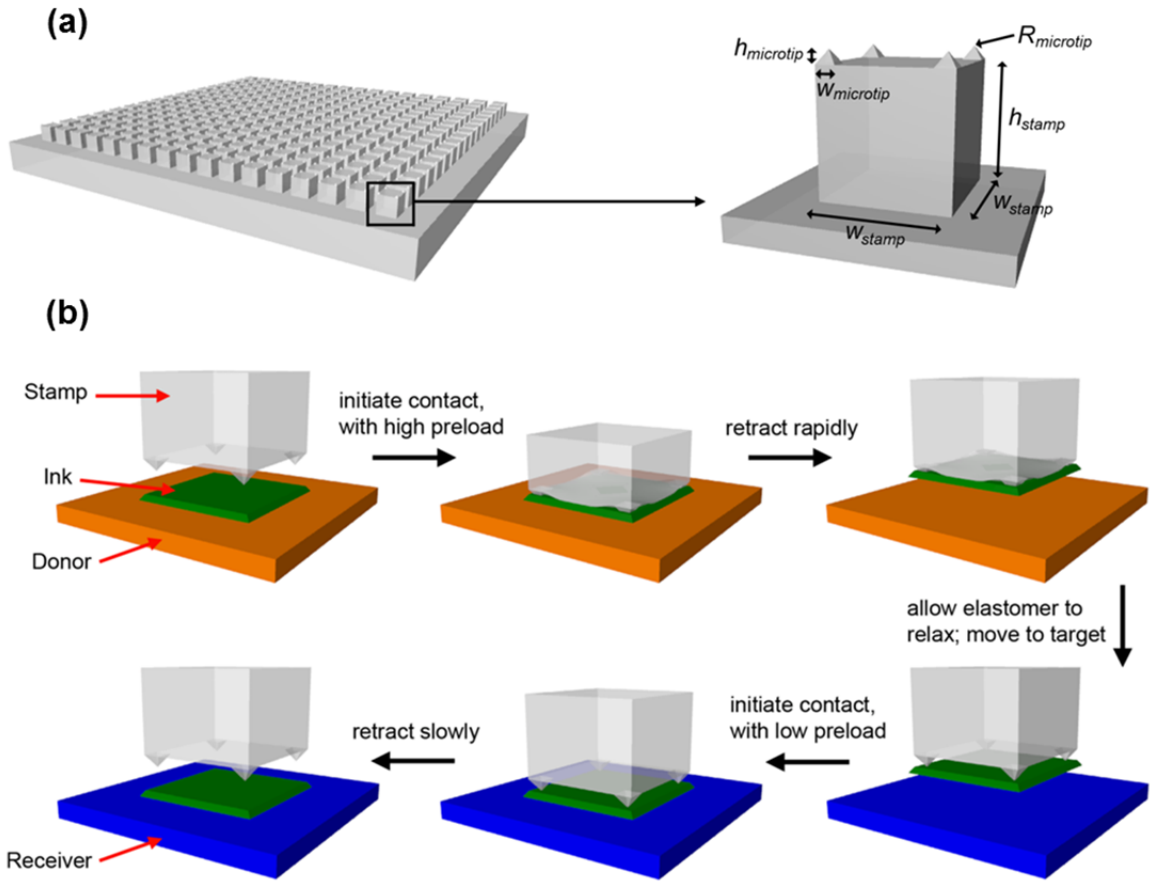

Figure 3.1. Implementation of elastomeric, microtip adhesive surface in a stamp for deterministic assembly by transfer printing. (a) Microtip adhesive surface consisting of four features of pyramidal relief on the surfaces of square posts in a square array. (b) Protocols for the printing process - mechanical sagging of the stamp between microtips to maximizes adhesion during retrieval while localized contact at the microtips during printing provides negligible adhesion.

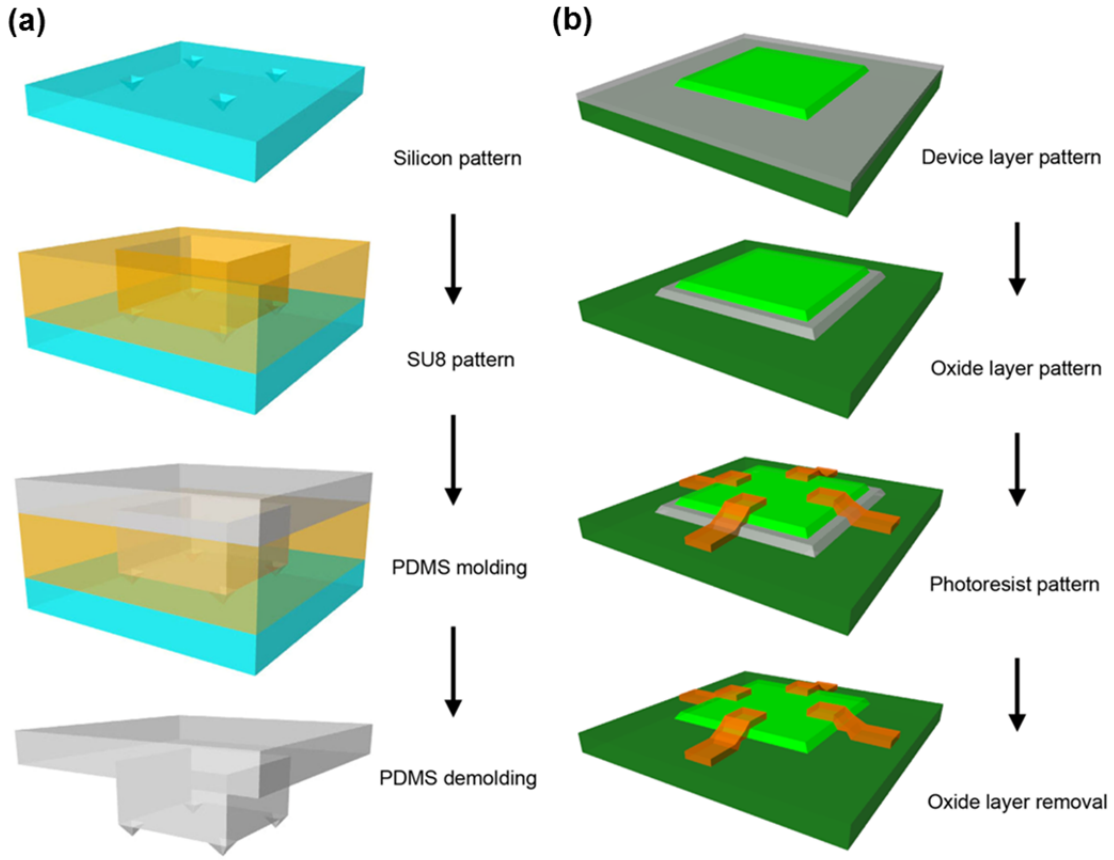

Figure 3.2. (a) Schematic illustration of the process for fabricating microtip stamps of PDMS by casting and curing against a photolithographically defined pattern of SU8 on an anisotropically (KOH) etched silicon (100) wafer. (b) Schematic illustration of the process for fabricating silicon platelets in printable configurations, starting with silicon-on-insulator (SOI) wafers with 3 μm or 260 nm thick top Si layers.

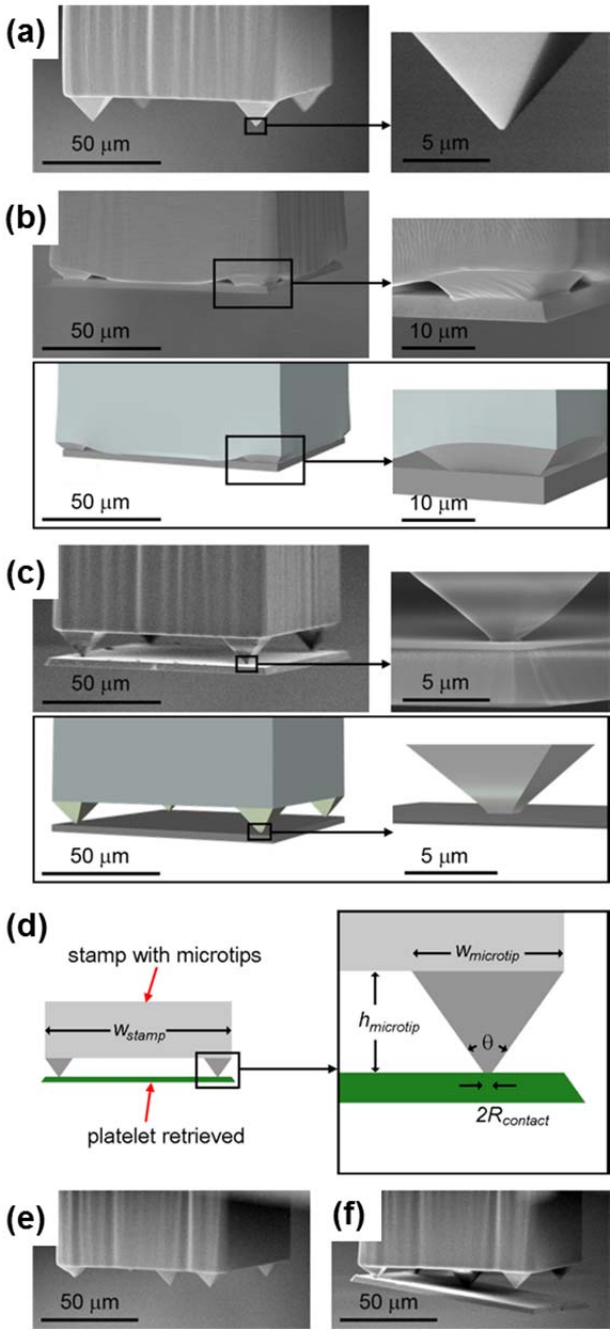

Figure 3.3. Scanning electron microscope (SEM) and finite element method (FEM) images of representative elastomeric stamps in microtip designs, with and without silicon platelets (3 μm thick; 100 × 100 μm) on their surfaces. (a)-(c) Four-tipped layout. The right frames provide magnified views of one of the microtips and the bottom frames provide corresponding images of the results of finite element modeling (b, c). (d) Schematic illustration for notation of the stamp dimension. (e, f) Five-tipped layout. In this design, the silicon platelet remains in contact only with the largest, central microtip in the final stages of the transfer printing process.

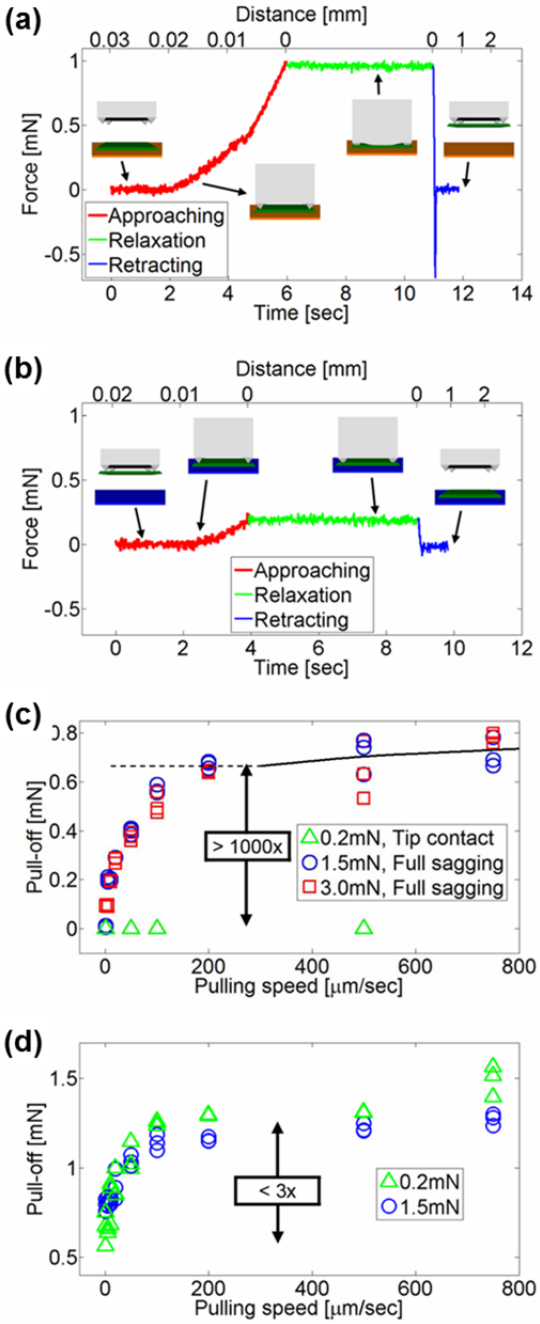

Figure 3.4. Typical force-time (bottom axis) and force-distance (top axis) curves associated with contact of a microtip surface with the flat surface of a silicon wafer (a, b). The inset illustrations correspond to the steps of retrieval (a) and delivery (b) for use of such a surface in a transfer printing mode. Plots of force required to remove a microtip surface (c) and a corresponding flat surface (d) from the silicon, as a function retraction speed for three different preload cases, simulating the steps of retrieval (0.2 mN) and delivery (1.5, 3 mN) in a printing process. Modeling results for the microtip surface are indicated as a black line (c).

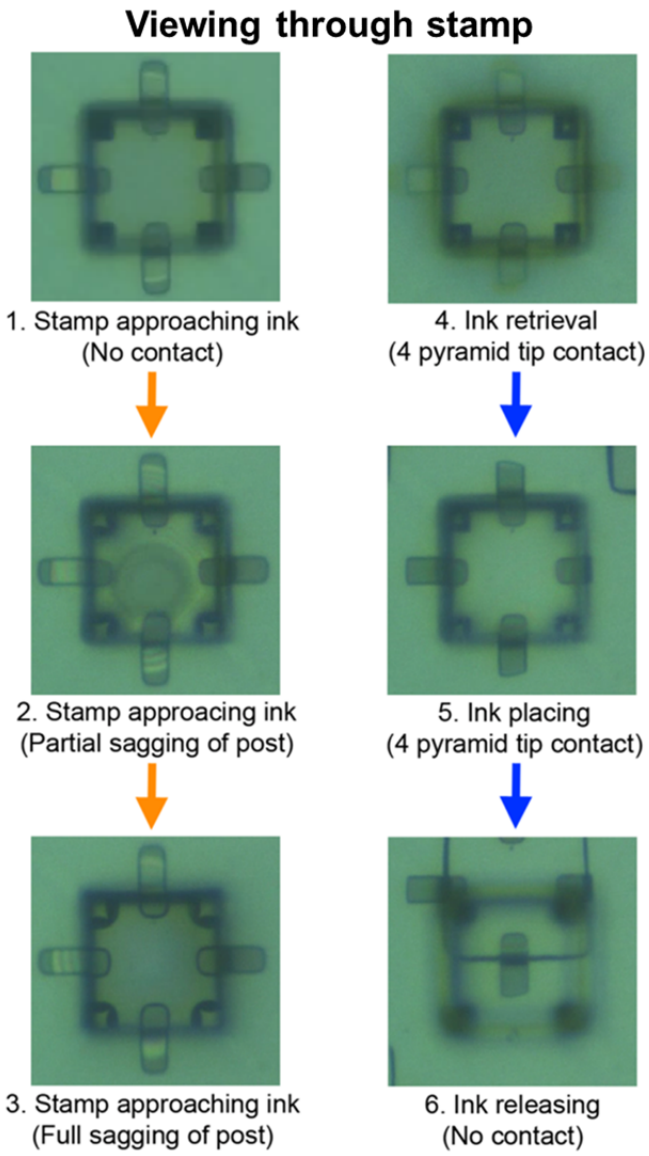

Figure 3.5. Optical microscope top view images, collected by viewing through a transparent microtip stamp, during various stages of the printing.

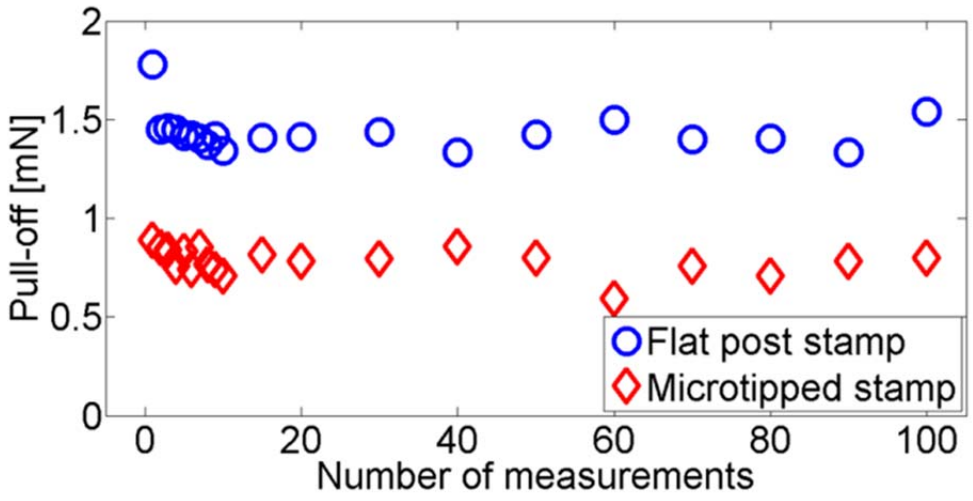

Figure 3.6. Pull-off force data of a stamp with four-tipped layout and a corresponding flat surface measured repeatedly with 200 μm/s retraction speed and 2 mN preload constantly up to 100 times.

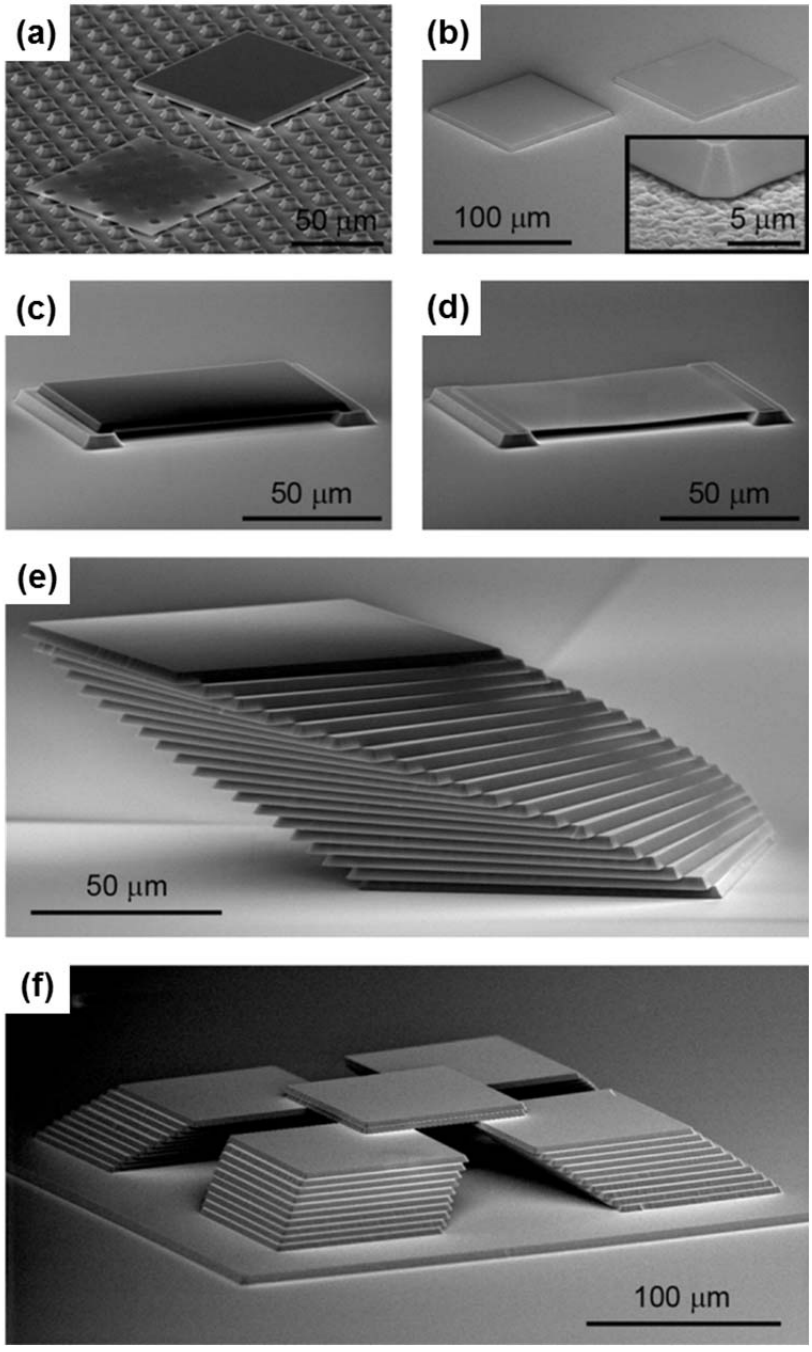

Figure 3.7. SEM images of representative printing results with thick (3 μm) and thin (260 nm) silicon platelets (100 × 100 μm squares) on different surfaces and in free standing and multilayer stacked geometries. (a) Image of platelets printed on an array of square islands. (b) Image of 3 μm thick silicon platelets printed on the rough surface of a film of ultrananocrystalline diamond on a silicon wafer. Images of 3 μm (c) and 260 nm (d) thick silicon platelets printed onto two silicon bars, to yield freely suspended structures. Images of multilayer configurations of 3 μm thick silicon platelets in a single stack with small incremental rotations and translations (e) and four similar stacks, capped with a pair of platelets in the center (f), both on flat silicon wafer substrates.

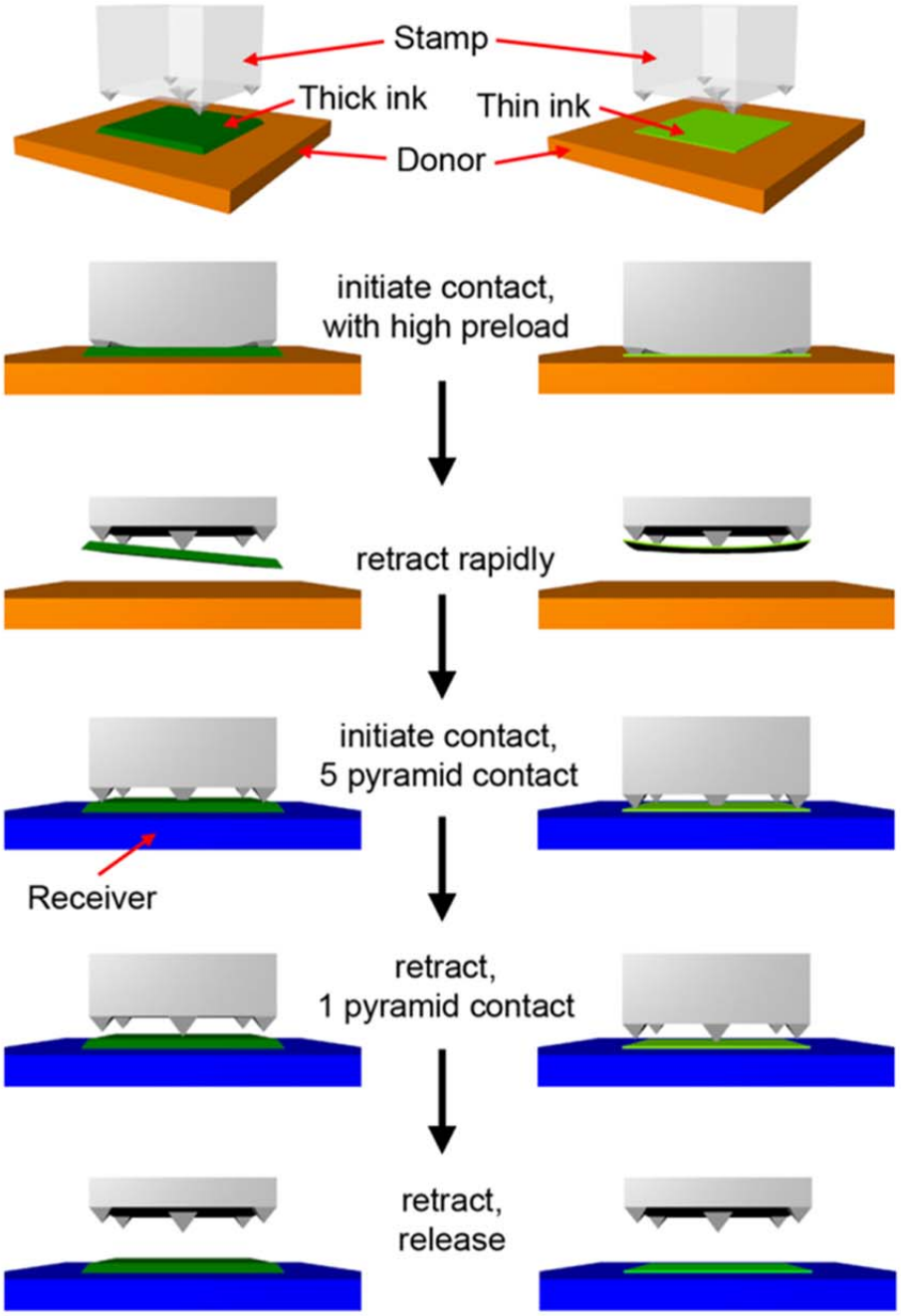

Figure 3.8. Schematic illustration of the process for transfer printing with a microtip stamp that has a five-tipped design. The largest microtip, located at center, is the only point of contact between the stamp and the ink at the final stage of the transfer process.

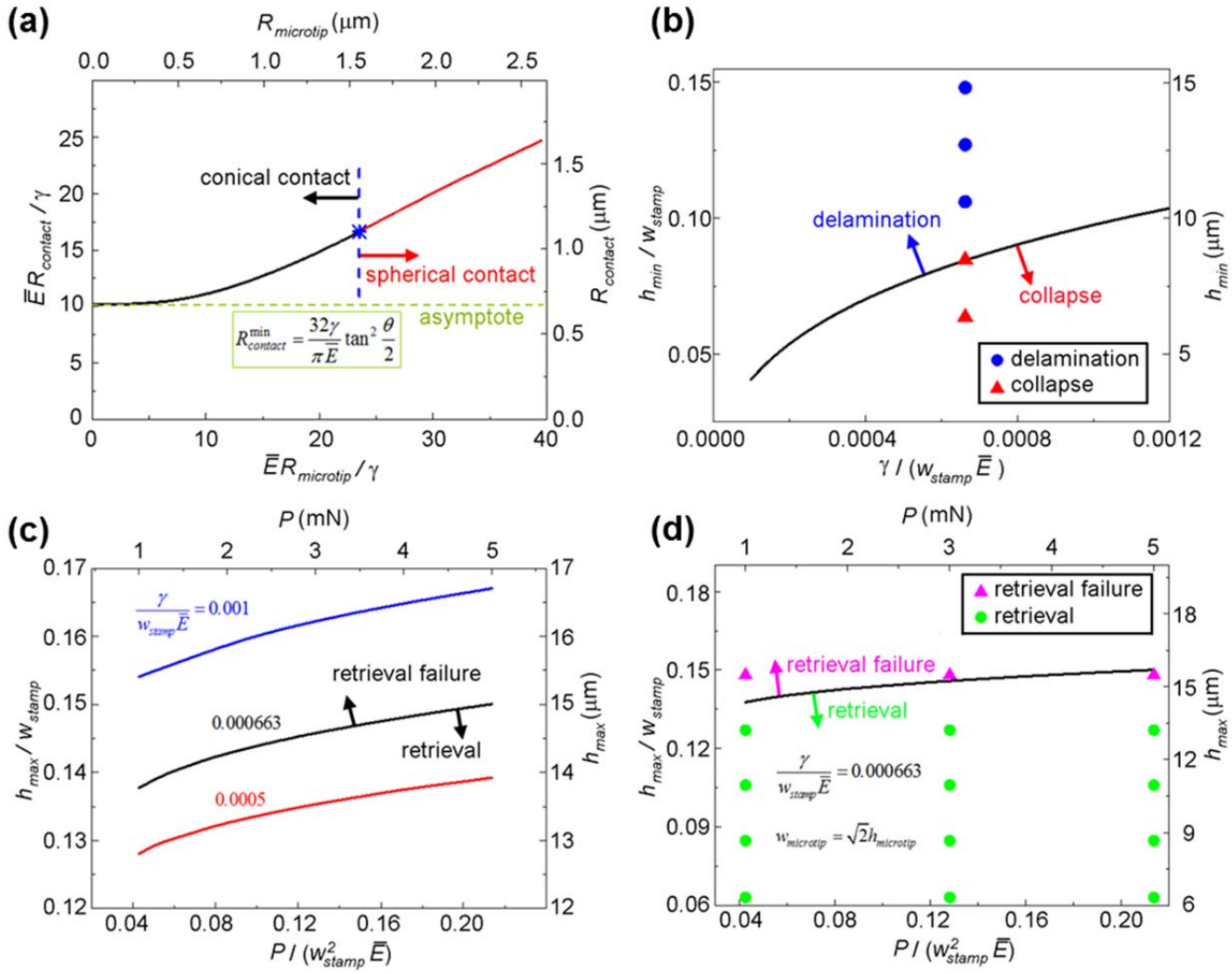

Figure 3.9. **(**a) The contact radius (at zero preload) between the microtips and platelet versus the microtip radius of curvature for the microtip cone angle $\theta = 90^o$. The asymptote for vanishing microtip radius gives minimal contact radius. (b) The minimum height of microtips versus the work of adhesion (normalized by the post width and plane-strain modulus of the stamp) for $\theta = 90^o$, together with the experimental data for delamination and collapse. (c) The maximum height of microtips versus the preload for several values of work of adhesion. (d) The maximum height of microtips versus the preload, together with the experimental data for retrieval and failure.

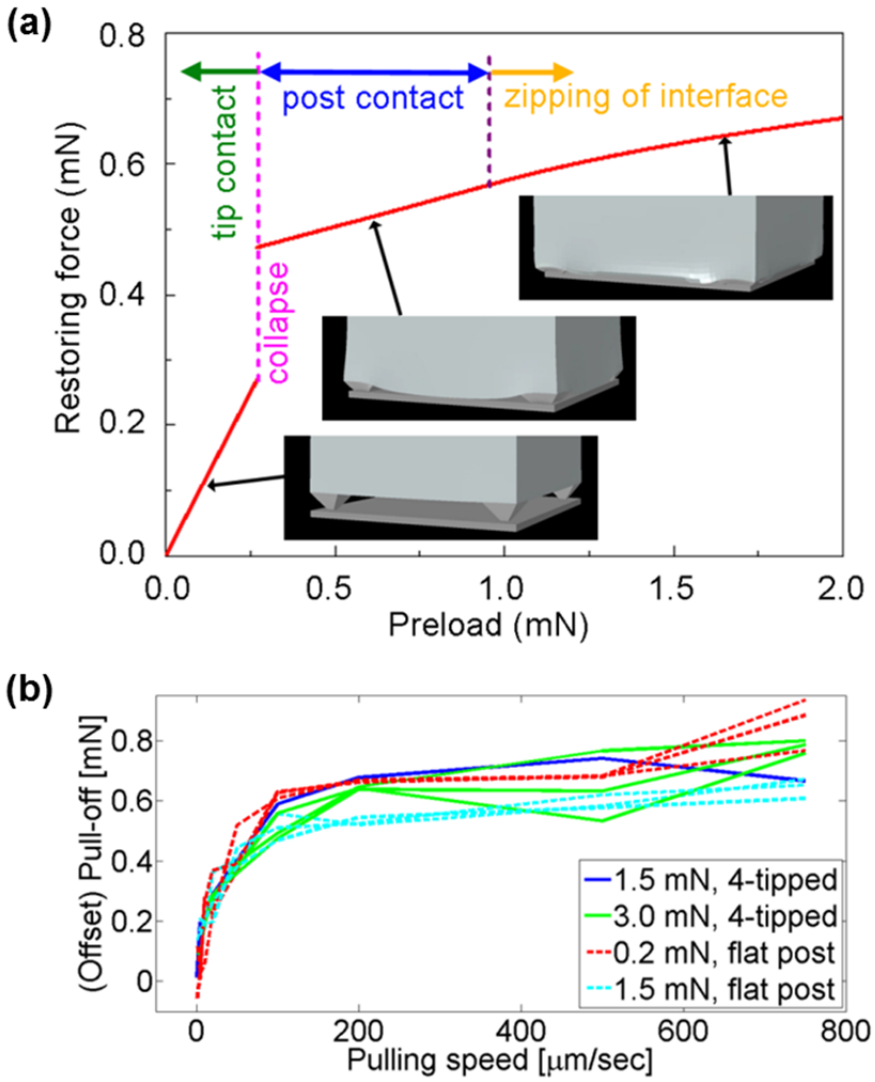

Figure 3.10. (a) Restoring force associated with compression of microtips on the surface of an elastomer as a function of preload, during loading with corresponding images of finite element modeling results. (b) Master plot of force required to separate an elastomer surface from a flat substrate, as a function of retraction speed for different preload cases from Fig. 4.4 c, d. The data include the cases of elastomeric posts that terminate in flat surfaces and in sets of four microtips, scaled to account for the mechanics of the microtips, according to theoretical modeling.

CHAPTER 4

SHEAR-ENHANCED ADHESIVELESS TRANSFER PRINTING FOR USE IN DETERMINISTIC MATERIALS ASSEMBLY[1,2,3]

4.1. Abstract

This chapter describes an alternative protocol for adhesiveless transfer which can provide complementary functionality to the methods presented in previous sections. Here, the physics and application of targeted shear loading to a stamp surface having vertical and angled relief is explored for modulation and/or switching of interfacial adhesion, in a controlled and repeatable fashion. Experimental measurement of adhesive forces as functions of shear and stamp dimension reveal key scaling properties and provide a means for comparison to theory and modeling. An analytical model for sheared vertical relief structures is developed which describes the influence of remote mechanical loading on the system in terms of stamp material properties and the geometry of contact. Finite element analysis using Griffith's fracture criterion confirm trends predicted from the model and experiments. Examples of printed structures in suspended and multilayer configurations and a roller-type printing tool demonstrate some capabilities in micro/nanoscale materials assembly.

[1] Reprinted, with permission from A. Carlson, H.-J. Kim-Lee, J. Wu, P. Elvikis, H. Cheng, A. Kovalsky, S. Elgan, Q. Yu, P.M. Ferreira, Y. Huang, K.T. Turner, J.A. Rogers, "Shear-Enhanced Adhesiveless Transfer Printing For Use in Deterministic Materials Assembly," *App. Phys. Lett.* **98**, 264104 (2011). Copyright: 2011 American Institute of Physics.

[2] Reprinted, with permission from H. Cheng, J. Wu, Q. Yu, A. Carlson, K.T. Turner, K.-C. Hwang, Y. Huang, J.A. Rogers, "An Analytical Model for Shear-Enhanced Adhesiveless Transfer Printing," *submitted*.

[3] Reprinted, with permission from S.Y. Yang, A. Carlson, H. Cheng, Q. Yu, N. Ahmed, J. Wu, S. Kim, M. Sitti, P.M. Ferreira, Y. Huang, J.A. Rogers, "Elastomer surfaces with directionally dependent adhesion strength and their use in transfer printing with continuous roll-to-roll applications," *submitted*.

4.2. Introduction

Orientation-dependent dry adhesives[1-5] represent an interesting class of synthetic materials finding many applications in robotics and reversible, pressure sensitive adhesives.[2, 6, 7] Borrowing geometries and formats from naturally occurring systems, these materials are typically fabricated in compliant materials, such as PDMS and polyurethane,[3] and rely on direction-specific mechanical displacements to engage or disengage adhesive forces. For example, angled fibers (both spatulated and blunt-ended)[3, 7] demonstrate enhanced adhesion when loading along the fiber axis (angle of inclination, 'stiff adhere direction') and enhanced release when loading in the counter direction ('compliant direction').[1, 8, 9] Systematic experimental and theoretical studies have provided insight into optimized parameters such as fiber angle, geometry, and contact surface (all three define the elastic anisotropy of contact) to maximize adhesion.[3, 9] Release mechanisms for these types of structures however, almost universally rely on shear displacements applied against the angle of fiber inclination. Fracture mechanics studies using an interfacial crack model between two elastic solids demonstrated a directional dependence on the adhesion, with fibers likely to bend and deform during compliant direction shear.[1, 8, 9] This extreme deformation can mechanically initiate separation or alter interface loading at the structured, adhesive surface.[2, 5, 10] In a related study, shearing of a glass lens against a continuous PDMS surface caused reduction in the recorded vertical direction separation loads.[9] Decreases in pull-off forces continued as tangential forces were increased. While these studies were performed to validate the general enhancement of adhesion using fiber and spatulated surface relief, they also provide interesting concepts for novel transfer printing protocols.

In this chapter we develop a printing modality which uses related concepts to the shear-mediated release schemes just described. Here, targeted, remote shear loading of single or arrayed rectangular posts molded onto the surface of a PDMS stamp is utilized to controllably modulate its adhesive strength. Relating measured pull-off forces to shear strains in the stamp demonstrate the process utility to achieve, reproducibly and without complex surface hierarchy, adhesion strength significantly below the slow-peel limit of rate-dependent adhesives. Detailed mechanical modeling relates the decrease in adhesion to surface moments generated at the stamp/substrate interface. Analytical models for the interfacial strain are developed and confirmed via finite element analysis. As a variant to the shear-enhanced printing, we briefly consider a related geometry utilizing angled posts which provide adhesion switching by control of the direction of retraction. For this unique geometry, we discuss how the structures can be operated in normal, batch mode, and how they can be implemented with cylindrical stamps as a pathway to continuous, roll-to-roll operation.

4.3. Results and Discussion

4.3.1. Shear-enhanced printing capabilities

Figure 4.1a presents a schematic illustration of shear-assisted printing with an elastomeric stamp comprising a single, rectangular post mounted to a thick backing layer (950 μm, inset, Figure 4.1a). Lateral post dimensions directly match the underlying ink, here illustrated as a green plate.[11-13] During retrieval, the stamp is conformally contacted to the ink and then rapidly retracted to maximize adhesion through viscoelastic effects.[14, 15] To print, the stamp, inked in this manner, is placed in contact with a receiver substrate. Next, the receiver is

displaced laterally (through motion of the underlying stage) to induce shearing stresses and the stamp is then slowly delaminated. This displacement generates a shear deformation in the stamp that reduces the normal component of the force required to induce delamination, thereby facilitating efficient release of the ink onto the receiver. Figure 4.1b provides a series of plan view optical images from a shear-assisted printing event highlighting contact, shearing, and release between a representative poly(dimethylsiloxane) (PDMS, 5:1 monomer:crosslinking agent) stamp (100 ×100 × 50 μm), a monocrystalline silicon ink (100 × 100 × 3 μm), and a silicon wafer substrate.

It is well established that shear can generate mixed-mode loading at interfaces, in a way that influences the failure behavior.[16-19] Remote application of shear force can also affect the overall stress distribution at the interface. To evaluate stamp adhesion under various shear loading conditions, normal direction pull-off forces were measured using a custom setup.[20] PDMS stamps with square ends, fabricated via established casting and curing techniques,[20, 21] with lateral dimensions ranging from 100 μm to 250 μm, were mounted to motorized *x, y, z* stages and a precision load cell (Transducer Techniques, GSO-10) to measure forces in the *z*-direction. Lateral displacement of the stage in *x* followed by retraction of the stamp in *z* provided force-displacement curves (Figure 4.2) from which pull-off forces could be determined by measuring the magnitude of the sharp negative features. Figure 4.3a shows the dependence of the peak pull-off force *F* on shear displacement *u*, corresponding to decreasing adhesion with increasing shear, for four different post sizes. Here, the velocities for shearing and retracting were fixed at 10 μm/s. The measurements from stamps with different lateral dimensions all exhibit a similar behavior, as shown in Figure 4.3b when the forces are normalized as $P = F/\left(EL^2\right)$ and the shear displacements are converted to shear strain γ, where *E* is the

Young's modulus and *L* is the lateral dimension of the post. In these calculations and others in the chapter, the Young's modulus and Poisson's ratio are taken as E=2.1 MPa and ν=0.49, respectively.[14, 20] Similar trends are evident for other shear and delamination velocities, as presented in Figure 4.4.

Several practical implementations of shear-assisted printing are demonstrated in Figure 4.5. Studies of printing yield illustrate the improvements enabled by shear. Figure 4.5a provides a relationship between applied shear strain and yields for silicon plates printed on the bare surface of a silicon wafer. Procedures for fabrication of the inks are provided in the experimental section and described schematically in Figure 4.6; they are similar to methods described previously.[20, 22, 23] A ~10x increase in yield is observed for shear strains of 14%. These improvements expand the capabilities of transfer printing, to allow delivery of inks onto otherwise challenging receiver substrates. An example of a textured surface appears in Figure 4.5b, where the relief consists of lines and spaces (3 μm lines, 17 μm spacing) molded onto the surface of a substrate of PDMS (2:1 monomer:crosslinking agent mixing ratio). The contact area here corresponds to <15% of the area of the ink, thereby providing adhesion that would be too low to enable printing with previously reported peel-rate control strategies. Freely suspended structures and multilevel arrangements of inks, such as the collection of overhanging and stacked plates printed onto silicon substrates shown in Figure 4.5c, d, respectively, represent some other examples enabled by shear, of possible use in fabricating unusual microelectromechanical systems, bolometers and other integrated devices. Figure 4.5e demonstrates the transfer of two prefabricated InGaN microscale light emitting diodes (μ-ILED)[24] as one demonstration of advanced ink transfer.

4.3.2. Analytical and finite element models for shear-enhanced transfer

The shear strain in the post γ is determined from the shear displacement, u, and post stamp geometry through a mechanics analysis that accounts for the compliance of the backing layer that supports the post. The backing layer is much wider and thicker than the post, and is modeled as a semi-infinite solid subjected to a shear stress τ in the x direction over the post area $L \times L$ at the surface of z=0 as shown in Figure 4.7. For a concentrated shear force $\tau dx_0 dy_0$ at (x_0,y_0) over an infinitesimal area $dx_0 dy_0$ of the bottom surface, the x-direction displacement at (x,y) on the surface is[25] $dw = \dfrac{\tau dx_0 dy_0}{2\pi\mu\sqrt{(x-x_0)^2+(y-y_0)^2}}\left[1-\nu+\nu\dfrac{(x-x_0)^2}{(x-x_0)^2+(y-y_0)^2}\right]$[26],

where μ and υ are the shear modulus and Poisson's ratio of the stamp, respectively. For a uniform shear stress τ applied to the post, the displacement at (x,y) is

$$w(x,y) = \int_{L\times L} dw = \frac{\gamma}{2\pi}\int_{-L/2}^{L/2} dx_0 \int_{-L/2}^{L/2} \frac{1}{\sqrt{(x-x_0)^2+(y-y_0)^2}}\left[1-\nu+\nu\frac{(x-x_0)^2}{(x-x_0)^2+(y-y_0)^2}\right]dy_0, \quad (4.1)$$

where $\gamma = \tau/\mu$ is the shear strain in the post. The average displacement $\bar{u}$ along the shear (x) direction is obtained by integrating Eq. (4.1),

$$\bar{u} = \frac{1}{L\times L}\int_{-L/2}^{L/2} dx \int_{-L/2}^{L/2} w(x,y)\,dy = \frac{2-\nu}{\pi}\gamma L \ln\left(\sqrt{2}+1\right) \quad (4.2)$$

The measured shear displacement u is the sum of $\bar{u}$ and the shear displacement γh across the post, i.e.,

$$u = \bar{u} + \gamma h\,. \quad (4.3)$$

Substitution of Eq. (4.2) into Eq. (4.3) yields the shear strain in the post,

$$\gamma = \frac{u}{h + \frac{2-\nu}{\pi} L \ln\left(\sqrt{2}+1\right)} \approx \frac{u}{h + \frac{3}{2\pi} L \ln\left(\sqrt{2}+1\right)}, \tag{4.4}$$

where the Poisson's ratio $\nu \approx 1/2$ for a PDMS stamp.

A fracture mechanics model was developed to calculate the pull-off force. Figure 4.8 shows an edge crack of length *a* at the interface between the post and micro-device. The post is subjected to a pull-off force *F* and shear strain γ. The bending moment that results from the shear stress τ (or shear strain γ) is $M = \tau L h = \mu \gamma L h$. The stress intensity factors are obtained analytically as[27]

$$K_1 = \sqrt{\frac{\pi L}{(1-\lambda)^3}} \left[\frac{F}{L^2} \left(0.379 + 0.624\lambda - 0.062 e^{-12\frac{\lambda}{1-\lambda}} \right) + \frac{M}{L^2} \left(2.005 - 0.72 e^{-9\frac{\lambda}{1-\lambda}} \right) \right]$$

$$K_{II} = \sqrt{\frac{\pi L}{(1-\lambda)^3}} \left\{ \frac{F}{L^2} \left[0.126 - 0.24\lambda - 0.023(1-\lambda)^5 \right] + \frac{M}{L^2} \left[-0.228 + (1-\lambda)^4 \left(0.577 - 0.2\lambda + 0.8\lambda^2 \right) \right] \right\} \tag{4.5}$$

where $\lambda = a/L$. For an infinitesimal crack, $\lambda \to 0$, the above equation is simplified to

$$K_1 = \sqrt{\pi L} \left(0.317 \frac{F}{L^2} + 1.285 \frac{M}{L^2} \right), \quad K_{II} = \sqrt{\pi L} \left(0.103 \frac{F}{L^2} + 0.349 \frac{M}{L^2} \right). \tag{4.6}$$

The crack tip energy release rate is given by $G = \left(K_I^2 + K_{II}^2 \right) / \left(2\bar{E} \right)$, where the plane-strain modulus of the stamp $\bar{E} \approx 4E/3$, *E* is the Young's modulus, and the factor ½ accounts for the large elastic mismatch between the stamp and micro-device.[28] The substitution of Eq. (4.6) into the crack tip energy release rate gives

$$G = \pi E L \left[0.0417 \left(\frac{F}{EL^2} \right)^2 + 0.0701 \left(\frac{\gamma h}{L} \right)^2 + 0.108 \frac{F}{EL^2} \frac{\gamma h}{L} \right]. \tag{4.7}$$

For the fracture toughness Γ_0 of the stamp/micro-device interface, the Griffith fracture criterion $G=\Gamma_0$ gives the normalized pull-off force

$$\frac{F}{EL^2}=\sqrt{24.0\frac{\Gamma_0}{\pi EL}-1.72\cdot 10^{-3}\left(\frac{\gamma h}{L}\right)^2}-1.30\frac{\gamma h}{L}, \tag{4.8}$$

which has an excellent approximation

$$\frac{F}{EL^2}+\frac{13\gamma h}{10L}\approx 2\sqrt{\frac{6\Gamma_0}{\pi EL}}. \tag{4.9}$$

As shown in Figure 4.9, the pull-off force decreases linearly with the shear strain in the post for the stamp elastic modulus E=1.8 MPa,[20] post height h=50 μm and width L=200 μm and 250 μm in experiments. For the fracture toughness of the stamp/micro-device interface $\Gamma_0=0.1\,\mathrm{N/m}$, the pull-off force in Eq. (4.8) or (4.9) agrees well with the pull-off force experiments.

Substitution of the shear strain in Eq. (4.4) into Eq. (4.9) gives the pull-off force directly in terms of the shear displacement u as

$$\frac{F}{EL^2}+\frac{u}{L\left(0.769+0.324\frac{L}{h}\right)}\approx 2.76\sqrt{\frac{\Gamma_0}{EL}}. \tag{4.10}$$

The normalized pull-off force $P=F/\left(EL^2\right)$ decreases linearly with the normalized shear displacement u/L, and such a linear dependence depends only the post aspect ratio L/h and normalized interfacial fracture toughness $\Gamma_0/\left(EL\right)$.

In general, the interface fracture toughness Γ_0 depends on the mode mixity around an interfacial crack tip. The finite element analysis presented next shows that the phase angle, which represents the mode mixity, is small (~20°) and does not change in the range of applied shear strain in experiments. It is therefore not unreasonable to use constant fracture toughness in the present analysis.

Equation (4.9) also gives the critical shear strain for stamp/micro-device delamination without any pull-off force, $\gamma \approx 2.13\sqrt{\Gamma_0 L/\left(Eh^2\right)}$, which agree well with the experimental data for the vanishing pull-off force. For the other limit of vanishing shear, Eq. (4.9) gives the pull-off force $F \approx 2.76\sqrt{\Gamma_0 EL^3}$.

A 3-D finite element (FE) model of the post-ink system that includes the full stamp geometry was also developed to help understand the adhesion data. Using the FE model with the applied shear displacements and measured pull-off forces as inputs, the average normal and shear stresses on the posts at failure were calculated (Figure 4.10b). Similar to Figure 4.3b, the data from multiple posts of different widths collapse to nearly a single line. This result clearly shows that the average normal stress at failure decreases with increasing shear and also demonstrates the validity of the analytical shear strain expression. In fact, for h=50 μm and L=100, 150, 200 and 250 μm, the average shear strains obtained by the finite element method differ by only 2.2%, 5.6%, 8.6% and 3.9% from the analytical results of Eq. (4.4). The FE simulations also provide insight into the local stress distribution near the interface. Under pure normal loading the normal stress distribution in the post just above the stamp-ink interface is symmetric with stress concentrations at the edges (black line, Figure 4.10a). As shear displacement is applied, the stress distribution becomes asymmetric and produces a larger normal stress at the trailing edge (dotted lines, Figure 4.10a). This change arises because the shear force is applied some distance above the interface and thus generates a moment on the interface. This moment and the asymmetric stress distribution that it induces is the key reason that the pull-off force is reduced with applied shear. Similar moments generated by shear displacement have previously been used to explain the stick-slip motion of an elastic block.[29, 30]

While the stress distribution provides a qualitative picture of changes in interfacial loading with applied shear, the magnitude of the stresses at the interface cannot be meaningfully used to predict delamination because of the presence of an edge singularity. As such, a fracture mechanics approach, in which a small edge crack is assumed, is used to allow quantitative analysis. An initial crack, 200 nm in length, is incorporated in the FE model at the edge of post–ink interface and the mode I and mode II strain energy release rates (G_I and G_{II}) are calculated using the FE model and virtual crack closure technique (VCCT).[31] While the assumed initial crack length here is arbitrary as it cannot be measured directly in the experiments, the calculations are still expected be able to capture the overall trend of data. The total strain energy release rate, $G = G_I + G_{II}$, for a post of width L = 150 μm is plotted as a function of applied normal and shear strain in Figure 4.10c. Assuming a Griffith fracture criterion, the crack will propagate when $G>\Gamma_0$, where Γ_0 is the interface toughness; a representative PDMS-Si toughness of 50 mJ/m^2 is shown in Figure 4.10c. The results in Figure 4.10c illustrate that the failure criterion is reached at lower normal forces with increasing applied shear strain. Figure 4.10d shows the combination of normal stress and shear stress to satisfy the fracture criterion with Γ_0=50 mJ/m^2 for the 150 μm post in Figure 4.10c as well posts with L = 100, 200, and 250 μm. The FE predictions in Figure 4.10d exhibit a similar trend to the experimental results in Figure 4.3b. While the overall behavior is similar, the slope of the critical normal-shear stress boundary predicted by the model is steeper than that observed in the experiments. This difference is likely due to the assumptions (e.g., initial crack length, interface toughness, perfect alignment, lateral stiffness of the measurement setup) and simplifications (simple fracture criterion, linear elasticity of PDMS) made in the model. Nevertheless, these modeling results effectively demonstrate the

mechanism by which applied shear displacement reduces the normal pull-off force in shear assisted transfer printing.

4.3.3. Angled posts for directionally-dependent adhesion switching

Figure 4.11a provides scanning electron microscope (SEM) images of a stamp made of poly(dimethylsiloxane) (PDMS) with a uniformly arranged collection of angled posts, molded on its surface. Critical design aspects include well-defined structures (Figure 4.11b) with sharp perimeter edges to facilitate controlled crack initiation and propagation for efficient printing, as described subsequently. To achieve this structure, a combination of anti-reflection (thickness ~ 160 nm) and adhesion promoting (thickness ~ 13 nm) layers were applied to a silicon substrate, followed by photopatterning of a thick layer of epoxy through a photomask in an angled exposure geometry (Figure 4.12). Casting and curing a prepolymer of PDMS onto this substrate, and then peeling the resulting material away yielded the desired stamps. For cases reported here, the tilt angle was 17^{o}.

Figure 4.13a illustrates the principle behind the dependence of adhesion strength on the direction of retraction. An angled post in contact with a substrate has natively asymmetric contact angles (θ_a and θ_b , inset, Figure 4.13a), in contrast to the symmetric, 90^{o} angles of vertical post designs explored previously (inset of Figure 4.13b). The two contact angles satisfy $\theta_a + \theta_b = 180^{o}$, due to the parallel configuration of the two sides of the post. Since θ_a is smaller than θ_b, a crack at the post/substrate interface propagates preferentially from the corner at θ_a, corresponding to a characteristic pull-off force (F_2) when a vertical force is applied to the stamp. Pulling the post with a component of applied force that lies in a direction opposite to that of the

orientation of the angle accelerates crack propagation from the corner θ_a, resulting in a reduced pull-off force ($F_3 < F_2$). By contrast, crack propagation is frustrated when the pulling direction involves force aligned along the other orientation, leading to increased pull-off force ($F_1 > F_2$). Thus, three different regimes of pull-off force ($F_1 > F_2 > F_3$) can be achieved, simply by controlling the direction of the applied separation loads. In transfer printing, these conditions correspond to different magnitudes of force applied to material structures, and can be exploited in this process by choosing the retraction direction during retrieval and delivery to lie along and against the angled axis, respectively.

To quantify this adhesion physics, we evaluated the normal direction pull-off forces under various loading conditions. An adhesion test setup described elsewhere,[20, 32] was used to bring a single angled post into intimate contact with the clean surface of a silicon wafer, and then to subject it to increasing displacements, u, in the $\pm x$ directions (corresponding to a well-defined shear strain), with a final retraction in the z direction, away from the substrate surface. Pull-off forces, F, for each displacement were determined by recording force-distance curves with a precision load cell.[20] This combination of lateral displacements and vertical pulling simulates directional retraction along or against the orientation of angle of the angled post. Pull-off forces for a vertical post stamp under the same displacement procedures were also measured for comparison. Figure 4.14 provides schematic illustrations for each test.

Figure 4.13a, b show the normalized pull-off force, $P = F/\left(EL^2\right)$ where E and L are the Young's modulus and width of the PDMS posts, respectively, as function of shear strain γ for the angled and the vertical post cases, respectively. For a vertical post, the peak value of P (P_{max}) appeared at $\gamma = 0$, with a symmetric distribution around this condition (Figure 4.13b). By

contrast, for an angled post, the shear strain corresponding to P_{max} for this case was shifted to a positive value of γ (3.6 and 4.8 % from experimental data and theoretical result, respectively), with an overall asymmetric distribution (Figure 4.13a). These results indicate that the adhesion behavior in an angled stamp is dependent on the displacement direction, with large values of P obtained by applying optimum γ along directions that inhibit crack propagation (+x direction in Figure 4.13a). Comparatively small values of P occur for shear strains along the direction that accelerates crack propagation (-x direction in Figure 4.13a), or large values in either direction. These effects were confirmed by detailed mechanical modeling of interfacial delamination and subsequent finite element analysis which are beyond the scope of this thesis, but can be found in the manuscripts.[33]

As shown in Figure 4.13c, d, F measured using the angled post also exhibit rate-dependent behaviors consistent with viscoelastic materials.[14, 15] For zero and optimum positive shear strain conditions, F exhibited a monotonic increase with retraction speed. The values of F at $\gamma = 0$ were smaller than those at the optimum γ (+3.6 %) irrespective of the retraction speed, as predicted above ($F_1 > F_2 > F_3$).

Although the performance of the angled post is similar to that of the corresponding vertical case in terms of adhesion switchability under strain (a factor of ~100), the angular dependence of the angled post offers some interesting possibilities. One example is in the realization of roller modes of operation for transfer printing. To demonstrate feasibility, a cylindrical angled post stamp (Figure 4.15a) was fabricated by wrapping a thin sheet of PDMS with angled posts around an aluminum cylinder. The adhesion switchability of such a stamp can be demonstrated, and quantified, by rolling it down an inclined glass plate and comparing the behaviors for the two possible rolling directions. For the case of forward rolling, the angled

posts formed a relatively small contact angle to the plate (upper inset, Figure 4.15b). The opposite (backward) rolling direction involved larger contact angles (lower inset, Figure 4.15b). In both cases, the stamp reached constant rolling speed (terminal velocity), due to viscoelastic effects. The energy release rate can be calculated from the rate of loss in gravitational potential energy for rolling in this regime.[15] As shown in Figure 4.15b, the energy release rate for the backward direction is substantially lower than that for the forward, for all rolling speeds, consistent with expectation. Finite element modeling (FEM) can be used to calculate the energy release rate G for these two cases. The length of edge crack along the PDMS/glass interface ranges from zero (for an infinitesimal crack) to the post width (for complete delamination of the interface), and G is then averaged over all crack lengths to represent the average energy release rate during steady-state rolling. Under the same gravitational force, G for forward rolling is larger than that for backward rolling. For a PDMS/glass interface, the interfacial fracture toughness, or critical energy release rate G_c, increases monotonically with the terminal velocity v due to viscoelasticity of PDMS, and can be expressed via a power-law[14, 34, 35]

$$G_c = G_0\left[1+\left(\frac{v}{v_0}\right)^n\right]. \tag{4.11}$$

Feng et al.[14] reported the exponent $n = 0.65$ and reference speed $v_0 = 1.55\ \mathrm{cm\cdot s^{-1}}$ in experiments with flat slabs of PDMS; G_0 is the critical energy release rate for a vanishing crack tip speed, and $G_0 = 0.195\ \mathrm{J\cdot m^{-2}}$ is used in the present study. The terminal velocity is determined by equating the energy release rate G obtained by FEM to the critical energy release rate G_c in Equation (4.1); a larger G for forward rolling then yields a larger terminal velocity v than that for backward rolling. Figure 4.15b shows the predicted G-v curves for forward and

backward rolling, which agree well with the experiments. It should be pointed out that $G_0 = 0.195\ \mathrm{J \cdot m^{-2}}$ used in the present study of discrete PDMS posts is smaller than that reported by Feng et al.[14] for a continuous PDMS film. This result is reasonable because the PDMS/glass energy release rate reported in the present experiments is averaged over the entire area, including the gaps between PDMS posts.

4.4. Conclusions

In summary, the work presented here introduces an advanced mode of transfer printing in which controlled shear loading of vertical or angled rectangular posts on a stamp surface allows programmed modulation of interfacial adhesion. Analytical and finite element mechanics models provide an understanding of experimental measurements and demonstrate that the decrease in pull-off force occurs as a result of the moment generated at the interface by the applied shear displacement. Examples of printed structures in suspended and stacked arrangements demonstrate the capabilities and advantages of this type of shear-assisted printing. Additionally, for angled surface relief, a roller-style printing tool was developed that naturally exploited the directional-dependence of adhesion switching. The versatility of these techniques and its compatibility with semiconductor and other classes of micro/nanoscale inks could provide means to assemble device structures in electronics, optoelectronics and other areas of interest.

4.5. Experimental

Fabrication of elastomeric vertical stamps: PDMS (Sylgard 184, 5:1 monomer:crosslinking agent) pre-polymer was poured into a petri dish, degassed at 50 mTorr in an evacuated chamber for 1 hour and then poured onto a template consisting of rectangular recesses in a photodefined epoxy (50 μm thick, SU8-50, MicroChem). The template was positioned between two flat polycarbonate plates separated by precision 1 mm spacers; small holes along the plate perimeter allowed access for the liquid PDMS to infill the patterned feature geometry. The entire setup was cured in an oven at 70˚C for 2 hours. After curing and demolding from the template, a scalpel was used to cut out the PDMS into the desired stamp shape and size. Prior to testing the stamps were cleaned with commercial pressure sensitive adhesives (e.g, Scotch™ tape).

Fabrication of elastomeric angled stamps: The fabrication involved soft lithographic procedures of casting and curing a prepolymer to PDMS (Sylgard 184, Dow Corning, 5:1 monomer:crosslinking agent) against a photodefined collection of angled, square recesses (lateral dimensions of 100 μm x 100 μm; thickness ~ 100 μm) in a layer of epoxy (SU-8 50, MicroChem). The patterning relied on ultraviolet (UV) exposure of a film of SU-8 on a silicon wafer coated with an antireflection layer (XHRiC-16, Brewer Science) and an adhesion promoter (OmniCoat, MicroChem), mounted on a stage tilted to an angle of 34^{o}. Developing away the exposed regions of the SU-8, functionalizing the native oxide surface of the silicon with a fluorinated silane (tridecafluoro-1,1,2,2-tetrahydrooctyl-1-trichlorosilane, FOTCS, Gelest), casting the PDMS on top, thermally curing (70^{o}C for 1 hour in convection oven), and peeling away the PDMS yielded an elastomeric angled stamp.

Transfer printing: Transfer printing followed the steps shown in **Figure 4.16**. In particular, an angled stamp mounted on a holder provided precise translational, rotational and vertical

positional control relative to donor/receiver substrates. Automated stages controlled shear motion and retraction speeds.

Rolling tests: The roller consisted of an aluminum cylinder (9.5 mm of diameter, 9.5 mm of height and 1.915 g of mass) wrapped with a thin, flexible stamp that had an array of angled relief features (total 1820 angled reliefs in an array, area of an array of 8.2 mm x 19.3 mm, lateral dimensions of each relief of 100 μm x 100 μm with height of 100 μm, center to center distance between relief structures of 300 μm, angle of 17^{o} relative to the normal to the backing layer surface). Placing such an object on an inclined glass plate led to rolling motion, driven by gravity. A ruler placed near the rolling path and a video camera allowed measurement of both the rolling distance and time. The terminal velocity corresponds to the constant speed reached by the roller, as determined from the video footage.

4.6. References

[1] S. Chen, J. Gao, *J. Mech. Phys. Solids* **2007**, *55*, 1001.
[2] M.P. Murphy, B. Aksak, M. Sitti, *Small* **2009**, *5*, 170.
[3] M.P. Murphy, B. Aksak, M. Sitti, *J. Adhesion Sci. Technol.* **2007**, *21*, 1281.
[4] S. Gorb, M. Varenberg, A. Peressadko, J. Tuma, *J. R. Soc. Interface* **2007**, *4*, 271.
[5] M. Varenberg, S. Gorb, *J. R. Soc. Interfaces* **2007**, *4*, 721.
[6] B. Aksak, M.P. Murphy, M. Sitti. *Gecko inspired micro-fibrillar adhsives for wall climbing robots on micro/nanoscale rough surfaces*. in *2008 IEEE International Conference on Robotics and Automation*. 2008. Pasadena, CA.
[7] B. Aksak, M.P. Murphy, M. Sitti, *Langmuir* **2007**, *23*, 3322.
[8] H. Yao, H. Gao, *J. Mech. Phys. Solids* **2006**, *54*, 1120.
[9] H. Yao, G.D. Rocca, P.R. Guduru, H. Gao, *J. R. Soc. Interface* **2008**, *5*, 723.
[10] R.K. Kramer, C. Majidi, R.J. Wood, *Adv. Mater.* **2010**, *22*, 3700.
[11] J.-H. Ahn, H.-S. Kim, K.J. Lee, S. Jeon, S.J. Kang, Y. Sun, R.G. Nuzzo, J.A. Rogers, *Science* **2006**, *314*, 1754.
[12] K.J. Lee, H. Ahn, M.J. Motala, R.G. Nuzzo, E. Menard, J.A. Rogers, *J. Micromech. Microeng.* **2010**, *20*, 075018.
[13] A.J. Baca, M.A. Meitl, H.C. Ko, S. Mack, H.-S. Kim, J. Dong, P.M. Ferreira, J.A. Rogers, *Adv. Func. Mater.* **2007**, *17*, 3051.

[14] X. Feng, M.A. Meitl, A.M. Bowen, Y. Huang, R.G. Nuzzo, J.A. Rogers, *Langmuir* **2007**, *23*, 12555.
[15] M.A. Meitl, Z.-T. Zhu, V. Kumar, K.J. Lee, X. Feng, Y.Y. Huang, I. Adesida, R.G. Nuzzo, J.A. Rogers, *Nat. Mater.* **2006**, *5*, 33.
[16] J. Dundurs, *J. Appl. Mech.* **1969**, *36*, 650.
[17] J. Hutchinson, Z. Suo, *Advances in Applied Mechanics* **1992**, *29*, 63.
[18] H.K. Mueller, W.G. Knauss, *J. Appl. Mech.* **1971**, *38*, 483.
[19] F. Saulnier, T. Ondarcuhu, A. Aradia, E. Raphael, *Macromolecules* **2004**, *37*, 1067.
[20] S. Kim, J. Wu, A. Carlson, S.H. Jin, A. Kovalsky, P. Glass, Z. Liu, N. Ahmed, S.L. Elgan, W. Chen, P.M. Ferreira, M. Sitti, Y. Huang, J.A. Rogers, *P. Natl. Acad. Sci. U.S.A.* **2010**, *107*, 17095.
[21] T.-H. Kim, A. Carlson, J.-H. Ahn, S.M. Won, S. Wang, Y. Huang, J.A. Rogers, *Appl. Phys. Lett.* **2009**, *94*, 113502.
[22] Y. Yang, Y. Hwang, H.A. Cho, J.-H. Song, S.-J. Park, J.A. Rogers, H.C. Ko, *Small* **2010**.
[23] M.A. Meitl, X. Feng, J. Dong, E. Menard, P.M. Ferreira, Y. Huang, J.A. Rogers, *Appl. Phys. Lett.* **2007**, *90*, 083110.
[24] H. Kim, E. Brueckner, J. Song, Y. Li, S. Kim, C. Lu, J. sulking, K. Choquette, Y. Huang, R.G. Nuzzo, J.A. Rogers, *Proc. Natl. Acad. Sci. U.S.A.* **2011**, *108*(25), 10072.
[25] L.D. Landau, E.M. Lifshitz, *Theory of Elasticity*. 3rd ed. 1986, Oxford: Butterworth Heinermann.
[26] L.D. Landau, E.M. Lifshitz, *Theory of Elasticity* 3rd edition ed. 1986, Oxford, England: Butterworth Heinemann.
[27] H.T.P.C.P.G.R. Irwin, *The stress analysis of cracks handbook* 3rd edition ed. 2000, New York.
[28] Y.Y. Huang, W. Zhou, K.J. Hsia, E. Menard, J.-U. Park, J.A. Rogers, A.G. Alleyne, *Langmuir* **2005**, *21*, 8058.
[29] J. Scheibert, D.K. Dysthe, *Europhys. Lett.* **2010**, *29*, 54001.
[30] C. Rand, A.J. Crosby, *Appl. Phys. Lett.* **2006**, *89*, 261907.
[31] R. Krueger, *Appl. Mech. Rev.* **2004**, *57*, 109.
[32] A. Carlson, H.-J. Kim-Lee, J. Wu, P. Elvikis, H. Cheng, A. Kovalsky, S. Elgan, Q. Yu, P.M. Ferreira, Y. Huang, K.T. Turner, J.A. Rogers, *Appl. Phys. Lett.* **2011**, *98*, 264104.
[33] S.Y. Yang, A. Carlson, H. Cheng, Q. Yu, N. Ahmed, J. Wu, S. Kim, M. Sitti, P.M. Ferreira, Y. Huang, J.A. Rogers, *submitted*.
[34] A.N. Gent, *J. Polym. Sci. B: Polym. Phys.* **1994**, *32*, 1543.
[35] A.N. Gent, *Langmuir* **1996**, *12*, 4492.

4.7. Figures

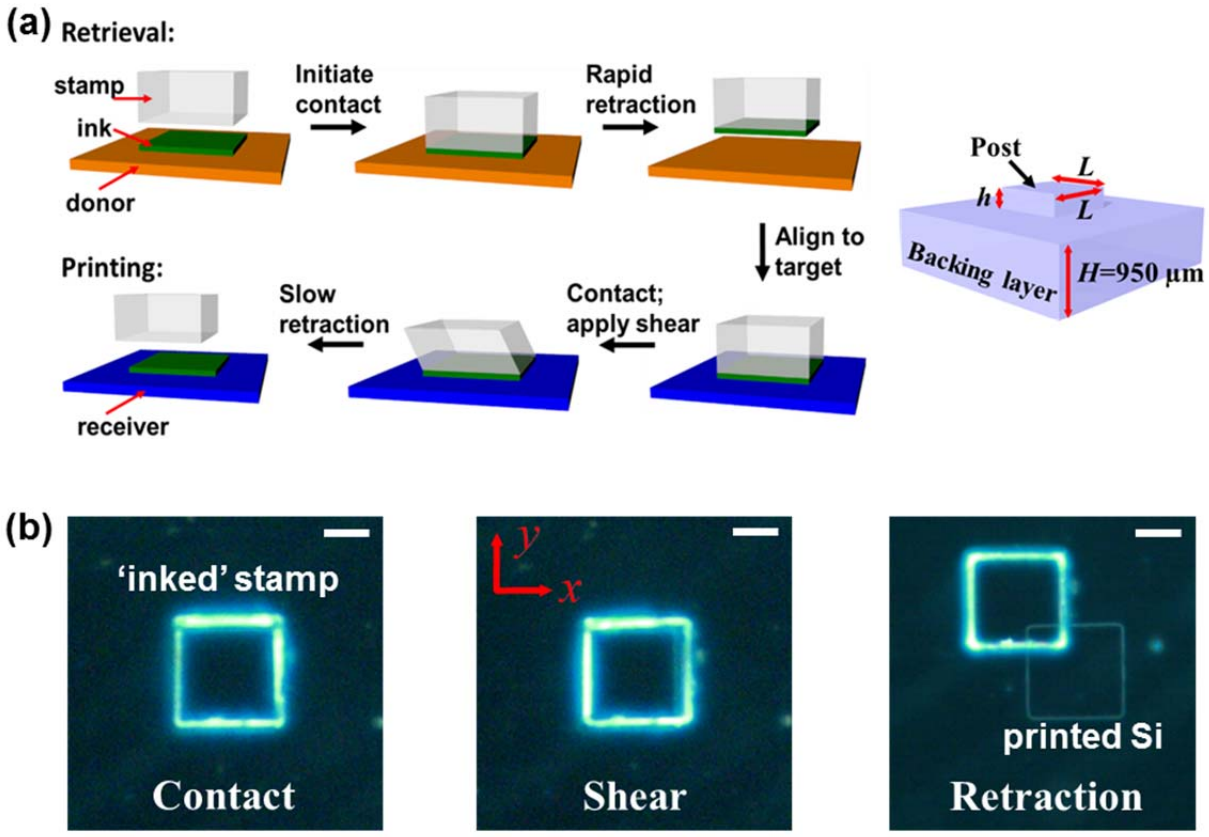

Figure 4.1. (a) Steps for transfer printing with an elastomeric stamp, where applied shear stresses are used to control the strength of adhesion. Inset shows a schematic illustration and critical dimensions of the post structure on the stamp and its backing layer. (b) Optical micrographs collected by imaging through the transparent stamp, during the printing steps. A stamp 'inked' with a silicon plate (100 × 100 × 3 μm) is brought into contact with a silicon substrate, sheared by 12.5 μm ($\gamma = 0.14$) in the -*x*-direction, and then slowly retracted, to transfer the plate from stamp to substrate. Scale bars correspond to 50 μm.

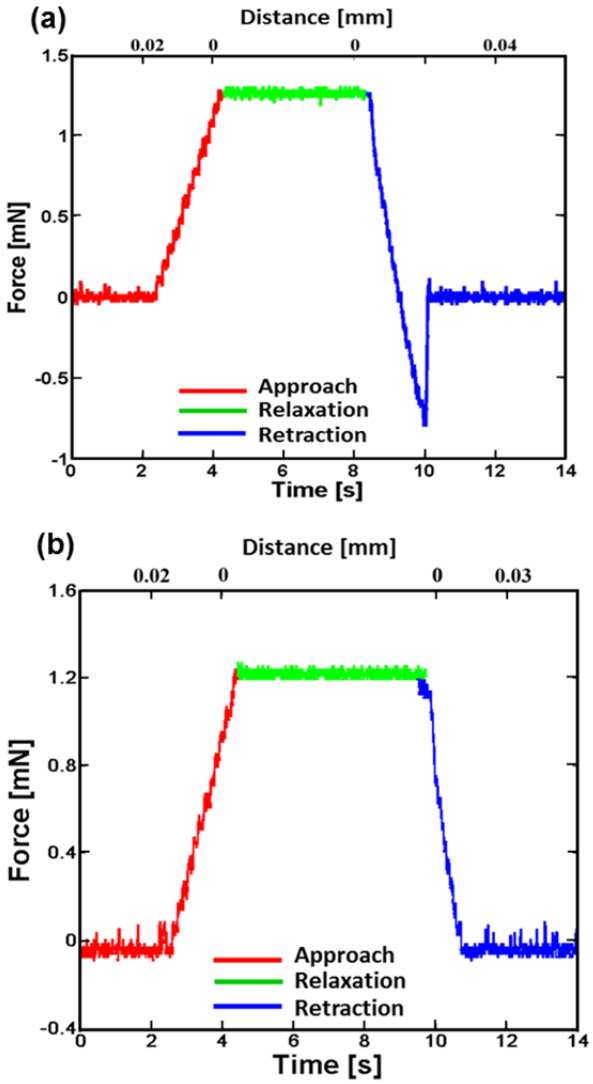

Figure 4.2. Representative force-time (bottom axis) and force-distance (top axis) curves for contact between an elastomeric microstructured stamp and a flat silicon surface. (a) Contact between a rectangular PDMS post (100 × 100 × 50 μm) and silicon wafer without any applied shear. The sharp negative feature highlighted in blue corresponds to the force necessary to separate the stamp from the silicon at a velocity of 10 μm/s. (b) Separation of the same stamp as in (a) with post shear strains of ~14%, leading to disappearance of the sharp negative feature.

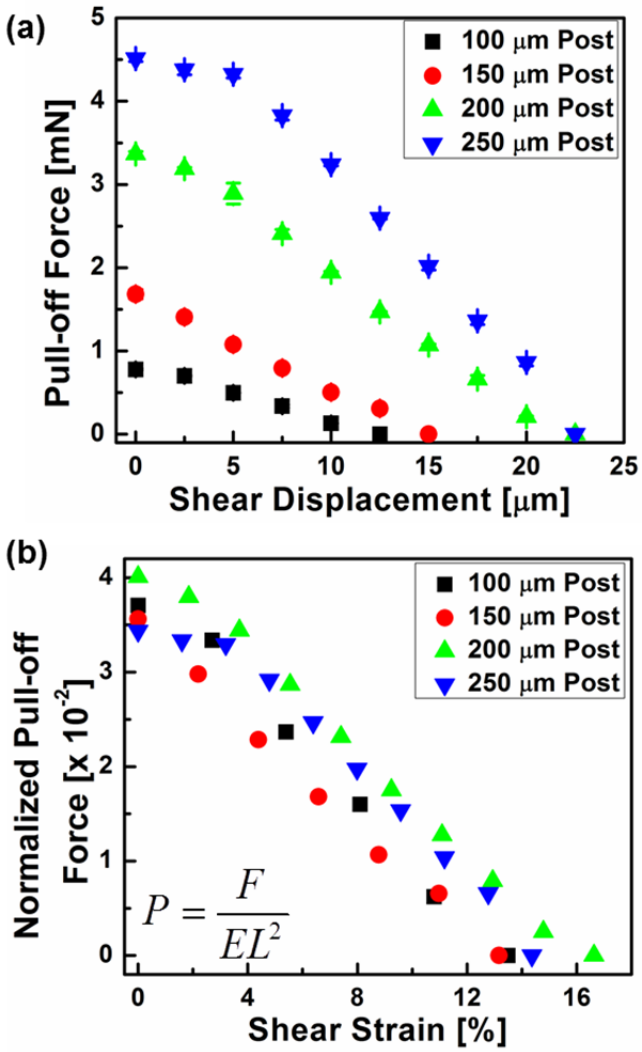

Figure 4.3. (a) Measured pull-off forces required to delaminate stamps from a flat silicon substrate, as a function of shear displacement (i.e. transverse motion of the silicon substrate). The posts on the stamps have fixed heights of 50 μm and lateral dimensions up to 250 μm; retraction and shear velocities were fixed at 10 μm/s. (b) Normalized pull-off forces, P, from (a) as a function of shear strain in the post. The data from posts with different sizes collapse, approximately, onto a single line.

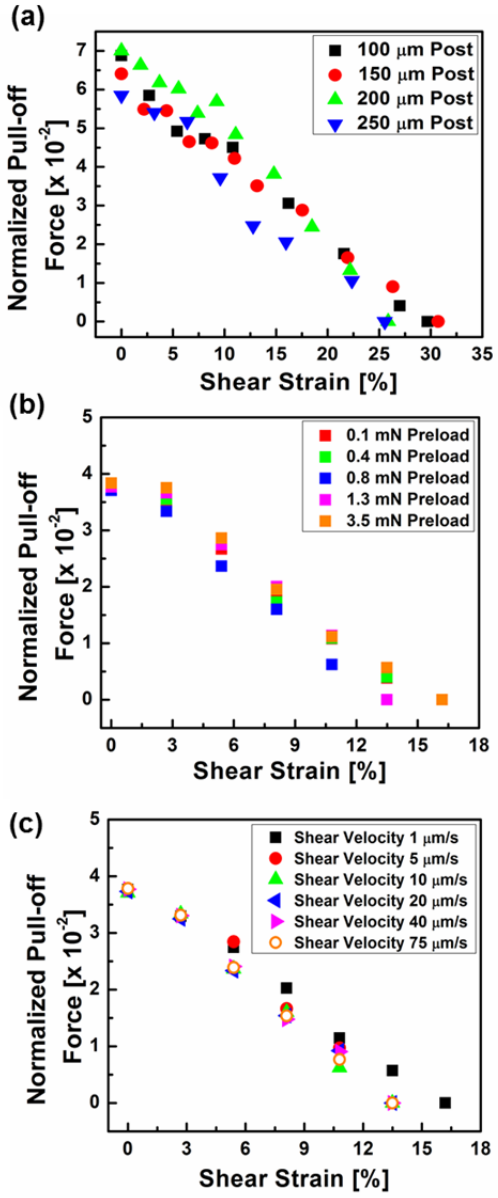

Figure 4.4. (a) Measured pull-off forces, normalized by $P = F/EL^2$, for rectangular stamps delaminating from a flat silicon surface with increasing amounts of applied shear. Stamp posts have fixed heights of 50 μm, varying lateral dimensions ranging up to 250 μm, and a retraction velocity of 500 μm/s. The normalized pull-off forces collapse to approximately a single line. Comparison of normalized pull-off forces with applied shear strains for a rectangular post (100 × 100 × 50 μm) under different preloading conditions, (b), and shearing rates, (c). Retraction velocity was fixed at 10 μm/s.

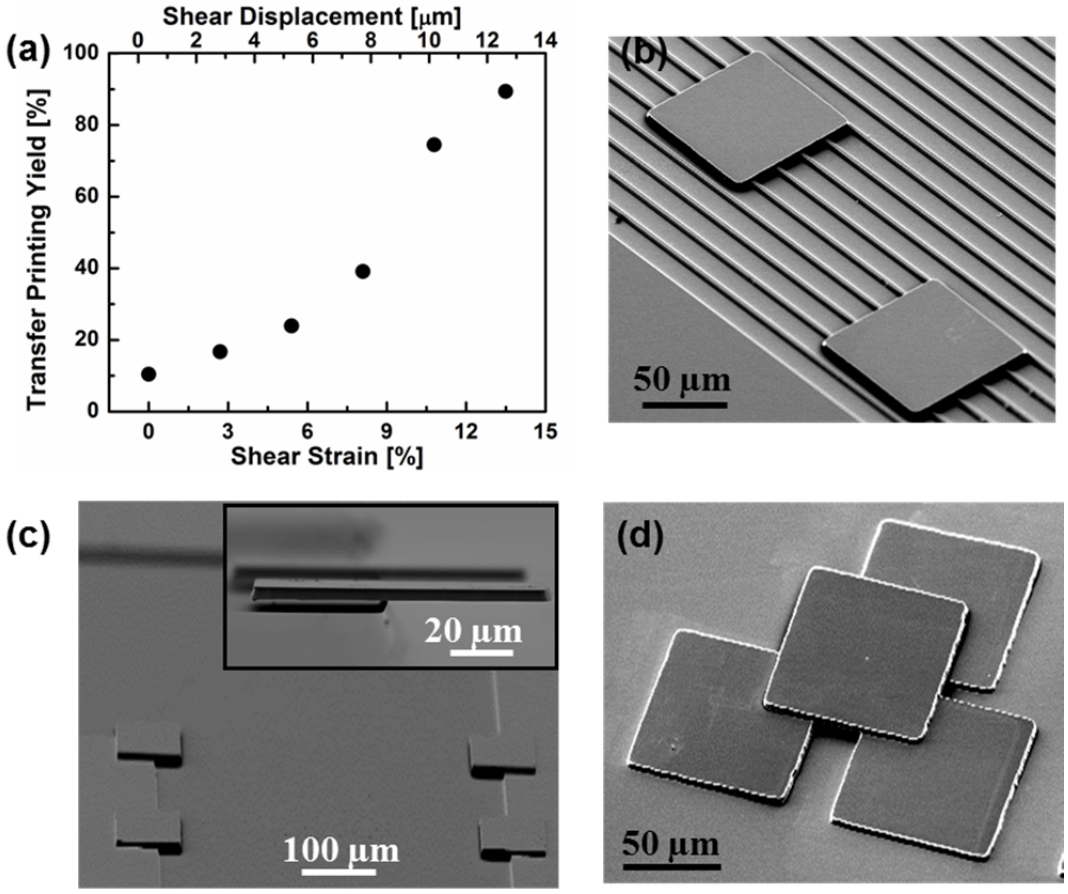

Figure 4.5. Demonstrations of printing silicon plates (100 × 100 × 3 μm) using shear to control the adhesion. Yields for transfer printing onto a bare silicon substrate (a) and onto a structured (line and space geometry; 3 μm lines, 17 μm spacing) PDMS substrate, (b). (c) Collection of partially suspended plates printed onto a ledge micromachined on the surface of a silicon wafer. The inset shows a magnified view of the overhanging structures. (d) Overlapping, stacked configuration of plates printed onto flat silicon wafer surface.

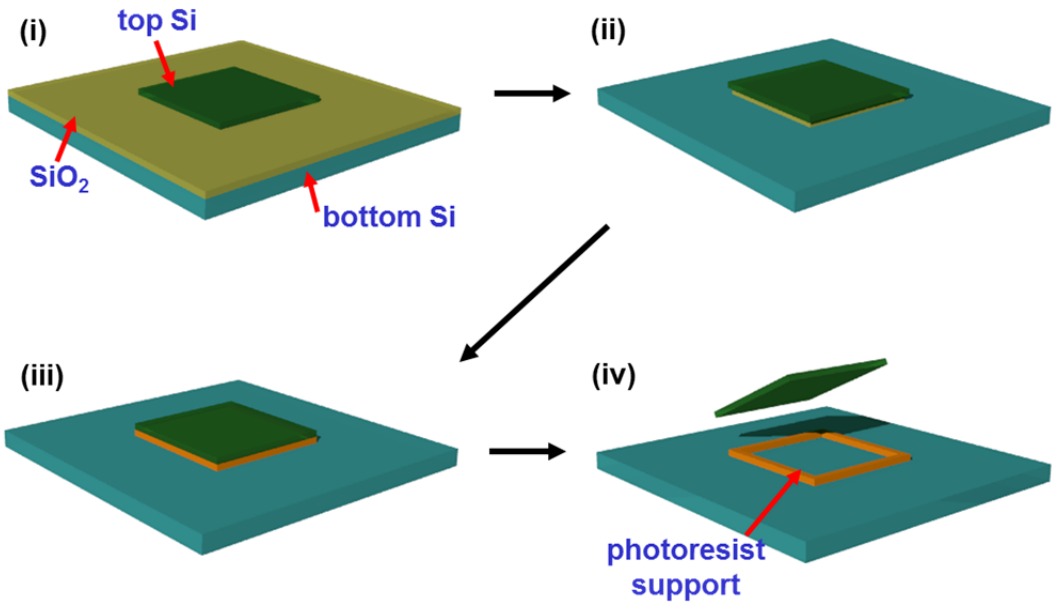

Figure 4.6. Overview of process flow used to fabricate silicon plate ink materials. (i) Top layer of silicon is patterned and etched on a silicon-on-insulator (SOI) source wafer. (ii) The exposed buried oxide layer (BOx) is etched in concentrated HF, resulting in a small undercut trench around the top silicon plate perimeter. (iii) The sample is coated with photoresist and flood exposed to UV radiation. After development, a narrow photoresist rim remains along undercut trench. (iv) The remainder of the BOx is removed and the top silicon is suspended on the photoresist ready for retrieval.

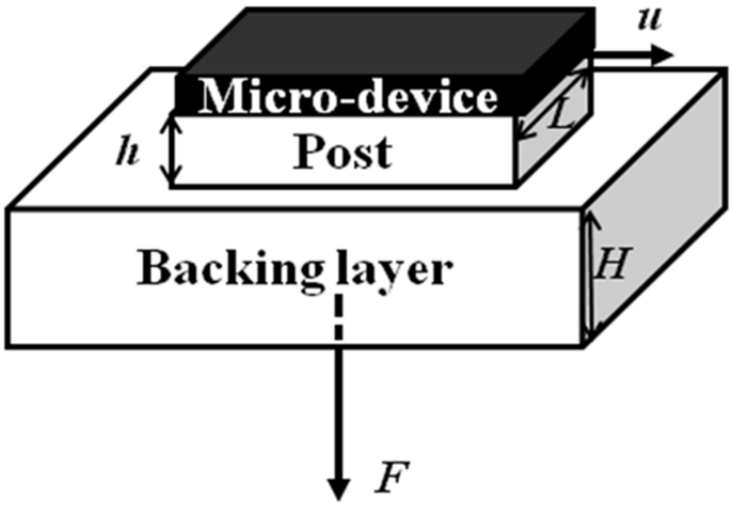

Figure 4.7. The critical dimensions of the post and backing layer and loading conditions in a custom adhesion test set up.

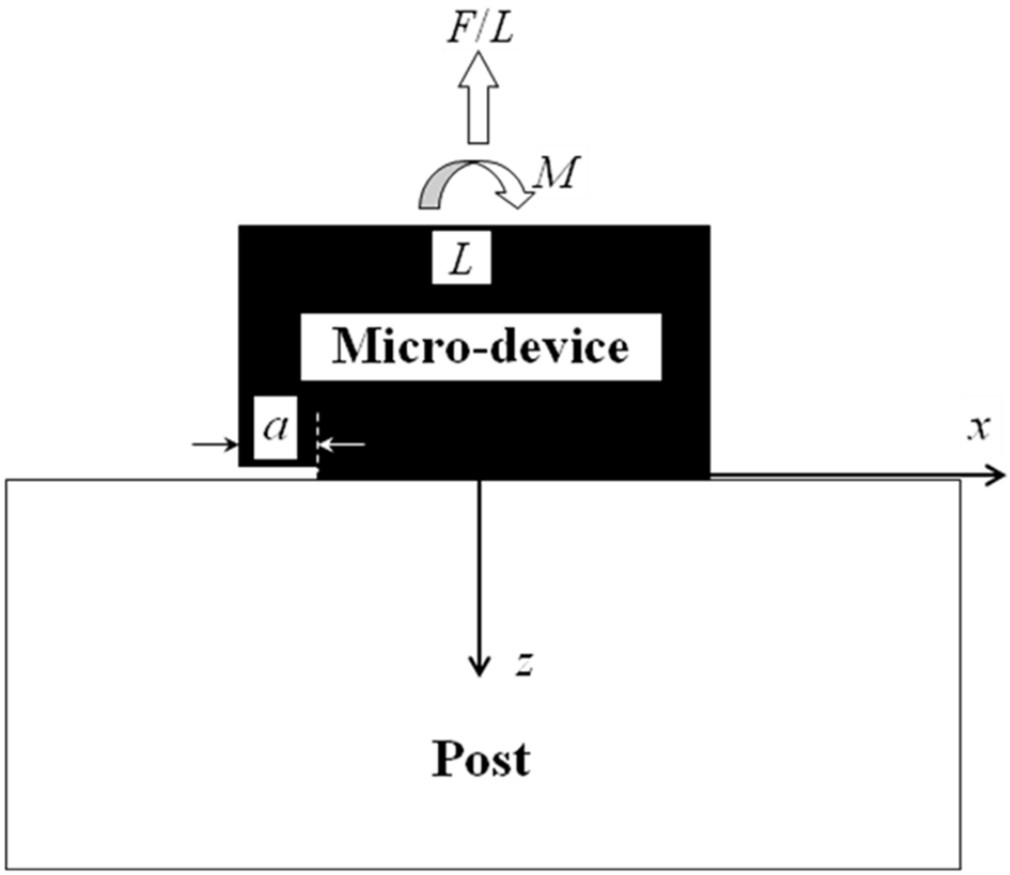

Figure 4.8. Schematic illustration of the fracture mechanics model used to study the relationship between vertical pull-off and applied shear in shear-enhanced transfer printing.

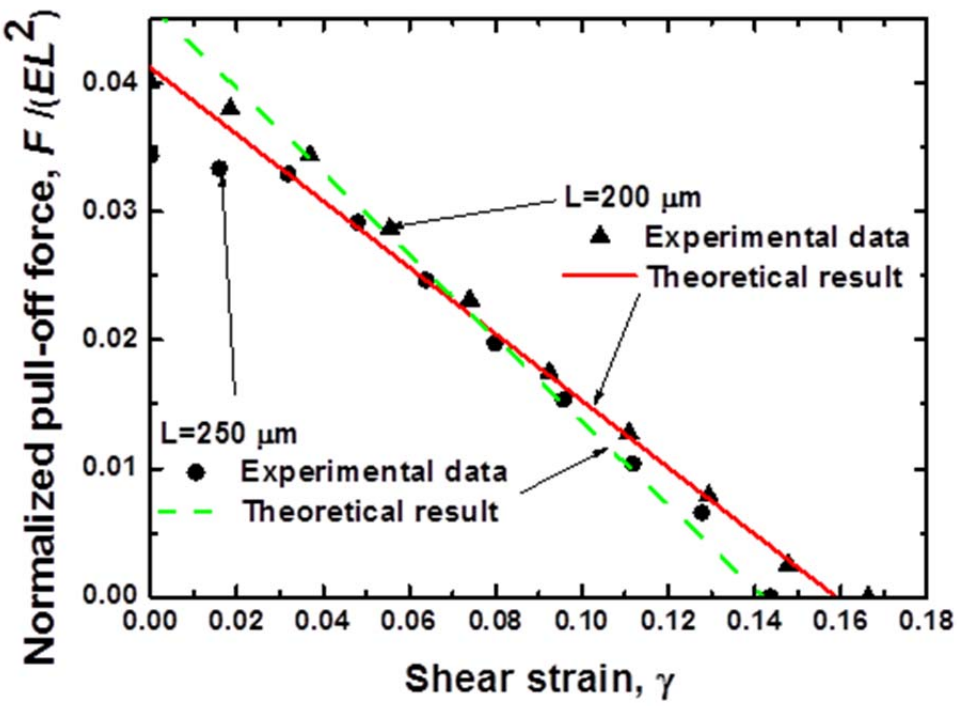

Figure 4.9. The normalized pull-off force P as a function of the shear strain γ for post height h=50 μm and post width L=200 μm and L=250 μm. Symbols and lines represent experimental and theoretical results, respectively.

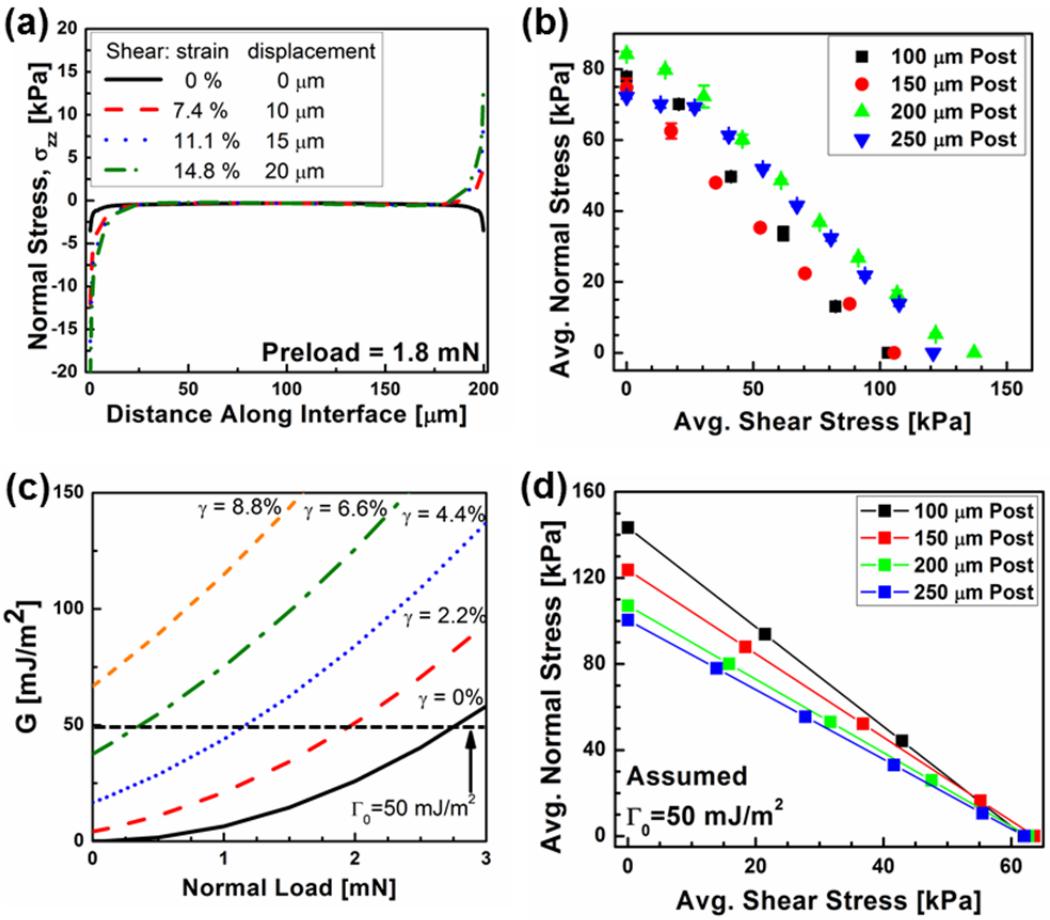

Figure 4.10. (a) Calculated normal stress distributions in a 200 μm wide post 1 μm above the stamp-ink interface for shear strains between 0% - 14.8%. (b) Average normal stress as a function of average shear stress at the interface for the pull-off forces in Figure 4.3. The stresses were determined from measured loads and applied shear displacements using a finite element model. The data collapse onto approximately a single line, similar to the normalized data presented in Figure 4.3b. (c) Strain energy release rate, G, calculated using finite element analysis, for a stamp with a post width L = 150 μm at different applied shear strains and normal forces. The pull-off force at failure can be determined from the intersection of the curves with the toughness of the interface (black dashed line shows a representative toughness of Γ_0=50 mJ/m^2). (d) Average normal stress vs. average shear stress at failure of the stamp-Si interface predicted from fracture-based finite element calculations assuming Γ_0=50 mJ/m^2. Modeling results exhibit similar behavior to the experimental results in (b).

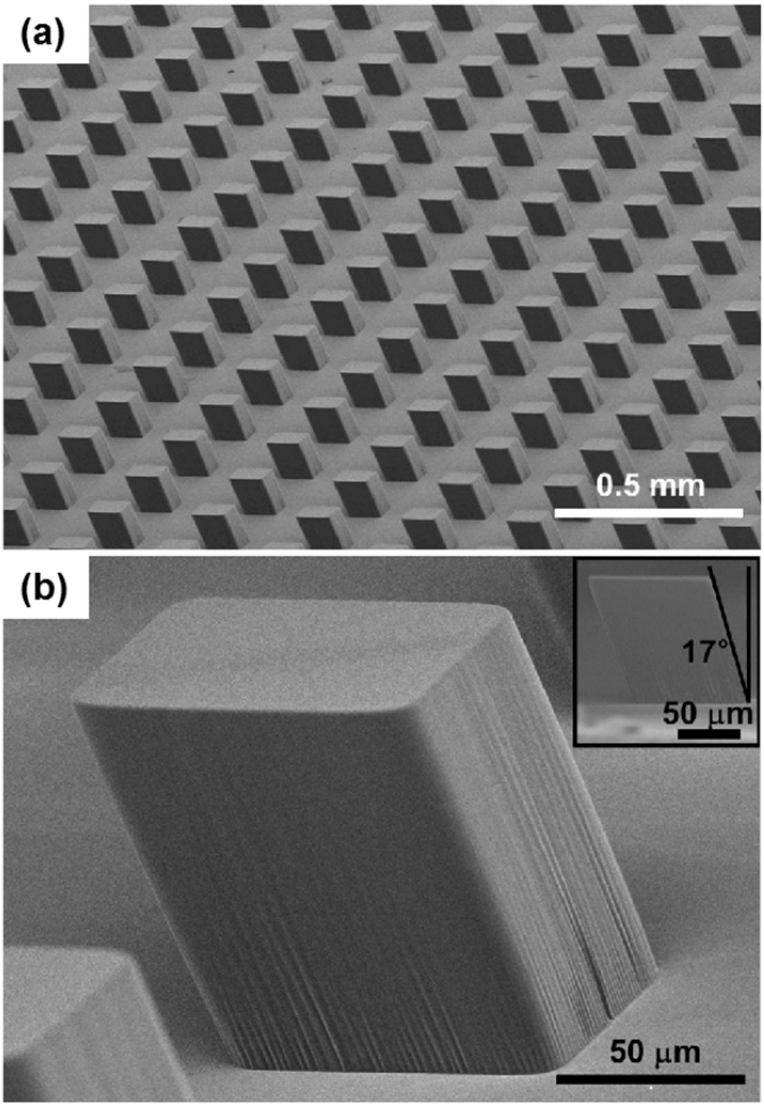

Figure 4.11. (a) SEM image of an elastomeric stamp with an array of angled posts on its surface. The lateral dimensions of an individual post are 100 μm × 100 μm with a vertical heights of 100 μm. The rectangular stamp (8.2 mm x 19.3 mm) includes 1820 angled posts. (b) SEM image of a single, angled post. The angle of inclination is ~17^{o} relative to surface normal.

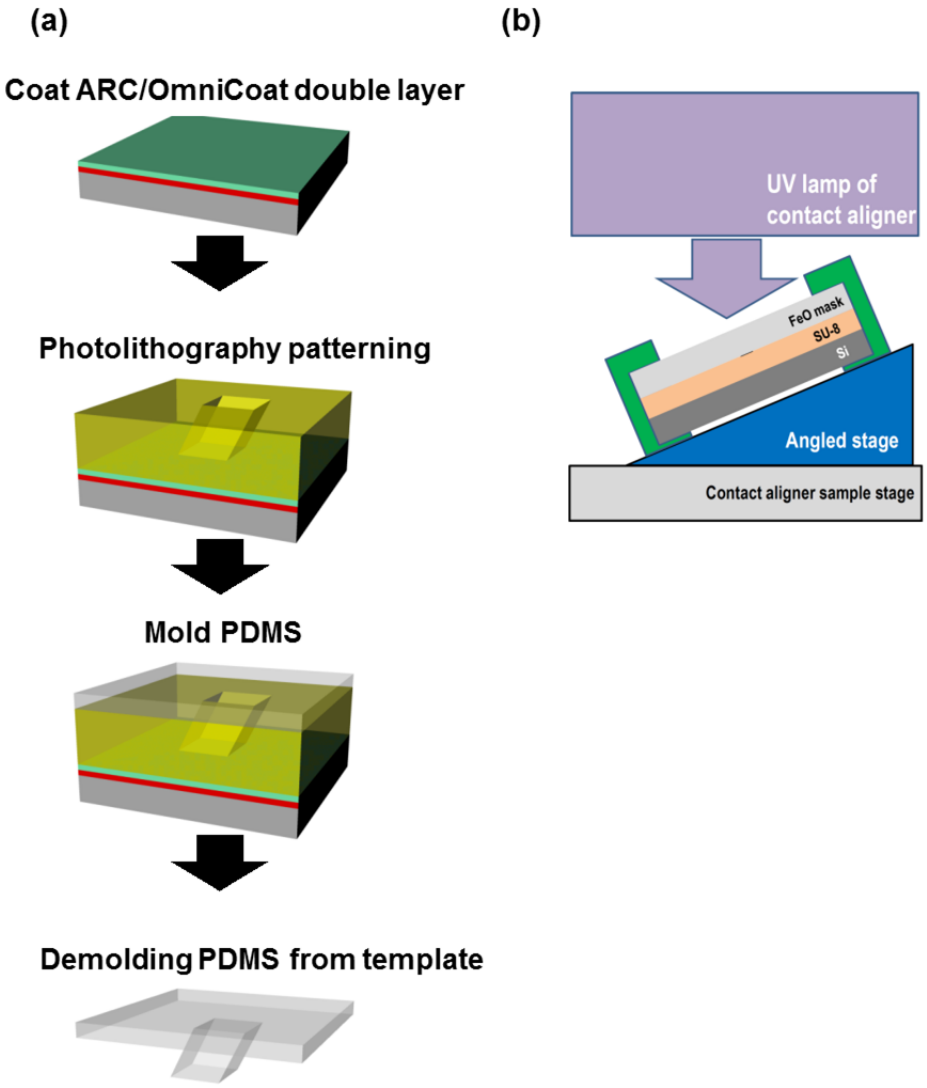

Figure 4.12. (a) Schematic illustration of PDMS fabrication process. (b) UV exposure process on the tilted stage mounted on a contact aligner system.

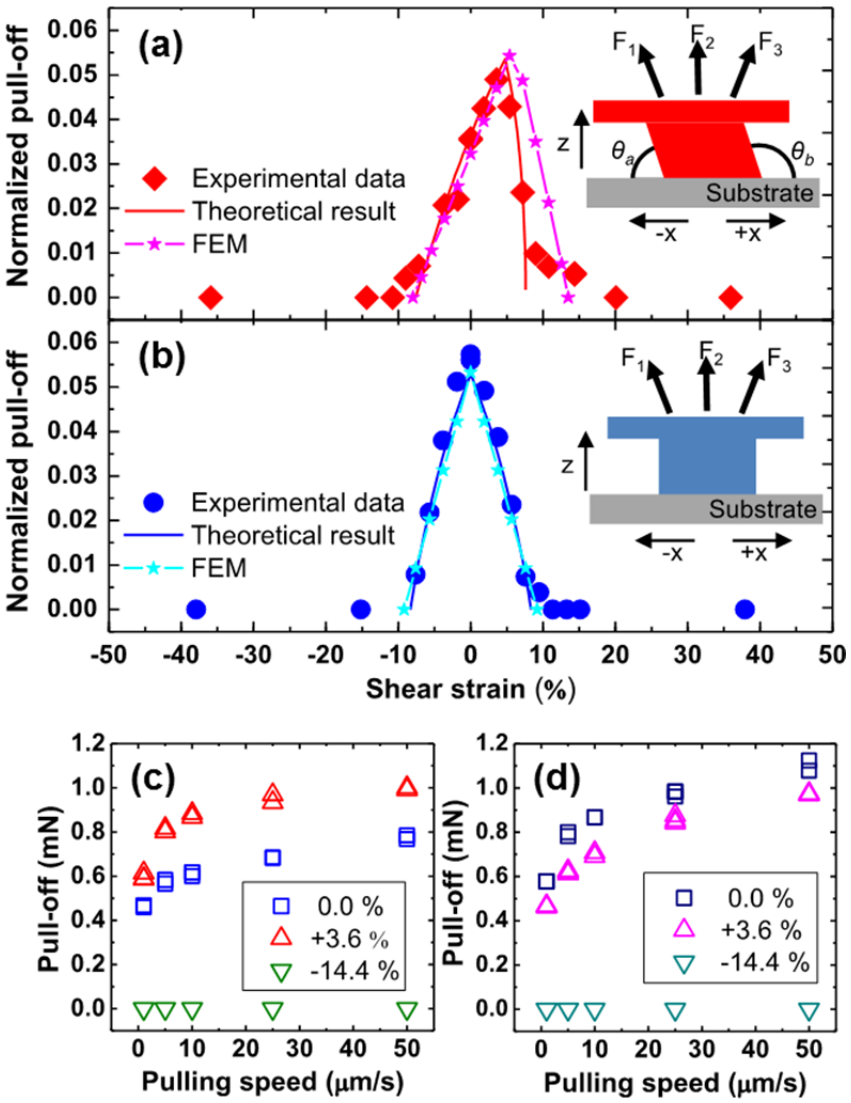

Figure 4.13. Normalized pull-off force for (a) an angled and (b) a vertical post as a function of shear strain. Symbols (diamonds) and lines represent experimental and theoretical results, respectively. Lines with star symbols show results from finite element method (FEM). The pulling speed in both cases was 10 μm/s. Insets in (a) and (b) show the geometries for an angled and a vertical post, respectively. Arrows over the posts indicate the retraction directions and F_1, F_2, and F_3 are the corresponding forces required for the delamination of post from a substrate. Measured pull-off forces for (c) an angled and (d) a vertical post as a function of pulling speed for three different shear strains.

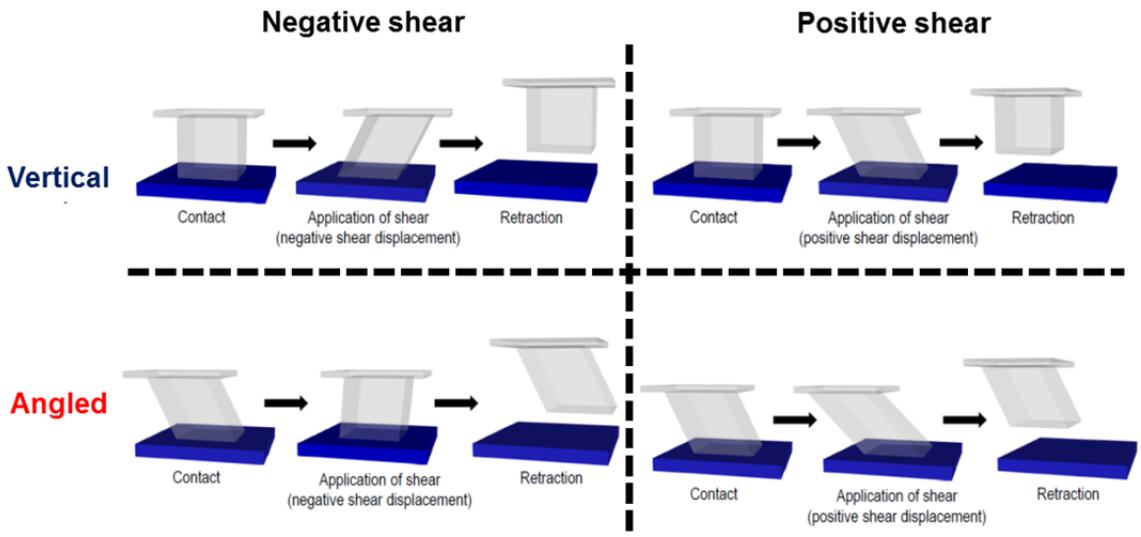

Figure 4.14. Schematic illustration of adhesion test with application of different lateral displacements to a vertical and an angled post.

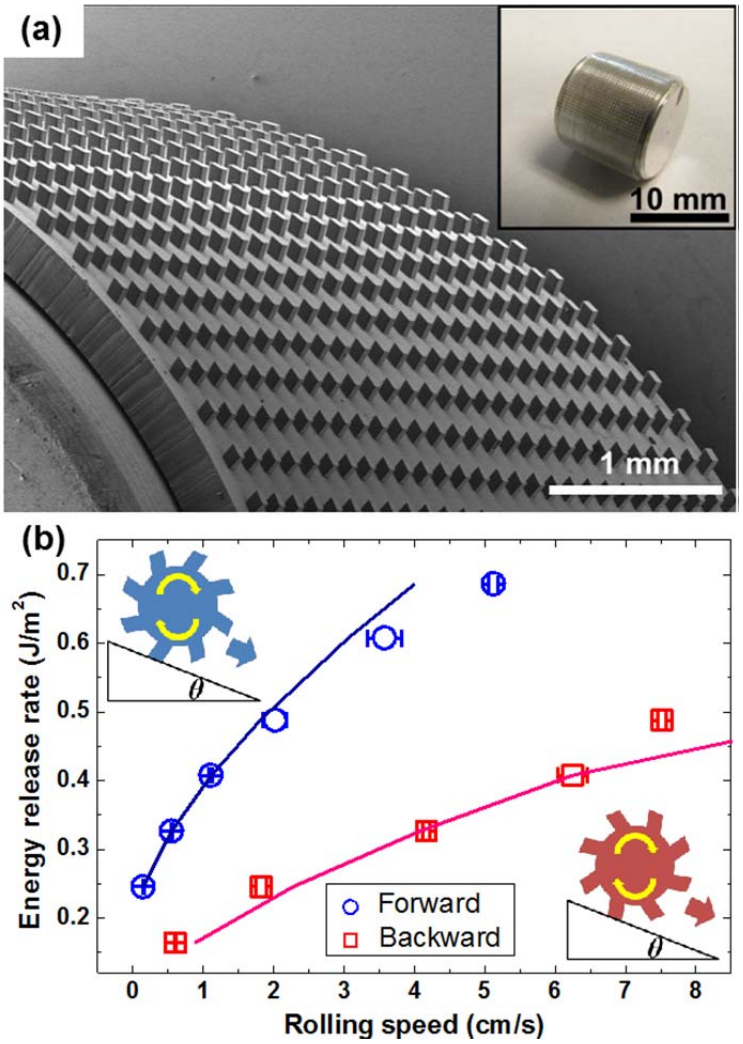

Figure 4.15. Demonstrations of rotation direction-dependent adhesion of an angled post roller. (a) SEM image of a cylinder surface wrapped by a flexible stamp with an array of angled posts. The inset shows a photograph of a stamp roller. (b) Energy release rate of an angled post roller as a function of rolling speed with two different orientations of the angled posts with respect to an inclined glass plate. Symbols and lines represent experimental and theoretical results, respectively. The insets in the upper left and lower right corners provide schematic representations for forward (high adhesion) and backward (low adhesion) rolling, respectively.

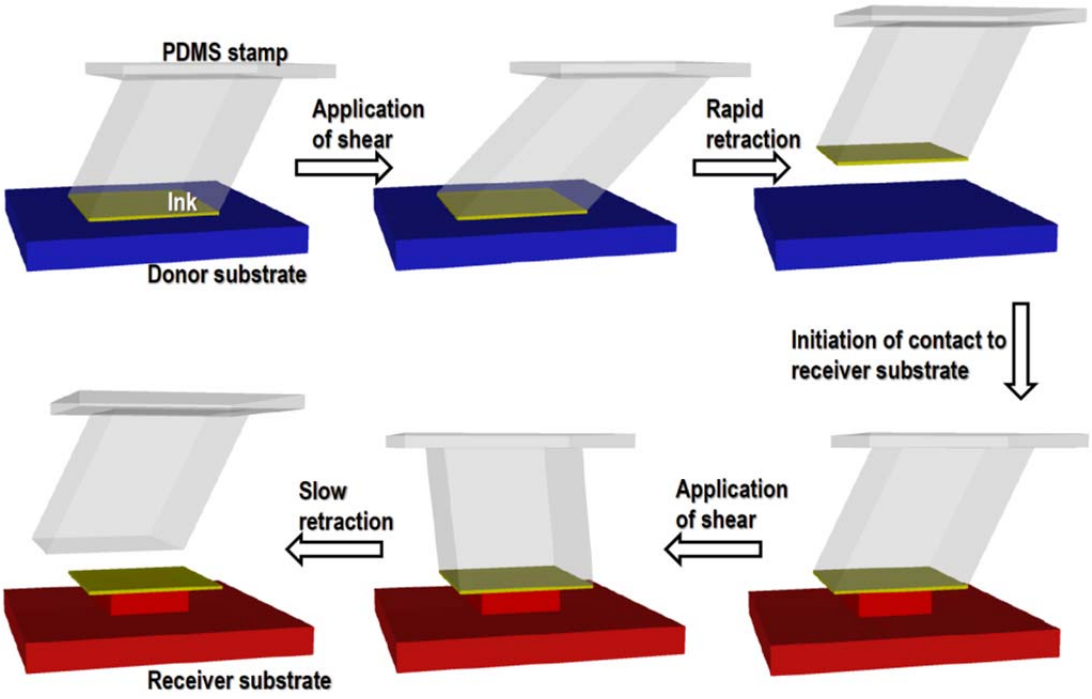

Figure 4.16. Adhesiveless transfer printing process using an angled post.

CHAPTER 5

ACTIVE, PROGRAMMABLE ELASTOMERIC SURFACES WITH TUNABLE ADHESION[1]

5.1. Abstract

This chapter describes an elastomeric stamp geometry which demonstrates active adhesion switchability through a combination of rate-dependent effects and actuation of embedded microstructures just below the stamp surface. Here, microchannels and reservoirs positioned under a thin surface membrane and co-located with flat, stiff inks can be pressurized from external sources, leading to various levels of inflation at the stamp surface and effective separation from the material to transfer. We present experimental and theoretical studies of this pressure and geometry modulated adhesion, demonstrating extreme levels of adhesive control. Implementing these concepts in single and multiply arrayed configurations enables their use for new types of deterministic assembly of solid materials onto exotic or challenging substrates. Collections of silicon plates printed with single or multiple, independently addressable embedded microstructures illustrate some of the capabilities.

5.2. Introduction

Assembly techniques based on transfer printing have become increasingly popular in the past several years, due to their unique capabilities in micro- and nano-scale materials integration

[1] Reprinted, with permission from A. Carlson, S.Wang, P. Elvikis, P.M. Ferreira, Y. Huang, J.A. Rogers, "Active, programmable elastomeric surfaces with tunable adhesion for deterministic assembly by transfer printing," *submitted*.

and fabrication.[1-9] Central to these techniques is the use of strategies that facilitate the transfer of chemical or physical 'inks' (semiconductor nanomaterials,[10-12] functional polymers,[13-15] organic molecular materials[16-19] and others) in useful two or three dimensional layouts, on substrates of interest, including unusual or exotic materials. The most general form of this process utilizes a soft, elastomeric element (i.e. a stamp) to mediate physical mass transfer between a host or 'donor' wafer and a secondary, receiving substrate. In many cases, thin adhesive layers or surface chemical modifications of the critical interfaces ensures efficient transfer.[20-22] A versatile alternative exploits rate-dependent viscoelastic effects to modulate adhesion to the stamp, through peeling velocity. In this 'adhesiveless' mode, the velocity of separation of the stamp from a surface influences the adhesive strength, with higher velocities yielding proportionally larger adhesion.[9, 23] In this way, material retrieval and delivery during printing occurs at high (~10 cm/s or greater) or low (< 1 mm/s) velocities, respectively, using a single stamp element. A growing number of applications in micro and nanotechnology benefit from or are enabled by printing-based assembly, particularly in systems requiring heterogeneous integration of inorganic semiconductor materials into functional arrangements on plastic or rubber substrates. Examples include selective manipulation or massively parallel assembly of diverse collections of materials (i.e. Si,[2, 12] GaN,[24] GaAs,[3, 25, 26] mica,[9] silica, etc) with various structural forms and sizes (nanometers to macroscopic dimensions), to yield high performance electronic and optoelectronic systems.

Efficient transfer relies critically on switching between strong (i.e., inking) and weak (i.e. printing) adhesion states in a rapid, robust, and repeatable manner. Of particular importance is achieving suitably weak adhesion to the stamp element during the delivery step. Kinetic approaches to decreasing adhesion are useful, but the minimum adhesion states are often larger

than desired, thereby limiting their broad utility. Recent efforts demonstrate strategies that can complement, or be used in conjunction with, those based on rate. In one example, targeted shear loading can facilitate interface fracture between a stamp and an ink, to enhance efficiency in release.[27] In another, switchability occurs through controlled sagging of a structured surface that supports pyramidal microtips.[28] Here, we report a protocol, shown in Figure 5.1, that reproduces the adhesion and release strategies of an aphid *pulvillus*[29] in which localized regions of a microstructured elastomeric stamp are inflated/deflated in a fashion analogous to that of a balloon. This construct yields continuously tunable and reversible levels of nonspecific, generalized adhesion. Mechanisms revealed by theoretical and experimental studies provide insights into the operation. We demonstrate these concepts in printing-based assembly of silicon plates onto a variety of substrates and configurations not easily accessible with other methods. To illustrate the versatility of this type of stamp and the feasibility of scaling it for use in massively parallel printing modes, we develop multiple independently-addressable and interconnected microstructured surfaces, capable of programmable operation. Silicon plates printed in a variety of orientations, geometries, and densities provide examples of some possibilities.

5.3. Results and Discussion

5.3.1. Microreservoir Stamp Design and Adhesiveless Transfer Printing Protocol

Figure 5.1 shows a schematic illustration of the transfer printing procedure. Here, the stamp has circular reservoirs embedded under its contacting surface, each of which can be inflated locally as a means of dynamically altering interfacial contact, and corresponding

adhesive forces. For the retrieval step, the stamp surface is brought into intimate contact with the object to be transferred (green plate in Figure 5.1), positioned to be co-centered above a reservoir. Rapid retraction of the stamp in the deflated state (i.e. flat contacting surface) retrieves the plate, with an adhesion strength that is maximized by viscoelastic effects and complete areal interfacial contact. The stamp, 'inked' in this way, is then brought into contact with a receiving substrate (lavender surface in Figure 5.1). Pressurizing the reservoir causes the stamp surface to bulge around the interface. Upon slow retraction, the membrane inflates and peels continuously out of contact with the ink, starting at the outer perimeter and propagating toward the center. The equilibrium shape of the inflated membrane at any given stage of this process is defined by a complex interaction of reservoir pressure and contact area with the ink surface. As the retraction proceeds, however, the surface assumes an increasingly hemispherical geometry, thereby decreasing contact with the plate, ultimately to a central point, after which separation is completed.

Such stamps incorporate three critical components: (1) reservoirs underneath raised features of relief on the surface of the stamp, (2) narrow channels connecting these reservoirs to an external pressurization source (i.e. compressed gas), and (3) a thin (~30 μm) membrane that covers the reservoirs and channels, which serves as the tunable interface between the stamp and ink. Such structures can be fabricated using techniques adapted from those used in the microfluidics community.[30-33] Figure 5.2a provides a scanning electron microscope (SEM) image of a simple stamp of this type, created using soft lithographic methods from the elastomer polydimethylsiloxane (PDMS, Dow Corning Sylgard 184). This design incorporates a circular reservoir (225 μm in diameter and 70 μm in depth) and narrow channels (50 μm in width) embedded in a rectangular support. A membrane layer, composed of low modulus PDMS,

completely covers the microstructured regions and bonds to the support post of Figure 5.2a, in a way that leaves it freely suspended across the reservoir and channels. An external pressure source connects to outlets from the channels, at the perimeter of the structure (overall dimensions ~10 mm × 10 mm). Pressurizing the reservoir with N_2 induces inflation in the membrane. Figure 5.2b, c shows optical images of inflation under ~12 psi without and with a thin silicon platelet (250 × 250 × 3 μm) on its surface, respectively. Figure 5.2d provides an estimate of the membrane curvature at the center of the circular reservoir, obtained by molding inflated stamps in low viscosity photo-curable polyurethane and performing surface profilometry on the molded imprints. As expected, the points of maximum membrane deflection from the surface of the support post (flat, deflated state) increase with pressure.

The fabrication procedures for stamps such as the one in Figure 5.2 use multilevel molding and bonding steps with different layers of PDMS.[34] The bulk of the stamp including the body and the surface that supports the reservoir and microchannel structures are formed by partially curing PDMS (5:1 monomer:crosslinking agent) against a lithographically patterned template. A thin stainless steel washer laminated against the template provides additional levels of relief in the stamp body to configure it for integration with a custom automated transfer printing tool. Circular punches (~600 μm, diameter) around the perimeter of the stamp serve as interfaces between external gas sources and the microchannels/reservoirs. A thin membrane of partially cured PDMS (20:1 monomer:crosslinking agent) bonds to the molded stamp surface upon thermal curing, to yield structures that can withstand pressures greater than 12.5 psi before rupture.

5.3.2. Measuring Adhesion of Actuated Stamps

Vertical pull-off forces measured under a variety of reservoir pressures using a custom measurement tool quantify the effect of inflation and deflation on stamp adhesion characteristics. The measurement setup, described in Chapter 1, consists of a precision load cell (GSO-10, Transducer Techniques) supported on a manual tip/tilt platform and attached to automated *x*-, *y*-translational stages. An independent vertical translational stage (Aerotech PRO 165) coupled with a rotation platform is used to contact the stamp with a target substrate (for this work a silicon wafer) connected to the load cell at controlled velocities, displacements, and alignments. A microscope objective mounted with the vertical stage and attached to its own secondary lateral translation axes provides visual evaluation of stamp contact and retraction events. The experiments involve contact with a clean, untreated piece of silicon wafer (~5 mm x 5 mm, attached to the load cell) at a rate of 5 μm/s and compressed 10 μm to ensure intimate contact between substrate and stamp. After a relaxation period of 5 seconds, the stamp is retracted at a controlled velocity. From the resulting force-displacement curves recorded by the load cell, the maximum pull-off force could be determined for any given delamination speed and reservoir pressure, in a manner similar to that reported previously.[28] Effects of inflation on stamp adhesion, prior to relaxation, are evaluated with reservoirs pressurized to desired levels. After relaxation, retraction of the stamps at 10 μm/s, a velocity consistent with speeds employed in rate-dependent adhesiveless printing, define characteristic pull-off forces.

Representative data for elastomeric stamp with and without embedded reservoirs appear in Figure 5.3. For the case of active stamps, the membranes remain deflated, giving rise to a strong velocity dependence in the measured adhesion. The functional dependence, consistent with flat surfaces of similar contact area and having no embedded active regions, arise from the viscoelastic nature of PDMS and demonstrate that the embedded microstructures do not alter

significantly the adhesive behavior of the stamp when deflated. Figure 5.3b, c present schematic details of a mechanics model developed to describe printing from an inflated stamp which is described in the next section. Figure 5.3d shows a comparison of the measured pull-off forces for reservoirs with depths of 30, 70, and 110 μm at increasing levels of inflation pressure. For the three depths investigated, pull-off forces monotonically decrease with increased inflation, leading to minimum adhesion values between 10 and 12 psi. Reservoirs with depths of 110 μm and pressurized to 10 psi exhibit adhesive forces below the measurement capabilities of the load cell; those with depths of 70 μm approach this limit at pressures in excess of 12 psi. These pull-off forces represent a nearly 50X reduction from the deflated state. Furthermore, by modulating the inflation pressure via electronic switches and gas flow regulators, the pull-off forces can be controllably tuned to specific values through mechanisms external to the stamp/transfer printing system. This type of active, tunable control of adhesion yields new levels of versatility and operational modes in transfer printing, as demonstrated subsequently.

5.3.3. Mechanics Modeling of Active, Inflatable Stamps

An analytical mechanics model was developed to study the printing process. Figure 3b shows all key geometric and material properties of an inflatable stamp, a thin plate of ink and a receiver substrate. The reservoir and the membrane are modeled as beams (illustrated in insets of Figure 5.3c), and the inflation pressure is treated as a uniform distributed pressure denoted by p. A displacement V applied at the top of the bulk region of the stamp results in a displacement (stretch) V_0 at the top of the reservoir (horizontal dash line in Figure 5.3b). The relation between V_0 and V is defined by the equilibrium of the bulk. For small V (and therefore small V_0), the interfacial adhesion between the ink and the stamp prevents the membrane from

delaminating. In this regime, only the reservoir is stretched and bent by the inflation pressure. Our model treats the system as a double clamped beam subjected to pressure p, where the deflection, w_R is given by, $w_R = py^2(y-H)^2/(2E_R A^3)$, where H, A and E_R are the depth, width and Young's modulus of the reservoir (Figure 5.3b). The coordinate y=0 and y=H denote the two ends of the reservoir. The potential energy $U_{stretch}$ includes contributions from the membrane and bending energies of the reservoir, and the work done by p, which yields

$$U_{stretch} = \frac{E_R A}{2}\left(\frac{V_0}{H}\right)^2 H + \int_0^H \frac{E_R A^3}{24}\left(w_R''\right)^2 dy - \int_0^H p w_R dy = \frac{E_R A V_0^2}{2H} - \frac{p^2 H^5}{120 E_R A^3} \tag{5.1}$$

As the displacement V_0 increases, the membrane starts to delaminate from the ink. If l denotes the delamination length (starting at the outer perimeter), then the potential energy $U_{delaminte}$ consists of the membrane and bending energies of the reservoir and the bending energy of the membrane, the work done by p, and also the adhesive energy of the interface. Minimization of potential energy $\partial U_{delaminate}/\partial l = 0$ gives the delamination length l and therefore $U_{delaminate}$ as:

$$U_{delaminate} = \gamma H \cdot f\left(\frac{V_0}{H\sqrt{\frac{\gamma}{E_R A}}}, \frac{pH}{\sqrt{\gamma E_R A}}, \frac{A}{H}, \frac{E_M h^3}{E_R A^3}\right) \tag{5.2}$$

where E_M and h are the Young's modulus and thickness of the membrane, respectively, and γ is the work of adhesion of the stamp/ink interface. Equation (5.2) holds until the membrane completely delaminates from the ink, i.e., when the delamination length l reaches the half width L of the membrane (Figure 5.3b), after which $U_{delaminate}$ does not increase with V_0 (or V, as illustrated in Figure 5.3c).

Figure 5.3c compares the energies for the two deformation modes in Equations (5.1) and (5.2) versus the displacement V at the top of the bulk. A critical displacement V_{crit} separates the two deformation modes: for $V<V_{crit}$, $U_{stretch}$ is smaller than $U_{delaminate}$ and there is no delamination; for $V>V_{crit}$, delamination is energetically favored. The maximum pulling force is reached when $V=V_{crit}-0$, just prior to delamination. The resulting maximum pulling force agrees well with the experiments (Figure 5.3d), and so does the critical displacement (Figure 5.3e) under various inflation pressures between 0~12 psi and for different reservoir depths. Figure 5.3b-e suggest that, as the inflation pressure increases, the pull-off force and the critical displacement to delaminate the stamp from the ink decrease, thereby promoting release of inks onto receiver substrates. Similar trends are evident for reservoirs with differing geometries.

5.3.4. Transfer Printing Capabilities Enabled by Active Stamp Designs

Examples of enhanced printing capabilities enabled by the stamps described in previous sections appear in Figure 5.4, in which multiple silicon plates are integrated onto a variety of unusual surfaces not easily accessible through other schemes. Figure 5.4a presents an optical image of silicon plates (250 × 250 × 3 μm) arranged in a 3×3 array on a bare sheet polyethylene terephthalate (PET; 50 μm in thickness), bent around a glass cylinder (20 mm radius of curvature) after printing. The inset of Figure 5.4a shows an angled array of plates as they wrap around the curve of the underlying cylinder. An example of printing of similar structures onto commercially available card stock (smooth, non-matte finish), appears in Figure 5.4b, and is potentially relevant to paper-based electronics.[35, 36] Printing onto textured surfaces, as in Figure 5.4c which shows a SEM micrograph of a silicon plate (200 × 200 × 3 μm) delivered onto

a photonic crystal (PC) surface consisting of close-packed array of SiO_2 microspheres (600 nm in radius). This type of integration could be of interest in unusual opto-electronics systems.[37, 38]

Figure 5.4d provides a similar demonstration of adhesiveless transfer onto a surface with substantial relief, in this case onto the underside of a leaf. As shown in the image, silicon plates are located over the lower cuticle of the leaf as well as the venation and part of the midrib. Due to the coarse and non-planar nature of the venation, the plates are unable to establish complete contact with the cuticle, leaving them propped and partially suspended. Active stamps are particularly effective in this case due to the ease with which the rigid plates can rotate and deflect along with the thin, soft inflated membrane, allowing them to self-position on the receiver and maintain maximum available contact. Passive stamp designs, such as those that use solid, molded posts, do not offer this type of self-adjustment due to their comparatively high levels of rigidity. The ability to print single crystal silicon structures directly onto naturally occurring, biological surfaces could be of value in the integration of semiconductor device functionality with living systems.[39-43] Figures 5.4e-g show additional printing demonstrations including silicon chips deployed onto coinage (Figure 5.6e, f) and in highly aligned multilayer stacks (Figure 5.6g).

5.3.5. Programmable, Multi-Reservoir Active Stamps

The designs described here can be scaled to include multiple reservoir features connected in independent and interconnected layouts. Figure 5.5a provides a series of optical images that demonstrate the arrangement and printing of five, independently addressable reservoirs, each with layouts like those in Figure 5.2. Simultaneous inking of all five active regions occurs by contacting the stamp to an array of silicon plates with separations that match those of the

reservoirs. After retrieval, an inked stamp of this type can be positioned over a target substrate (PDMS coated paper) as shown in panel *(i)*. Panels *(ii)* and *(iii)* correspond to actuation of the first, third, and fifth reservoirs and the second and fourth reservoirs, respectively, achieved by activating individual switches connected to gas inlets for each reservoir. To demonstrate independent printing capabilities, panels *(iv)* – *(vi)* show arrangement and delivery of selected silicon plates onto the substrate surface, highlighting the unique assemblies that can be obtained with this multi-reservoir design. Independent actuation of selected reservoirs out of an array enables rapid deployment of large quantities inks in a controlled, deterministic manner which is not limited to density, pitch, or layout limitations of the donor material. Figure 5.5b provides an optical image of silicon plates printed in diverse arrangements using the stamp shown in Figure 5.5a. As demonstrated here, a variety of different layouts can be accommodated with a single stamp, potentially increasing printing throughput with massively parallel assembly strategies.

Multi-reservoir designs can also be used in ways such that different active regions are coupled with neighboring structures to provide extended regions of inflation for printing large or asymmetric ink structures. Figure 5.5c shows a 5×5 array of cross-shaped reservoirs connected via microchannels along vertical rows, resulting in long columns that are actuated independently or with other regions of the stamp. Actuating alternating reservoir columns yields responses illustrated in magnified views of Figure 5.5d and e, respectively, where inflated columns are denoted by dark outlining along the reservoir perimeters. To ensure proper inflation over the extended active regions, compressed gas is provided from two inlets on the top and bottom of each column. The large, interconnected layout provides many of the same capabilities as the independently addressable reservoirs, such as pitch control and versatility of ink arrangement, but adds flexibility in the size, type, and configuration of the ink material available for printing.

5.4. Conclusions

In summary, advanced stamp designs that embed actuatable reservoirs and microchannels in microstructured elastomeric surfaces allow controllable tuning of the strength and geometry of interfacial adhesion. Through selective pressurization of the reservoirs, localized regions of the stamp surface can be inflated, thereby inducing interfacial bending moments and initiating separation between a stamp surface and semiconductor ink, factors that enhance printing capabilities. Comparison of active stamps in inflated and deflated states show a linearly monotonic decrease in adhesive strength with increasing pressure as well as the ability to tune stamp adhesion through an external pressurization source. To understand the adhesive behavior of the active stamp designs, a comprehensive model based on energy minimization of the pressurized reservoirs was developed. As determined from the model, during retraction of an inflated stamp from an ink material (here a silicon plate during the printing step), a critical displacement marks the transition from a stretching mode to actual separation and printing. Comparison of theoretical and measured critical displacement values show good agreement as do predicted and measured pull-off forces from the adhesion tests. The lowered adhesive strength of the stamp is also demonstrated through delivery of silicon plate inks onto a variety of unusual or challenging surfaces such as flat plastic and card stock and rough or non-planar active surfaces such as a photonic crystal of SiO_2 microspheres or the lower cuticle and venation of a leaf. Extending the single reservoir designs in multiple, independently addressable or interconnected systems demonstrates the versatility for scale-up of this printing technique as well as relaxing restrictions on complex stamp and ink layouts previously required for heterogeneous assembly. The use of active stamp designs to extend adhesiveless printing capabilities may provide a route to developing novel forms of electronics and opto-electronics which require

intimate contact with substrates in curvilinear formats or unusual environments or a universal printing tool which can access a wide range of ink materials and geometries.

5.5. Experimental

PDMS Stamp Template Fabrication: Bare silicon wafers (Montco Silicon) were degreased with acetone, isopropyl alcohol, and deionized water prior to exposure to a UV/ozone environment for 5 minutes. Spin casting defined a layer of negative tone photoactive epoxy (SU8-50, MicroChem; 70 μm in thickness) that was then baked at 120 ˚C on a hotplate for 10 minutes to remove residual solvent. Photoexposure to 185 mJ cm^{-2} of UV radiation (λ=365 nm) through a quartz mask defined desired patterns, followed by a second annealing step for 10 minutes on a hotplate at 120 ˚C. Development resulted in a patterned structure for direct molding of PDMS. Prior to molding, the surface of the template was treated (tridecafluoro-1,1,2,2-tetrahydrooctyl) trichlorosilane (FOTCS, Gelest) via vapor deposition.

Active Stamps with Embedded Circular Reservoirs: Fabricating stamps with embedded reservoirs and microchannels involved a series of molding and bonding steps with different layers of PDMS.[34] The stamp body with molded surface relief was first generated by pouring a precursor of liquid PDMS (5:1 monomer:crosslinking agent) against a lithographically patterned template. A thin (3 mm) washer inserted against the template prior to applying the liquid PDMS created a multilevel stamp with a wide base for integration with a custom automated transfer printing tool. The PDMS was then partially cured in an oven at 70 ºC for 20 minutes, cooled, and demolded from the template and washer. After cooling, circular holes were formed by punching a 20 gauge, blunt-edge syringe needle attached to a manual drill press through the stamp bulk. The punches were positioned so that only microchannels connecting to

the active reservoir regions are pierced. The stamps were then cleaned with Scotch Tape™ prior to application of the capping membrane.

The thin surface membrane was formed by spin coating (3000 RPM, 30 seconds) a PDMS mixture of 20:1 monomer:crosslinking agent onto a silicon wafer treated with FOTCS anti-adhesion layers and partially curing at 70 ºC for 11 minutes on a hotplate. Following curing, the molded 5:1 PDMS was immediately placed onto the warm membrane and cured in an oven at 75 ºC for 4 hours. When removed from the oven and cooled, the now-bonded stamp was peeled off the wafer surface intact, the membrane being securely bonded to the stamp bulk.

Active Stamp Imprints and Characterization: Imprints of active stamps with circular reservoirs were obtained under different levels of membrane inflation. Small plastic containers were filled with 4 cc of a low viscosity, photo-curable polyurethane (NOA 65, Norland Optical Adhesives) and attached to manual *x-, y*-stages under a stereoscope. Active stamps on an independent *z*-stage were lowered to bring the inflatable regions into contact with the NOA. After ~5 minutes in this position, the stamps were inflated and held in the inflated state for another 5 minutes to allow the fluid to flow around and conform to the active regions. The entire setup was then exposed to UV light for 60 minutes to cure the NOA. The reservoirs were deflated, carefully demolded, and cleaned. The imprints were evaluated with a surface profilometer (Dektak 3030). Line scans obtained at the center of the imprint (coinciding with the center of the reservoir) were used to calculate the maximum deflection of the membranes under increasing inflation pressure.

Semiconductor Ink Fabrication: Silicon plates used these experiments were fabricated using the same techniques detailed in other chapters of this thesis and the literature.[44]

Transfer Printing: Precision translation and rotational stages controlled the positions of stamp, ink, and receiver substrates during the various printing steps illustrated in Figure 5.1. An independent optical microscope and video acquisition system enabled visual monitoring of the process while an external gas source delivered compressed nitrogen for local inflation of the microreservoirs and channels. The stages also accommodated a custom adhesion measurement system designed to measure pull-off forces of stamp under various amounts of inflation.

5.6. References

[1] J.-H. Ahn, H.-S. Kim, K.J. Lee, S. Jeon, S.J. Kang, Y. Sun, R.G. Nuzzo, J.A. Rogers, *Science* **2006**, *314*, 1754.

[2] J. Yoon, A.J. Baca, S.-I. Park, P. Elvikis, J.B.G. III, L. Li, R.H. Kim, J. Xiao, S. Wang, T.-H. Kim, M.J. Motala, B.Y. Ahn, E.B. Duoss, J.A. Lewis, R.G. Nuzzo, P.M. Ferreira, Y. Huang, A. Rockett, J.A. Rogers, *Nat. Mater.* **2008**, *7*, 907.

[3] J. Yoon, S. Jo, I.S. Chun, I. Jung, H.-S. Kim, M. Meitl, E. Menard, X. Li, J.J. Coleman, U. Paik, J.A. Rogers, *Nature* **2010**, *465*, 329.

[4] A. Javey, S. Nam, R.S. Friedman, H. Yan, C.M. Lieber, *Nano Lett.* **2007**, *7*, 773.

[5] K. Takei, T. Takahashi, J.C. Ho, H. Ko, A.G. Gillies, P.W. Leu, R.S. Fearing, A. Javey, *Nat. Mater.* **2010**, *9*, 821.

[6] D.R. Hines, A.E. Southard, A. Tunnell, V. Sangwan, T. Moore, J.-H. Chen, M.S. Fuhrer, E.D. Williams, *Proc. of SPIE* **2007**, *6658*, 66580Y.

[7] Q. Cao, J.A. Rogers, *Adv. Mater.* **2009**, *21*, 29.

[8] Y. Lee, S. Bae, H. Jang, S. Jang, S.-E. Zhu, S.H. Sim, Y.I. Song, B.H. Hong, J.-H. Ahn, *Nano Lett.* **2010**, *10*, 490.

[9] M.A. Meitl, Z.-T. Zhu, V. Kumar, K.J. Lee, X. Feng, Y.Y. Huang, I. Adesida, R.G. Nuzzo, J.A. Rogers, *Nat. Mater.* **2006**, *5*, 33.

[10] H.C. Ko, A.J. Baca, J.A. Rogers, *Nano Lett.* **2006**, *6*, 2318.

[11] A.J. Baca, M.A. Meitl, H.C. Ko, S. Mack, H.-S. Kim, J. Dong, P.M. Ferreira, J.A. Rogers, *Adv. Func. Mater.* **2007**, *17*, 3051.

[12] A.J. Baca, J.-H. Ahn, Y. Sun, M.A. Meitl, E. Menard, H.-S. Kim, W.M. Choi, D.-H. Kim, Y. Huang, J.A. Rogers, *Angew. Chem. Int. Ed.* **2008**, *47*, 5524.

[13] J. Yeom, M.A. Shannon, *Adv. Func. Mater.* **2010**, *20*, 289.

[14] Y. Xia, G.M. Whitesides, *Angew. Chem. Int. Ed.* **1998**, *37*, 551.

[15] J.L. Wilbur, A. Kumar, H.A. Biebuyck, E. Kim, G.M. Whitesides, *Nanotechnology* **1996**, *7*, 452.

[16] Z. Bao, J.A. Rogers, H.E. Katz, *J. Mater. Chem.* **1999**, *9*, 1895.

[17] A.L. Briseno, M. Roberts, M.-M. Ling, H. Moon, E.J. Nemanick, Z. Bao, *J. Am. Chem. Soc.* **2006**, *128*, 3880.

[18] G.B. Blanchet, Y.-L. Loo, J.A. Rogers, F. Gao, C.R. Fincher, *Appl. Phys. Lett.* **2003**, *82*, 463.
[19] M.M. Stevens, M. Mayer, D.G. Anderson, D.B. Weibel, G.M. Whitesides, R. Langer, *Biomaterials* **2005**, *26*, 7636.
[20] E. Menard, K.J. Lee, D.-Y. Khang, R.G. Nuzzo, J.A. Rogers, *Appl. Phys. Lett.* **2004**, *84*, 5398.
[21] E. Menard, M.A. Meitl, Y. Sun, J.-U. Park, D.J. Shir, Y.-S. Nam, S. Jeon, J.A. Rogers, *Chem. Rev.* **2007**, *107*, 1117.
[22] Y. Sun, H.-S. Kim, E. Menard, S. Kim, I. Adesida, J.A. Rogers, *Small* **2006**, *2*, 1330.
[23] X. Feng, M.A. Meitl, A.M. Bowen, Y. Huang, R.G. Nuzzo, J.A. Rogers, *Langmuir* **2007**, *23*, 12555.
[24] H. Kim, E. Brueckner, J. Song, Y. Li, S. Kim, C. Lu, J. sulking, K. Choquette, Y. Huang, R.G. Nuzzo, J.A. Rogers, *Proc. Natl. Acad. Sci. U.S.A.* **2011**, *108*(25), 10072.
[25] Y. Sun, S. Kim, I. Adesida, J.A. Rogers, *Appl. Phys. Lett.* **2005**, *87*, 083501.
[26] S.-I. Park, Y. Xiong, R.-H. Kim, P. Elvikis, M. Meitl, D.-H. Kim, J. Wu, J. Yoon, C.-J. Yu, Z. Liu, Y. Huang, K.-C. Hwang, P. Ferreira, X. Li, K. Choquette, J.A. Rogers, *Science* **2009**, *325*, 977.
[27] A. Carlson, H.-J. Kim-Lee, J. Wu, P. Elvikis, H. Cheng, A. Kovalsky, S. Elgan, Q. Yu, P.M. Ferreira, Y. Huang, K.T. Turner, J.A. Rogers, *Appl. Phys. Lett.* **2011**, *98*, 264104.
[28] S. Kim, J. Wu, A. Carlson, S.H. Jin, A. Kovalsky, P. Glass, Z. Liu, N. Ahmed, S.L. Elgan, W. Chen, P.M. Ferreira, M. Sitti, Y. Huang, J.A. Rogers, *P. Natl. Acad. Sci. U.S.A.* **2010**, *107*, 17095.
[29] A.D. Lees, J. Hardie, *J. Exp. Biol.* **1987**(136), 209.
[30] P. Kim, K.W. Kwon, M.C. Park, S.H. Lee, S.M. Kim, K.Y. Suh, *Biochip J.* **2008**, *2*, 1.
[31] D.C. Duffy, J.C. McDonald, O.J.A. Schueller, G.M. Whitesides, *Anal. Chem.* **1998**, *70*, 4974.
[32] J.C. McDonald, D.C. Duffy, J.R. Anderson, D.T. Chiu, H. Wu, O.J.A. Schueller, G.M. Whitesides, *Electrophoresis* **1999**, *21*, 27.
[33] J.C. McDonald, G.M. Whitesides, *Acc. Chem. Res.* **2002**, *35*, 491.
[34] M.A. Unger, H.-P. Chou, T. Thorsen, A. Scherer, S.R. Quake, *Science* **2000**, *288*, 113.
[35] D.-H. Kim, Y.-S. Kim, J. Wu, Z. Liu, J. Song, H.-S. Kim, Y.Y. Huang, K.-C. Hwang, J.A. Rogers, *Adv. Mater.* **2009**, *21*, 3703.
[36] J.A. Rogers, Z. Bao, K. Baldwin, A. Dodabalapur, B. Crone, V.R. Raju, V. Kuck, H. Katz, K. Amundson, J. Ewing, P. Drzaic, *Proc. Natl. Acad. Sci. U.S.A.* **2001**, *98*, 4835.
[37] S. Kim, Y. Su, A. Mihi, S. Lee, Z. Liu, T.K. Bhandakkar, J. Wu, J.B.G. III, H.T. Johnson, Y. Zhang, J.-K. Park, P.V. Braun, Y. Huang, J.A. Rogers, *Small* **2011**, 1.
[38] A. Mihi, C. Zhang, P.V. Braun, *Agnew. Chem. Int. Ed.* **2011**, *50*, 5712.
[39] D.-H. Kim, N. Lu, R. Ma, Y.-S. Kim, R.-H. Kim, S. Wang, J. Wu, S.M. Won, H. Tao, A. Islam, K.J. Yu, T.-I. Kim, R. Chowdhury, M. Ying, L. Xu, M. Li, H.-J. Chung, H. Keum, M. McCormick, P. Liu, Y.-W. Zhang, F.G. Omenetto, Y. Huang, T. Coleman, J.A. Rogers, *Science* **2011**, *333*, 838.
[40] D.-H. Kim, N. Lu, R. Ghaffari, Y.-S. Kim, S.P. Lee, L. Xu, J. Wu, R.-H. Kim, J. Song, Z. liu, J. Viventi, B.d. Graff, B. Elolampi, M. Mansour, M.J. Slepian, S. Hwang, J.D. Moss, S.-M. Won, Y. Huang, B. Litt, J.A. Rogers, *Nat. Mater.* **2011**, *10*, 316.

[41] D.-H. Kim, J. Viventi, J.J. Amsden, J. Xiao, L. Vigeland, Y.-S. Kim, J.A. Blanco, B. Panilaitis, E.S. Frechette, D. Contreras, D.L. Kaplan, F.G. Omenetto, Y. Huang, K.-C. Hwang, M.R. Zakin, B. Litt, J.A. Rogers, *Nat. Mater.* **2010**, *9*, 511.
[42] J. Viventi, D.-H. Kim, J.D. Moss, Y.-S. Kim, J.A. Blanco, N. Annetta, A. Hicks, J. Xiao, Y. Huang, D.J. Callans, J.A. Rogers, B. Litt, *Sci. Transl. Med.* **2010**, *2*, 24ra22.
[43] J. Viventi, D.-H. Kim, L. Vigeland, E.S. Frechette, J.A. Blanco, Y.-S. Kim, A.E. Avrin, V.R. Tiruvadi, S.-W. Hwang, A.C. Vanleer, D.F. Wulsin, K. Davis, C.E. Gelber, L. Palmer, J.V.d. Spiegel, J. Wu, J. Xiao, Y. Huang, D. Contreras, J.A. Rogers, B. Litt, *Nat. Neurosci.* **2011**, *14*, 1599.
[44] Y. Yang, Y. Hwang, H.A. Cho, J.-H. Song, S.-J. Park, J.A. Rogers, H.C. Ko, *Small* **2011**, *7*, 484.

5.7. Figures

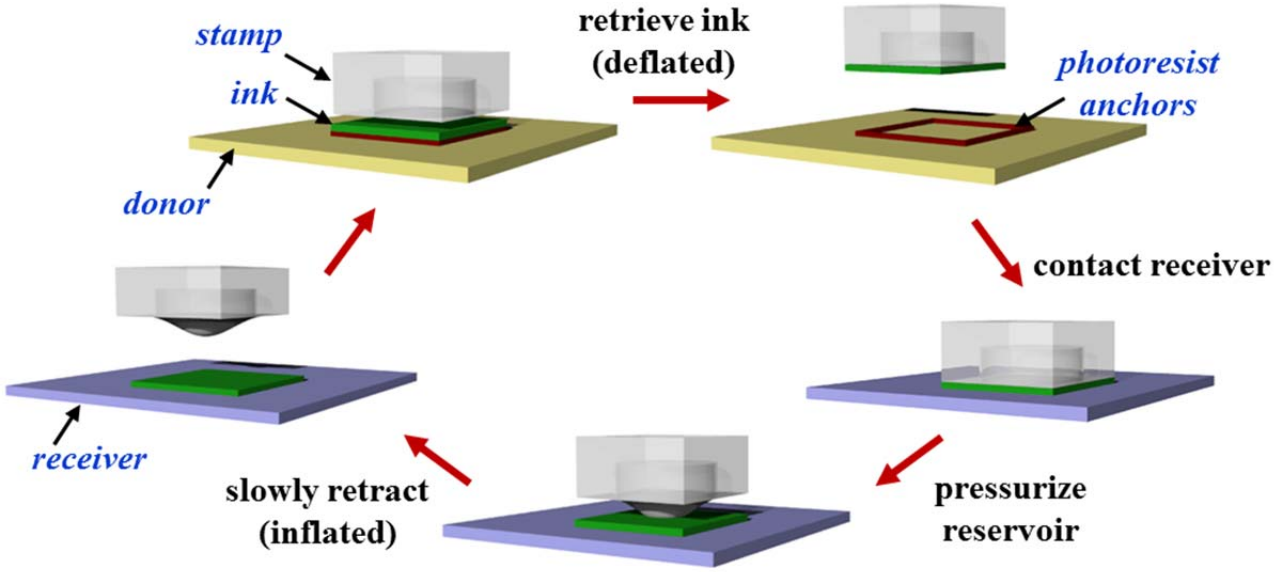

Figure 5.1. Procedure for printing via an actuated stamp. Initially the stamp, in a deflated state, is brought into contact with a rigid plate 'ink' supported on a donor substrate and rapidly retracted to retrieve the plate onto the stamp surface. The 'inked' stamp is then lightly contacted to a non-native receiver substrate and the microreservoirs pressurized, causing inflation. The stamp is slowly pulled out of contact while inflated, delivering the plate to the receiver substrate.

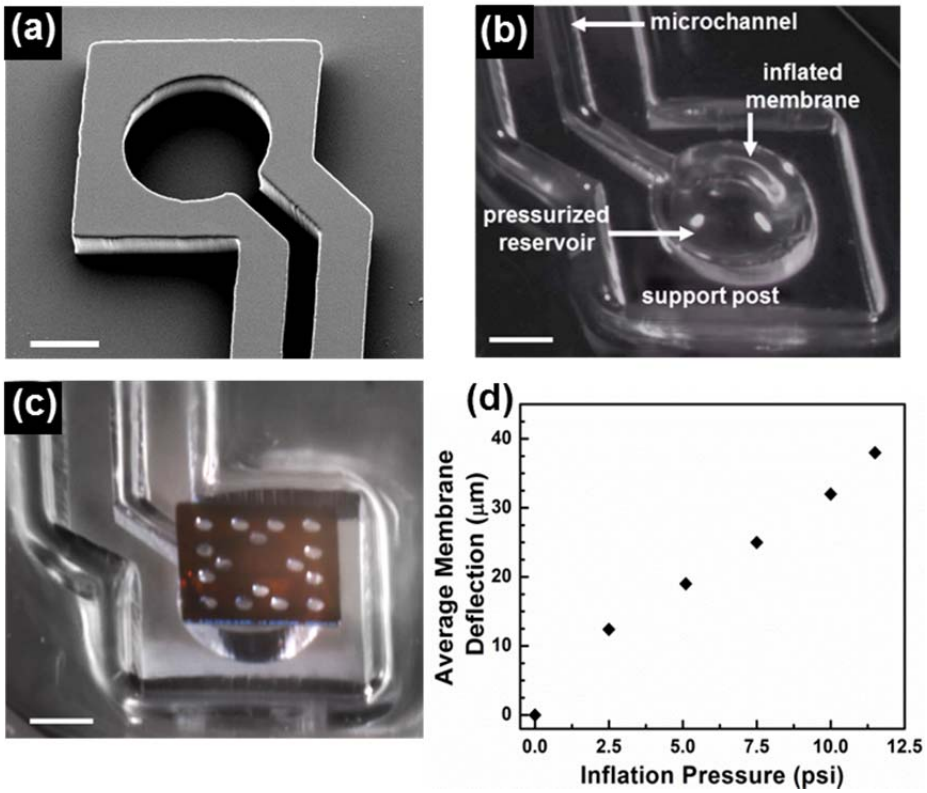

Figure 5.2. (a) Scanning electron microscope (SEM) image of an active stamp without the top thin PDMS membrane. The microchannel leads directly from the remote gas inlet (not pictured) to the circular central reservoir of the stamp. Optical microscope images of an actuated stamp without (b) and with (c) a silicon plate on the inflated membrane; with critical features labeled. During inflation, the plate is brought out of contact with the stamp support post and remains connected only via the bulged membrane. Images are obtained from compiling *z*-stack frames in a scanning stereomicroscope. (d) Average deflection of the membrane during inflation, measured at the point directly above reservoir center. Scale bars correspond to 100 μm.

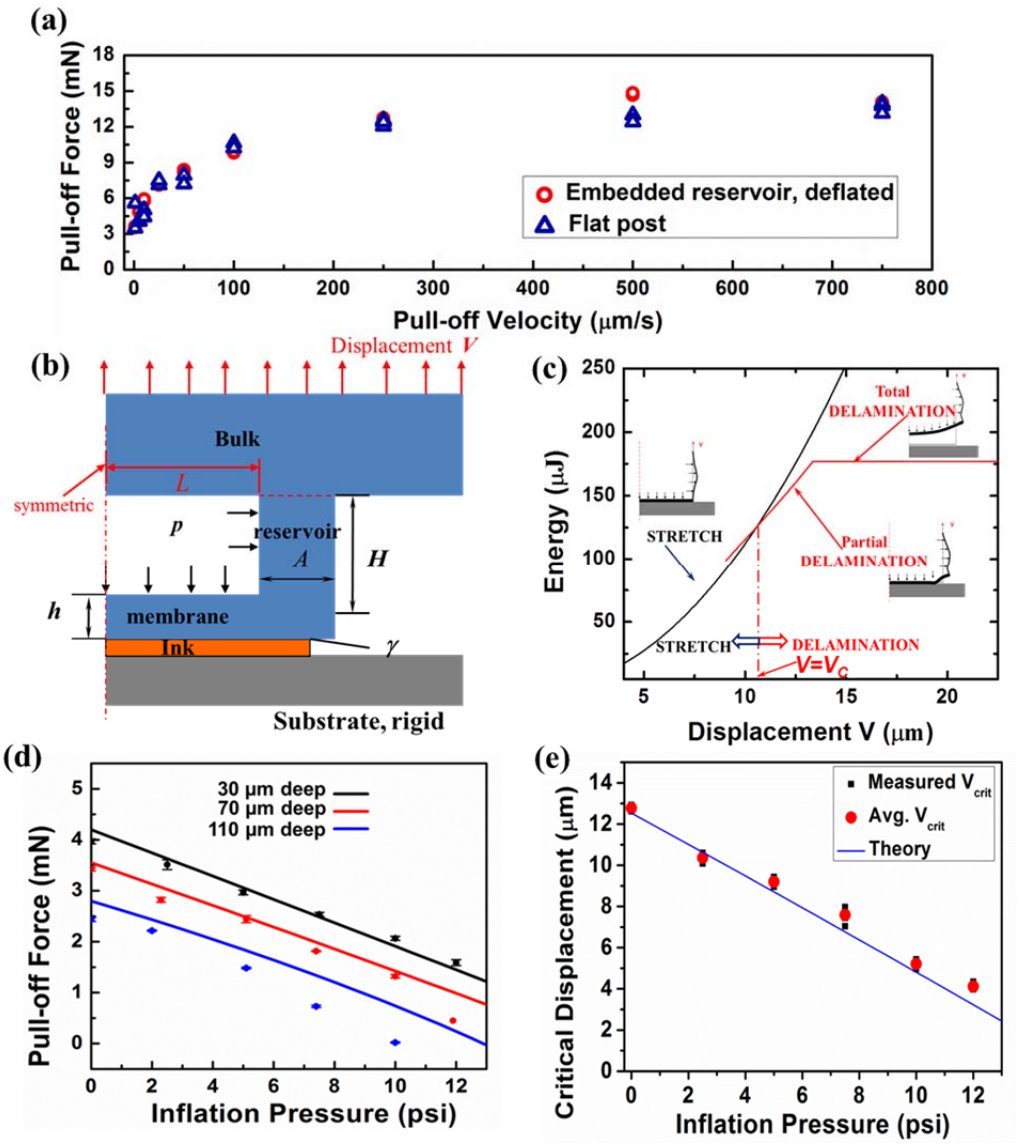

Figure 5.3. (a) Comparison of pull-off forces between stamps having embedded active regions (deflated state) and stamps without reservoir microstructures. (b) Schematic cross sectional illustration of an active stamp, with key dimensions, parameters and materials labeled. (c) Energy curves for different deformation modes and the critical displacement that separates these modes. (d) Experimental and theoretically predicted decrease in stamp/silicon interfacial adhesion (maximum pull-off force) with increasing inflation pressure. (e) Experimental and theoretically predicted decrease in critical displacements with increasing inflation pressures.

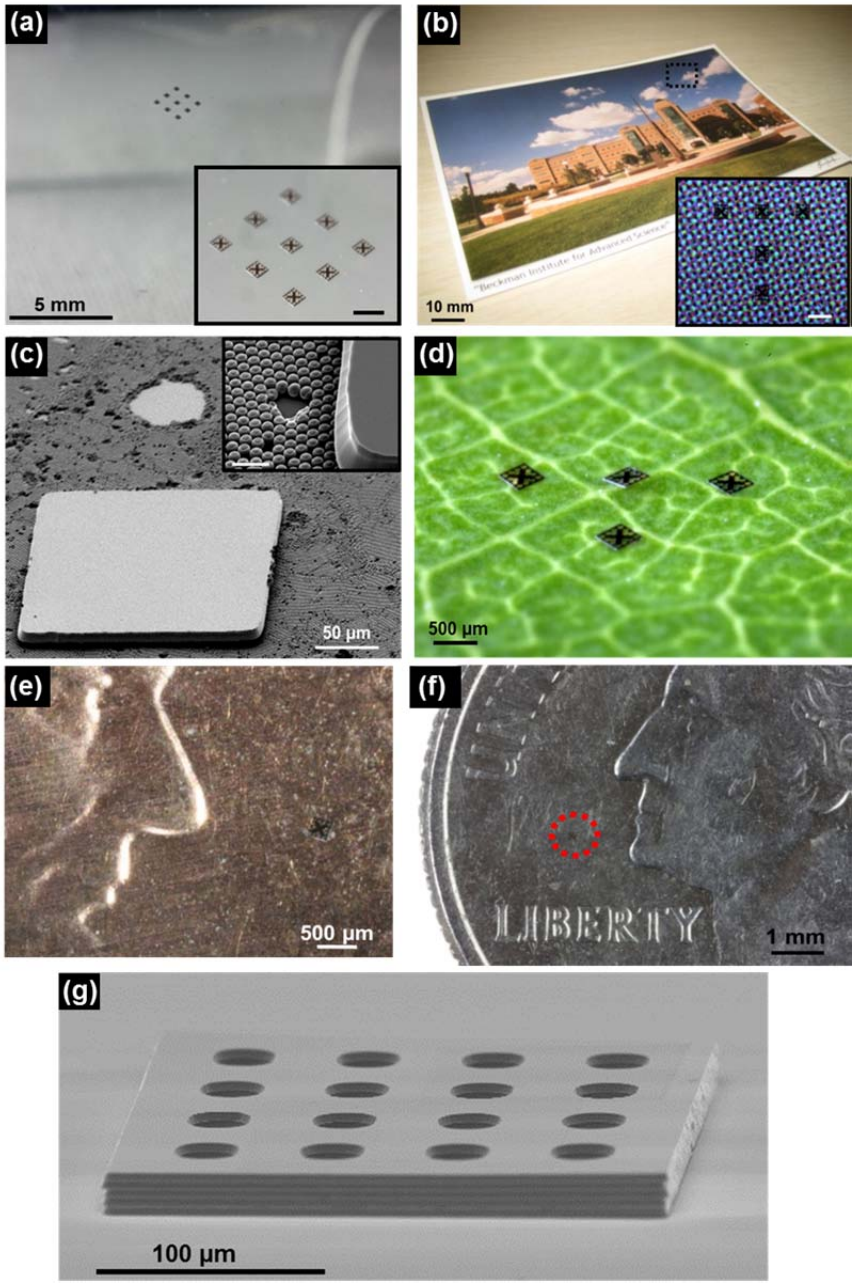

Figure 5.4. Printing capabilities demonstrated by actuated PDMS stamps. Stamps pressurized to 12 psi enabled delivery of silicon plates (250 × 250 × 3 µm) onto a number of unusual substrates, without the use of adhesive layers, such as (a) plastic sheets (PET, 50 µm thick), (b) glossy card stock, (c) photonic crystals (PC), (d) organic matter such as a leaf, and (e, f) coinage. (g) shows a 5 plate stack with highly registered placement between levels. Insets in (a) and (b) show printed arrays of plates on the respective substrates with scale bars corresponding to 250 µm. Inset in (c) shows the PC surface composed of SiO_2 microspheres, scale bar corresponds to 4 µm.

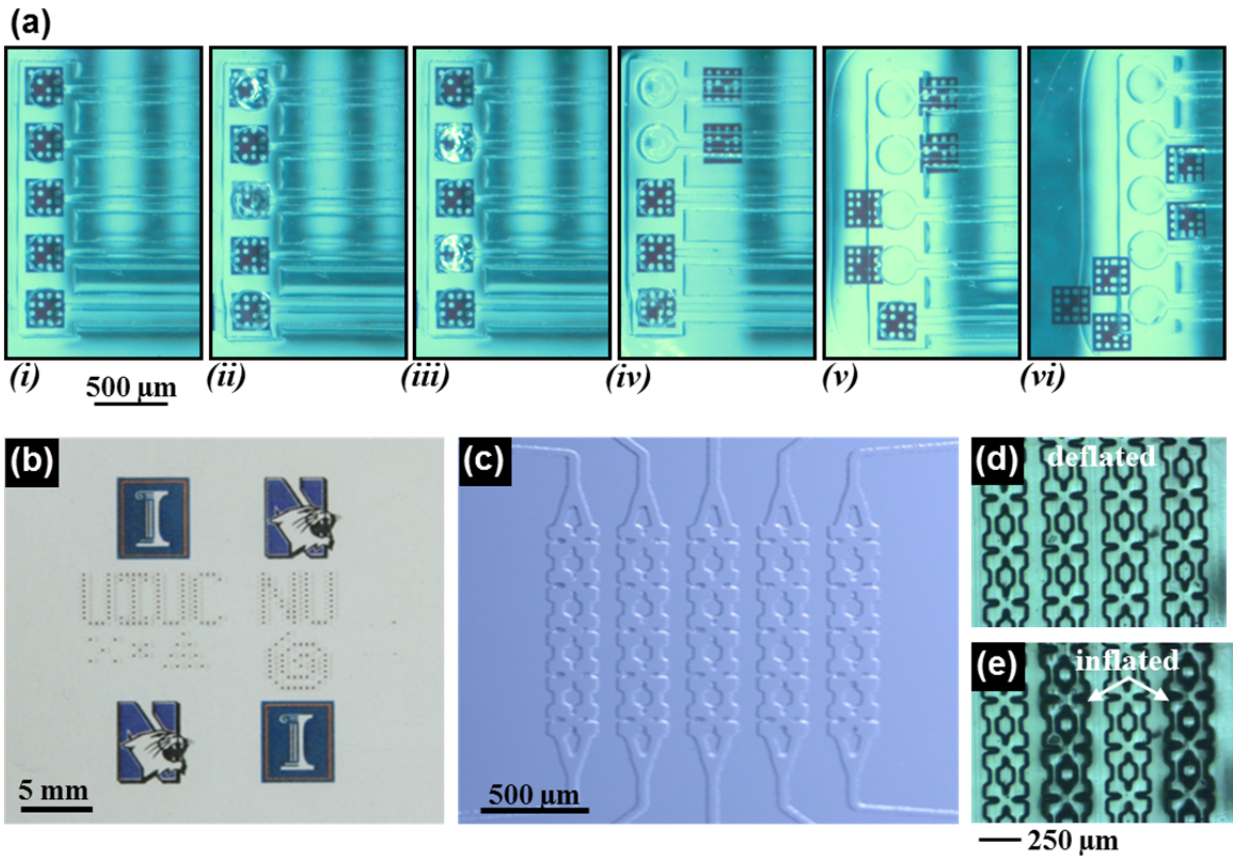

Figure 5.5. Multiple, independently addressable stamps configured for programmable printing modalities. (a) Series of frames demonstrating actuation and printing of 5 microreservoirs in a single stamp. After retrieval, (*i*), the inked stamp is positioned above a 1 mm thick sheet of PDMS laminated to a business card. (*ii*) and (*iii*) show actuation of the first, third, and fifth reservoir and second and fourth reservoir, respectively. After printing the first two plates, (*iv*), the stamp is moved to a different location to print the third and fourth plates, (*v*). Finally the last plate is delivered near the fourth chip, (*vi*), demonstrating the positioning and deployment capabilities of a programmable stamp. (b) Silicon plates printed in various geometries on a PDMS sheet laminated against a piece of paper using a stamp similar to the one in (a). Other configurations of programmable stamps are also demonstrated in (c), including series of interconnected reservoirs used to actuate entire columns of a stamp. (d) illustrates a magnified view of (c) with interlinked reservoirs which can inflate alternating columns when pressurized, (e).

CHAPTER 6

MULTILEVEL PRINTED SILICON NANOMEMBRANES AS NOVEL DEVICE PLATFORMS[1]

6.1. Abstract

Here we describe how the printing modalities developed throughout this body of work and related processes can be used to construct interesting device platforms based on stacked arrays of large-are silicon nanomembrane sheets. Specifically we introduce two techniques for realizing multilayer device formats: a "print-and-pattern" process characterized by sequential printing and lithographic steps and a self-aligned process where patterning is achieved through a printed stack of different materials. To demonstrate the utility of these concepts, we present preliminary work on a double layer 1 × 12 multimode-interference (MMI) coupler. Optical characterizations confirm low insertion loss and uniform outputs from early devices.

6.2. Introduction

Single crystal semiconductor nanomembranes (NM) represent an interesting material format for many emerging classes of electronics and optoelectronics.[1-6] The dimensional anisotropy (microns to centimeters in lateral dimensions, nanometers in thickness) ensures that these structures are extremely flexible while still retaining their exceptional performance capabilities. The combination of high performance and mechanical flexibility make them

[1] Reprinted, with permission from Y. Zhang, A. Carlson, S.Y. Yang, A. Hosseini, D. Kwong, J.A. Rogers, R.T. Chen, "Double-layer photonic devices based on transfer printing of silicon nanomembranes for three-dimensional photonics," *submitted*.

appealing for heterogeneously integrated systems where conformal contact to curvilinear substrates is critical, such as in devices for neural and cardiac monitoring.[7-13] Other areas where single crystal inorganic semiconductor nanomembranes have proven to be interesting platforms include flexible electronics and optoelectronics such as GaAs solar cells,[14] Ge PIN photodetectors,[15] InP solar cells,[16] and Si Fano filters[6, 17] where printing-based assembly techniques have shown to be uniquely suited to device organization in two- and three-dimensional layouts.

As one example, vertical integration of multiple layers of active and passive photonic components can provide a simple resolution to problems of limited real estate on a single layer silicon photonic integrated circuit.[18] To date, deposited polysilicon has been used extensively for photonic integration[19] due in part to its applicability for fabricating 3D photonic devices. However, the lowest reported propagation loss for polycrystalline silicon waveguides is 6.45dB/cm for rectangular cross section dimensions of approximately 450 × 250 nm.[20] Similar waveguide geometries in crystalline silicon exhibit only ~1dB/cm loss.[21] Additionally, polysilicon processes requires high temperature crystallization anneals (~1100˚C), which limits its applicability in active photonic devices, such as thermal-optic structures.

In this chapter we demonstrate, as a motivating example, a novel 3D photonic integration scheme using transfer printing of silicon nanomembranes to serve as top layer device platforms. We develop two assembly techniques, a ‘print and pattern’ approach to generate overlaid, multilevel devices and a self-aligned technique to give perfectly aligned structures across different layers of the structure. We fabricate double layer 1 × 12 multimode-interference (MMI) couplers, with bottom structures on a silicon-on-insulator (SOI) device layer and top device on a transfer printed silicon nanomembrane.

6.3. Results and Discussion

6.3.1. Print-and-Pattern Approach

MMI couplers can be used for efficient on-chip splitting when coupled with optimized design schemes.[22] For devices fabricated via the print-and-pattern approach, multimode waveguide width was chosen to be W_{MMI} = 60μm with a corresponding multimode waveguide length, L_{MMI} = 553.4μm. The input and output access waveguide width was W_w = 2.6 μm. At this size, the modal phase errors were expected to be greatly reduced. The output waveguides were designed to taper down gradually from 2.6 to 0.5 μm for single mode operation.

Figure 6.1a provides a schematic illustration of the assembly process for fabricating double-layer silicon nanomembrane device platforms through transfer printing and patterning steps. Device fabrication started with commercially available SOI (Soitec) with a 3 μm buried oxide layer (BOx) and 250 nm silicon device layer. The fabrication of the first layer MMI coupler utilized electron beam lithography (EBL) and reactive-ion-etching (RIE) techniques described in the literature.[23] After etching of the silicon device layer, a SiO_2 film 1.5μm thick was deposited using plasma-enhanced chemical vapor deposition (PECVD) as the interlayer dielectric positioned between the bottom and top layer. Next, a thin layer (~500 nm) of photoactive epoxy adhesive (SU8) was spin-cast onto the silicon dioxide surface. Partial curing of the adhesive layer via heating and UV flood exposure (~100 mJ/cm^2) provided a flat, firm surface for mounting additional silicon nanomembranes as top layers.

The topmost silicon layers were derived from a SOI wafer which had been thermally oxidized to consume the top 70 nm or silicon. Nanomembrane structures were lithographically patterned on the SOI surface and dry etched into the thinned device layer. Heterogeneous

anchors, similar to those discussed in other portions of this thesis and in the literature,[24] were used to tether the nanomembranes during undercut release etch of the BOx in concentrated (49%) hydrofluoric acid for 19 hours. After release, nanomembranes measuring 2.05mm × 8.05mm × 230 nm were retrieved by a bulk piece of PDMS mounted to a rigid glass backing. Figure 6.1b shows a single silicon nanomembrane on the surface of the stamp after retrieval. The inked PDMS was brought into contact with the adhesive-bearing material stack using a custom alignment system with an integrated heating platform. While in contact, the stamp/nanomembrane/substrate system was heated to ~70˚C for 10 minutes to fully cure the adhesive. After curing, the stamp is slowly (~500 μm/s) retracted from the surface, transferring the aligned silicon nanomembrane to the material stack as the top device layer. Figure 6.1c shows a silicon nanomembrane printed onto multilayer stack without the first layer device patterning. A SiO_2 layer of 40 nm was deposited onto the stack using e-beam evaporation to serve as the hard mask for subsequent top layer silicon etching. The MMI coupler on the nanomembrane layer was fabricated using the same EBL and RIE process as the one on the bottom layer.

Figure 6.2a shows an optical microscope image of the fabricated double-layer MMI coupler fabricated via the print-and-pattern technique while Figure 6.2b provides a SEM view of the cross-section of an output waveguide. An automated aligner system was used to couple transverse electric (TE) polarized light at 1550 nm from a polarization maintaining lensed fiber (PMF) with a 2.5 μm output mode diameter into the waveguide inputs. An IR CCD camera connected to a variable objective lens captured the top-down near field images of the output waveguides' facets. A fanout design (Figure 6.2a) was used to increase the separation of each output waveguide to 30 μm to easily resolve the 12 output intensities for near field imaging.[23]

In order to separate the outputs in the bottom layer from those in the top layer, we etched the output waveguides of the top layer to terminate them well-ahead of the bottom layer waveguide terminals, as shown in Figure 6.2c. Figure 6.22d provides initial results from this device of simultaneous excitation of MMI couplers on both layers. Efforts are underway to characterize and optimize the device performance, and also assemble large numbers of stacked silicon nanomembranes and active layers into the device platform. As a proof-of-concept demonstration, Figure 6.3 shows different levels of nanomembrane stacks with either thin (~500 nm) epoxy layers (Figure 6.3a, b) separating the nanomembrane layers, or thick (~5.1 μm) photocurable polyurethane (NOA 61, Norland Optical Adhesive) (Figure 6.3c). Figure 6.3c shows the cross-section of an interesting 8-layer, manually aligned nanomembrane assembly.

6.3.2. Self-Aligned Structures

In some cases, interlayer alignment requirements are strict enough to require alternate multilayer assembly techniques than the print-and-pattern approach. In this case, a self-aligned process, in which all of the material layers are printed prior to patterning, can generate multilevel structures with minimal loss of registration. Figure 6.4 provides a schematic illustration of this self-aligned process for a two layer system. Here, this model system includes silicon nanomembranes, dielectric cladding and isolation layers, and metal layers for electrical contact. Initially, a silicon nanomembrane is transferred to a target substrate supporting a dielectric layer that can also serve as an adhesive for transfer. Application of a dielectric (waveguide cladding for first layer device) followed by deposition and patterning of metallic layers provide isolated thermo-optic heating pads and electrical interconnection points and completes the first material

stack for the bottom layer device. Similar stacks can be assembled through repeated processes to build subsequent device layers. After stacking, patterning of the top layer followed by etching or milling through all of the materials stacks can transfer the device structures to each layer in a self-aligned manner. This process flow is advantageous for relaxing overlay requirements for printing nanomembranes onto layers that have already undergone extensive fabrication and device definition.

The most challenging obstacle in this process flow is likely to be optimizing etch protocols for the variety of materials in the different layers. An alternative to etching involves focused ion beams (FIB) to mill patterns directly through the stacks.[25, 26] Since this process relies on physical sputtering of the material from the surface, it relaxes potential material-compatibility issues associated with etch chemistries. Figure 6.5a shows a model system incorporating layers of NOA, silicon, SU8 epoxy (~1 μm), and Cr/Au (5/100 nm) layers in one and two layer stacks. Here, the NOA separates the silicon nanomembranes from the substrate while the SU8 provides a dielectric between the silicon and metallic layers. Figure 6.5b shows SEM images of the two layer stack after partial etching with a focused ion beam (left panel Figure 6.5c). Cross-sections during this partial mill demonstrate that microscale features are easily patterned through the various layers without much damage to the surface. Figure 6.5c shows a cross-section of the waveguides after milling and polishing is complete in which the different material layers are visible in the approximately rectangular waveguide form. This process, with continued refining, can prove to be a valuable technique for realizing self-aligned, multilevel device structures. Finally, by utilizing advanced milling tools and techniques, complex, nanoscale geometries can be achieved, enabling new types of functional design to the multilevel format.[27]

6.4. Conclusions

In summary, we present two methods for fabricating multilevel stacked nanomembranes via transfer printing. These material formats can provide interesting platforms for device fabrication. An example of a novel vertical integration scheme for large photonic components on multilayers of low loss single crystalline silicon nanomembranes was demonstrated. We developed and demonstrated the patterning and printing processes for assembling double-layer photonic devices, and suggested integration pathways to even larger (areal and vertical dimensions) numbers of stacked nanomembrane based on repeated patterning and printing. We also demonstrated proof-of-concept principles for assembling different material layers into self-aligned geometries defined by traditional patterning and ion beam milling. These schemes represent a potential solution to limited silicon real estate for vertical integration of photonic devices, and also serves as platform for novel forms of integrated optical devices.

6.5. References

[1] F. Cavallo, M.G. Lagally, *Soft Matter* **2010**, *6*, 439.

[2] Z. Qiang, H. Yang, L. Chen, H. Pang, Z. Ma, W. Zhou, *Appl. Phys. Lett.* **2008**, *93*, 061106.

[3] M.M. Roberts, L.J. Klein, D.E. Savage, K.A. Slinker, M. Friesen, G. Celler, M.A. Eriksson, M.G. Lagally, *Nat. Mater.* **2006**, *5*, 388.

[4] L. Sun, G. Qin, J.-H. Seo, G.K. Celler, W. Zhou, Z. Ma, *Small* **2010**, *6*, 2553.

[5] H. Yang, H. Pan, Z. Qiang, Z. Ma, W. Zhou, *Electron. Letters* **2008**, *44*, 858.

[6] W. Zhou, Z. Ma, H. Yang, L. Chen, W. Yang, Z. Qiang, G. Qin, H. Pang, S. Chuwongin, D. Zhao, *Proc. of SPIE* **2010**, *7606*, 76060U-1.

[7] J. Viventi, D.-H. Kim, J.D. Moss, Y.-S. Kim, J.A. Blanco, N. Annetta, A. Hicks, J. Xiao, Y. Huang, D.J. Callans, J.A. Rogers, B. Litt, *Sci. Transl. Med.* **2010**, *2*, 24ra22.

[8] D.-H. Kim, N. Lu, R. Ghaffari, Y.-S. Kim, S.P. Lee, L. Xu, J. Wu, R.-H. Kim, J. Song, Z. liu, J. Viventi, B.d. Graff, B. Elolampi, M. Mansour, M.J. Slepian, S. Hwang, J.D. Moss, S.-M. Won, Y. Huang, B. Litt, J.A. Rogers, *Nat. Mater.* **2011**, *10*, 316.

[9] M.J. Slepian, R. Ghaffari, J.A. Rogers, *Interv. Cardiol.* **2011**, *3*, 417.

[10] D.-H. Kim, N. Lu, R. Ma, Y.-S. Kim, R.-H. Kim, S. Wang, J. Wu, S.M. Won, H. Tao, A. Islam, K.J. Yu, T.-I. Kim, R. Chowdhury, M. Ying, L. Xu, M. Li, H.-J. Chung, H. Keum, M. McCormick, P. Liu, Y.-W. Zhang, F.G. Omenetto, Y. Huang, T. Coleman, J.A. Rogers, *Science* **2011**, *333*, 838.
[11] D.-H. Kim, J. Viventi, J.J. Amsden, J. Xiao, L. Vigeland, Y.-S. Kim, J.A. Blanco, B. Panilaitis, E.S. Frechette, D. Contreras, D.L. Kaplan, F.G. Omenetto, Y. Huang, K.-C. Hwang, M.R. Zakin, B. Litt, J.A. Rogers, *Nat. Mater.* **2010**, *9*, 511.
[12] R.-H. Kim, D.-H. Kim, J. Xiao, B.H. Kim, S.-I. Park, B. Panilaitis, R. Ghaffari, J. Yao, M. Li, Z. Liu, V. Malyarchuk, D.G. Kim, A.-P. Le, R.G. Nuzzo, D.L. Kaplan, F.G. Omenetto, Y. Huang, Z. Kang, J.A. Rogers, *Nat. Mater.* **2010**, *9*, 929.
[13] J. Viventi, D.-H. Kim, L. Vigeland, E.S. Frechette, J.A. Blanco, Y.-S. Kim, A.E. Avrin, V.R. Tiruvadi, S.-W. Hwang, A.C. Vanleer, D.F. Wulsin, K. Davis, C.E. Gelber, L. Palmer, J.V.d. Spiegel, J. Wu, J. Xiao, Y. Huang, D. Contreras, J.A. Rogers, B. Litt, *Nat. Neurosci.* **2011**, *14*, 1599.
[14] J. Yoon, S. Jo, I.S. Chun, I. Jung, H.-S. Kim, M. Meitl, E. Menard, X. Li, J.J. Coleman, U. Paik, J.A. Rogers, *Nature* **2010**, *465*, 329.
[15] H.-C. Yuan, J. Shin, G. Qin, L. Sun, P. Bhattacharya, M.G. Lagally, G.K. Celler, Z. Ma, *Appl. Phys. Lett.* **2009**, *94*, 013102.
[16] W. Yang, H. Yang, G. Qin, Z. Ma, J. Berggren, M. Hammar, R. Soref, W. Zhou, *Appl. Phys. Lett.* **2010**, *96*, 121107.
[17] L. Chen, H. Yang, Z. Qiang, L. Sun, Z. Ma, J. Xu, R. Pate, A. Stiff-Roberts, G.J. Brown, W. Zhou, *Proc. of SPIE* **2010**, *7609*, 7609E-1.
[18] J.A. Kash, *OSA Photonics in Switching* **2007**, 55.
[19] K. Preston, S. Manipatruni, A. Gondarenko, C.B. Poitras, M. Lipson, *Opt. Express* **2009**, *17*, 5118.
[20] Q. Fang, J.F. Song, S.H. Tao, M.B. Yu, G.Q. Lo, D.L. Kwong, *Opt. Express* **2008**, *16*, 6425.
[21] M. Gnan, S. Thoms, D.S. Macintyre, R.M.D.L. Rue, M. Sorel, *Electonics Letters* **2008**, *44*, 115.
[22] A. Hosseini, D. Kwong, Y. Zjang, H. Subbaraman, X. Xu, R.T. Chen, *IEEE Journal of Selected Topics in Quantum Electronics* **2011**, *17*, 510.
[23] D. Kwong, Y. Zhang, A. Hosseini, Y. Liu, R.T. Chen, *Electonics Letters* **2010**, *46*, 1281.
[24] Y. Yang, Y. Hwang, H.A. Cho, J.-H. Song, S.-J. Park, J.A. Rogers, H.C. Ko, *Small* **2011**, *7*, 484.
[25] S. Reyntijens, R. Puers, *J. Micromech. Microeng.* **2001**, *11*, 287.
[26] T. Ishitani, T. Yaguchi, *Microscopy Research and Technique* **1998**, *35*, 320.
[27] D. Chanda, K. Shigeta, S. Gupta, T. can, A. Carlson, A. Mihi, A.J. Baca, G.R. Bogart, P. Braun, J.A. Rogers, *Nat. Nanotechnol.* **2011**, *6*, 402.

6.6. Figures

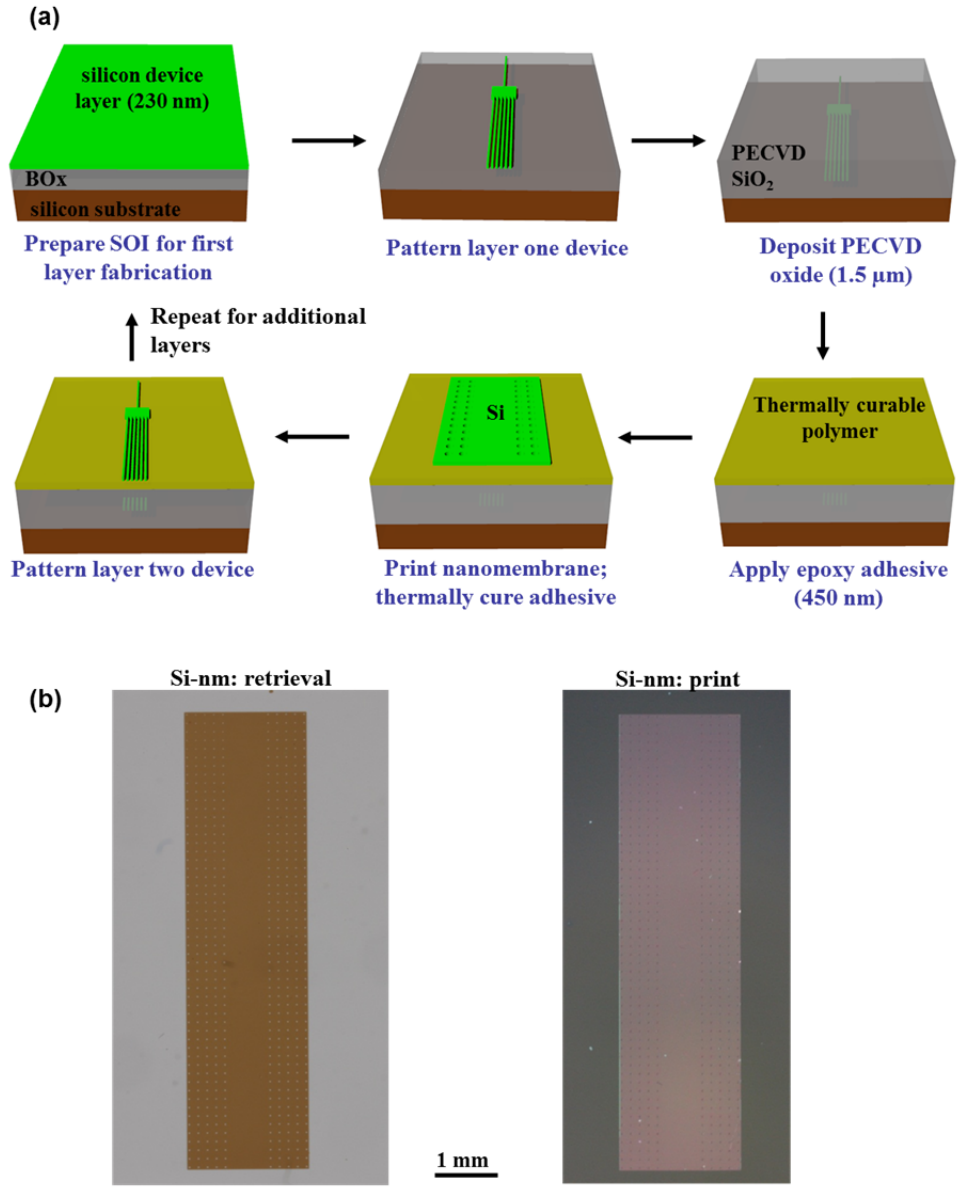

Figure 6.1. (a) Schematic process flow for assembling double-layer device using printed silicon nanomembranes for top layer devices. (b) Silicon nanomembrane on the stamp after retrieval and on the multilayer stack.

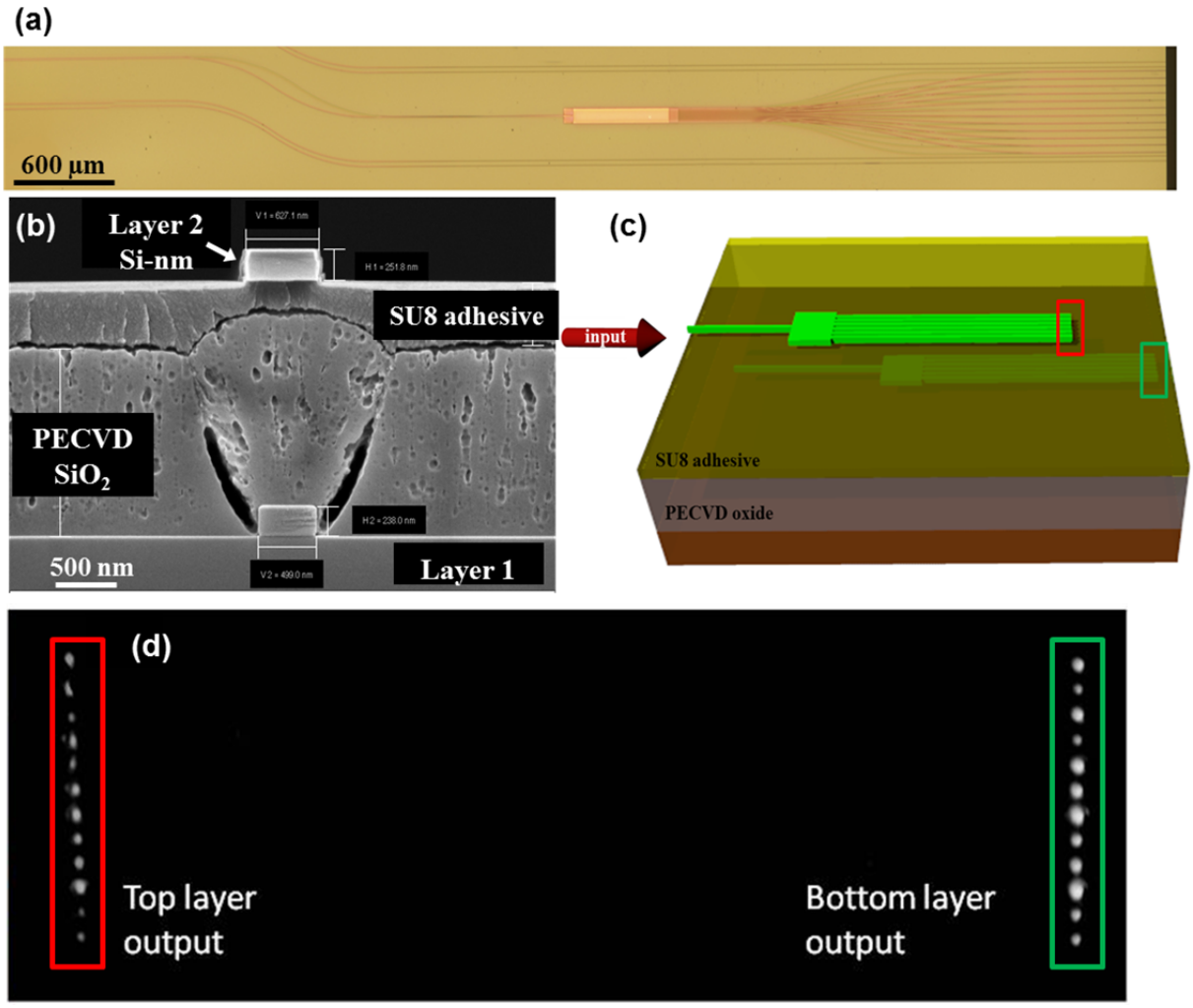

Figure 6.2. (a) A microscope image of the fabricated double-layer MMI coupler. (b) A SEM cross-section of an output waveguide. (c) A schematic showing separated outputs of bottom and top layers. (d) A top-down IR image of the two 1x12 MMI couplers with simultaneous excitation in both layers.

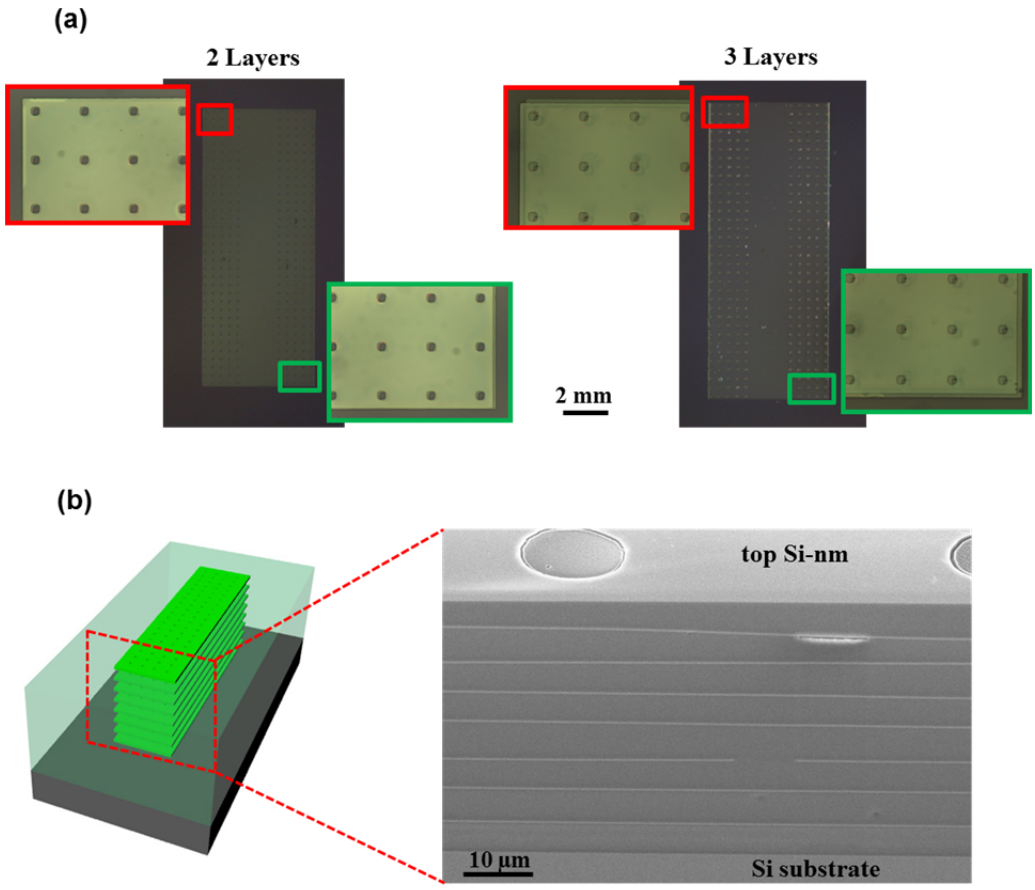

Figure 6.3. (a) Optical images of printed nanomembrane stacks using manual alignment (insets). (b) SEM cross-section and schematic of an eight alternating layers of silicon nanomembranes (250 nm thick) and polyurethane (5.1 µm thick) adhesive.

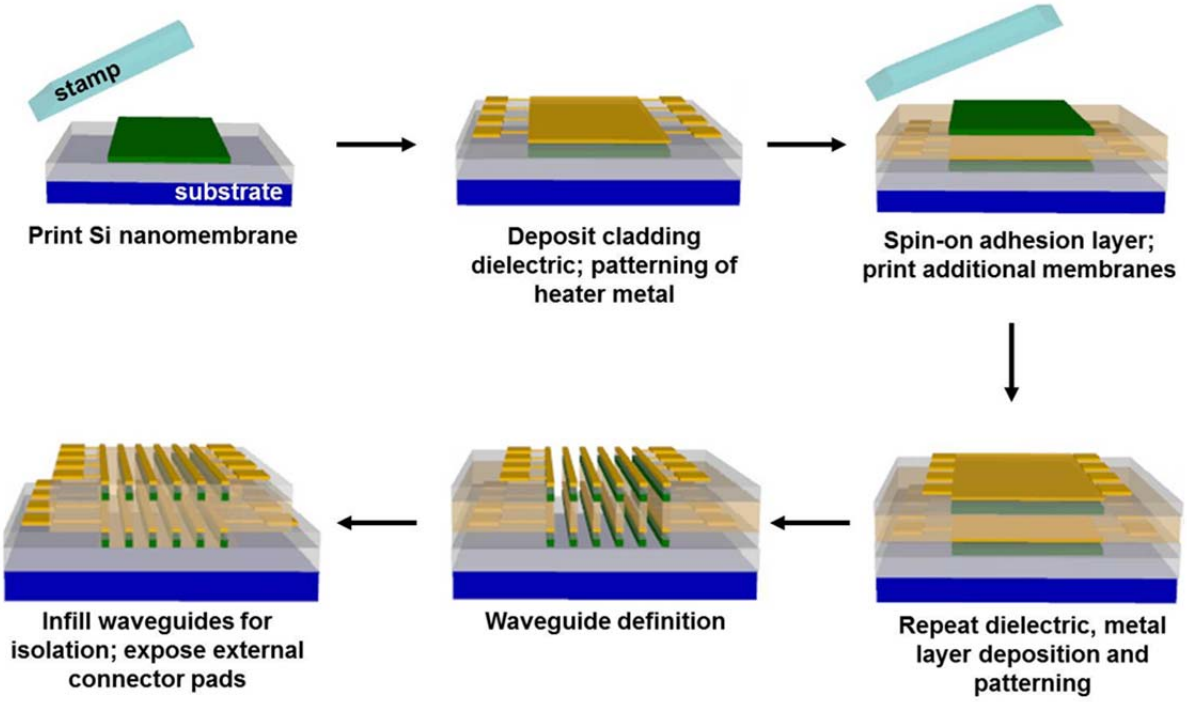

Figure 6.4. Schematic fabrication route for multilayer nanomembrane waveguides and devices. Repeated printing and metallization of the different layers followed by ion milling or dry etching to generate the waveguide structures creates self-aligned devices for high performance operation.

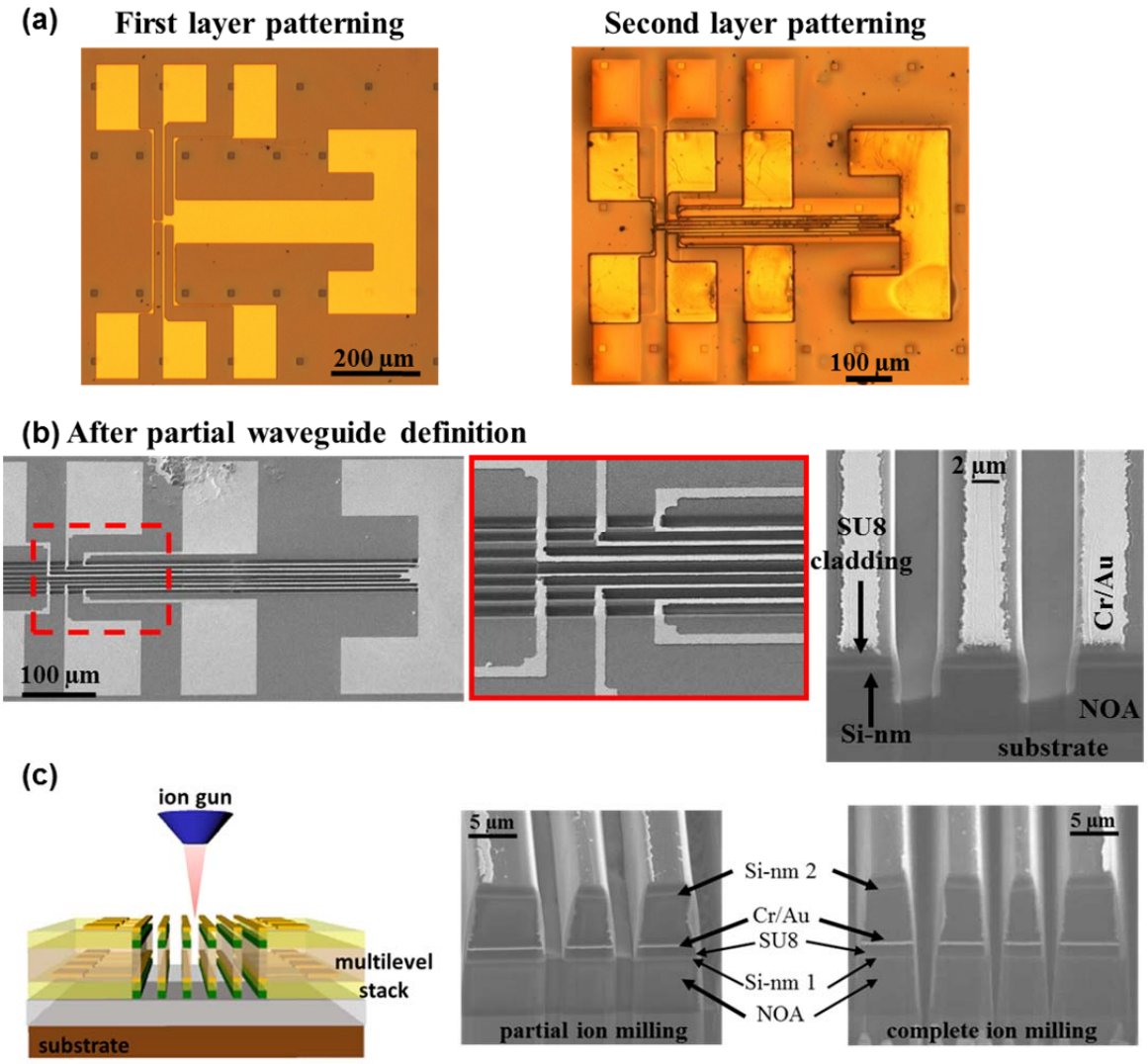

Figure 6.5. Proof-of-concept fabrication scheme for generating self-aligned multilayer stacks of materials for nanomembrane device platforms. (a) Optical images of a first and second layer device after nanomembrane printing and metallization. (b) Partial milling of the waveguide region for the two layer device shown in (a). The cross-section demonstrates the utility of ion milling for accessing deep layers in the stacks. (c) Schematic and cross-section of waveguides after milling through the stack layers. Small aperture polishing can be used to smooth out and shape the rectangular waveguide geometry.

APPENDIX A

ANALYTICAL AND FINITE ELEMENT MODELING FOR MICROSTRUCTURED ELASTOMERIC SURFACES WITH REVERSIBLE ADHESION[1]

A1. Introduction

This appendix provides additional analytical and finite element model methodologies for characterizing microtip stamps, as discussed in Chapter 3.

A2. Models

Contact radius at zero preload

The shape of microtips can be represented by a spherical portion near the tip and a conical portion in the cylindrical coordinates (r,z),

$$z = f(r) = \begin{cases} R_{microtip} - \sqrt{R_{microtip}^2 - r^2} & 0 \le r \le R_{microtip}\cos\dfrac{\theta}{2} \\ \dfrac{r}{\tan\dfrac{\theta}{2}} - R_{microtip}\left(\dfrac{1}{\sin\dfrac{\theta}{2}} - 1\right) & r > R_{microtip}\cos\dfrac{\theta}{2} \end{cases} . \quad \text{(A1)}$$

The contact mechanics model[1] relates the radius of contact $R_{contact}$ to the above shape function $f(r)$, work of adhesion γ, and plane-strain modulus $\overline{E}$ by

[1] Reprinted, with permission from S. Kim, J. Wu, A. Carlson, S.H. Jin, A. Kovalsky, P. Glass, Z. Liu, N. Ahmed, S.L. Elgan, W. Chen, P.M. Ferreira, M. Sitti, Y. Huang, J.A. Rogers, "Microstructured Elastomeric Surfaces with Reversible Adhesion and Examples of Their Use in Deterministic Assembly by Transfer Printing," *Proc. Natl. Acad. Sci. U.S.A.* **107**, 17095 (2010) Copyright: 2010 National Academy of Science.

$$\frac{\overline{E}R_{contact}}{2\pi}\left[\frac{\delta}{R_{contact}}-\int_0^{R_{contact}}\frac{f'(r)\,dr}{\sqrt{R_{contact}^2-r^2}}\right]^2=\gamma\,, \tag{A2}$$

where δ is related to the preload P by

$$P=2\overline{E}\int_0^{R_{contact}}\left[\delta-t\int_0^t\frac{f'(r)\,dr}{\sqrt{t^2-r^2}}\right]dt\,. \tag{A3}$$

For zero preload $P = 0$, δ is given by

$$\delta=\frac{1}{R_{contact}}\int_0^{R_{contact}}\sqrt{R_{contact}^2-r^2}\,f'(r)\,dr\,. \tag{A4}$$

Its substitution in Eq. (A2) gives the equation for $R_{contact}$

$$\frac{\overline{E}}{2\pi R_{contact}^3}\left[\int_0^{R_{contact}}\frac{r^2 f'(r)\,dr}{\sqrt{R_{contact}^2-r^2}}\right]^2=\gamma \tag{A5}$$

For the shape function in Eq. (A1), Eq. (A5) gives the following equation for the ratio of radii

$$\eta=\frac{R_{microtip}}{R_{contact}}\,,$$

$$\eta-\frac{\cos^{-1}\left(\eta\cos\frac{\theta}{2}\right)}{\tan\frac{\theta}{2}}-\eta\frac{\sqrt{1-\eta^2\cos^2\frac{\theta}{2}}}{\sin\frac{\theta}{2}}+\left(1+\eta^2\right)\ln\frac{\sqrt{1-\eta^2\cos^2\frac{\theta}{2}}+\eta\sin\frac{\theta}{2}}{1+\eta}+2\sqrt{\eta}\sqrt{\frac{2\pi\gamma}{\overline{E}R_{microtip}}}=0\,. \tag{A6}$$

This gives the implicit expression in Eq. (A1).

Equation (A6) holds only for contact between the microtips and platelet reaches the conical portion. This requires small microtip radius of curvature,

$$\frac{\overline{E}R_{microtip}}{\gamma}\le\frac{8\pi\cos^3\frac{\theta}{2}}{\left[\left(1+\cos^2\frac{\theta}{2}\right)\ln\left(\tan\frac{\theta}{4}\right)+\cos\frac{\theta}{2}\right]^2}\,. \tag{A7}$$

For microtip radius of curvature exceeding this critical value, the contact between the microtips and platelet remains in the spherical portion, and the corresponding contact radius has been obtained analytically.[1]

Finite element analysis of contact radius

The contact radii in Eqs. (A1) and (A2) are derived from classical models of contact mechanics,[1] originally developed for the case of a rigid indenter in contact with a soft material. Similar models can be applied to soft indenters in contact with hard materials. For example, Lim and Chaudhri[2] measured the indentation load-displacement curve for a conical indenter of soft rubber in contact with a hard, soda-lime glass. The Young's moduli of rubber (2.45 MPa) and glass (70 GPa) are comparable to those of PDMS (1.8 MPa) and silicon (130 GPa), respectively. Table A1.1 summarizes the geometry and elastic properties of the conical indenter with a round tip used in Lim and Chaudhri's experiments.[2]

Axisymmetric indentation problems were studied using the finite element method (FEM), which accounts for the geometric nonlinearity (large change of indenter shape) during indentation. We used axisymmetric elements for the rubber indenter, including the detailed geometry of the indenter tip. The element size was ~0.0345 mm, which is 7 times smaller than the indenter tip radius, and 150 times smaller than the maximum indenter radius. Refined meshes were used to ensure that the numerical results converge. The contact between the rubber indenter and the glass expands from an initial cone tip to a conical region as the indentation load increases. The finite sliding, hard contact model in ABAQUS[3] was used, to allow for the possibility of sliding between contact surfaces without interpenetration. The normal and shear stress were continuous within the contact process zone. The friction at the contact interface was

also accounted for, but it had negligible effect on the indentation load-displacement: the difference between frictionless contact and contact with a large friction coefficient was less than 0.2%. The results of the indentation load versus displacement indicate excellent agreement between FEM and experiments. This outcome validates the use of FEM for a soft indenter in contact with a hard material.

The same FEM techniques were used to model the experimental configuration described in Chapter 3. Table A1.2 summarizes the geometry and elastic properties of pyramid microtips of PDMS used in the experiments. Silicon served as the contacting substrate. The element size was ~1.5 nm, which is 70 times smaller than the indenter tip radius, and 7,000 times smaller than the maximum height of microtip. Figure A.1 shows the resulting force versus displacement curve on each microtip, and a comparison to the contact mechanics model (with cone angle 90^{o}))[1] specified in Eqs. (A2) and (A3), in which P and δ represent the indentation load and displacement, respectively. The numerical and analytical results agree well at small displacements, but begin to deviate as the displacement increases beyond a couple of microns. The present use of the contact mechanics model[1] involves the determination of contact area in the limit of extremely small displacements, associated with zero imposed compressive load. The results in Figure A.1 indicate that the model[1] is applicable in this regime.

A more direct validation of the contact mechanics model[1] is to use FEM to determine the contact radius for the experimental system. To accomplish this goal, we compressed the microtips into contact with the silicon, and then released the load completely, which delaminates the microtip/platelet interface, as simulated by the Cohesive Behavior Model in ABAQUS,[3] with a work of adhesion γ=155 mJ/m^2, which is consistent with the value reported in the main text. FEM gives a contact radius of 732 nm, which is slightly larger than 680 nm obtained from

Eq. (A2) based on the contact mechanics model.[1] Both values, however, agree, to within experimental uncertainties (~100 nm), with that determined from analysis of scanning electron microscope images (i.e. 750 nm).

Minimum height of microtips

Similar to [4], the minimum height corresponds to the critical state of vanishing preload at which the elastic energy in the stamp due to the collapse of the post equals the adhesion energy between the stamp and platelet. The latter equals the product of work of adhesion γ and contact area, while the former can be obtained using an approach based on fracture mechanics,[4] which accounts for the finite geometry of the stamp, such as the stamp width w_{stamp} and contact radius $R_{contact}$ between the microtips and platelet. The contact area is determined analytically by minimizing the total potential energy, which equals the elastic energy in the stamp subtracted by the adhesion energy. The minimum height of microtips is then obtained analytically as

$$h_{min} = \sqrt{\frac{w_{stamp}\gamma}{\overline{E}}\left[3.04\,ln\left(\frac{w_{stamp}}{R_{contact}}\right) - 4.44\right]}, \tag{A8}$$

where the factors 3.04 and 4.44 result from the stress intensity factor for finite geometry in fracture mechanics. The substitution of the asymptote in Eq. (A2) for $R_{contact}$ leads to the analytical expression in Eq. (A3).

Analysis of stamp collapse process

For the microtip height larger than h_{min} in Eq. (A3), the process of stamp collapse consists of 4 stages as the preload P increases, (i) microtip contact, during which only microtips contact

the platelet; (ii) post collapse, which corresponds to a sudden increase of contact area between the post and platelet; (iii) post contact, during which the contact area remains the same as the preload increases; and (iv) zipping of interface, which corresponds to the increase of contact area with the preload.

(i) microtip contact: The deformation in the microtips and post is studied by linear elasticity, where the microtips are subject to uniaxial compression, and the post is subject to the preload and reaction forces from the microtips.

(ii) post collapse: The analysis is similar to that for the minimum height, except that the total potential energy includes the external work of the preload. It gives following three equations to determine the ratio $c_{collapse}$ of contact area to stamp area at collapse, the corresponding critical load $P_{collapse}$, and the compressed height $h_{collapse}$ of microtips at collapse,

$$\begin{aligned}
&\frac{1}{F_1(b)}\left(\frac{h_{collapse}}{w_{stamp}}\right)^2 \frac{K\left(\frac{c_{collapse}}{b}\right)}{K\left[\sqrt{1-\left(\frac{c_{collapse}}{b}\right)^2}\right]} \\
&-\frac{h_{collapse}}{w_{stamp}}\frac{P_{collapse}}{w_{stamp}^2\bar{E}}\left[c_{collapse}+\left(\sqrt{2bc_{collapse}+2c_{collapse}^2}-2c_{collapse}\right)F_2\left(b-c_{collapse}\right)\right] \quad , \qquad \text{(A9)} \\
&+\frac{3h_{microtip}}{4w_{stamp}}(1-b)\left(\ln\frac{h_{collapse}}{h_{microtip}}\right)^2-\frac{4h_{microtip}}{3w_{stamp}}\frac{1}{1-b}\left(\frac{P_{collapse}}{w_{stamp}^2\bar{E}}\right)^2-\frac{2\gamma}{w_{stamp}\bar{E}}c_{collapse}=0
\end{aligned}$$

$$\frac{1}{F_1(b)}\left(\frac{h_{collapse}}{w_{stamp}}\right)^2 \frac{d}{dc}\left\{\frac{K(c/b)}{K\left[\sqrt{1-(c/b)^2}\right]}\right\}\Bigg|_{c=c_{collapse}}$$
$$-\frac{h_{collapse}}{w_{stamp}}\frac{P_{collapse}}{w_{stamp}^2\overline{E}}\left[\begin{array}{l}1+\left(\dfrac{b+2c_{collapse}}{\sqrt{2bc_{collapse}+2c_{collapse}^2}}-2\right)F_2\left(b-c_{collapse}\right)\\ -\left(\sqrt{2bc_{collapse}+2c_{collapse}^2}-2c_{collapse}\right)F_2'\left(b-c_{collapse}\right)\end{array}\right]-\frac{2\gamma}{w_{stamp}\overline{E}}=0 \quad , \quad \text{(A10)}$$

$$\frac{1}{F_1(b)}\frac{h_{collapse}^2}{w_{stamp}h_{microtip}}\frac{K\left(\dfrac{c_{collapse}}{b}\right)}{K\left[\sqrt{1-\left(\dfrac{c_{collapse}}{b}\right)^2}\right]}+\frac{3(1-b)}{4}\ln\frac{h_{collapse}}{h_{microtip}}$$
$$-\frac{h_{collapse}}{h_{microtip}}\frac{P_{collapse}}{w_{stamp}^2\overline{E}}\left[F_2\left(b-c_{collapse}\right)\left(\sqrt{2bc_{collapse}+2c_{collapse}^2}-2c_{collapse}\right)-1+c_{collapse}\right]=0 \quad , \quad \text{(A11)}$$

where $b=1-\dfrac{4w_{microtip}^2}{3w_{stamp}^2}$, $K(k)=\displaystyle\int_0^{\pi/2}\frac{d\varphi}{\sqrt{1-k^2\sin^2\varphi}}$ is the elliptical function of the first kind,

$F_1(k)=-0.417-1.07\ln(1-k)$, and $F_2(k)=\left(1-0.25k+0.093k^2-0.005k^3\right)\Big/\sqrt{1-0.5k}$.

(iii) post contact: The contact area is the same as that in (ii), but the energy release rate at the boundary of contact decreases as the preload increases. The compressed height h' of microtips decreases with the increase of preload, and is given by

$$\frac{1}{F_1(b)}\frac{h'^2}{w_{stamp}h_{microtip}}\frac{K\left(\dfrac{c_{collapse}}{b}\right)}{K\left[\sqrt{1-\left(\dfrac{c_{collapse}}{b}\right)^2}\right]}+\frac{3(1-b)}{4}\ln\frac{h'}{h_{microtip}}$$
$$-\frac{h'}{h_{microtip}}\frac{P}{w_{stamp}^2\overline{E}}\left[F_2\left(b-c_{collapse}\right)\left(\sqrt{2bc_{collapse}+2c_{collapse}^2}-2c_{collapse}\right)-1+c_{collapse}\right]=0 \quad . \quad \text{(A12)}$$

(iv) zipping of interface: The energy release rate at the boundary of contact reaches and remains at zero, and the contact area increases with the preload. The ratio c of contact area to stamp area increases with the preload, while the opposite holds for the compressed height h' of microtips, and they are given by

$$\begin{aligned}&\frac{1}{F_1(b)}\frac{h'^2}{w_{stamp}h_{microtip}}\frac{K\left(\frac{c}{b}\right)}{K\left[\sqrt{1-\left(\frac{c}{b}\right)^2}\right]}+\frac{3(1-b)}{4}\ln\frac{h'}{h_{microtip}} \\ &-\frac{h'}{h_{microtip}}\frac{P}{w_{stamp}^2\bar{E}}\left[F_2(b-c)\left(\sqrt{2bc+2c^2}-2c\right)-1+c\right]=0\end{aligned}, \tag{A13}$$

$$h'=F_1(b)\frac{P}{w_{stamp}\bar{E}}\left(1-\frac{c}{b}\right)\sqrt{\frac{c}{2}(b+c)}K\left[\sqrt{1-\left(\frac{c}{b}\right)^2}\right]F_2(b-c). \tag{A14}$$

This analysis gives the slope change in the preload-distance curve, maximum height of microtips, and restoring force in microtips.

Slope change in the preload-distance curve

The distance in Figure 3.4a before post collapse consists of the (compressive) displacements in microtips and in the post. The microtips are subject to uniaxial compression, while the post is modeled as a semi-infinite solid subject to remote compression and forces from the microtips on the surface. The ratio of preload to this distance gives the slope $k_{microtip}$

$$\frac{1}{k_{microtip}}=\frac{1}{w_{microtip}E}\left[\frac{3h_{microtip}}{4w_{microtip}}+\frac{1}{\pi}\left(\frac{w_{microtip}}{w_{stamp}}-\frac{2w_{microtip}^3}{w_{stamp}^3}\right)\ln\left(\frac{w_{stamp}^2}{2w_{microtip}^2}-1\right)\right]+\frac{h_{stamp}}{w_{stamp}^2E}, \tag{A15}$$

where h_{stamp} is the effective height of the stamp.

The change of distance in Figure 3.4a after post collapse also consists of contributions from the microtips and from the post, but the former becomes negligible as compared to the latter. The ratio of preload increment to distance increment gives the slope k_{post}

$$\frac{1}{k_{post}} = \frac{h_{stamp}}{w_{stamp}^2 E}. \tag{A16}$$

Eqs. (A15) and (A16) lead to Eq. (3.5).

Restoring force in microtips

The restoring force microtips is given by

$$F = P\left[\left(\sqrt{2bc+2c^2}-2c\right)F_2\left(b-c\right)-1+c\right]-\frac{w_{stamp}\overline{E}}{F_1(b)}\frac{K\left(\frac{c}{b}\right)}{K\left(\sqrt{1-\frac{c^2}{b^2}}\right)}h', \tag{A17}$$

where c and h' are determined from Eqs. (A9) to (A14) for stages (ii)-(iv).

Maximum height of microtips

The maximum height of microtips is determined by equating the energy release rate to the work of adhesion, which gives the following relation to determine c

$$\frac{\pi P^2}{4w_{stamp}^3\overline{E}}\left(b-c\right)\left[F_2\left(b-c\right)\right]^2 = \gamma. \tag{A18}$$

Eq. (A14) then gives explicitly h'. The maximum height of microtips, h_{max}, is then obtained from Eq. (A13) by replacing $h_{microtip}$ with h_{max}.

Figure 3.9c shows the maximum height of microtips, normalized by post width w_{stamp}, increases with the preload as well as the work of adhesion γ but decreases with the plane-strain modulus of the stamp. The maximum height for the material properties and post width in experiments is also shown. The experimental data for retrieval (below the curve) and failure (above the curve) agree well with the model.

Viscoelastic analysis

For operation in retrieval mode, the PDMS stamp is retracted sufficiently quickly to ensure that the platelet/substrate interface fractures, but the stamp/platelet interface does not, due to effects of viscoelastic behavior in the PDMS. The creep compliance of PDMS is an important material property that governs this process. This quantity, as measured by Xu et al.,[5] can be represented by a piece-wise relation

$$\frac{C(t)}{C(\infty)} = \begin{cases} 0.198 \times \left[6.14 + \log(t) \right] & 0.0001 < t < 0.08 \\ 1 & 0.08 < t \end{cases}, \tag{A19}$$

which is a non-decreasing function of time t (unit: second). The viscoelastic energy release rate G is related to the stress intensity factor $K(t)$ via the creep compliance by[6]

$$G = \frac{1}{2\bar{E}} \frac{C(t)}{C(\infty)} K^2(t), \tag{A20}$$

where $\bar{E}$ is the plane-strain modulus of PDMS, and the factor 1/2 accounts for the elastic mismatch between PDMS and silicon.[4] The stress intensity factor $K(t)$ is given by

$$K_I = \frac{\bar{E} h''}{F_1(b)} \sqrt{\frac{\pi}{2 w_{stamp} c \left[1 - \left(\frac{c}{b} \right)^2 \right]}} \frac{1}{K\left[\sqrt{1 - \left(\frac{c}{b} \right)^2} \right]} + \frac{P''}{2 w_{stamp}} \sqrt{\frac{\pi (b-c)}{w_{stamp}}} F_2(b-c), \tag{A21}$$

where w_{stamp} is the stamp width, b and functions F_1 , F_2 and K are defined after Eq. (A11), c is solved from Eqs. (A13) and (A14), P'' is the pull-off force, and the microtip height h'' is related to P'' by

$$\frac{1}{F_1(b)}\frac{h''^2}{w_{stamp}h_{microtip}}\frac{K\left(\frac{c}{b}\right)}{K\left[\sqrt{1-\left(\frac{c}{b}\right)^2}\right]}+\frac{3(1-b)}{4}\ln\frac{h''}{h_{microtip}} \quad , \tag{A22}$$
$$+\frac{h''}{h_{microtip}}\frac{P''}{w_{stamp}^2\overline{E}}\left[F_2(b-c)\left(\sqrt{2bc+2c^2}-2c\right)-1+c\right]=0$$

which is identical to Eq. (A13) except that P and h' are replaced by $-P''$ and h'', respectively.

The pull-off force is related to the pulling speed $v_{pulling}$ and time t by

$$P'' = w_{stamp}E\left(v_{pulling}t - L_{compression}\right), \tag{A23}$$

after the compression force P is relaxed, where $L_{compression}$ is the compressed distance of the stamp due to P, and $L_{compression}$ = 20 μm.

The stamp/platelet interface will not delaminate if the viscoelastic energy release rate remains smaller than the work of adhesion γ, i.e.,

$$G < \gamma . \tag{A24}$$

For the material properties given in Chapter 3, the creep compliance in Eq. (A19), and pulling speed $v_{pulling}$ = 460 μm/s, the above inequality gives a critical time of 0.052 seconds for the stamp/platelet interface starting to debond. The pull-off force is then obtained from Eq. (A23).

A3. References

[1] D. Maugis, *Langmuir* **1995**, *11*, 679.
[2] Y.Y. Lim, M.M. Chaudhri, *Philos. Mag.* **2003**, *83*, 3427.
[3] *Abaqus analysis user's manual*: USA.
[4] Y.Y. Huang, W. Zhou, K.J. Hsia, E. Menard, J.-U. Park, J.A. Rogers, A.G. Alleyne, *Langmuir* **2005**, *21*, 8058.
[5] Z. Xu, K. Kim, Q. Zou, P. Shrotriya, *Appl. Phys. Lett.* **2008**, *93*, 133103.
[6] R.A. Schapery, *Int. J. Fracture* **1975**, *11*, 369.

A4. Tables

Cone angle	Maximum radius	Tip radius	Young's modulus	Poisson's ratio
60 degree	5 mm	0.23 mm	2.45 MPa	0.4999999

Table A1.1. Geometry and elastic properties of the rubber indenter

Pyramid angle	Maximum height	Tip radius	Young's modulus	Poisson's ratio
90 degree	10.6 μm	100 nm	1.8 MPa	0.48

Table A1.2. Geometry and elastic properties of PDMS microtips

A5. Figures

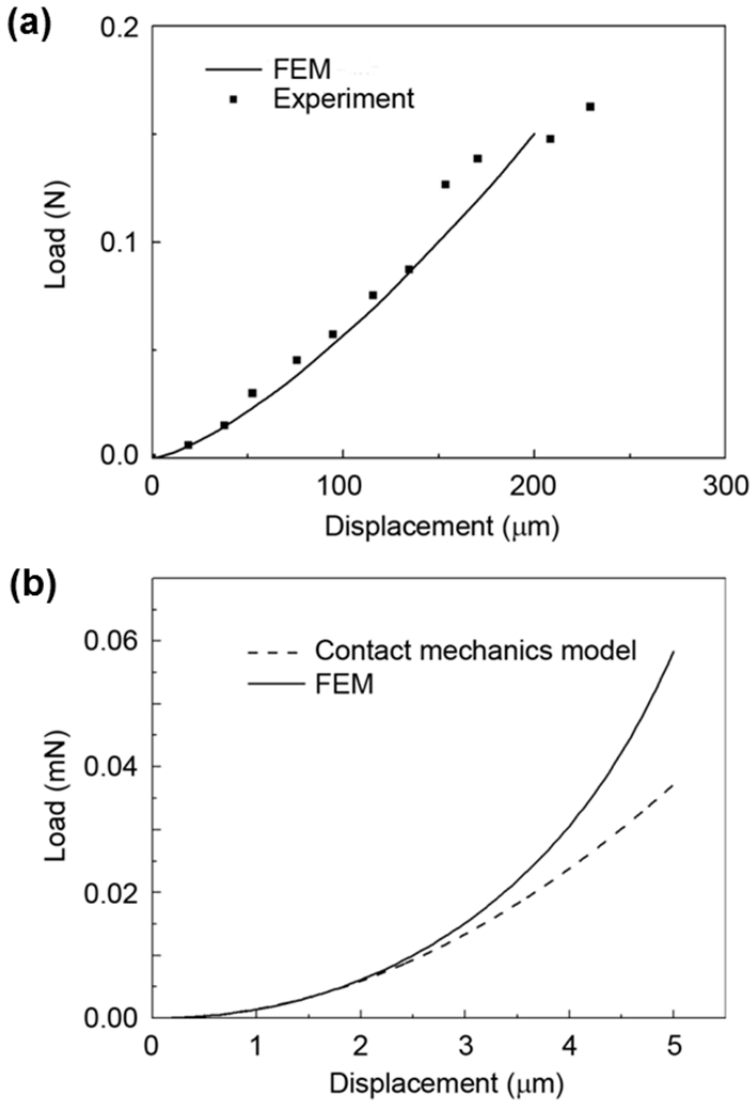

Figure A.1. (a) Load-displacement comparison between FEM results and experimental data for the case of the system of Lim and Chaudhri. (b) Load-displacement comparison between FEM results and contact mechanics model for a PDMS microtip pressed against a silicon substrate.

APPENDIX B

TRANSFER PRINTING TECHNIQUES FOR MATERIALS ASSEMBLY AND MICRO/NANODEVICE FABRICATION[1]

B1. Introduction

This Review addresses the current literature and recent developments in transfer printing, a potentially transformational approach to materials assembly and micro-/nanofabrication with far-ranging fields of use. At the heart of the method is the use of highly parallel protocols to print 'inks', here defined as a diversity of material classes with a wide range of geometries and configurations having broadly adaptable levels of functional integration, into the precise architectures required by devices. Recent rapid progress in the field has expanded the competencies of transfer printing, in terms of both the range of materials for patterning and scope of applications enabled. Inspired by the scalability and cost advantage of various forms of commercial printing and soft lithography, transfer printing has evolved into an exceptionally sophisticated approach to materials assembly and device fabrication. As the content of this Review will illustrate, essentially any class of material can be developed in the form of an ink appropriate for transfer printing-based fabrication schemes – from complex molecular scale materials (self-assembled monolayers (SAMs),[1-4] nanotubes and graphene,[5-8] functional polymers,[9-11] DNA,[12-14] photoresists,[15] etc.), to high performance hard materials (single-crystalline inorganic semiconductors,[16-20] metals,[21-24] oxide thin films,[25, 26] etc.), to fully integrated device structures (thin film transistors (TFTs),[16, 27-30] light emitting diodes (LEDs),[31, 32] complementary metal oxide semiconductor (CMOS) circuits,[33-35] sensing arrays,[36, 37] solar cells,[38, 39] etc.). Elegant demonstrations of unique material constructs

[1] Reprinted, with permission from A. Carlson, A.M. Bowen, Y. Huang, R. G. Nuzzo, J. A. Rogers, "Transfer Printing Techniques for Materials Assembly and Micro/Nanodevice Fabrication,"*submitted*.

and devices created by advanced forms of transfer printing appear in Figures B.1a-f. These examples illustrate functional integration of some of the materials and geometries discussed in detail throughout this Review and demonstrate how the myriad capabilities inherent to transfer printing can enable new fabrication routes such as multidimensional assembly (Figure B.1a),[40] large-area deployment of nanostructured materials (Figure B.1b),[41] and manufacture of passive (Figure B.1c-d)[42, 43] and active (Figure B.1e-f)[44-46] devices in lightweight, flexible, and curvilinear formats.

The printing protocols discussed in this Review directly address the adaptation of a wide range of material classes - in many cases, the highest performance materials known for specific applications - to challenging and unusual environments. Figure B.2 shows three distinct categories of transfer: *additive transfer*, *subtractive transfer*, and *deterministic assembly*; all printing techniques discussed in the following utilize one or more these methods. The third protocol is particularly powerful, due to its natural compatibility with high performance, single crystalline semiconductor materials (such as Si, GaAs, GaN, InP, etc.)[16, 18, 20, 47, 48] in micro- or nanostructured forms. Transfer printing such materials with a soft, elastomeric stamp enables their deterministic assembly onto nearly any type of substrate, at room temperature, with high yields and accurately registered placement, in rapid, parallel fashion. When repeated, this process provides a high resolution large-area assembly technique, with capabilities in two or three dimensional layouts and in heterogeneous levels of materials integration, all of which lie beyond the competency of any other method.[1, 3, 4]

In all three methods of Figure B.2 a molded stamp, or one whose surface chemistry is adjusted in a patterned way to control adhesion, affects physical mass transfer between two intrinsically different substrates. The first two have the additional feature that the stamp itself

plays a critical role in the structuring of relevant materials into forms with desired lateral geometries. We refer to the first case (Figure B.2a) as *additive transfer*, an effective modality for manipulating many types of organic and inorganic materials,[49-58] in which transfer occurs between an entire ink layer, or selected parts of it, that have been deposited on the surface of a stamp, and a receiving substrate. Inking of the stamp can be achieved through a variety of methods, from solution casting to physical vapor deposition, as discussed throughout the sections of this Review.[15, 59-61] Layers printed by additive techniques can provide a variety of functions, such as forming integrated device components or serving as etch masks for subsequent processing.[32, 62-64]

The second method, *subtractive transfer*, shown schematically in Figure B.2b, utilizes a stamp to selectively retrieve regions of a blanket film. This printing modality can be used to directly pattern an active layer or to open windows in etch masks, allowing access to underlying layers of materials for subsequent processing.[65, 66] As in the case of additive printing, chemical modification of the receiver, heat, and thin intermediate polymeric adhesion promoting layers between the stamp and ink can aid the transfer.[66, 67] Unlike additive printing, this mode requires cohesive fracture of the ink layer and, therefore, an additional set of considerations in engineering design. In some instances, *subtractive transfer* represents the inking step for the *additive transfer* process. Such methods, or more conventional processing or growth techniques, can form defined structures on a donor substrate, for use in *deterministic assembly* techniques, shown in Figure B.2c. This strategy is valuable, in part, because it dramatically expands the materials possibilities in fabrication by separating growth and processing of the inks from the stamp and the receiving substrate. These methods often rely on

a dynamic, reversible modulation of adhesion forces to the stamp, using techniques described in the next section.

A key advantage of the procedures outlined in Figure B.2 is that they enable rapid delivery of materials in sparse or dense layouts over large substrate areas, specifically via multiple stamp inking and printing cycles. Several variants of sequential inking and printing can be used: in the first method, delineated ink structures on a donor wafer can be translated directly to a receiver, either by use of a stamp with a flat surface or one in which the surface relief pattern is directly matched to the format of the donor ink. Final layouts for the donor are determined during processing of the ink and can exploit precise positioning and size control available to the lithographic fabrication steps used to construct the ink.[68, 69] A second method utilizes molded reliefs on a stamp to determine pitch, layout, and critical dimensions of the printed inks, independent of the configuration on the donor substrate. Figures B.3a-c demonstrate a case of area expansion in which densely packed thin plates of compound semiconductor (here in the form of epitaxial stacks of materials designed for light emitting diodes) on the donor are selectively retrieved with a microstructured stamp and printed, with expanded pitch, across a sparsely populated area on the target.[31] Printing in this manner enables transformation of the donor wafer geometry upon translation to the receiver, as demonstrated in Figures B.3b-c where the pitch of the inks is expanded by ~7 times from the donor to the target array. This capability has several advantages, including efficient use of ink materials, precise control of ink spacing and density, and access to final layouts that are not restricted by the substrate size limitations of traditional lithography tools. Figures B.3d-e show optical images of small 250 μm x 250 μm x 2.5 μm plates sparsely assembled over transparent substrates. Figure B.3d presents an image of ~1600 such structures printed onto a plastic sheet that is subsequently wrapped around a glass

cylinder. Figure B.3e illustrates the same type of devices printed onto a glass substrate that rests above a sheet of paper with lettering and logos to demonstrate transparency and relative size scales.[31]

Some of the diverse materials classes, geometries, and printing modalities that have been reported in the literature over the last 15 years appear in Table B.1 along with the general chemical or surface modification techniques adopted to facilitate printing. The following sections of this Review summarize recent progress, organized according to the materials classes of the inks, and beginning with the two -- inorganic semiconductors and metals -- that have been demonstrated at the highest levels of engineering sophistication. A concluding section outlines some of the most promising device and system-level applications, along with needs and opportunities to expand the scope of capabilities and modes of use. We start, however, with some general considerations related to the mechanics and materials aspects of the transfer process itself.

B2. Materials Science and Mechanics of Transfer Printing

Effective transfer, using any of the three modes of Figure B.2, relies, fundamentally, on control of adhesion and fracture mechanics at the critical interfaces between the ink/donor, the ink/stamp and the ink/receiver. A first consideration is the chemistry and generalized adhesion forces at these interfaces. In a broad sense, the only interface that should bond permanently is the one between the ink and the receiver substrates; all others should be reversible and, preferably, switchable in a passive or active mode. For *subtractive transfer* and *deterministic assembly*, release at the interface between the ink/donor must occur. This release can involve cohesive fracture in the ink, in some other class of material that temporarily bonds the ink to the

donor, or between the ink and the donor itself. In most cases, this ink/donor interface can be engineered to enable release onto unmodified surfaces of elastomeric stamps that are capable of soft, conformal contact, via the action of van der Waals or related forces. The delivery part of the printing process requires a difference in work of adhesion between the stamp/ink and ink/receiver.

Physical effects in the stamps can strongly enhance the efficiency of transfer, in a way that can complement strategies based on interfacial materials designs. One powerful and widely used such strategy exploits rate-dependent effects with viscoelastic stamps, such as those made of poly(dimethylsiloxane) (PDMS).[16, 18-20, 25, 27, 28, 30, 38, 47, 68-77] Here, the velocity of separation of the stamp from a surface influences the adhesive strength, with higher velocities yielding proportionally larger adhesion.[47] Ink retrieval and delivery can, therefore, occur efficiently at velocities on the order of 10 cm/s or greater and a few mm/s or less, respectively.[47] This process can be modeled as the initiation and propagation of interfacial cracks,[70, 78] with each interface providing a competing fracture pathway that has a characteristic steady-state energy release rate G defined as:

$$G = \frac{F}{w} \tag{B1}$$

where F is the force applied to the stamp in the normal direction and w is the stamp width. While G is a measure of the interfacial adhesive strength between the stamp and its contacting substrate, it differs from the work of adhesion described earlier since it accounts for both interfacial bond breaking and viscoelastic energy dissipation surrounding the crack tip. [47, 79-82] Separation at either the stamp/ink or ink/substrate interface corresponds to a critical value of the energy release rates, $G_c^{stamp/ink}$ and $G_c^{ink/sub}$, respectively and comparison of these values provides criteria for predicting retrieval or printing:[65]

$$G_c^{stamp/ink} < G_c^{ink/sub} \quad \text{for printing} \tag{B2a}$$

$$G_c^{stamp/ink} > G_c^{ink/sub} \quad \text{for retrieval} \tag{B2b}$$

The elastic nature of both the rigid ink and substrate implies that $G_c^{ink/sub}$ is constant, to first approximation, with no dependence of interfacial strength on velocity. By contrast, the viscoelasticity of the stamp leads to a velocity dependent $G_c^{stamp/ink}$, i.e. $G_c^{stamp/ink} = G_c^{stamp/ink}(v)$.[70, 79-82] At a critical velocity v_c, the energy release rates for both interfaces are equal, leading to the condition:

$$G_c^{stamp/ink}(v) = G_c^{ink/sub} \tag{B3}$$

marking the transition from a retrieval to printing regime, as shown in Figure B.4a. A general power-law relationship fits the rate-dependence, according to (B4):

$$G_c^{stamp/ink}(v) = G_0[1 + (\tfrac{v}{v_0})^n] \tag{B4}$$

where G_0 is the zero-velocity energy release rate similar to a fatigue limit fracture energy, v is the separation velocity, v_o a reference velocity associated with G_0, and n the scaling parameter.[47, 70, 83] Rearranging equation (B.4) provides an analytical expression for the critical separation velocity:

$$v_c = v_0[\frac{G_c^{stamp/ink} - G_0}{G_0}]^{1/n} \tag{B5}$$

Kinetically controlled printing can be influenced by ambient environment, such as temperature, or by selection of elastomer materials for the stamps.[70] The structure of the stamp (e.g. contact area) and the nature of loading forces (e.g. shear, in addition to normal) can also be important. As an example of the former, PDMS stamps with pyramidal microtips at the corners of the contacting regions can be designed to allow reversible, pressure-controlled contact

areas, and therefore adhesion strength.[40] Figure B.4b shows scanning electron microscope (SEM) images of such a stamp, in high and low adhesion states (ON and OFF, respectively) against a platelet of silicon as the ink. Quantitative measurements reveal the capabilities of this approach to switching adhesion, particularly when combined with the viscoelastic effects described above (Figure B.4b).[40] Similar types of operation are possible with other schemes, including shear loading and various bio-inspired surface structures. For the case of shear-assisted transfer, targeted loading of a microstructured PDMS stamp can induce strong interfacial moments between the stamp surface and a rigid ink (e.g. a silicon platelet) that locally weakens stamp adhesion around the molded surface relief. Increasing shear strains in the stamp can effectively modulate the total stamp adhesive strength to negligible levels, enabling efficient delivery of inks into a variety of configurations.[84] As for the case of stamps with surface microtips, shear transfer can be coupled with rate-dependent printing modalities to enhance the various printing protocols discussed in Figure B.2, particularly *deterministic assembly*.

B3. Inorganic Semiconductors

In many functional devices, the semiconductor represents often the most enabling, and challenging, material. Performance is generally highest with high purity, single crystalline inorganic materials. When implemented with micro- and nanostructures of such classes of semiconductors, *deterministic assembly* (Figure B.2) provides a simple, yet powerful pathway to useful system or device configurations that cannot be achieved through any other technique. A recent, promising direction involves advanced electronic materials grown and processed on a substrate and then transferred over large areas in step-and-repeat type processes,[47, 85] (Figure B.3), while preserving spatial orientation and electronic properties, to yield integrated circuits on

sheets of plastic or slabs of rubber. This strategy bypasses the standard requirement that materials which comprise the circuit must be compatible with all of the processes used in integrated fabrication.[4, 30] While a wide variety of methods exist for forming inorganic semiconducting inks,[18, 20] this Review focuses mainly on techniques for transfer printing such structures, with a focus on single-crystalline materials, organized according to their structural forms.

B3.1. Nanomembranes, nanoribbons, platelets and bars

The earliest reports of transfer printing of inorganic semiconductors used structures of silicon with thicknesses ranging from a few nm's to a few tens of microns and lateral dimensions between tens of nm's and mm's, derived from silicon-on-insulator (SOI) donor wafers and referred to originally as microstructured silicon (μs-Si). Fabrication involves anisotropic wet chemical etching, or dry etching, of selected exposed regions of the top layer silicon, and then undercut removal of the buried oxide with hydrofluoric acid to release silicon structures[16, 27, 30, 86, 87] in the various geometries and sizes, most commonly nanoribbons/nanomembranes (NMs) or microbars/plates, optimized for incorporation into transistors and solar cells, respectively. Van der Waals forces tether the silicon structures to the underlying wafer, in their lithographically defined locations, for use in the *deterministic assembly* process of Figure B.2. Comparative literature analysis indicates that stamp-mediated transfers of this type provide much greater degrees of alignment and placement control than is possible with other printing or assembly techniques based on solution casting.[16, 17, 59] Recent research advances have greatly increased the sophistication of silicon ink geometries, with an example in Figure B.5a.[16] While silicon can be created in this manner easily, the high cost of SOI might represent a

disadvantage for certain applications. Newer processing schemes allow the fabrication directly from low cost bulk silicon wafers.[28, 68, 73] These procedures, when repetitively applied, can efficiently utilize material through the entire thickness of the wafer.[28, 68] A single wafer can yield large quantities of μs-Si, as much as several hundred square feet of Si ribbons from 1 ft^2 of starting material.[28, 73]

A significant additional advancement in design involves the use of anchoring schemes that retain precise spatial layouts of the undercut μs-Si prior to and during transfer, with levels of control that cannot be achieved with the original schemes based on van der Waals adhesion.[88] In addition to holding the inks in place, anchors must fracture easily during delamination of the stamp. Early generations of such anchors consisted of vertical columns of buried oxide designed to remain after undercutting an SOI wafer.[18, 20, 30, 69, 89] The vertical loads associated with stamp contact can fracture such anchors, to facilitate effective retrieval.[89] One disadvantage of this design is that small oxide particulates can remain on the μs-Si after anchor fracture; in many cases, their removal requires an additional HF etching step.[89] Optimized designs feature anchors that lie in the plane of the device and are significantly easier to fabricate and refine.[29] These anchors may consist of the same material as the ink ('homogeneous' anchors)[88], as shown in images of Figure B.5a,b collected before and after printing. In other cases, anchors of a distinct material ('heterogeneous' anchors), such as the photoresist posts highlighted in Figure B.5c, can be used.[31, 90] The colorized SEM of Figure B.5c demonstrates a version of these anchors in a "diving board" configuration where support is provided only on one side of the ink. Figure B.5d, e show another type of heterogeneous photoresist anchors, referred to as perimeter pedestals, which exist underneath the ink layer around its periphery.[90] These anchors are sufficiently strong to withstand undercut etching, but can be significantly easier to fracture than

homogeneous anchors, thereby facilitating retrieval. Additionally, from the standpoint of materials utilization, such schemes provide pathways for highly efficient use of the ink, through formation of dense arrays of structures. Figure B.5c presents one such layout, from which selected layers are retrieved as in Figure B.3a.

As discussed in Section 2, printing depends on exploiting the differential adhesion developed between the ink/stamp interface and the ink/substrate interface through chemical and/or dynamic mechanisms. As an example of the first possibility, hydroxyl groups formed on the μs-Si surface and an oxide-bearing layer on the receiving substrate can lead to –Si-O-Si bonds at the interface, upon contact.[56, 91-94] Alternatively, a separate adhesive layer can be used. Partially cured polymers such as photodefinable epoxies (SU-8),[30] polyimide (PI),[27, 71] or benzocyclobutene (BCB)[34] can flow around the μs-Si edges and, when cured, create strong bonding forces that promote efficient transfer, in a way that simultaneously planarizes the top surface to facilitate the formation of electrical interconnects, for example. The adhesive can also serve as an integrated component (e.g. as a gate dielectric), although with modest performance compared to that possible with dielectrics, such as thermal oxide, grown directly on the silicon.[30] For demanding applications, devices (such as silicon transistors) can be fabricated in their entirety prior to release from the donor wafer onto the stamp.[16, 27, 28, 30, 69] Integrated circuits printed in this way perform extremely well[34, 71] and will be discussed in subsequent sections of this Review. Similar classes of materials and devices can be printed directly, using the donor wafer itself as the stamp, as demonstrated in both strained[95-97] and unstrained silicon NMs.[98] The use of the wafer is convenient, but brings some disadvantages – it is generally opaque, rigid and difficult to handle in the context of an automated tool, and is not easily implemented in a step and repeat mode – compared to stamp-based approaches.

Nevertheless, the simplicity of this method makes it useful for research purposes, in devices such as thin film transistors[97] and ultracompact Fano filters[98, 99].

Many other semiconductors can be processed as inks in a conceptually similar manner to the examples of silicon provided above.[17, 19, 29, 48, 72, 74, 75, 100] Demonstrated cases include III-V materials, such as single-crystalline GaAs, GaN and InP, of interest due to their high electron mobilities, high saturated drift velocities, direct band gaps, and tolerance to a large range of operation and process temperatures.[75] Complex and diverse forms of compound semiconductor inks (e.g. GaAs and InP nanowires and nanoribbons)[74, 75, 100] can be produced from wafers using processes comparable to those described for the fabrication of silicon micro/nanostructures from bulk Si wafers. An example is the fabrication of the GaAs (or InP) nanowires/ribbons by anisotropic chemical etching. Newer approaches exploit more conventional forms of wafer level fabrication in conjunction with heterogeneous anchors[31] and sacrificial epitaxial layers that can be selectively removed by undercut etching, to yield compound semiconductor inks.[31, 88, 101] In an alternative approach, sheets or platelets of AlGaN/GaN (used to fabricate HEMTs)[29] or GaN/AlN grown on bulk silicon wafers with (111) orientation can be released by anisotropic undercut etching of the Si[17]. Many classes of devices, from photodetectors,[35, 101] to light emitting diodes,[31]solar cells[101] and transistors[35] are possible, in which formation of ohmic contacts can be accomplished on the donor wafer prior to retrieval, again separating the required high temperature processes from the temperature sensitive plastic substrates. Large area coverage can be achieved through multiple inking and printing steps.[19, 48, 72]

Related protocols can affect heterogeneous and/or three dimensional integration by fabricating semiconductor inks from multiple types of wafers and then repeating the described

printing process.[35, 102] In certain such cases, the electrical/optical/thermal properties of the interfaces between the different materials and/or the receiving substrate can be important. Although surface modifications and/or adhesives can be effective for transfer, they often alter, in unwanted ways, these critical interface characteristics. For these situations, completely adhesiveless schemes for *deterministic assembly*, such as those described in Section 2, are important. For structures that are not easily printed via practically achievable speeds, automated transfer printing tools can be employed. Such toolsets allow finer optimization of the strain-rate dependent adhesion than can be accomplished by hand, as well as more accurate placement of printed objects. Examples of the capabilities of such tools are discussed briefly in Section 10.5.

Other approaches to printing of inorganic semiconductors exploit *subtractive transfer* techniques. One example, based on nanocontact electrification, utilizes the charged surface of a structured PDMS stamp to remove layers of silicon (up to 5 mm lateral dimensions) from a patterned donor substrate.[103] Levels of surface charge on the PDMS are precisely maintained through plasma activation and soaking in either acidic or basic solutions to form protonated or deprotonated surfaces while control over the stamp surface relief ensures only selected regions of silicon would be subtractively removed. In an advanced form of this technique, patterned silicon retrieved with charged PMDS could be subsequently transferred to other stamps, provided the new stamps have higher charge density.[103] The ability to manipulate the silicon ink only via surface charge could provide a complementary route to material assembly to the strategies described in Figure B.2.

Another interesting example of *subtractive transfer*, referred to as dry-removal soft lithography,[104-106] uses a PDMS stamp to retrieve porous silicon microstructures from a bulk donor wafer. Pressing a stamp into contact and then peeling it away retrieves silicon, in its

porous form, in isolated features on the raised regions of relief on the stamp. A transparent hydrophobic polymer poly[(vinyl butyral)-*co*-(vinyl alcohol)-*co*-(vinyl acetate)] (PVB) can be drop cast, cured, and then peeled off of the stamp, to remove the silicon structures. The optical properties of the porous silicon surface are unharmed by this process, and the transferred materials can be further integrated into a variety of optical devices.[107-110] One demonstration used the porous Si as a freestanding Bragg mirror[110-115] supported on a transparent polymeric substrate. Similar patterning schemes can produce arrays of porous silicon photonic crystals and free-standing thin porous silicon sheet micro-hole arrays.[105, 114, 115]

B3.2. Nanowires

One-dimensional inorganic semiconductors, i.e. nanowires, offer an interesting collection of electronic and optoelectronic properties that also enable the fabrication of useful devices embedding design rules down to the molecular scale. The availability of techniques to manipulate the size, structure, composition, and morphology of such nanowires makes them useful as building blocks for various applications in the fields of electronics,[116-118] photonics,[119, 120] sensors,[121-123] and energy conversion (specifically battery electrodes and heterojunctions in photovoltaics).[124] Although top-down approaches such as those described in the previous section can provide access to such materials, some of the most widely explored methods rely on synthetic growth techniques. Integration into devices can occur directly through precise control over size and position of the resulting nanowires, in their as-grown configurations. An alternative involves separate steps of synthesis followed by organized assembly. The first option can be addressed, to some extent, with approaches that use CVD growth from ordered catalyst arrays[125-127] fabricated by such techniques as AFM lithography,

electron-beam lithography, nanosphere lithography, nanoimprint lithography, self-assembled templates.[128, 129] The conditions, however, often preclude the use of low temperature substrates and scaling to large areas is challenging. The second approach of organized assembly typically relies on controlled precipitation of nanowires separately formed by hydrothermal/solvothermal processes, solution-liquid-solid (SLS) or vapor-liquid-solid (VLS) methods, solution-phase techniques based on capping reagants, or low temperature aqueous-solution processes.[127, 128, 130] Although certain degrees of alignment and positioning can be achieved through the application of electric fields,[131] microfluidic flows,[132] directed adsorption through surface patterning with self-assembled monolayers,[133] and magnetic-force-driven self-assembly,[134] these methods, in their current forms, are only useful for organizing nanowires over relatively small areas, with modest levels of control. The practical development of nanowire-based technologies demands improved precision in patterning and alignment, with methods that are compatible with conventional microfabrication processes and which can be scaled up for production. Transfer printing is well suited to address these limitations. To pattern single and multilayer nanowire assemblies, arrays are most commonly formed on a donor substrate or in a reaction vessel that is specifically optimized for nanowire growth, followed by transfer to a desired receiving substrate. Such printing-based transfers have now been demonstrated for many classes of nanowires, including those based on III-V semiconductors and group IV materials.[102, 116, 118, 119, 135]

One of the most powerful printing schemes in this context falls into the *deterministic assembly* category, and involves a directional sliding process[102, 116, 118, 136, 137] in which a substrate with a dense, nanowire deposit is dragged across a receiving substrate that supports patterns of photoresist, areas of differing surface energy, or charge.[138] As the nanowires are

sheared by the sliding contact, they detach from the growth substrate surface and adhere to the receiver through either van der Waals forces or more specific chemical interactions. Sufficiently strong bonding interactions can be achieved easily in practice, as demonstrated in the example given in Figure B.6a. Selective functionalization of a surface with SAMs, and therefore sites of preferential adhesion, provides a means to affect a hierarchical patterning in the printed nanowires. For example, organofluorine modified surfaces resist nanowire deposition, while amine-terminated SAM surfaces enable high efficiency transfers.[136, 137] Chemical modifications of this type also allow control over the densities of the nanowires in transferred arrays.[136] More recent variations of the process utilize a lubricant, to facilitate contact between the donor and receiving substrates, thereby minimizing fracture, detachment, and misalignment of the nanowires during transfer.[136]

As with other forms of transfer printing, this process can be implemented in a roller format, in which a cylindrical growth substrate connects to a wheel assembly to accomplish the frictional sliding transfers.[138, 139] The initially randomly oriented crystalline nanowires on the cylinder can be transferred to and aligned with a variety of rigid or flexible receiving substrates (i.e. Si, glass, plastic, paper) using this method.[118, 136, 139] In the example shown, the rolling mechanism has a slightly smaller radius than the inked cylindrical substrate, which results in the necessary sliding motion. Silicon, InAs, and Ge nanowires are among the materials that have been contact printed successfully by this method.[116] Large-scale heterogeneous integration of CdSe and Ge/Si core/shell nanowires into model ‘all nanowire’ circuits that are able to detect and amplify optical signals, or applied pressure with high sensitivity and precision have also been demonstrated.[102] The latter is presented in some detail in Section 10.2.

Multilayers of nanowires are also possible, in a transfer mode that involves spin-cast polymer buffer layers to provide electrical isolation and promote adhesion upon subsequent transfers. Patterning and rinsing away of select regions of the buffer layer allows control over the density and alignment, down to the single-wire level.[118, 138] Such schemes can be adapted for fabrication of 3-D integrated circuits with combinations of materials and/or substrates that involve incompatible processing/growth conditions. Figure B.6b provides a representative schematic of the multi-layer patterning scheme and an optical image of a 10 layer stack of nanowires printed in this way; each layer is offset to provide full view of the stack.[118]

Nanowires dispersed in solvents or synthesized by sol-gel methods (e.g. V_2O_5 nanowires) [140] require an inking step based on solution casting. Recent work reports that controlled drying can align wires relative to the features of relief on the stamp, and that this alignment can be retained in the subsequent transfers, in a form of *additive transfer*.[141] The character of the transfer printing also can be varied by modifying the surface properties of the stamps to control nanowire wetting in different regions.[142] In a similar method, arrays of GaAs nanowires coated with a thin film of gold can be retrieved with PDMS-supported thermal release tape, as part of a *subtractive transfer* process.[143] Here, the gold serves as a sacrificial 'carrier' film that this is etched away to expose the nanowire array (in this example, now heterogeneously integrated on silicon).

B3.3. Quantum Dots

Quantum dots (QDs) represent another important class of semiconductor structure.[144-147] Recent work illustrates impressive capabilities in patterning QD inks by transfer printing, examples of which are shown in Figure B.7. Due to their excellent luminescent properties, high photoluminescence efficiency, good external quantum efficiency, photochemical stability, and

the ability to tune color emission over a wide range of wavelengths but with narrow linewidths, colloidal semiconductor QDs of materials such as CdS, CdSe, ZnS, and ZnSe, are being intensively investigated for use as components of electroluminescent devices,[148-153] such as light-emitting diodes, for use in novel lighting applications and full-color flat panel display technologies. The active region in one design for these devices embeds an ordered array of QDs atop a hole-transporting organic semiconducting material. Formation of the QD layer can occur through spin coating or drop casting from solution, electrodeposition,[154] Langmuir-Schaefer transfer,[155-157] and controlled phase separation.[158] Transfer printing enables integration into devices, on substrates of interest, in a way that also provides a convenient mechanism for laterally patterning the materials in layouts designed for pixilation in a display, for example. In one published case, QDs assemble into a close-packed film by solvent evaporation and, once dry, are retrieved, by conformal contact with the raised regions of relief on a PDMS stamp, in a process that resembles *subtractive transfer*. The inked stamp can then transfer patterns of QDs onto a receiving substrate, comprised of a conducting polymer film (or small molecule semiconductor) that also acts as an adhesive.[159] The schematic in Figure B.7a depicts a sophisticated version of this type of process.[44] A donor substrate is first rendered hydrophobic through the formation of an octadecyltrichlorosilane monolayer on its surface, a property that promotes even spreading of a solution of aliphatic capped QDs. Next, the solvent is evaporated and the structured PDMS stamp is brought into conformal contact with the QD film and peeled back quickly under optimized applied pressure. The QDs are picked up onto the stamp in the areas of contact, and the inked stamp is then used to print the QD pattern onto a substrate containing a pre-fabricated TFT array coated with an organic hole-transporting layer by slowly

removing the stamp from the substrate surface, to exploit rate-dependent adhesion physics. Examples of representative printed QD patterns are shown in Figures B.7b-c.

Inking by direct spin coating of QD films onto PDMS stamps has proven more problematic due to the imperfect colloidal films that result and the adverse interactions that can occur between the stamp and the necessary solvents. By protecting the surface of the PDMS with a coating of epoxy or parylene,[160] QD suspensions can be directly spin-cast onto the PDMS stamp without undesirable swelling. These protective coatings also lower the surface energy of the stamp, allowing even spreading of the colloidal dispersion as well as easy release from the stamp to the receiving substrate. This technique has been used to fabricate white electroluminescence hybrid LEDs using red, blue, and green emitting CdSe/ZnS QDs (with variable diameters).[161] Multicolored LEDs are also possible using multiple registered printing steps to deposit, with precise placement, QDs of differing spectral emission side-by-side on the same substrate.[160]

In addition to their use in electroluminescent displays, QDs can also be used as sources on illumination on tips designed for atomic force and near-field scanning optical microscopies. Both kinds of integration can be accomplished with transfer printing.[162-164] In these cases, the tips themselves are used to retrieve small scale arrays of QDs, where the area that is transferred is dictated by the applied force and depth of the penetration of the tip into a QD film. This process is adaptable to many types of nanostructured surfaces, with applications being described for optical fibers, sensors, quantum logic devices, as well as nanoscale magnetometry.[165]

B4. Metals

Semiconductor materials must, in most cases, be combined with metals to yield useful devices. Metals can also, of course, themselves be useful as electrodes, antenna structures, and as critical constituents of metamaterials and plasmonic devices. In many cases, the required feature resolution, layouts and/or materials choices can be uniquely addressed by techniques of transfer printing. The following sections describe examples, organized according to origins of the metal structures, as with the discussion of semiconductors.

B4.1. Metal Films in Flat and Structured Forms

One of the first examples of metal transfer printing represented a form of *additive transfer*.[21, 23, 49, 52, 166-171] Figure B.8a shows an early embodiment, referred to as nanotransfer printing (nTP), where a SAM (from a 3-mercaptopropyltrimethoxysilane) on a silicon substrate facilitates transfer of a layer of gold deposited on a PDMS stamp by electron beam evaporation with a collimated source.[172] Related chemistries (SAMs formed by 1,8-octanedithiol functionalization of a GaAs substrate[168]) are also possible, as in Figure B.8b. For surfaces that present silanol groups, depositing a Ti film on the surface of the gold[49] enables formation of a native oxide[173] that can promote formation of interfacial Ti-O-Si bonds as a result of reactions similar to those that have been used to bond PDMS and SiO_2.[94, 174-176] Related schemes are applicable for SiO_2 treated surfaces[177] and Al films, in which interfacial Si-O-Al bonds form, in ways that can be enhanced by thin layers of water that form capillary bridges to pull the surfaces together as the water evaporates.[178, 179] Heating can facilitate these and other interface chemistries. In extreme cases of laser-induced heating, the thermal mechanism itself can weaken the adhesion and, in some cases, actively eject the metal from the

surface. This process can be used with a stamp[180] or with a flat plate, in which the resolution of the transferred metal features is determined by the pattern of exposure light.[181]

Heating can be particularly valuable when used with a thermoplastic adhesive (e.g. polymethylmethacrylate, PMMA or polystyrene). Here, contacting an inked stamp against a substrate coated with such an adhesive layer, heating to temperatures above the glass transition, and then cooling the system and peeling the stamp away leaves a metal pattern embedded in and bonded to the polymer. Two-layer printed structures are possible (e.g. by printing a flat metal film on the surface of a patterned metal film in which some areas of the polymer adhesive are exposed),[182, 183] for use as vertical interconnects in devices on plastic substrates.[184] The method can also be used to invert a stacked integrated structure, as demonstrated in the printing of metal/polymer bi-layers on polymeric substrates.[185] Plasticizing solvent vapor can decrease the glass transition temperature, to further facilitate printing in this mode.[186]

In a conceptually similar technique, mechanical loading of a flexible stamp can be an effective transfer agent for systems in which additional adhesive layers are undesirable. For example, controlled buckling of micro and nanoscale patterned relief on polystyrene stamps, at elevated temperatures, can enable transfer of imprinted gold sheets to –OH bearing silicon surfaces. Free-standing gold patterns are then "developed" by sonication in toluene during which regions of highly stressed gold fracture and wash away, leaving select hierarchically nanopatterned regions on the surface.[187] An extreme example of deformation assisted transfer involves stamps that are themselves soluble. Examples of this type have been explored with poly(vinyl alcohol) (PVA) stamps,[188] in which metal is transferred, or more precisely left behind, when the PVA is removed by dissolution in water.

Subtractive transfer of metal films is also possible with the collection of strategies described above, in some cases where additional control of the adhesion is afforded by viscoelastic effects described previously.[47, 70, 189, 190] The resulting fracture interfaces can be quite sharp and well defined, when applied in an optimized way to suitable materials and film thicknesses. One of the earliest examples of this patterning exploited cold welding between a Mg:Ag cathode and Cr/Ag coated stamp to selectively remove layers of metal-covered organic semiconductors. The separated regions (cathode and organic) defined the pixel layouts for organic light-emitting diodes (OLED) comprising a 17x17 monochrome passive matrix display.[191] Patterned structures resulting from related modalities can also provide a variety of other useful functionalities, such as contacts to classes of devices like those based on organic semiconductors that are incompatible with traditional microelectronic fabrication techniques.[189, 192, 193]

An important capability of *additive transfer* is that conformally coating the stamp with a metal, can lead to 3D structures upon transfer. Implementing the process in multiple cycles on a single region of a substrate yields hierarchical 3D multilayers, as shown in examples of Figures B.8c-d where the transfers in this case are facilitated by cold welding associated with gold-gold contacts.[166, 191, 194, 195] When slightly modified, these printing strategies are equally effective at generating 3D structures with other metal inks. Incorporating anti-adhesion layers between the stamp and metal serves to weaken the stamp interface, thereby facilitating release. Likewise, thin metallic 'strike layers' on the receiver provide sites for enhanced cold welding, but can be easily removed after transfer.[194, 196] Incorporating one or both of these additional layers can increase the diversity of available metallic inks. An alternative strategy to creating 3D structures through multiple, repetitive printing steps is to generate complex, multilayer

assemblies by sequential deposition of different materials onto a single stamp. In such cases, the entire multilayer can be printed in a single step. Examples include printed metal-insulator-metal capacitors[21] and negative index metamaterials,[41] the latter of which is described in some detail in Section 9.2.

In favorable cases, resolution of the most well developed additive methods is limited by the grain size of the deposited metal and its thickness; 5 nm edge resolution and 70 nm feature sizes have been demonstrated.[21, 49, 168] Such outcomes require careful control over the process, both at the level of the stamp and the deposited metals. As an example of attention to the latter, stress releasing features in multilayer stacks, such as alternating gold and alkane-dithiol monolayers, have been shown to reduce defects associated with cracking.[197] The conditions for depositing metals onto the stamps also require attention.[52] Cumulative heating, for example, can lead to unwanted effects due to the large differences in coefficients of thermal expansion (CTE) between the metal and the PDMS.[198-201] The use of high modulus supports with low CTE can minimize such effects, and at the same time reduce mechanical sagging into the recessed regions and buckling due to thermal cycling of the stamp and film.[24, 166] Similar outcomes can be achieved using different formulations of the stamp material. For example, PDMS variants with a 5 to 10 fold increase in elastic modulus can be used. Perfluorinated polyethers (PFPE) offer similar advantages in mechanics, together with highly non-adherent surfaces that can facilitate transfer.[202, 203]

In certain instances, stamps can be built using high-modulus, non-elastomeric materials, as a way to further minimize mechanical deformations during transfer. Early work showed, the ability to accomplish metal transfers with etched substrates of GaAs and glass.[21, 49] The main disadvantage of these types of stamps is that achieving conformal contact with the target

substrate can be difficult, compared to elastomers such as PDMS or PFPE. In part for this reason, polyurethane acrylate (PUA) polymers have attracted some attention, in stamp configurations that involve flexible backing layers.[32, 50, 204] Gold, for example, can be printed via transfer from a PUA stamp using a (3-mercaptopropyl) trimethoxysilane (MPTMS) functionalized surface (e.g. indium-tin-oxide, ITO),[170] or into a partially cured polyurethane coatings on a receiving substrate (e.g. on polyethylene terephthalate, PET).[204] Such procedures can be used to form a number of interesting metal patterns with challenging design rules, including metal nanocones,[170] and in two-step transfers that allow selective printing of metal patterns of different feature sizes from a single stamp. In the latter case, a first transfer prints metal from the raised regions of relief; the second step involves imprinting into a polymer film and simultaneously transferring metal from the recessed regions.[204, 205]

The materials science of the stamps can be important in other ways, as observed in the case of printing of copper. Here, unlike many other metals, which are unaltered by the transfer process, copper loses its conductivity when printed by nTP.[23] In this case, mobile oligomers in the PDMS stamps[206-208] diffuse from near the surface of the stamp into the bulk of the copper film, specifically between the copper grains, thereby disrupting pathways for conductive percolation. To mitigate this effect and decrease the amount of unreacted oligomers present, the PDMS can be leached extensively in a high swelling organic solvent[23, 206] to eliminate the oligomers. In a completely different strategy, these oligomers are used to advantage, as release agents in the transfer. In particular, mild heating (50-80°C) induces mobile oligomers to migrate from the PDMS stamp, causing a reduction in interfacial adhesion strength between the stamp and metal film due to its inherent low surface energy (~ 19.8 mJ/m^2).[207, 209-212] Using control mechanisms afforded by regulation of temperature, contact time, surface energies of each

surface, and substrate roughness, transfer can be accomplished without reliance on specific forms of surface chemistry other than those of nominally weak non-covalent interactions.[53]

An important feature of these collective sets of transfer schemes is that they enable metal patterning on unusual or exotic substrates and in environments that would be challenging using traditional techniques. For example, silver patterns can be transferred from a nanopatterned PMMA stamp onto a flat MPTMS modified PDMS substrate[169] as a route to creating large-area, conformal metal-bearing surfaces. Conductive layers similarly deposited onto pre- or post-strained PDMS surfaces can be laterally deformed to modify the spacing between surface features. Such actuatable nanostructures have been suggested for use in surface enhanced Raman spectroscopy (SERS) or surface plasmon resonance (SPR) sensors.[213, 214] Transfer can also be used to integrate patterned metal layers with organic semiconductors.[53, 191, 196, 215] A recent additional example involved MPTMS treated electroactive (cotton cellulose) paper[216-219] as a substrate for transfer of arrays of gold electrodes.[220, 221] Paper is a challenging substrate for patterning fine feature sizes, as it is not robust to the wet chemical processes that are necessary for conventional photolithography. Metals can be used as the desired materials, as described above, or as interfacial layers to facilitate transfer, as demonstrated recently with thin films of gold.[24] Such layers can also reduce degradation due to the oxidation of air sensitive materials.[24]

In addition to flat surface patterning, metal transfer printing is compatible with non-planar surfaces,[22] which are difficult or impossible to process using other approaches.[22, 222, 223] In a demonstration of this capability, a PDMS-supported thiolene film can retrieve pre-patterned gold structures and transfer them to a substrate, in a variant of the *deterministic assembly* mode. The thiolene transfer film can then be removed by oxygen plasma cleaning. By

using a flat stamp as a transfer element, the pattern does not suffer from the same types of limitations that result from mechanical instabilities of structured PDMS stamps with challenging design rules. A number of other transfer chemistries have been developed to facilitate this form of nTP, including the use of hydroxamic or phosphonic acid SAMs that strongly bond to the native oxides formed on metals.[224, 225]

B4.2. Nanowires and Nanoparticles

Nanostructured forms of metals are of interest for a wide array of applications, ranging from plasmonics and broader areas of optics, to biology and catalysis and for this reason are a natural area of interest in transfer printing. For such particles to function in a useful manner, precise control over their placement must be achieved. One interesting method for forming metallic nanostructures in highly ordered and deterministic fashion takes advantage explicitly of 3D relief that can be molded into a stamp surface. This process, known as nanotransfer edge printing,[171, 226, 227] can pattern narrow metal features through a two-step process that affords the selective transfer of metals from the sidewall regions of relief on the stamp. Resulting patterned features have shown nanowires diameters of 20 nm extending over 5 mm with pitch dependent on stamp relief dimensions. Multiple edge transfers have been sequentially applied to generate complex and multilayer arrangements.[171]

In the case of metal nanoparticles, long range pattern control and individual particle placement in patterns deposited directly from a colloidal suspension generally requires that the receiving substrate is first patterned in a way that controls the deposition process typically via self or directed assembly.[228, 229] An advanced form of *additive transfer*, shown in Figures B.9a,[60] provides an alternative approach - a direct delivery of nanoparticles from colloidal

suspensions into recessed regions of stamps. Colloidal suspensions are used to directly ink stamps through rigorous control over particle transport variables such as the contact angles, temperature, and particle concentrations. When the process is optimized, the particles trap in the recessed regions of the stamps, and the excess particles are removed by the motion of the meniscus. The inked stamps, once dry, are then contacted to the surface of the receiving substrate, and the particles transferred via a gradient adhesion mechanism. The resulting patterns mimic those of the relief features, taking the form of lines and complex patterns of particles with single particle resolution, as shown in examples given in Figures B.9b-c.

B5. Carbon

In pure, covalently bonded frameworks, carbon offers a remarkable array of superlative properties, in the form of diamond, tubes/fibers and graphene/graphite. These materials lie at the center of broad efforts in research, where end applications demand integration into mechanical, thermal or electronic systems. The techniques of transfer printing have been demonstrated to be useful for manipulating each of these three classes of carbon, as described in the following.

B5.1. Thin Film Diamond

Transfer printing, in the *deterministic assembly* mode, is immediately applicable to various classes of thin film diamond and diamond-like carbon films, using the same types of ideas and processes described in previous sections. Ultrananocrystalline diamond (UNCD), deposited by CVD onto SiO_2/Si, is emerging as an interesting class of material for use in thermal management, as well as for functional elements in microelectromechanical systems (MEMS),[230, 231][230, 231][230, 231230, 231230, 231230, 231230, 231230, 231230, 231230, 231230, 231236, 237 optoelectronics, and biological sensors where its highly unreactive, biocompable surfaces are

important.[231-234] Transfer printing of UNCD is possible by using adapted versions of the procedures developed for μs-Si derived from SOI. Here, UNCD inks can be produced by patterned RIE with an oxygen plasma[25] to delineate desired lateral dimensions, followed by undercut etching of the SiO_2 with HF to free micro/nanostructures of UNCD, tethered with homogeneous anchors, for printing by rate-dependent pickup and transfer[47] (adhesiveless or using a BCB adhesive). Material in this form can be easily integrated into other systems. As a simple example, printed ribbons of UNCD were used to facilitate thermal spreading when integrated directly on top of heat-generating devices on plastic.

B5.2. Graphene

Graphene, a 2-dimensional semi-metallic material made up of one atomic layer of hexagonal arrangements of carbon atoms, can also be manipulated by the techniques of transfer printing. The details depend on the synthetic routes for the graphene which are topics of other reviews.[235-238] The most widely used approaches involve mechanical or chemical exfoliation[235-237] of graphite, graphitization of SiC[238] or CVD on catalytic metal films[238-240]. In the latter two methods, the growth substrates are often not desirable for envisioned applications, or even for fundamental study. For example, the metal films needed for CVD growth provide low resistance transport pathways that lie in parallel with the overlying graphene coating. For graphene formed on SiC, the areas are limited by the available sizes of the wafers. In these and many other situations, an ability to transfer the films from the growth substrate to a different surface, either selectively or in uniform sheets, is needed.[241] The mechanical exfoliation approach launched the field, and can be thought of as a transfer printing procedure, although poorly controlled and performed with Scotch™ tape as a stamp. Early work

also demonstrated the use of PDMS stamps in a related type of mode.[47] More sophisticated versions use either a piece of graphite with features of relief etched onto its surface to yield a kind of stamp,[242, 243] or a separate stamp of silicon[244] in a process in which *subtractive transfer* against graphite inks the stamp and *additive transfer* represents the printing step. Graphene sheets, in this case, are cut from near surface region of the graphite by high stress gradients that form at the edges of the stamp due to applied pressure. Separation exfoliates thin layers of graphene that remain adhered to the raised features of relief on the stamp. Printing with applied pressure onto a target surface, such as oxygen plasma cleaned SiO_2, completes the process.[243, 244]

By contrast to mechanical exfoliation, chemical schemes typically produce bulk quantities of single or few layer graphene pieces in solution suspension.[245] In the simplest method, printing can be performed using *subtractive transfer* of a film consisting of flakes of graphene formed by casting onto a solid substrate or by passing the suspension through a filter.[246, 247] PDMS stamps brought into conformal contact can retrieve collections of flakes from selected regions of such films, for patterned transfer to a substrate such as silicon. In some cases, transfer can be enhanced by heating (2 hours at 50°C or 30 minutes at 75°C) to drive PDMS oligomers to the surface to improve release, as described previously the case of metal transfer printing.[246] *Additive transfer* can also be utilized to assemble graphene infiltrated polymer layers from solution.[237, 238, 248] In one interesting example, graphene-electrolyte multilayers were fabricated in a layer-by-layer process.[249] Here, solutions of graphene in sulfonated polystyrene (PSP) alternate with layers of poly-(diallyldimethylammonium chloride) (PDAC) on a structured PDMS stamp which is inked through repeated dipping and rinsing steps in the oppositely charged solutions. Laminating the inked stamp to a polyelectrolyte-treated

SiO_2 surface for one hour followed by gentle delamination transfers the graphene/PSP-PDAC layers in geometries matching the surface relief of the PDMS stamp.[249] Sequential inking and printing steps can be used to fabricate large-area patterns of the multilayer assemblies.

For uniform layers of graphene on SiC, printing can also be useful. Often, thin polymer or metal films serve as sacrificial 'carriers' to facilitate transfer, as described in the case of nanowires in Section 3.2. PDMS, thermal release tapes, dissolvable layers of PMMA or other types of stamps can be used effectively in this type of procedure, with several demonstrated examples.[239, 240, 250-252] Of particular interest is the ability to print, one layer at a time, individual or few-layer graphene sheets removed from multilayer deposits formed on SiC.[253, 254] Related printing schemes are also useful in the case of CVD graphene, where release can be facilitated by removal of the underlying metal films by etching.[255] In one example, the substrate (e.g. a plastic such as PET) and the graphene film are brought into contact with each other and heated above the T_g of the polymer substrate (T_g of PET is 170°C) under applied pressure (500 psi). The resulting plastic flow establishes conformal contact of the polymer with the graphene sheet, to mediate transfer. This technique is quite versatile and can be used to reproducibly transfer a wide array of thicknesses (ranging from a single graphene sheet to more bulk-like quantities of graphite).[255] Other, related methods use PDMS or PDMS-supported thermally sensitive tapes to transfer CVD graphene films onto flexible or stretchable substrates.[240, 251] This procedure involves contacting the graphene film with the tape or PDMS, releasing the graphene from the growth substrate by ultra-sonication or etching, and then placing the inked stamp onto a receiving substrate. For the case of thermal tape, heating to ~120°C dramatically decreases the strength of adhesion, thereby transferring the graphene; an example of wafer-scale graphene printed onto a rubber substrate this way is shown in Figure

B.10a.[251] For stamps without additional thermal release tape layers, kinetic effects similar to those described for *deterministic assembly* can be used to directly transfer sheets of graphene to the receiver.[240] The graphene sheets can be patterned before or after transfer, as shown in the image in Figure B.10b. These and similar techniques can be integrated into roll-to-roll type processes to generate large-area sheets of high quality graphene. Recent implementation of roller-type applications have demonstrated over 30" (diagonal) sheets graphene mounted on PET, as shown in Figure B.10c.[250]

B5.3. Carbon Nanotubes

Like graphene, carbon nanotubes, particularly single-walled nanotubes (SWNTs), are of significant interest due to their excellent electronic, thermal, and mechanical properties. Films consisting of random networks or aligned arrays of SWNTs represent realistic routes to integration in practical devices. The advantage of such arrangements is that they mitigate the consequences of the heterogeneity of the electronic properties associated with directly synthesized SWNTs via statistical averaging effects, and they also enable large current carrying capacities.[256] Such films are often deposited by casting from solution or they are directly grown by CVD, both in layouts that are suitable for integration into planar device geometries, for applications ranging from field effect transistors[6, 45, 257] and related semiconductor components to transparent electrodes for use as conductors in organic light emitting diodes and solar cells.[258] Transfer printing represents one of the most promising ways to achieve integration. In one class of approach, solution deposition techniques can be used to coat PDMS stamps with SWNTs, in random or aligned configurations.[59, 259] Stamps inked in this way can print patterns of SWNTs with controlled densities, in some cases on amine terminated gold

surfaces to mediate the transfer through electrostatic interactions.[259] When inked with higher concentrations of SWNTs, the stamps can be reused multiple times without re-inking.[259] Due to the elastomeric nature of the PDMS, this approach is also useful for transferring patterned SWNT films to the surface of non-planar substrates.[59]

Printing processes for dry, pre-formed films of SWNTs can also be effective.[260-262] In a simple form of transfer printing using a PDMS stamp, a solution of SWNTs passed through an alumina filtration membrane traps the SWNTs at the surface of the membrane as the solvent is pulled through the pores. A PDMS stamp can peel the loosely bound film of SWNTs off of the surface of the membrane. The inked stamp is then used to print the SWNT film onto a receiving substrate (i.e. glass, flexible polyester, PET, PMMA, silicon, etc.) by applying pressure and low heat for a short time (100°C for 1 minute[258] or 80°C for 10 min[263]). Once printed, the transferred films are strongly bound to the substrate, with adhesion sufficient to pass Scotch™ tape adhesion tests.[263] Alternatively, metal or polymer layers can act as sacrificial 'carrier' films. The resulting films, with SWNTs embedded in their surfaces, can then be processed and transferred using techniques described in previous sections. The final step involves removal of the film to leave only the SWNTs behind. Many demonstrations have been reported in such processes that use PDMS as the stamp, in single or multilayer geometries.[6, 46, 264-267] In other examples, thermal release tapes can be used instead of PDMS.[268] A notable feature is the retention of alignment in arrays of SWNTs grown on substrates such as quartz, thereby enabling SWNT arrays, crossbars or more complex layouts to be achieved by printing.[264] Figure B.10d shows aligned arrays of SWNTs for fabrication of transistors. Here, grown SWNTs span pre-patterned source and drain electrodes that can enable devices with varying channel widths, as illustrated in Figure B.10e. The same method can be adapted to printing of an

individual CNT that bridges two electrodes. This type of configuration is difficult to achieve without the use of transfer printing, as it would require multiple corrosive etching steps that would compromise the electronic properties of the nanotube. By repeating the transfer printing step multiple times, it is possible to print multiple overlapping or suspended CNTs per device (Figure B.10f).[269, 270] This same type of approach can be applied to other classes of nanomaterials[271] , even fragile systems, with no resulting damage.

B6. Organic Materials

Organic small molecule materials and polymers can serve as alternatives to or can be used in conjunction with the inorganic semiconductors, metals and carbon-based systems described in the previous sections. Semiconducting, metallic and dielectric properties are possible, with appropriate chemistries and doping techniques. The methods of transfer printing are well suited, and well developed, for manipulating all such types of organics. The following subsections present some examples, starting with organic semiconductors, then PDMS and various other polymers.

B6.1. Organic Semiconductors

Organic semiconducting materials represent valuable classes of ink for transfer printing because of their critical roles in organic active electronic and optoelectronic devices, including in certain applications where films of SWNTs or sheets of graphene are also thought to be useful. The ability to pattern and transfer organic semiconductors at high spatial resolution, without sacrificing their electrical properties or altering the characteristics of the receiving substrates, is imperative.[4, 10, 215] Notable examples of transfer printing such materials are given in Figure

B.11. Solvent-free, direct methods are of interest because they eliminate constraints due to requirements on solvent compatibility. The most well developed such techniques use scanned lasers, in a process of thermal imaging.[272] Local, laser-induced heating decomposes materials at the interface between a donor substrate and a uniform coating of material to be printed, in a manner that releases selectively those heated regions onto a receiving substrate. An example of conducting polymers printed in this way is dinonyl-naphthalene sulfonic acid doped polyaniline (DNNSA-PANI), a material useful for its properties as an environmentally and thermally stable conducting polymer.[273] Repetitive application in of this process enables multilayer devices.[272, 274] A sophisticated version of this transfer process, termed Laser Induced Thermal Imaging (LITI), enables efficient delivery of active material stacks for complex device structures. This process has proven highly effective in fabrication of LCD color filters and OLED displays, with multi-color OLEDs being transferred simultaneously to a receiver plane.[275]

Additive transfer processes with stamps eliminate both the need for a laser and the constraints associated with heating, to deliver organic films to a receiving substrate by exploiting favorable van der Waals interactions[276], specific surface chemistries that induce strong bonding, [277] or adhesiveless modes. Films of the organic semiconductor pentacene can, as an example of the last method, be printed with PDMS stamps directly onto ITO electrodes.[278] A water soluble sacrificial layer deposited on the surface of a donor substrate can facilitate release, if necessary.[279] Other schemes to enhance transfer use heat and pressure, as demonstrated in the printing of poly(3,4-ethylenedioxythiophene) (PEDOT) onto pentacene.[280] Similar ideas can be implemented to transfer all of the separate components of an organic thin film transistor (OTFT), including the metal, polymer, and organic semiconductor layers, occasionally with the

assistance of intervening adhesive layers.[281-283] Also, printed bi-layers of **p**oly(3,4-ethylenedioxythiophene) poly(styrenesulfonate) (PEDOT:PSS) and Au to N,N'-di(naphthalene-1-yl)-N,N'-diphenylbenzidine (NPB) can form OLEDs.[284] Entire OLED devices can be transferred in this way,[32, 62-64] in which multiple printing steps yield arrays of red, green and blue OLEDs.

Subtractive transfer is also possible; one example uses an organic semiconductor film deposited on a substrate that supports a patterned film of gold.[285] Contacting a flat stamp and then peeling it away removes only material on top of the gold features, due to comparatively poor adhesion in these locations. Figure B.11d shows an array of patterned pentacene field effect transistors (FETs), illustrating the ability to fabricate complete organic electronic devices by this method. It is also possible, for select solution-processible organic semiconductors, to use *subtractive transfer* in which a PDMS stamp selectively retrieves contacted areas of a uniform film by means of diffusion into the stamp. [286]

As a final example, transfer printing can define patterns that guide assembly of organic semiconducting films from solution. A hydrophobic pattern can be defined on a substrate simply by transfer printing PDMS oligomers, using approaches described previously.[287] The associated spatial modulation in surface energy directs deposition during dip coating, thereby creating a pattern of solution processed organic materials such as PEDOT.[288]

B6.2. PDMS

In addition to PDMS oligomers, it is possible to print solid two and three dimensional structures of PDMS, onto both planar and non-planar surfaces.[57] The methods, known as decal transfer lithography,[55-57, 289] take two forms: selective pattern release (SPaR) and

cohesive mechanical failure (CMF). SPaR prints a thin releasable patterned film of PDMS from a PDMS stamp, while CMF prints features that fracture from the bulk of a stamp.[56] Both rely on the ability of PDMS exposed to ozone and atomic oxygen generated by ultraviolet light (referred to as UVO treatment) to form an irreversible seal with an oxide bearing surface that can present hydroxyl groups, through bonding chemistries similar to those described previously.[56, 92, 290] Substrates that do not normally present surface hydroxyl groups can be coated with a thin film of SiO_2 , or related materials, to yield this type of chemistry; examples include substrates coated with copper or with a planarizing layer of photoresist (Microposit, Shipley 1805) overcoated with SiO_2.[58, 291] An alternative approach uses gold and silver films treated with MPTMS, to yield thiolate based SAMS with free siloxy groups (on hydrolysis) that can bind to modified PDMS.[58] In addition to oxygen plasma treatments as alternatives to UVO, buffered oxide etchant (BOE) and NaOH can modify the PDMS to yield similar surface chemistries.[292-294] Photo-assisted polymer transfer lithography[295] uses light activated chemistry in films of titanium dioxide that are deposited onto the receiving substrate and annealed to form an anatase crystalline phase. Contacting a patterned PDMS stamp with this titania film and exposing it to $\lambda = 463$ nm light promotes adhesion to the PDMS via photocatalytic reaction with the TiO_2 film. The methyl groups in PDMS are thought to be decomposed by electron-hole pairs generated in the TiO_2, thereby causing the remaining siloxane groups to react with the TiO_2 film. Printing proceeds as for the other PDMS transfer methods, but through the formation of strong Si-O-Ti bonds, instead of siloxane bonds. Other variants are also possible. For example, treating a PDMS stamp with an O_2 plasma can induce bonding to a planar thin film of PDMS on a separate substrate.[296] Upon removal, the contacted areas of the PDMS film are removed, in a form of *subtractive transfer*.

As with oligomers, printed PDMS can form hydrophobic patterns for local control over wettability,.[294] The PDMS structures also, however, have sufficient thickness to serve as effective masks for dry reactive ion etching processes. High aspect ratio PDMS features, which are often needed for deep etching, can be patterned using a closed form SPaR (shown in Figure B.12a) which transfers the desired pattern by means of a sacrificial connecting film. This covering membrane stabilizes PDMS features that would otherwise be mechanically unstable to collapse. Prior to use as an etch mask, this layer of PDMS is etched away with a fluorine-containing reactive ion etch chemistry.[54] SEM images of representative printed PDMS resists appear in Figures B.12b-c. After the etching of the underlying substrate is complete, the remaining PDMS can be removed with a tetrabutylammonium fluoride wet etchant.[54, 297]

Another convenient method for printing PDMS, known as masterless soft lithography,[55] uses a microreactor mask placed in direct contact with a flat PDMS stamp, as a means to expose selected regions of the stamp to UVO. Such microreactors provide enough oxygen to modify the PDMS surface while limiting diffusion of the reactive species outside of the pattern boundaries. Once activated in this way, the stamp is immediately placed in contact with an oxide bearing surface and modestly heated to bond it, selectively, in the patterned regions. Cohesive mechanical failure of the bulk of the PDMS upon peel-back represents the printing step. The heights of these features can be controlled by varying the contact time and the oxygen plasma treatment of the stamp as well as the receiving substrate.[298]

Even though thin films of PDMS can be printed using *additive transfers* described above, the stamp is gradually consumed with repeated use. PDMS coatings on the stamps can eliminate this disadvantage. In one example, a thin film of a monoglycidyl ether-terminated PDMS prepolymer is cast onto a pentaerythritol propoxylater triacrylate (PPT) stamp treated with 3-

aminopropyl triethoxysilane. The covalent bond formed by the epoxy-amine chemistry creates a stable patterned film. After deposition, sonication of the mold in solvent (IPA) removes any unreacted PDMS, and the stamp can then be used for repeated transfers.[299]

B6.3. Other Organics and Polymers

A variety of organic materials and polymers, ranging from mesogenic liquid crystals,[300] to polyelectrolytes, and block copolymers can also be transfer printed.[301, 302] These layers can play intrinsic roles in a device or structure, or they can be sacrificial. One example of the former is molecular transfer printing (MTP) whereby a master surface template of organized block copolymer domains is reproduced exactly on a replica substrate. The *additive transfer* process relies on selective segregation of block copolymer 'inks' in a blend film that is laminated between the template and replica surfaces. After annealing and rinsing, guided assembly of the polymer ink patterns and chemical bonding to the replica surface create a mirror image of the master template. After replication, both the original master and newly created replica can serve as templates for further assembly.[302] The patterned surfaces have features on the order of domain size in the block copolymer film, can be coupled with traditional lithographic techniques to generate complex feature geometries, and can be extended to massively parallel processing schemes.

Another interesting example is the printing of photoresist.[15] This process first uses *subtractive transfer* to pattern a photoresist film supported on a flat PDMS slab by placing it in contact with an etched silicon stamp, annealing, and then quickly removing the stamp to peel away all contacting regions of resist. The resulting pattern of photoresist on PDMS can then be delivered to a receiving substrate, in *additive transfer*, by applying heat while in contact and then

slowly peeling the PDMS away, as per the printing step in Figure B.2a. Demonstrations of photoresist patterns transferred to both planar and non-planar substrates are presented in Figures B.13a-d. The significance of patterning photoresist without photolithography is interesting not only from the standpoint of simplicity in processing, but also as a facile pathway for fabricating curved and multi-level patterns. Figure B.13e, for example, is an image of an etched silicon wafer with photoresist stripes printed perpendicular to the silicon trenches, such that after etching by RIE, a two-level pattern in Figure B.13f results.

Polyelectrolytes, such as poly(acrylic acid)/poly(allylamine hydrochloride) (PAA/PAH), can be printed onto an appropriately functionalized substrates, e.g. amine-terminated surface in the case of PAA/PAH. The acid groups on the PAA bind via dipole-dipole interactions, hydrogen bonding, and/or ionic interactions with the amine groups on the substrate, and through the formation of amide groups.[301] To accomplish multi-level patterning, a PDMS stamp is inked with a polyelectrolyte multilayer by alternating adsorption of the polyanion/polycation pair directly onto the stamp surface. The inked stamp is brought into contact with the substrate, which is engineered to carry opposite charge as the top layer of the polyelectrolyte multilayer. For printing to occur, the hydrophobic interaction between the bottom layer of the polyelectrolyte and the PDMS stamp surface must be weaker than the electrostatic interactions between the top surface of the polyelectrolyte multilayer and the charged receiver substrate.[303] Three different types of patterns can be fabricated using the same stamp structure by optimizing the film thickness of the polyelectrolyte ink, processing times, and applied pressure: positive transfer; edge defined transfer; and negative molding and transfer.[304] For example, application of an inked stamp to a receiver under minimal or no external pressure transfers only regions of the polyelectrolyte film from raised relief on the PDMS surface (positive transfer).

Under high pressures, entire embossed films are transferred (negative molding and transfer) and for intermediate pressures, select regions of the surface relief are printed (edge defined transfer). Similar concepts of multilayer polyelectrolyte printing have been used to form self-assembled sheets of viruses that direct nanowire growth for fabrication of battery electrodes.[305] Polyelectrolyte films can also be printed directly onto the surfaces of individual colloidal particles. Using AFM tips modified with individual colloids, and controlling the applied force with a hybrid AFM/micro-interferometry setup, it is possible to define accurately the surface area of the colloidal particles that are contacted and thus coated with the polyelectrolyte ink.[306]

As with other material classes addressed in this review, alternative stamp materials are sometimes more desirable than PDMS for printing. For example, due to its relatively high modulus and ability to resist solvent swelling,[307] PMMA is useful for transfer printing of materials such as resists for electron beam lithography, hydrogen silsequioxane (HSQ), and conductive silver paste.[307] Previously described PUA stamps have also been used to print polymers, by first coating their surfaces with aluminum to facilitate release, and then with a desired polymer film (such as poly(vinyl acetate) (PVAc)). Upon contact with a receiving substrate, followed by mild heating the patterned PVAc film detaches upon removal of the PUA stamp. Printing is once again driven by differential adhesion strength at the aluminum/PVAc and PVAc/substrate interfaces. A variant of this method uses a double roller setup to press the inked PUA/PET stamp into contact with a moving, large area receiver substrate.[50] A related procedure, also conducted with PUA stamps, is known as polymer spin transfer printing.[308] Here, spin-coating the stamp with a polymer to be printed and then exposing its surface to an oxygen plasma generates a negative charge that facilitates its transfer to a substrate coated with a polyelectrolyte that displays positive charge, such as poly(diallyldimethylammonium chloride)

(PDAC). Mild heating softens the PUA to enhance release. This method has been used to transfer nanopatterned structures of a variety of polymers onto different substrates.[308] *Subtractive transfer* is also possible, due to the relatively high surface energy of PUA stamps (59.8 mJ/m^2).[15, 66] A similar mode, termed hot lift-off, can be performed with a partially cured epoxy stamp which, upon curing, provides sufficiently strong adhesion for this type of process.[67, 309, 310] Ultraviolet (UV) light can alternatively be used to mediate transfer,[311, 312] in which a PDMS stamp coated with an organic material is brought into contact with a photocurable resin (e.g. acrylate) distributed on the receiver substrate, then exposed to UV light, allowing the resin to cure through radical polymerization.[311, 312]

B7. Colloids

Colloidal crystals[313, 314] are ordered structures made up of arrayed polymeric or inorganic particles, useful for applications in chemical or biological sensing, optics, photonics (i.e. photonic band gap materials), high strength ceramics, battery electrodes, separation membranes and others. [315-318] To realize optimal properties, such crystals must be patterned in a controlled and spatially organized manner. Most techniques form colloidal crystals in desired geometries via directed self-assembly or using external stimuli based on electrostatics, topography,[319] or surface energy.[320] Soft lithography methods utilize microfluidic channels to physically confine colloids in the desired configuration. Such strategies require continuous flow pathways and channel geometries that promote capillary action of the colloidal suspensions. [94, 321, 322]

Subtractive transfer printing techniques provide useful, complementary capabilities.[323, 324] The first step involves formation of close-packed crystal made up of inorganic or

polymeric colloids by a traditional method, such as the solution evaporation technique.[317] The upper layer of the colloidal crystal can then be removed in selected regions by contact with a PDMS stamp under pressure and moderate heat. Multiple rounds of such patterning with accurate registration can yield crystals with complex patterns.[323] Similar steps, in *additive transfer* mode, can yield patterned colloids on planar, non-planar, or topographically complex surfaces.[325] The parallel operation offers advantages compared to schemes that require individual placement of colloidal particles using optical tweezers,[326] or atomic force microsopes (AFM).[327] Furthermore, the inked PDMS stamp can be swelled with an organic solvent[206] or mechanically deformed (stretched) to alter the lattice spacing of the colloidal crystal while still preserving long range order in the array.[324]

In some examples, such printing occurs into a heated adhesive layer, such as poly(vinyl alcohol) (PVA).[325] Water can, in certain cases, be substituted as a transient adhesion promoter, in a process where hydrophilic colloids on a hydrophobic PDMS stamp move towards the hydrophilic receiving substrate by means of capillary action, forming a "liquid bridge."[178, 328] Evaporation of the water brings the colloids and the substrate into conformal contact. If the colloids and the substrate are able to form strong physical or covalent linkages (such as that between silica and oxidized Si), the patterned colloidal crystal film will attach to the receiving substrate and become durably bonded.

The relief on the stamp can be exploited to yield printable clusters of colloids, using ideas similar to those described for the printing of metal nanoparticles.[329] The method involves a colloidal assembly step and subsequent binding of the resulting clusters to lock in the patterned assemblies and impart structural stability. A proof-of-concept system uses cyclodextrin-capped polystyrene colloids grouped into clusters by convective assembly within the relief features of a

PDMS stamp.[329] A supramolecular glue (an adamantyl-terminated poly(propylene imine) dendrimer) infiltrated into the constrained clusters creates a strong bond between the particles by means of host-guest interactions involving the cyclodextrin and the dendrimer. The resulting 3D clusters are then directly printed from the reliefs of the PDMS stamp onto a cyclodextrin functionalized surface, where they are fixed and locked into their as-printed configuration. These constructs can also be used as free-standing particle bridges that span relief features present on a receiving substrate.[330]

A related approach exploits segregation of colloids at a phase separated liquid-liquid interface, such as that between paraffin oil and water.[331] Colloids (e.g. polystyrene beads) collect at the interface to form a close-packed assembly. When a PDMS stamp is pushed through the liquid-particle-liquid interface, energy minimization redistributes the colloidal particles, confining them in the relief features of the stamp. The particles remain on the stamp until it passes all the way through the liquids and comes into contact with a receiving substrate at the bottom of the container housing the liquids. Printing is achieved by heating the mixture slightly above the glass transition temperature of the colloids, allowing the particles to adhere to each other as well as the receiving substrate. When the PDMS stamp and both liquids are removed, a stable patterned array of molded particles remains on the substrate. A similar approach also has been used to ink PDMS stamps.[332] Instead of utilizing heat to bond the confined material to a receiver, the inked stamp is allowed to dry and then is used to contact print the colloidal particles in a pattern following that of the relief of the PDMS stamp.

B8. Biological Materials and Living Cells

Applications in biotechnology demand the ability to pattern relevant bio-organic materials, ranging from small molecule drug candidates to living cells. Several transfer printing protocols are available for such purposes. Most simply, hydrophobic patterns achieved by transfer printing silicone oligomers from a PDMS stamp onto a hydrophilic substrate can facilitate assembly of stretched DNA molecules on patterned glass[12] and selective adsorption of proteins from solution.[333] PDMS stamps can also be used to print DNA and other biomaterials directly.[334-337] Depositing a DNA solution on unmodified PDMS yields highly aligned patterns of stretched DNA molecules, facilitating their use as probes for gene mapping. For accurate positioning of DNA into a precise array, a capillary assembly can be used to deliver DNA solutions to specific regions on a PDMS stamp.[338] Contact with a receiving substrate, such as hydrophilic glass or mica, elicits printing.[13] When the substrate is coated with 3-aminopropyltrimethoxysilane, DNA transfer results from electrostatic binding;[338] sequential prints produce multi-layered DNA patterns.[13] Additionally, covalent attachment of dendrimers to PDMS can create patterns of positive charge on a stamp surface, which in turn can be used to bind the negatively charged amino-modified DNA or RNA molecules in a "layer-by layer" arrangement. Arrays of this type can be printed onto aldehyde-functionalized surfaces.[339]

Oligonucleotide patterns can also be replicated at high resolution by other forms of printing. Supramolecular nanostamping encompasses a class of protocols that form patterns of single stranded DNA (ssDNA) molecules with exceptional resolution.[14, 340-343] In a first step, complementary DNA molecules are hybridized to a master surface that supports a pattern of ssDNA. The complementary DNA molecules have end groups that covalently bond upon

contact with a receiver. For example, a PMMA substrate functionalized with reactive aldehyde groups enables printing and capture of amine-terminated DNA via imine linkages.[341, 342] Once contact is achieved, the sample is heated to dehybridize the DNA strands. Upon separation of the substrates, the ssDNA master is retained in its original form and the receiver hosts a complementary DNA strand pattern mimicking the spatial layout of the ssDNA master.[14, 340]

Another transfer method applicable to biomaterials, known as affinity contact printing, uses non-covalent chemical recognition to select a specific target protein from a complex mixture. Here, a PDMS stamp is functionalized with appropriate capture molecules to drive high affinity selective binding,[344-346] after which the captured proteins are printed by contacting the inked stamp to the surface of a suitably modified receiving substrate. This method can create patterns on a flat stamp by defining open microwells on its surface and filling each with a solution that affects the attachment of a specific capture molecule.[344] A *subtractive transfer* version of this patterning method uses a silicon stamp, which on contact with a planar PDMS slab captures specific protein targets. Complex arrays of capture molecules suitable for specific multi-protein inking from a solution can be fabricated in this way, with high selectivity over many patterning cycles.[344] Such printed protein patterns can immobilize and direct cell growth, define organization of focal adhesions, and guide axon outgrowth.[345] Printed DNA patterns have also been broadly used, most notably for genetic phenotyping and diagnostic sensing.[12, 335, 346]

The current literature suggests that affinity contact printing can be adapted to virtually any ligand-analyte pair with nanomolar range affinity, provided that background levels due to non-specific binding can be suitably controlled.[345] For this reason, and due to its more general importance to all other forms of biomolecular printing, much work focuses on the

development of surface chemistries to resist such adsorption.[347-349] Hyaluronic acid (HA), a polysaccharide, is used extensively in processes for patterning proteins and cells, due to its ability to resist adsorption/adhesion to many biomolecular adsorbate materials.[350, 351] This chemistry provides a control strategy for assembly in which well-defined patterns of HA are printed onto a substrate (including SiO_2, poly-2-hydroxyethyl methacrylate (poly(HEMA)), polystyrene culture dishes, and poly(lactic-co-glycolic acid) (PLGA)) through printing and application of a secondary adsorbate organized via orthogonal assembly.[348] In one such embodiment, a PDMS stamp is first rendered hydrophilic by an oxygen plasma treatment and then inked using an aqueous HA solution.[348]

Soft stamps of polar materials provide substitutes for PDMS, specifically engineered for use with biomolecular inks where requirements exist to maximize wetting while minimizing irreversible binding of adsorbates present in compositionally complex aqueous ink solutions. The most popular material for this purpose is agarose, a hydrogel material that can be molded with relief features using soft lithographic methods.[352] These stamps are remarkably durable[352-355] and can pattern a wide range of biomolecular inks, including proteins and cell membrane protein-receptor fragments, on various substrates (e.g. glass, plastic, etc.).[353, 356] In general, agarose stamps use significantly less material during inking and printing than PDMS, which is especially important for efficient utilization of precious and/or difficult-to-harvest materials.[357] Agarose stamps also support the printing of protein gradients, a form of patterning mediated by diffusion within the stamp.[353] Delivering a printed gradient pattern to a receiving substrate provides a simple route to fabricate useful grayscale molecular patterns.

Perhaps the most remarkable property of agarose stamps is their ability to print patterns of living cells. Cell-inked agarose, a “living stamp,” has been used to fabricate patterns for a

variety of cell types, including one exemplary model array of osteoblasts on hydroxyapatite scaffolds, as shown in Figures B.14a-b.[358] Entire bacterial colonies can also be printed, as shown in Figures B.14c-f.[354, 355] Alternatively, printed patterns of cell adhesive proteins, can elicit hierarchical organizations in plated cell cultures. One reported example immobilized these ligand proteins on a thermoresponsive poly(N-isopropylacrylamide) (PIPAAm) functionalized culture plate and subsequently used them to direct the growth of confluent aligned human aortic vascular smooth muscle cell sheets.[352] These sheets can be viably released from the culture surface via a polymer phase change (driven thermally by lowering the substrate temperature) and can further function as living inks for use in more complex forms of patterning.

B9. Integrated Devices

The printing techniques highlighted in this review can be used to assemble diverse and disparate classes of materials, from GaAs nanowires, to graphene sheets and living cells, into single and multilevel functional systems. Materials configured in this way can serve a variety of roles in operational devices from passive elements, such as electrodes or transparent contacts or photonic elements, to active semiconducting or sensing components. These assembly methods also provide an effective means to integrate different functionalities (electronic, optical, biological, mechanical, etc.) into heterogeneous configurations. Notable examples range from simple thin-film transistors (TFTs) and single level biological sensor elements to full arrays of multi-level logic structures designed to mimic high performance devices fabricated via traditional CMOS processes. In the following sections, examples of printed devices embedding challenging features, the printing techniques utilized in their fabrication, and their relative (and generally high level of) performance are discussed.

B9.1. Transistors, Light Emitting Diodes and Solar Cells

Unique classes of large scale, heterogeneously integrated devices, specifically enabled by transfer printing, have been extensively explored as a means to circumvent limitations in integration density, operation speed, and power consumption of current high performance electronics.[20, 35, 46, 118] These systems also enable other useful properties, including flexible and even stretchable forms, curvilinear shapes, and lightweight, mechanically rugged construction. Inorganic semiconducting nanowires, nanoribbons and nanomembranes represent preferred materials in these applications, due to their favorable mechanics, ease of fabrication, and superior performance. Printing techniques such as those discussed in Sections 3.1 and 3.2 have been utilized with exceptional success to pattern regions of single crystalline nanomaterials of InP, InAs, Ge, GaN, GaAs, and Si as active components of LEDs, metal oxide semiconductor field effect transistors (MOSFETs), metal semiconductor field effect transistors (MESFETs), TFTs, solar cells, various sensors and other active and passive components.[27, 29, 43, 116, 118, 359] As an example, printed top-gate Si TFT (channel length, width of 9 and 200 μm) on plastic exhibit mobilities of > 600 cm^2/V-s and 530 cm^2/V-s in the linear and saturation regimes, respectively, ON/OFF ratios > 10^5, and switching frequencies of 515 MHz.[27] More recent results describe full radio frequency operation, with unity current gain at switching speeds greater than 10 GHz.[360] Compound semiconductor devices such as printed GaAs MESFETs[19, 101] and InAs nanowire FETs[361] on plastic also offer GHz operation. In the latter case, transistors demonstrate high saturation velocities (>1.3 x 10^7 cm/s at a field of 16 kV/cm), maximum oscillation frequencies of 1.8 GHz, and a transconductance of 1.1 mS.[361] The devices are mechanically robust, with the ability to withstand mechanical bending cycles (radius of curvature of < 18 mm) without performance degradation. Other flexible device

geometries have also been realized, including GaAs and GaN HEMTs,[19, 35]making them potentially useful platforms for ultra-high frequency electronics.

Transistors built on plastic and other substrates with printed films of SWNTs (networks, perfectly aligned arrays or anything in between) or graphene offer additional features. In the former cases, GHz operation is possible in functional RF devices such as radios,[6, 362] and full integrated circuits can be achieved.[6, 45] Repetitive printing enables transparent, 'all-SWNT' transistors in which films of SWNTs serve not only as the semiconductor but also as the electrodes.[46] In conceptually similar integration schemes, transfer printing of high-quality graphene sheets can yield graphene-based CMOS-compatible electronic and optoelectronic devices,[244, 252, 255] in transistors that show ambipolar behavior,[244, 251] and electron and hole mobilities of 800 cm^2/V-s and ~3700 cm^2/V-s, respectively.[244] Top-gate dielectrics of Al_2O_3 nanoribbons printed onto mechanically exfoliated graphene enable superior graphene-dielectric interface properties as well as enhanced device functionality.[363] Figure B.15a provides a schematic of the process flow to fabricate such devices, and Figures B.15b-d shows current-voltage characteristics. From these curves, an electron mobility of 22,600 cm^2/Vs was determined, one of the largest reported values for top-gate configurations. Figure B.15c, d compare transfer characteristics and transconductances of top-gate and bottom-gate (inset) devices, demonstrating the advantages of the former.

Printing techniques can also be used to form multilevel electronic devices that use multiple classes of semiconductor materials described above.[35, 118, 135] As an example of three dimensional heterogeneous integration (3D HGI) of this type, [35] three-layer stacks of high performance devices were constructed that integrate GaN nanoribbon HEMTs, Si nanoribbon MOSFETs, and SWNT network TFTs. Figures B.16a, b present a plane view and a

confocal 3D colorized image, respectively, which clearly illustrate the three distinct device layers printed on a 25 μm thick PI substrate.[35] Figure B.16c shows an optical image of the three device layers held in a bent configuration during probing. Figures B.16d-f provide device performances for the different layers: the GaN HEMTs have threshold voltages V_{TH} = -2.4 ± 0.2 V, ON/OFF ratio > 10^6, and transconductances of 0.6 ± .05 mS; the SWNT TFTs have V_{TH} = -5.3 ± 1.5 V, ON/OFF ratio > 10^5, and linear mobilities of 5.9 ± 2.0 cm^2/Vs; and the Si MOSFETs have V_{TH} = 0.2 ± 0.3 V, ON/OFF ratio > 10^4, and linear mobilities of 500 ± 30 cm^2/Vs, all consistent with performance of conventionally fabricated devices having the same geometries.[35]

Optoelectronic devices utilizing printed inorganic semiconductor materials can also be assembled into similar heterogeneous, mechanically flexible formats. Arrays of red (AlInGaP)[31] and blue (InGaN)[43] LEDs, visible[102] and near infrared[35, 101] photodetectors and high performance solar cells[38], have been printed into functional arrays on substrates ranging from glass to plastic to rubber. In all cases, performance comparable to or better than that of corresponding devices on wafer substrates is possible.

B9.2. Negative Index Metamaterials

Passive optical elements, such as lenses, waveguides, splitters, polarizers and other components, often serve critical roles in these types of optoelectronic systems. Negative index metamaterials (NIMs) enable emerging classes of optical elements in which engineered structures offer optical properties not found in naturally occurring materials. Recent work shows that focused ion beam lithography, multilayer electron beam lithography and related techniques can be used to achieve small-scale (i.e. < a few hundred μm^2) NIMs with interesting

characteristics, including negative index behavior in the optical regime.[364] A key challenge is in fabrication with sizes and throughputs necessary for realistic applications in superlensing, invisibility cloaking and others. Printing techniques, such as the nTP method described in Section 4.1, have exceptional capabilities for forming large-area, high-quality NIMs with three-dimensional, multilayer mesh formats (i.e. fishnet NIMs).[41] The process involves blanket deposition of multilayer stacks of alternating layers of silver (Ag) and magnesium fluoride (MgF_2), using a directional flux on top of a thin release layer (SiO_2) on a silicon stamp. Transfer printing patterned multilayer structures from the raised regions onto rigid or flexible substrates, facilitated by removal of the SiO_2 layer by etching with hydrofluoric acid, completes the fabrication. Experimental and modeling results show that macroscale NIMs (> 75cm^2) formed in this way exhibit strong, negative index of refraction behavior in the near-IR spectral range, with excellent figures of merit, comparable to or better than small devices fabricated with much more complex techniques.[41] The materials can be formed on a variety of both flexible and rigid substrates.

B9.3. Mechanical Energy Scavengers

In addition to electronic, optoelectronic and optical components, transfer printing can yield interesting mechanical devices. For example, spatially organized, printed arrays of lead zirconate titanate (PZT) ribbons enable fabrication of mechanical energy harvesting devices supported on rubber or plastic substrates, suggesting new device platform possibilities.[365-370] The resulting generators demonstrate high efficiencies, in flexible/stretchable, wearable, and potentially implantable formats. Figure B.17a provides a schematic view of a printing process for integrating PZT transducers on plastic.[367, 368] PZT films (500 nm thick) are deposited,

thermally annealed and patterned into arrays of strips (5 μm wide) onto a MgO (100) donor wafer which also provides a sacrificial layer for release.[367, 368] Etching of the underlying surface regions of MgO releases the ribbons from the substrate sufficiently to enable retrieval with a flat PDMS stamp. The aligned orientation of the ribbon arrays is maintained over large areas during retrieval with the stamp as shown in Figure B.17a. Subsequent transfer onto an epoxy coated film of Kapton, followed by formation of interdigitated Cr/Au (10/250 nm thick) electrodes yields the mechanical energy harvester shown in Figures B.17b-c. Poling (field strength ~100 kV cm^{-1}) the ribbons ensures a maximum piezoelectric constant, d_{33}, in the plane of the device.[366, 368] Figure B.17d shows the short circuit current for devices consisting of 5 ribbons undergoing 8% strain. Under these optimal conditions, current density is estimated to be ~2.5 μA/mm^2, which is comparable to values measured in PZT-nanowire devices. More recent work demonstrates the ability to achieve similar performance, but in fully stretchable configurations using buckled PZT ribbons printed onto PDMS substrates.[369, 370]

B10. Advanced Systems

Not only are individual device components possible, as highlighted in the previous systems, but full integrated systems that contain many thousands of such devices can be achieved. This scaling provides strong evidence for printing as a core, enabling manufacturing process for new kinds of applications. The following sections review a few examples.

B10.1. Quantum Dot Displays

Printed films of QDs provide the starting point for fabricating arrays of QD LEDs in full, active matrix displays. Figure B.7c demonstrates simultaneous operation of RGB pixels formed

using this approach, described in detail in Section 3.3. After transfer of registered QD pixel layers onto an organic hole-transporting layer (HTL), the QDs are cross-linked and thermally annealed to reduce the hole injection barriers and interfacial electrical resistivities, respectively. An electron-transporting layer (ETL) of sol-gel TiO_2 applied to the QD surface along with aluminum cathodes and an encapsulation of cover glass under a nitrogen environment completes the fabrication of QD LEDs. Hafnium-indium-zinc oxide (HIZO) TFT arrays serve to drive the QD LED pixels in advanced switching modes. The transistors exhibit superior current stability and each pixel emits over a surface area of ~ 46 μm x 96 μm, comparable to the resolution in state-of-the-art high definition televisions. 4" (diagonal) full color active matrix displays with 320x240 pixels provides a system level example, as presented in Figure B.1e.[371] These materials and fabrication techniques have potential for scale-up in next generation displays.

B10.2. Flexible Pressure Sensor Arrays

Transistors for the active matrix display in Figure B.1e use conventional planar processing techniques on rigid substrates. Transfer printing enables similar functionality on arbitrary surfaces. In one example, printed nanowire arrays serve as the active materials for such circuits, where potential applications include not only displays but also other systems such as arrays of pressure sensors, strain gauges and photodetectors.[102, 372] A recently reported example of the first possibility is a large-area, pressure mapping device that incorporates printed arrays of Ge/Si core/shell (30 nm diameter) nanowires as channel materials for transistors on a thin polyimide substrate in a 19 x 18 active matrix array. The sensors in this case use a top layer of pressure sensitive rubber which also encapsulates and isolates individual pixels during operation.[372] Figure B.18a provides an optical image of one such fabricated device during

extreme mechanical flexure while Figure B.18b shows a pressure map of the same device when embossed with a molded PDMS stamp. The system can provide fast mapping of distributions of pressure in the range from 0 and 15 kPa.

B10.3. Bio-Integrated Electronics

Flexibility, such as that achieved by the pressure sensor arrays described in the previous section, is important for many applications. The optimal mode for integration with the human body, on the other hand, requires stretchability, in the sense of linear elastic mechanical response to large strain deformation. The capabilities of transfer printing enable devices that bond to and accommodate the motions of soft, elastomeric substrates, to provide 'tissue-like' physical properties (i.e. thin, soft, curvilinear), and resulting capacities to integrate intimately with organs of the body without any significant mechanical or mass loading effects. These characteristics enable conformable adhesion with electrical, thermal, optical and chemical access, and robust binding without irritation. Such devices can provide thousands or millions of interface points, with local electronics for advanced processing, monitoring, stimulating or other functions, along with multiplexed readout to minimize the number of wire connections. Examples include high resolution sensor sheets that laminate, like pieces of Saran Wrap, onto the surfaces of the heart[373] and the brain[374] for mapping electrophysiology, with unmatched temporal and spatial resolution. Example systems of this type include electronics with thousands of printed silicon nanomembrane MOSFETs. An important mode of operation for cardiac devices involves endocardial access, obtained through arteries or veins. Here, transfer printing allows integration of sophisticated device functionality onto the surfaces of otherwise conventional catheter balloons.[375, 376] Insertion of such 'instrumented' catheters into the interior of the heart,

followed by inflation softly presses the deformable membrane of the balloon against the endocardial surface, in a configuration where a surgeon can perform a range of sensing and therapeutic operations. An example of such a device appears in Figure B.19, where the functionality ranges from ECG mapping to temperature and tactile sensing, to flow monitoring, tissue ablation and LED-based activation of photosensitive drugs. The images show the balloon in deflated (top) and inflated (bottom) states.

In a most recent demonstration, advanced designs in related circuits have enabled their physical properties, ranging from modulus to degree of stretchability, areal mass density, thickness and flexural rigidity, to match the epidermis.[42] Here, lamination mounts the devices on the surface of the skin, in a manner much like a child's temporary transfer tattoo, to provide various types of healthcare and non-healthcare related functions, using demonstrated building blocks such as antennas, wireless power coils, silicon nanomembrane MOSFETs and diodes, strain and temperature gauges, along with RF inductors, capacitors and oscillators (Figure B.1c). Contact mounting yields low-impedance coupling of electrodes for electrophysiological measurements, without the use of conductive gels or penetrating pins, to allow high resolution electrocardiography, and electroencephalography and electromyography. Data in the last case can contain sufficient information for human-machine interfaces, as recently illustrated through a simple computer game controller based on EES measurements of muscle activity near the throat.[42]

B10.4. Hemispherical Digital Cameras

Extensions of the ideas presented in the previous section allow device geometries that are natively curvilinear.[37, 377] Such configurations offer broad new possibilities for system level

designs including classes of biologically inspired devices, such as hemispherical and parabolic imagers, that meld the high performance of conventional, wafer-based CMOS technology with form factors that mimic geometries optimized by evolution. In fabrication flows for such devices, the PDMS stamps not only provide tools for transfer, but also for geometry transformation (i.e. planar to curvilinear). For example, a thin PDMS stamp can be formed by molding against a substrate with a desired final geometry (hemisphere, paraboloid, golf ball, etc.). Placing the membrane in a state of radial tension flattens it into a drumhead shape, allowing conformal contact with a fully formed circuit or detector array in the form of a thin, open mesh. Peeling the stretched PDMS membrane away carries the mesh with it. Relaxation back to the original shape transforms the geometry of the mesh to the molded shape, in a process where engineered deformation and buckling of non-coplanar interconnects accommodates the associated strains.[378] For the case of matrix addressed arrays of photodetectors, transfer of the geometry-transformed mesh to a rigid substrate with the same shape as the relaxed PDMS stamp followed by external connection to a printed circuit board (PCB) for computer control and data acquisition yields a curved-surface, digital imager.

Figure B.20a shows a demonstrated electronic ‘eyeball’ camera that incorporates a hemispherically curved photodetector array with the size and shape of the human retina, coupling to a simple, plano-convex lens fixed in a transparent hemispherical shell. The fields of view, levels of aberration and illumination uniformity all exceed those achievable with otherwise similar, flat photodetector arrays when the same, simple optics are used. Figure B.20b presents a picture captured with this camera, rendered in the hemispherical geometry of the detector (top), and as a planar projection (bottom); the actual object appears in the right inset. The key feature of this device is that the shape of the photodetector array approximately matches that of the

image formed with the lens (i.e. the Petzval surface).[37] Precise matching for the case of the plano-convex lens involves surfaces in the shapes of elliptic paraboloids. Paths to more sophisticated devices, such as those with improved fill-factor[36, 378] and tunable curvature have recently been reported, along with quantitative experimental and theoretical analysis of the optics.[379]

B10.5. Microconcentrator Photovoltaics

The most technically mature example of transfer printing exists as part of a manufacturing flow for a class of high concentration photovoltaic module. Here, automated transfer printing tools, similar to the example shown in Figure B.21a, utilize composite stamp designs of molded thin elastomeric layers supported on high-modulus, flexible backing layers,[20, 166] to retrieve and print selected elements from a densely packed array of inks consisting of multi-junction compound semiconductor microscale solar cells (microcells), similar in dimensions to those reported in Reference 38. Repetition of this printing process in a parallel mode rapidly deploys the microcells over large areas ('area multiplication', Figure B.3) for direct integration into final devices that include microscale focusing elements. Such tools are nominally comprised of *x*-, *y*-, and *z*-axis linear stages with additional tilt- and rotation staging to enable controlled and reproducible manipulation of a stamp element independent of a host or receiving substrate. Integrated optics and high precision load cells provide alignment monitoring and force-feedback sensing to determine contact between a stamp and substrate on length scales ranging from microns up to centimeters or longer. Micron scale registration and positioning accuracy across stamp/substrate contact and a repeatable overlay accuracy (the ability to automatically return to the same location on a substrate) of less than 500 nm are characteristic

staging requirements. An example of a completed microconcentrator photovoltaic module is shown in Figure B.21b. The small surface area of each individual device provides efficient heat transfer without integration of a separate heat sink, lower series resistance as compared to larger devices, and most notably allows the use of small, lightweight concentrating optical elements (corresponding, in this case, to 1000x) with wide angle of acceptance, and optimized incident light intensity onto the microcells. The integrated modules (Figure B.21c) fabricated in this way provide a route to high volume production at low costs with impressive resulting device performance (>41% and >32% microcell and module efficiencies, respectively) thus promising an affordable source of energy at low start-up and lifetime costs.[380] Such strategies toward industrial scale-up of device module fabrication have strong potential to be extended to other application spaces, including those presented in other sections.

B11. Concluding Remarks

The patterning strategies discussed in this Review represent rapid developments in the field of transfer printing that have enabled a broad application space, one encompassing virtually all classes of materials. The ease with which most of these techniques are implemented with high throughput, provides an important route to affordable large area electronics constructed on a wide range of substrates. This advance broadens the range of materials that can be patterned (as well as patterned on), and allows for high performance applications to be realized with materials that were previously rendered useless due to incompatibility with patterning and deposition protocols. Materials prone to degradation during processing and chemical exposure can now be utilized in capacities not previously possible, through decoupling of the deposition, processing, patterning, and printing steps. Already, the ability to transfer print microstructures layer-by-

layer with precise spatial orientation, has led to elegant implementations of heterogeneous integration to develop novel circuitry, as addressed in the review. Further, these patterning platforms have enabled important developments in the field of non-planar and flexible electronics, not only as a method for printing and integrating microscale device arrays but also as a method for printing stretchable silicon. In this Review we discuss the far reaching application space that has been constructed as a result of the development of chemistries, materials, and fundamental mechanics used in transfer printing. The existing level of development in many of these methods enables their use for research applications, and prototyping of new devices. Many additional opportunities for research exist, in areas ranging from fundamental adhesion science, to materials and interface properties. Engineering efforts might establish new modes of operation, such as programmable stamps with actively controlled surfaces. These collective considerations suggest that this field of study will remain active and dynamic, promising even more complex constructs and advanced patterning schemes in the near future.

B12. References

[1] Y. Xia, G.M. Whitesides, *Angew. Chem. Int. Ed.* **1998**, *37*, 551.
[2] Y. Xia, G.M. Whitesides, *Annu. Rev. Mater. Sci.* **1998**, *28*, 153.
[3] J.A. Rogers, R.G. Nuzzo, *Mater. Today* **2005**, *8*, 50.
[4] E. Menard, M.A. Meitl, Y. Sun, J.-U. Park, D.J. Shir, Y.-S. Nam, S. Jeon, J.A. Rogers, *Chem. Rev.* **2007**, *107*, 1117.
[5] R.H. Baughman, A.A. Zakhidov, W.A. deHeer, *Science* **2002**, *297*, 787.
[6] Q. Cao, J.A. Rogers, *Adv. Mater.* **2009**, *21*, 29.
[7] T. Dürkop, S.A. Getty, E. Cobas, M.S. Fuhrer, *Nano Lett.* **2004**, *4*, 35.
[8] J. Kong, N.R. Franklin, C. Zhou, M.G. Chapline, S. Peng, K. Cho, H. Dai, *Science* **2000**, *287*, 622.
[9] G. Malliaras, R. Friend, *Phys. Today* **2005**, *58*, 53.
[10] T.W. Kelley, P.F. Baude, C. Gerlach, D.E. Ender, D. Muyres, M.A. Haase, D.E. Vogel, S.D. Theiss, *Chem. Rev.* **2004**, *16*, 4413.
[11] J.M.J. Frechet, *Science* **1994**, *263*, 1710.
[12] P. Bjork, S. Holmstrom, O. Inganas, *Small* **2006**, *2*, 1068.
[13] H. Nakao, M. Gad, S. Sugiyama, K. Otobe, T. Ohtani, *J. Am. Chem. Soc.* **2003**, *125*, 7162.

[14] A.A. Yu, F. Stellacci, *J. Mater. Chem.* **2006**, *16*, 2868.
[15] J. Yeom, M.A. Shannon, *Adv. Func. Mater.* **2010**, *20*, 289.
[16] E. Menard, K.J. Lee, D.-Y. Khang, R.G. Nuzzo, J.A. Rogers, *Appl. Phys. Lett.* **2004**, *84*, 5398.
[17] K.J. Lee, J. Lee, H. Hwang, Z.J. Reitmeier, R.F. Davis, J.A. Rogers, R.G. Nuzzo, *Small* **2005**, *1*, 1164.
[18] Y. Sun, J.A. Rogers, *Adv. Mater.* **2007**, *19*, 1897.
[19] Y. Sun, H.-S. Kim, E. Menard, S. Kim, I. Adesida, J.A. Rogers, *Small* **2006**, *2*, 1330.
[20] A.J. Baca, J.-H. Ahn, Y. Sun, M.A. Meitl, E. Menard, H.-S. Kim, W.M. Choi, D.-H. Kim, Y. Huang, J.A. Rogers, *Angew. Chem. Int. Ed.* **2008**, *47*, 5524.
[21] Y.-L. Loo, R.L. Willett, K.W. Baldwin, J.A. Rogers, *J. Am. Chem. Soc.* **2002**, *124*, 7654.
[22] E.J. Smythe, M.D. Dickey, G.M. Whitesides, F. Capasso, *ACS Nano* **2009**, *3*, 59.
[23] K. Felmet, Y.-L. Loo, Y. Sun, *Appl. Phys. Lett.* **2004**, *85*, 3316.
[24] H. Schmid, H. Wolf, R. Allenspach, H. Riel, S. Karg, B. Michel, E. Delamarche, *Adv. Func. Mater.* **2003**, *13*, 145.
[25] T.-H. Kim, W.M. Choi, D.-H. Kim, M.A. Meitl, E. Menard, H. Jiang, J.A. Carlisle, J.A. Rogers, *Adv. Mater.* **2008**, *20*, 2171.
[26] A. Kawahara, H. Katsuki, M. Egashira, *Sens. Actuator, B* **1998**, *49*, 273.
[27] J.-H. Ahn, H.-S. Kim, K.J. Lee, Z. Zhu, E. Menard, R.G. Nuzzo, J.A. Rogers, *IEEE Electron Device Lett.* **2006**, *27*, 460.
[28] S. Mack, M.A. Meitl, A.J. Baca, Z.-T. Zhu, J.A. Rogers, *Appl. Phys. Lett.* **2006**, *88*, 213101.
[29] K.J. Lee, M.A. Meitl, J.-H. Ahn, J.A. Rogers, R.G. Nuzzo, V. Kumar, I. Adesida, *J. Appl. Phys.* **2006**, *100*, 124507.
[30] E. Menard, R.G. Nuzzo, J.A. Rogers, *Appl. Phys. Lett.* **2005**, *86*, 093507.
[31] S.-I. Park, Y. Xiong, R.-H. Kim, P. Elvikis, M. Meitl, D.-H. Kim, J. Wu, J. Yoon, C.-J. Yu, Z. Liu, Y. Huang, K.-C. Hwang, P. Ferreira, X. Li, K. Choquette, J.A. Rogers, *Science* **2009**, *325*, 977.
[32] J.-H. Choi, K.-H. Kim, S.-J. Choi, H.H. Lee, *Nanotechnology* **2006**, *17*, 2246.
[33] D.-H. Kim, Y.-S. Kim, J. Wu, Z. Liu, J. Song, H.-S. Kim, Y.Y. Huang, K.-C. Hwang, J.A. Rogers, *Adv. Mater.* **2009**, *21*, 3703.
[34] D.-H. Kim, J.-H. Ahn, H.-S. Kim, K.J. Lee, T.-H. Kim, C.-J. Yu, R.G. Nuzzo, J.A. Rogers, *IEEE Electron Device Lett.* **2008**, *29*, 73.
[35] J.-H. Ahn, H.-S. Kim, K.J. Lee, S. Jeon, S.J. Kang, Y. Sun, R.G. Nuzzo, J.A. Rogers, *Science* **2006**, *314*, 1754.
[36] I. Jung, G. Shin, V. Malyarchuk, J.S. Ha, J.A. Rogers, *Appl. Phys. Lett.* **2010**, *96*, 021110.
[37] H.C. Ko, M.P. Stoykovich, J. Song, V. Malyarchuk, W.M. Choi, C.-J. Yu, J.B.G. III, J. Xiao, S. Wang, Y. Huang, J.A. Rogers, *Nature* **2008**, *454*, 748.
[38] J. Yoon, A.J. Baca, S.-I. Park, P. Elvikis, J.B.G. III, L. Li, R.H. Kim, J. Xiao, S. Wang, T.-H. Kim, M.J. Motala, B.Y. Ahn, E.B. Duoss, J.A. Lewis, R.G. Nuzzo, P.M. Ferreira, Y. Huang, A. Rockett, J.A. Rogers, *Nat. Mater.* **2008**, *7*, 907.
[39] A.J. Baca, K.J. Yu, J. Xiao, S. Wang, J. Yoon, J.H. Ryu, D. Stevenson, R.G. Nuzzo, A.A. Rockett, Y. Huang, J.A. Rogers, *Energy Environ. Sci.* **2010**, *3*, 208.
[40] S. Kim, J. Wu, A. Carlson, S.H. Jin, A. Kovalsky, P. Glass, Z. Liu, N. Ahmed, S.L. Elgan, W. Chen, P.M. Ferreira, M. Sitti, Y. Huang, J.A. Rogers, *P. Natl. Acad. Sci. U.S.A.* **2010**, *107*, 17095.

[41] D. Chanda, K. Shigeta, S. Gupta, T. can, A. Carlson, A. Mihi, A.J. Baca, G.R. Bogart, P. Braun, J.A. Rogers, *Nat. Nanotechnol.* **2011**, *6*, 402.
[42] D.-H. Kim, N. Lu, R. Ma, Y.-S. Kim, R.-H. Kim, S. Wang, J. Wu, S.M. Won, H. Tao, A. Islam, K.J. Yu, T.-I. Kim, R. Chowdhury, M. Ying, L. Xu, M. Li, H.-J. Chung, H. Keum, M. McCormick, P. Liu, Y.-W. Zhang, F.G. Omenetto, Y. Huang, T. Coleman, J.A. Rogers, *Science* **2011**, *333*, 838.
[43] H. Kim, E. Brueckner, J. Song, Y. Li, S. Kim, C. Lu, J. sulking, K. Choquette, Y. Huang, R.G. Nuzzo, J.A. Rogers, *Proc. Natl. Acad. Sci. U.S.A.* **2011**, *108*(25), 10072.
[44] T.-H. Kim, K.-S. Cho, E.K. Lee, S.J. Lee, J. Chae, J.W. Kim, D.H. Kim, J.-Y. Kwon, S.Y. Lee, B.L. Choi, Y. Kuk, J.M. Kim, K. Kim, *submitted* **2010**.
[45] Q. Cao, H.-S. Kim, N. Pimparkar, J.P. Kulkarni, C. Wang, M. Shim, K. Roy, M.A. Alam, J.A. Rogers, *Nature* **2008**, *454*, 495.
[46] Q. Cao, J.A. Rogers, *Nano Res.* **2008**, *1*, 259.
[47] M.A. Meitl, Z.-T. Zhu, V. Kumar, K.J. Lee, X. Feng, Y.Y. Huang, I. Adesida, R.G. Nuzzo, J.A. Rogers, *Nat. Mater.* **2006**, *5*, 33.
[48] Y. Sun, S. Kim, I. Adesida, J.A. Rogers, *Appl. Phys. Lett.* **2005**, *87*, 083501.
[49] Y.-L. Loo, R.L. Willett, K.W. Baldwin, J.A. Rogers, *Appl. Phys. Lett.* **2002**, *81*, 562.
[50] D. Suh, S.-J. Choi, H.H. Lee, *Adv. Mater.* **2005**, *17*, 1554.
[51] D.R. Hines, S. Mezhenny, M. Breban, E.D. Williams, V.W. Ballarotto, G. Esen, A. Southard, M.S. Fuhrer, *Appl. Phys. Lett.* **2005**, *86*, 163101.
[52] J. Zaumseil, M.A. Meitl, J.W.P. Hsu, B.R. Acharya, K.W. Baldwin, Y.-L. Loo, J.A. Rogers, *Nano Lett.* **2003**, *3*, 1223.
[53] S.-H. Hur, D.-Y. Khang, C. Kocabas, J.A. Rogers, *Appl. Phys. Lett.* **2004**, *85*, 5730.
[54] H. Ahn, K.J. Lee, W.R. Childs, J.A. Rogers, R.G. Nuzzo, A. Shim, *J. Appl. Phys.* **2006**, *100*, 0849071.
[55] W.R. Childs, M.J. Motala, K.J. Lee, R.G. Nuzzo, *Langmuir* **2005**, *21*, 10096.
[56] W.R. Childs, R.G. Nuzzo, *J. Am. Chem. Soc.* **2002**, *124*, 13583.
[57] W.R. Childs, R.G. Nuzzo, *Adv. Mater.* **2004**, *16*, 1323.
[58] W.R. Childs, R.G. Nuzzo, *Langmuir* **2005**, *21*, 195.
[59] M.A. Meitl, Y. Zhou, A. Gaur, S. Jeon, M.L. Usrey, M.S. Strano, J.A. Rogers, *Nano Lett.* **2004**, *4*, 1643.
[60] T. Kraus, L. Malaquin, H. Schmid, W. Riess, N.D. Spencer, H. Wolf, *Nat. Nanotechnol.* **2007**, *2*, 570.
[61] K.J. Lee, H. Ahn, M.J. Motala, R.G. Nuzzo, E. Menard, J.A. Rogers, *J. Micromech. Microeng.* **2010**, *20*, 075018.
[62] S.Y. Park, T. Kwon, H.H. Lee, *Adv. Mater.* **2006**, *18*, 1861.
[63] S.-M. Seo, J.H. Kim, H.H. Lee, *Appl. Phys. Lett.* **2006**, *89*, 253515.
[64] K.-H. Kim, S.-Y. Huh, S.-M. Seo, H.H. Lee, *Org. Electron.* **2008**, *9*, 1118.
[65] J.A. Rogers, H.H. Lee, *Unconventional nanopatterning techniques and applications*. 2008, Hoboken: John Wiley & Sons, Inc. 598.
[66] J.K. Kim, J.W. Park, H. Yang, M. Choi, J.H. Choi, K.Y. Suh, *Nanotechnology* **2006**, *17*, 940.
[67] Z. Wang, J. Zhang, R. Xing, J. Yuan, D. Yan, Y. Han, *J. Am. Chem. Soc.* **2003**, *125*, 15278.
[68] A.J. Baca, M.A. Meitl, H.C. Ko, S. Mack, H.-S. Kim, J. Dong, P.M. Ferreira, J.A. Rogers, *Adv. Func. Mater.* **2007**, *17*, 3051.

[69] K.J. Lee, M.J. Motala, M.A. Meitl, W.R. Childs, E. Menard, A.K. Shim, J.A. Rogers, R.G. Nuzzo, *Adv. Mater.* **2005**, *17*, 2332.
[70] X. Feng, M.A. Meitl, A.M. Bowen, Y. Huang, R.G. Nuzzo, J.A. Rogers, *Langmuir* **2007**, *23*, 12555.
[71] J.-H. Ahn, H.-S. Kim, E. Menard, K.J. Lee, Z. Zhu, D.-H. Kim, R.G. Nuzzo, J.A. Rogers, I. Amlani, V. Kushner, S.G. Thomas, T. Duenas, *Appl. Phys. Lett.* **2007**, *90*, 2135011.
[72] Y. Sun, E. Menard, J.A. Rogers, H.-S. Kim, S. Kim, G. Chen, I. Adesida, R. Dettmer, R. Cortez, A. Tewksbury, *Appl. Phys. Lett.* **2006**, *88*, 183509.
[73] H.C. Ko, A.J. Baca, J.A. Rogers, *Nano Lett.* **2006**, *6*, 2318.
[74] Y. Sun, D.-Y. Khang, F. Hua, K. Hurley, R.G. Nuzzo, J.A. Rogers, *Adv. Func. Mater.* **2005**, *15*, 30.
[75] Y. Sun, J.A. Rogers, *Nano Lett.* **2004**, *4*, 1953.
[76] H.-C. Yuan, J. Shin, G. Qin, L. Sun, P. Bhattacharya, M.G. Lagally, G.K. Celler, Z. Ma, *Appl. Phys. Lett.* **2009**, *94*, 013102.
[77] T.-H. Kim, A. Carlson, J.-H. Ahn, S.M. Won, S. Wang, Y. Huang, J.A. Rogers, *Appl. Phys. Lett.* **2009**, *94*, 113502.
[78] T.L. Anderson, *Fracture mechanics: fundamentals and applications*. 2nd. ed. 1995, Boca Raton: CRC Press.
[79] K.H. Tsai, K.S. Kim, *Int. J. Solids. Struct.* **1993**, *30*, 1789.
[80] A.N. Gent, *J. Polym. Sci. B: Polym. Phys.* **1994**, *32*, 1543.
[81] A.N. Gent, *Langmuir* **1996**, *12*, 4492.
[82] K.S. Kim, J. Kim, *J. Eng. Mater. Technol.* **1988**, *110*, 266.
[83] K. Shull, D. Ahn, W.-L. Chem, C.M. Flanigan, A. Crosby, *Macromol. Chem. Phys.* **1998**, *199*, 489.
[84] A. Carlson, H.-J. Kim-Lee, J. Wu, P. Elvikis, H. Cheng, A. Kovalsky, S. Elgan, Q. Yu, P.M. Ferreira, Y. Huang, K.T. Turner, J.A. Rogers, *Appl. Phys. Lett.* **2011**, *98*, 264104.
[85] I. McMackin, J. Choi, P. Schumaker, V. Nguyen, F. Xu, E. Thompson, D. Babbs, S.V. Sreenivasan, M. Watts, N. Schumaker, *Proc. SPIE* **2004**, *5374*, 222.
[86] Y. Yin, B. Gates, Y. Xia, *Adv. Mater.* **2000**, *12*, 1426.
[87] Z.-T. Zhu, E. Menard, K. Hurley, R.G. Nuzzo, J.A. Rogers, *Appl. Phys. Lett.* **2005**, *86*, 133507.
[88] M.A. Meitl, X. Feng, J. Dong, E. Menard, P.M. Ferreira, Y. Huang, J.A. Rogers, *Appl. Phys. Lett.* **2007**, *90*, 083110.
[89] H. Onoe, E. Iwase, K. Matsumoto, I. Shimoyama, *J. Micromech. Microeng.* **2007**, *17*, 1818.
[90] Y. Yang, Y. Hwang, H.A. Cho, J.-H. Song, S.-J. Park, J.A. Rogers, H.C. Ko, *Small* **2011**, *7*, 484.
[91] C.L. Mirley, J.T. Koberstein, *Langmuir* **1995**, *11*, 1049.
[92] M. Ouyang, C. Yuan, R.J. Muisener, A. Boulares, J.T. Koberstein, *Chem. Mater.* **2000**, *12*, 1591.
[93] K. Efimenko, W.E. Wallace, J. Genzer, *J. Colloid Interface Sci.* **2002**, *254*, 306.
[94] D.C. Duffy, J.C. McDonald, O.J.A. Schueller, G.M. Whitesides, *Anal. Chem.* **1998**, *70*, 4974.
[95] M.M. Roberts, L.J. Klein, D.E. Savage, K.A. Slinker, M. Friesen, G. Celler, M.A. Eriksson, M.G. Lagally, *Nat. Mater.* **2006**, *5*, 388.

[96] J.L. Hoyt, H.M. Nayfeh, S. Eguchi, I. Aberg, G. Xia, T. Drake, E.A. Fitzgerald, D.A. Antoniadis, *Tech. Dig. - Int. Electron Devices Meet.* **2002**, 23.
[97] H.-C. Yuan, Z. Ma, M.M. Roberts, D.E. Savage, M.G. Lagally, *J. Appl. Phys.* **2006**, *100*, 013708.
[98] H. Yang, H. Pan, Z. Qiang, Z. Ma, W. Zhou, *Electron. Letters* **2008**, *44*, 858.
[99] Z. Qiang, H. Yang, L. Chen, H. Pang, Z. Ma, W. Zhou, *Appl. Phys. Lett.* **2008**, *93*, 061106.
[100] Y. Sun, R.A. Graff, M.S. Strano, J.A. Rogers, *Small* **2005**, *1*, 1052.
[101] J. Yoon, S. Jo, I.S. Chun, I. Jung, H.-S. Kim, M. Meitl, E. Menard, X. Li, J.J. Coleman, U. Paik, J.A. Rogers, *Nature* **2010**, *465*, 329.
[102] Z. Fan, J.C. Ho, Z.A. Jacobson, H. Razavi, A. Javey, *Proc. Natl. Acad. Sci. U.S.A.* **2008**, *105*, 11066.
[103] J.J. Cole, C.R. Bary, R.J. Knuesel, X. Wang, H.O. Jacobs, *Langmuir* **2010**, *27*, 7321.
[104] D.J. Sirbuly, G.M. Lowman, B. Scott, G.D. Stucky, S.K. Buratto, *Adv. Mater.* **2003**, *15*, 149.
[105] D.J. Gargas, O. Muresan, D.J. Sirbuly, S.K. Buratto, *Adv. Mater.* **2006**, *18*, 3164.
[106] Y.Y. Li, P. Kim, M.J. Sailor, *Phys. Status. Solidi A: Appl. Mater. Sci.* **2005**, *202*, 1616.
[107] C. Baratto, G. Faglia, G. Sberveglieri, Z. Gaburro, L. Pancheri, C. Oton, L. Pavesi, *Sensors* **2002**, *2*, 121.
[108] A. Loni, L.T. Canham, M.G. Berger, R. Arens-Fischer, H. Munder, H. Luth, H.F. Arrand, T.M. Benson, *Thin Solid Films* **1996**, *276*, 143.
[109] H. Ouyang, C.C. Striemer, P.M. Fauchet, *Appl. Phys. Lett.* **2006**, *88*, 163108.
[110] S.O. Meade, M.S. Yoon, K.H. Ahn, M.J. Sailor, *Adv. Mater.* **2004**, *16*, 1811.
[111] C. Mazzoleni, L. Pavesi, *Appl. Phys. Lett.* **1995**, *67*, 2983.
[112] J. Volk, J. Balázs, A.L. Tóth, I. Bársony, *Sens. Actuators, B* **2004**, *100*, 163.
[113] E. Xifré-Pérez, L.F. Marsal, J. Ferré-Borrull, J. Pallarès, *J. Appl. Phys.* **2007**, *102*, 063111.
[114] D. Mangaiyarkarasi, M.B.H. Breese, Y.S. Ow, *Appl. Phys. Lett.* **2008**, *93*, 221905.
[115] F. Cunin, T.A. Schmedake, J.R. Link, Y.Y. Li, J. Koh, S.N. Bhatia, M.J. Sailor, *Nat. Mater.* **2002**, *1*, 39.
[116] A.C. Ford, J.C. Ho, Z. Fan, O. Ergen, V. Altoe, S. Aloni, H. Razavi, A. Javey, *Nano Res.* **2008**, *1*, 32.
[117] A.C. Ford, J.C. Ho, Y.-L. Chueh, Y.-C. Tseng, Z.Y. Fan, J. Guo, J. Bokor, A. Javey, *Nano Lett.* **2009**, *9*, 360.
[118] A. Javey, S. Nam, R.S. Friedman, H. Yan, C.M. Lieber, *Nano Lett.* **2007**, *7*, 773.
[119] Y. Huang, X. Duan, C. Lieber, *Small* **2005**, *1*, 142.
[120] O.L. Muskens, S.L. Diedenhofen, B.C. Kaas, R.E. Algra, E.P.A.M. Bakkers, J.G. Rivas, A. Lagendijk, *Nano Lett.* **2009**, *9*, 930.
[121] Z.Y. Fan, J.G. Lu, *Appl. Phys. Lett.* **2005**, *86*, 123510.
[122] D.H. Zhang, Z. Liu, C. Li, T. Tang, X. Liu, S. Han, B. Lei, C. Zhou, *Nano Lett.* **2004**, *4*, 1919.
[123] H. Tang, M. Yan, X. Ma, H. Zhang, M. Wang, D. Yang, *Sens. and Actuators B* **2005**, *113*, 324.
[124] C.K. Chan, H. Peng, G. Liu, K. McIlwrath, X.F. Zhang, R.A. Huggins, Y. Cui, *Nature* **2008**, *3*, 31.

[125] W. Lu, J. Xiang, B.P. Timko, Y. Wu, C.M. Lieber, *Proc. Natl. Acad. Sci. USA* **2005**, *102*, 10046.
[126] K. Heo, C.-J. Kim, M.-H. Jo, S. Hong, *J. Mater. Chem.* **2009**, *19*, 901.
[127] W. Lu, C.M. Lieber, *J. Phys. D: Appl. Phys.* **2006**, *39*, R387.
[128] H.J. Fan, P. Wener, M. Zacharias, *Small* **2006**, *2*, 700.
[129] Y. Cui, M.T. Björk, J.A. Liddle, C. Sönnichsen, B. Boussert, A.P. Alivisatos, *Nano Lett.* **2004**, *4*, 1093.
[130] Y. Xia, P. Yang, Y. Sun, Y. Wu, B. Mayers, B. Gates, Y. Yin, F. Kim, H. Yan, *Adv. Mater.* **2003**, *15*, 353.
[131] P.A. Smith, C.D. Nordquist, T.N. Jackson, T.S. Mayer, B.R. Martin, J. Mbindyo, T.E. Mallouk, *Appl. Phys. Lett.* **2000**, *77*, 1290272.
[132] B. Messer, J.H. Song, P. Yang, *J. Am. Chem. Soc.* **2000**, *122*, 10232.
[133] S. Myung, M. Lee, G.T. Kim, J.S. Ha, S.Hong, *Adv. Mater.* **2005**, *17*, 2361.
[134] B.Y. Yoo, Y.W. Rheem, W.P. Beyermann, N.V. Myung, *Nanotechnology* **2006**, *17*, 2512.
[135] S.W. Nam, X. Jiang, Q. Xiong, D. Ham, C. Lieber, *Proc. Natl. Acad. Sci. U.S.A.* **2009**, *106*, 21035.
[136] Z. Fan, J.C. Ho, Z.A. Jacobson, R. Yerushalmi, R.L. Alley, H. Razavi, A. Javey, *Nano Lett.* **2008**, *8*, 20.
[137] T. Takahashi, K. Takei, J.C. Ho, Y.-L. Chueh, Z. Fan, A. Javey, *J. Am. Chem. Soc.* **2009**, *131*, 2102.
[138] Z. Fan, J.C. Ho, T. Takahashi, R. Yerushalmi, K. Takei, A.C. Ford, Y.-L. Chueh, A. Javey, *Adv. Mater.* **2009**, *21*, 3730.
[139] R. Yerushalmi, Z.A. Jacobson, J.C. Ho, Z. Fan, A. Javey, *Appl. Phys. Lett.* **2007**, *91*, 203104.
[140] S.J. Park, J.S. Ha, Y.J. Chang, G.T. Kim, *Chem. Phys. Lett.* **2004**, *390*, 199.
[141] Y.-K. Kim, P.S. Kang, D.-I. Kim, G. Shin, G.T. Kim, J.S. Ha, *Small* **2009**, *5*, 727.
[142] Y.K. Kim, S.J. Park, J.P. Koo, D.J. Oh, G.T. Kim, S. Hong, J.S. Ha, *Nanotechnology* **2006**, *17*, 1375.
[143] S.A. Fortuna, J. Wen, I.S. Chun, X. Li, *Nano Lett.* **2008**, *8*, 4421.
[144] P. Alivisatos, *Pure Appl. Phys.* **2000**, *72*, 3.
[145] C.B. Murray, C.R. Kagan, M.G. Bawendi, *Science* **1995**, *270*, 1335.
[146] J. Hu, L. Li, W. Yang, L. Manna, L. Wang, A.P. Alivisatos, *Science* **2001**, *292*, 2060.
[147] A.P. Alivisatos, *Science* **1996**, *271*, 933.
[148] S. Coe, W.-K. Woo, M. Bawendi, V. Bulovic, *Nature* **2002**, *420*, 800.
[149] P.O. Anikeeva, J.E. Halpert, M.G. Bawendi, V. Bulović, *Nano Lett.* **2007**, *7*, 2196.
[150] A. Rizzo, Y. Li, S. Kudera, F. Della-Sala, M. Zanella, W.J. Parak, R. Cingolani, L. Manna, G. Gigli, *Appl. Phys. Lett.* **2007**, *90*, 051106.
[151] J. Zhao, J.A. Bardecker, A.M. Munro, M.S. Liu, Y. Niu, I.K. Ding, J. Luo, B. Chen, A.K. Jen, D.S. Ginger, *Nano Lett.* **2006**, *6*, 463.
[152] Y. Li, A. Rizzo, M. Mazzeo, L. Carbone, L. Manna, R. Cingolani, G. Gigli, *J. Appl. Phys.* **2005**, *97*, 113501.
[153] Y.Q. Li, A. Rizzo, R. Cingolani, G. Gigli, *Adv. Mater.* **2006**, *18*, 2545.
[154] M.A. Islam, I.P. Herman, *Appl. Phys. Lett.* **2002**, *80*, 3823.
[155] V. Santhanam, R.P. Andres, *Nano Lett.* **2004**, *4*, 41.
[156] V. Santhanam, J. Liu, R. Agarwal, R.P. Andres, *Langmuir* **2003**, *19*, 7881.
[157] B.O. Dabbousi, C.B. Murray, M.F. Rubner, M.G. Bawendi, *Chem. Mater.* **1994**, *6*, 216.

[158] S. Coe-Sullivan, J.S. Steckel, W.-K. Woo, M.G. Bawendi, V. Bulovic, *Adv. Func. Mater.* **2005**, *15*, 1117.
[159] A. Rizzo, M. Mazzeo, M. Palumbo, G. Lerario, S. D'Amone, R. Cingolani, G. Gigli, *Adv. Mater.* **2008**, *20*, 1886.
[160] L. Kim, P.O. Anikeeva, S.A. Coe-Sullivan, J.S. Steckel, M.G. Bawendi, V. Bulovic, *Nano Lett.* **2008**, *8*, 4513.
[161] A. Rizzo, M. Mazzeo, M. Biasiucci, R. Cingolani, G. Gigli, *Small* **2008**, *4*, 2143.
[162] R.C. Dunn, *Chem. Rev.* **1999**, *99*, 2891.
[163] S.K. Buratto, *Curr. Opin. Solid St. M.* **1996**, *1*, 485.
[164] L. Novotny, S.J. Stranick, *Annu. Rev. Phys. Chem.* **2006**, *57*, 303.
[165] K. Hoshino, T.C. Turner, S. Kim, A. Gopal, X. Zhang, *Langmuir* **2008**, *24*, 13804.
[166] E. Menard, L. Bilhaut, J. Zaumseil, J.A. Rogers, *Langmuir* **2004**, *20*, 6871.
[167] Y.-L. Loo, D.V. Lang, J.A. Rogers, J.W.P. Hsu, *Nano Lett.* **2003**, *3*, 913.
[168] Y.-L. Loo, J.W.P. Hsu, R.L. Willett, K.W. Baldwin, K.W. West, J.A. Rogers, *J. Vac. Sci. Technol. B* **2002**, *20*, 2853.
[169] N.A. Abu-Hatab, J.M. Oran, M.J. Sepaniak, *ACS Nano* **2008**, *2*, 377.
[170] T.-I. Kim, J.-H. Kim, S.J. Son, S.-M. Seo, *Nanotechnology* **2008**, *19*, 1.
[171] M. Xue, Y. Yang, T. Cao, *Adv. Mater.* **2008**, *20*, 596.
[172] J.C. Love, L.A. Estroff, J.K. Kriebel, R.G. Nuzzo, G.M. Whitesides, *Chem. Rev.* **2005**, *105*, 1103.
[173] S.L. Lehoczkya, R.J. Ledericha, J.J.B. Jr., *Thin Solid Films* **1978**, *55*, 125.
[174] O.J.A. Schueller, D.C. Duffy, J.A. Rogers, S.T. Brittain, G.M. Whitesides, *Sens. Actuators, A* **1999**, *78*, 149.
[175] A. Plecis, Y. Chen, *Microelectron. Eng.* **2007**, *84*, 1265.
[176] Y. Berdichevsky, J. Khandurina, A. Guttman, Y.-H. Lo, *Sensor. Actuat. B-Chem* **2004**, *97*, 402.
[177] J.-W. Kim, K.-Y. Yang, S.-H. Hong, H. Lee, *Appl. Surf. Sci.* **2008**, *254*, 5607.
[178] B.H. Lee, Y.H. Cho, H. Lee, K.-D. Lee, S.H. Kim, M.M. Sung, *Adv. Mater.* **2007**, *19*, 1714.
[179] K. Oh, B.H. Lee, J.K. Hwang, H. Lee, K.H. Lee, S. Im, M.M. Sung, *Small* **2009**, *5*, 558.
[180] C.-H. Chen, Y.-C. Lee, *J. Micromech. Microeng.* **2007**, *17*, 1252.
[181] B. LeDrogoff, B. Cui, T. Veres, *Appl. Phys. Lett.* **2006**, *89*, 113103.
[182] Z. Wang, J. Yuan, J. Zhang, R. Xing, D. Yan, Y. Han, *Adv. Mater.* **2003**, *15*, 1009.
[183] M.-G. Kang, L.J. Guo, *J. Vac. Sci. Technol. B* **2008**, *26*, 2421.
[184] A.J. Tunnell, V.W. Ballarotto, D.R. Hines, E.D. Williams, *Appl. Phys. Lett.* **2008**, *93*, 193113.
[185] D. Suh, J. Rhee, H.H. Lee, *Nanotechnology* **2004**, *15*, 1103.
[186] X. Yu, S. Yu, Z. Wang, D. Ma, Y. Han, *Appl. Phys. Lett.* **2006**, *88*, 263517.
[187] F. Zhang, H.Y. Low, *Nanotechnology* **2008**, *19*, 415305.
[188] C.D. Schaper, *Nano Lett.* **2003**, *3*, 1305.
[189] J. Yu, V. Bulovic, *Appl. Phys. Lett.* **2007**, *91*, 043102.
[190] C.E. Packard, A. Murarka, E.W. Lam, M.A. Schmidt, V. Bulovic, *Adv. Mater.* **2010**, *22*, 1.
[191] C. Kim, P.E. Burrows, S.R. Forrest, *Science* **2000**, *288*, 831.
[192] T.-W. Lee, J. Zaumseil, Z. Bao, J.W.P. Hsu, J.A. Rogers, *Proc. Natl. Acad. Sci. U.S.A.* **2004**, *101*, 429.

[193] J. Zaumseil, K.W. Baldwin, J.A. Rogers, *J. Appl. Phys.* **2003**, *93*, 6117.
[194] C. Kim, M. Shtein, S.R. Forrest, *Appl. Phys. Lett.* **2002**, *80*, 4051.
[195] G.S. Ferguson, M.K. Chaudhury, G.B. Sigal, G.M. Whitesides, *Science* **1991**, *253*, 776.
[196] C. Kim, S.R. Forrest, *Adv. Mater.* **2003**, *15*, 541.
[197] A. Erbe, W. Jiang, Z. Bao, D. Abusch-Magder, D.M. Tennant, E. Garfunkel, N. Zhitenev, *J. Vac. Sci. Technol. B* **2005**, *23*, 3132.
[198] W.T.S. Huck, N. Bowden, P. Onck, T. Pardoen, J.W. Hutchinson, G.M. Whitesides, *Langmuir* **2000**, *16*, 3497.
[199] M.V. Kunnavakkam, F.M. Houlihan, M. Schlax, J.A. Liddle, P. Kolodner, O. Nalamasu, J.A. Rogers, *Appl. Phys. Lett.* **2003**, *82*, 1152.
[200] N. Bowden, W.T.S. Huck, K.E. Paul, G.M. Whitesides, *Appl. Phys. Lett.* **1999**, *75*, 2557.
[201] N. Bowden, S. Brittain, A.G. Evans, J.W. Hutchinson, G.M. Whitesides, *Nature* **1998**, *393*, 146.
[202] T.T. Truong, R. Lin, S. Jeon, H.H. Lee, J. Maria, A. Gaur, F. Hua, I. Meinel, J.A. Rogers, *Langmuir* **2007**, *23*, 2898.
[203] S.S. Williams, S. Retterer, R. Lopez, R. Ruiz, E.T. Samulski, J.M. DeSimone, *Nano Lett.* **2010**, *10*, 1421.
[204] M.K. Kwak, T.-I. Kim, P. Kim, H.H. Lee, K.Y. Suh, *Small* **2009**, *5*, 928.
[205] M.K. Kwak, P. Kim, J.K. Kim, C.I. Park, H.S. Cho, K.Y. Suh, *Proc. of SPIE* **2008**, *7039*, 70390D.
[206] J.N. Lee, C. Park, G.M. Whitesides, *Anal. Chem.* **2003**, *75*, 6544.
[207] J. Kim, M.K. Chaudhury, M.J. Owen, T. Orbeck, *J. Colloid Interf. Sci.* **2001**, *244*, 200.
[208] D. Bodas, C. Khan-Malek, *Sens. Actuators, B* **2007**, *123*, 368.
[209] J.L. Fritz, M.J. Owen, *J. Adhesion* **1995**, *54*, 33.
[210] D.T. Eddington, J.P. Puccinelli, D.J. Beebe, *Sens. Actuators, B* **2006**, *114*, 170.
[211] A. Oláh, H. Hillborg, G.J. Vancso, *Appl. Surf. Sci.* **2005**, *239*, 410.
[212] H. Hillborg, J.F. Ankner, U.W. Gedde, G.D. Smith, H.K. Yasuda, K. Wikstrom, *Polymer* **2000**, *41*, 6851.
[213] S. Olcum, A. Kocabas, G. Ertas, A. Atalar, A. Aydinli, *Opt. Express* **2009**, *17*, 8542.
[214] R.M. Cole, S. Mahajan, J.J. Baumberg, *Appl. Phys. Lett.* **2009**, *95*, 154103.
[215] S.R. Forrest, *Nature* **2004**, *428*, 911.
[216] J. Kim, S. Yun, *Macromolecules* **2006**, *39*, 4202.
[217] H.S. Kim, J. Kim, W. Jung, J. Ampofo, W. Craft, J. Sankar, *Smart Mater. Struct.* **2008**, *17*, 015029.
[218] J. Kim, Y.B. Seo, *Smart Mater. Struct.* **2002**, *11*, 355.
[219] S. Yun, Y. Chen, J.N. Nayak, J. Kim, *Sens. Actuators, B* **2008**, *129*, 652.
[220] H.G. Lim, G.Y. Cho, J. Kim, K.S. Kang, *J. Micromech. Microeng.* **2007**, *17*, 1415.
[221] J. Kim, S.-H. Bae, H.-G. Lim, *Smart Mater. Struct.* **2006**, *15*, 889.
[222] A.M. Bowen, R.G. Nuzzo, *Adv. Func. Mater.* **2009**, *19*, 3243.
[223] K.W. Rhee, L.M. Shirey, P.I. Isaacson, C.F. Kornegay, W.J. Dressick, M.-S. Chen, S.L. Brandow, *J. Vac. Sci. Technol. B* **2000**, *18*, 3569.
[224] J.P. Folkers, C.B. Gorman, P.E. Laibinis, S. Buchholz, G.M. Whitesides, *Langmuir* **1995**, *11*, 813.
[225] N. Adden, L.J. Gamble, D.G. Castner, A. Hoffmann, G. Gross, H. Menzel, *Langmuir* **2006**, *22*, 8197.
[226] M. Xue, Z. Zhang, N. Zhu, F. Wang, X. Zhao, T. Cao, *Langmuir* **2009**, *25*, 4347.

[227] M. Xue, S. Guo, X.S. Zhao, T. Cao, *Scripta Mater.* **2008**, *58*, 854.
[228] J. Aizenberg, P.V. Braun, P. Wiltzius, *Phys. Rev. Lett.* **2000**, *84*, 2997.
[229] N.V. Dziomkina, G.J. Vancso, *Soft Matter* **2005**, *1*, 265.
[230] S. Srinivasan, J. Hiller, B. Kabius, O. Auciello, *Appl. Phys. Lett.* **2007**, *90*, 134101.
[231] H.D. Espinosa, B.C. Prorok, B. Peng, K.H. Kim, N. Moldovan, O. Auciello, J.A. Carlisle, D.M. Gruen, D.C. Mancini, *Exp. Mech.* **2003**, *43*, 256.
[232] O.A. Williams, *Semicond. Sci. Technol.* **2006**, *21*, R49.
[233] O. Auciello, A.V. Sumant, *Diamond. Relat. Mater.* **2010**, *19*, 699.
[234] W. Yang, O. Auciello, J.E. Butler, W. Cai, J.A. Carlisle, J.E. Gerbi, D.M. Gruen, T. Knickerbocker, T.L. Lasseter, J. J.N. Russell, L.M. Smith, R.J. Hamers, *Nat. Mater.* **2002**, *1*, 253.
[235] S. Park, R.S. Ruoff, *Nat. Nanotech.* **2009**, *4*, 217.
[236] C. Soldano, A. Mahmood, E. Dujardin, *Carbon* **2010**, *48*, 2127.
[237] X. Huang, Z. Yin, S. Wu, X. Qi, Q. Zhang, Q. Yan, F. Boey, H. Zhang, *Small* **2011**, *7*, 1876.
[238] Y. Zhu, S. Murali, W. Cai, X. Li, J.W. Suk, J.R. Potts, R.S. Ruoff, *Adv. Mater* **2010**, *22*, 3906.
[239] X. Li, Y. Zhu, W. Cai, M. Borysiak, B. Han, D. Chen, R.D. Piner, L. Colombo, R.S. Ruoff, *Nano Lett.* **2009**, *9*, 4359.
[240] K.S. Kim, Y. Zhao, H. Jang, S.Y. Lee, J.M. Kim, K.S. Kim, J.-H. Ahn, P. Kim, J.-Y. Choi, B.H. Hong, *Nature* **2009**, *457*, 706.
[241] Y. Zhou, K.P. Loh, *Adv. Mater* **2010**, *22*, 3615.
[242] X. Liang, A.S.P. Chang, Y. Zhang, B.D. Harteneck, H. Choo, D.L. Olynick, S. Cabrini, *Nano Lett.* **2009**, *9*, 467.
[243] D. Li, W. Windl, N.P. Padture, *Adv. Mater* **2009**, *20*, 1243.
[244] X. Liang, Z. Fu, S.Y. Chou, *Nano Lett.* **2007**, *7*, 3840.
[245] G. Eda, G. Fanchini, M. Chhowalla, *Nat. Nanotech.* **2008**, *3*, 270.
[246] M.J. Allen, V.C. Tung, L. Gomez, Z. Xu, L.-M. Chen, K.S. Nelson, C. Zhou, R.B. Kaner, Y. Yang, *Adv. Mater.* **2009**, *21*, 1.
[247] D. Wei, Y. Liu, *Adv. Mater* **2010**, *22*, 3225.
[248] J.W. Suk, A. Kitt, C.W. Magnusson, Y. Hao, S. Ahmed, J. An, A.K. Swan, B.B. Goldberg, R.S. Ruoff, *ACS Nano* **2011**, *5*, 6916.
[249] T.R. Hendricks, J. Lu, L.T. Drzal, I. Lee, *Adv. Mater* **2008**, *20*, 2008.
[250] S. Bae, H. Kim, Y. Lee, X. Xu, J.-S. Park, Y. Zheng, J. Balakrishnan, T. Lei, H.R. Kim, Y.I. Song, Y.-J. Kim, K.S. Kim, B. Ozyilmaz, J.-H. Ahn, B.H. Hong, S. Iijima, *Nat. Nanotechnol.* **2010**, *5*, 574.
[251] Y. Lee, S. Bae, H. Jang, S. Jang, S.-E. Zhu, S.H. Sim, Y.I. Song, B.H. Hong, J.-H. Ahn, *Nano Lett.* **2010**, *10*, 490.
[252] L. Song, L. Ci, W. Gao, P.M. Ajayan, *ACS Nano* **2009**, *3*, 1353.
[253] K.V. Emtsev, A. Bostwick, K. Horn, J. Jobst, G.L. Kellogg, L. Ley, J.L. McChesney, T. Ohta, S.A. Reshanov, J. Röhrl, E. Rotenberg, A.K. Schmid, D. Waldmann, H.B. Weber, T. Seyller, *Nat. Mater.* **2009**, *8*, 203.
[254] J.D. Caldwell, T.J. Anderson, J.C. Culbertson, G.G. Jernigan, K.D. Hobart, F.J. Kub, M.J. Tadjer, J.L. Tedesco, J.K. Hite, M.A. Mastro, R.L. Myers-Ward, C.R. Eddy, P.M. Campbell, D.K. Gaskill, *ACS Nano* **2010**, *4*, 1108.

[255] J.-H. Chen, M. Ishigami, C. Jang, D.R. Hines, M.S. Fuhrer, E.D. Williams, *Adv. Mater.* **2007**, *19*, 3623.
[256] V.K. Sangwan, D.R. Hines, V.W. Ballarotto, G. Esen, M.S. Fuhrer, E.D. Williams, *Mater. Res. Soc. Symp. Proc. Vol.* **2007**, *963*, 0963Q1057.
[257] S.J. Kang, C. Kocabas, T. Ozel, M. Shim, N. Pimparkar, M.A. Alam, S.V. Rotkin, J.A. Rogers, *Nat. Nanotechnol.* **2007**, *2*, 230.
[258] D. Zhang, K. Ryu, X. Liu, E. Polikarpov, J. Ly, M.E. Tompson, C. Zhou, *Nano Lett.* **2006**, *6*, 1880.
[259] S. Li, Y. Yan, N. Liu, M.B. Chan-Park, Q. Zhang, *Small* **2007**, *3*, 616.
[260] C.L. Pint, Y.-Q. Xu, S. Moghazy, T. Cherukuri, N.T. Alvarez, E.H. Haroz, S. Mahzooni, S.K. Doorn, J. Kono, M. Pasquali, R.H. Hauge, *ACS Nano* **2010**, *4*, 1131.
[261] S. Tawfick, K. O'Brien, A.J. Hart, *Small* **2009**, *5*, 2467.
[262] H. Liu, D. Takagi, S. Chiashi, Y. Homma, *ACS Nano* **2010**, *4*, 933.
[263] Y. Zhou, L. Hu, G. Gruner, *Appl. Phys. Lett.* **2006**, *88*, 123109.
[264] S.J. Kang, C. Kocabas, H.-S. Kim, Q. Cao, M.A. Meitl, D.-Y. Khang, J.A. Rogers, *Nano Lett.* **2007**, *7*, 3343.
[265] S.J. Kang, C. Kocabas, T. Ozel, M. Shim, N. Pimparkar, M.A. Alam, S.V. Rotkin, J.A. Rogers, *Nat. Nanotech.* **2007**, *2*, 230.
[266] S.-H. Hur, O.O. Park, J.A. Rogers, *Appl. Phys. Lett.* **2005**, *86*, 243502.
[267] C. Kocabas, S.J. Kang, T. Ozel, M. Shim, J.A. Rogers, *J. Phys. Chem. C* **2007**, *111*, 17879.
[268] F.N. Ishikawa, H.-K. Chang, K. Ryu, P.-C. Chen, A. Badmaev, L.G. DeArco, G. Shen, C. Zhou, *ACS Nano* **2009**, *3*, 73.
[269] V.K. Sangwan, V.W. Ballarotto, M.S. Fuhrer, E.D. Williams, *Appl. Phys. Lett.* **2008**, *93*, 113112.
[270] C.C. Wu, C.H. Liu, Z. Zhong, *Nano Lett.* **2010**, *10*, 1032.
[271] L. Jiao, B. Fan, X. Xian, Z. Wu, J. Zhang, Z. Liu, *J. Am. Chem. Soc.* **2008**, *130*, 12612.
[272] G.B. Blanchet, Y.-L. Loo, J.A. Rogers, F. Gao, C.R. Fincher, *Appl. Phys. Lett.* **2003**, *82*, 463.
[273] G.B. Blanchet, C.R. Fincher, F. Gao, *Appl. Phys. Lett.* **2003**, *82*, 1290.
[274] M.M. Ling, Z. Bao, *Chem. Mater.* **2004**, *16*, 4824.
[275] S.H. Ko, ed. *Organic Light Emitting Diode - Material, Process, and Devices*. ed. S.H. Ko. 2011, InTech.
[276] C. Kim, Y. Cao, W.O. Soboyejo, S.R. Forrest, *J. Appl. Phys.* **2005**, *97*, 113512.
[277] H. Kim, B. Yoon, J. Sung, D.-G. Choi, C. Park, *J. Mater. Chem.* **2008**, *18*, 3489.
[278] D. Li, L.J. Guo, *J. Phys. D: Appl. Phys.* **2008**, *41*, 105115.
[279] K.-H. Yim, Z. Zheng, Z. Liang, R.H. Friend, W.T.S. Huck, J.-S. Kim, *Adv. Func. Mater.* **2008**, *18*, 1012.
[280] D. Li, L.J. Guo, *Appl. Phys. Lett.* **2006**, *88*, 063513.
[281] D.R. Hines, A.E. Southard, A. Tunnell, V. Sangwan, T. Moore, J.-H. Chen, M.S. Fuhrer, E.D. Williams, *Proc. of SPIE* **2007**, *6658*, 66580Y.
[282] D.R. Hines, A. Southard, M.S. Fuhrer, *J. Appl. Phys.* **2008**, *104*, 024510.
[283] J. Park, S.-O. Shim, H.H. Lee, *Appl. Phys. Lett.* **2005**, *86*, 073505.
[284] K.-H. Kim, K.-W. Bong, H.H. Lee, *Appl. Phys. Lett.* **2007**, *90*, 093505.
[285] S. Liu, H.A. Becerril, M.C. LeMieux, W.M. Wang, J.H. Oh, Z. Bao, *Adv. Mater.* **2009**, *21*, 1266.

[286] K.C. Dickey, S. Subramanian, J.E. Anthony, L.-H. Han, S. Chen, Y.-L. Loo, *Appl. Phys. Lett.* **2007**, *90*, 244103.
[287] S. Yunus, C. deCrombrugghe-deLooringhe, C. Poleunis, A. Delcorte, *Surf. Interface Anal.* **2007**, *39*, 922.
[288] A.L. Briseno, M. Roberts, M.-M. Ling, H. Moon, E.J. Nemanick, Z. Bao, *J. Am. Chem. Soc.* **2006**, *128*, 3880.
[289] K.S. Park, E.K. Seo, Y.R. Do, K. Kim, M.M. Sung, *J. Am. Chem. Soc.* **2006**, *128*, 858.
[290] Y. Berdichevsky, J. Khandurina, A. Guttman, Y.-H. Lo, *Sens. Actuators, B-Chem* **2004**, *97*, 402.
[291] H. Ahn, K.J. Lee, A. Shim, J.A. Rogers, R.G. Nuzzo, *Nano Lett.* **2005**, *5*, 2533.
[292] Y.-K. Kim, J.-H. Park, G.-C. Shin, J.S. Ha, S.J. Park, S.M. Yi, G.T. Kim, *J. Phys.* **2007**, *61*, 560.
[293] Y.-K. Kim, G.T. Kim, J.S. Ha, *Adv. Func. Mater.* **2007**, *17*, 2125.
[294] Z. Zheng, O. Azzaroni, F. Zhou, W.T.S. Huck, *J. Am. Chem. Soc.* **2006**, *128*, 7730.
[295] I.-S. Park, M. Jang, J. Ahn, *Microelectron. Eng.* **2007**, *84*, 1511.
[296] A.L. Thangawng, M.A. Swartz, M.R. Glucksberg, R.S. Ruoff, *Small* **2007**, *3*, 132.
[297] S. Takayama, E. Ostuni, X. Qian, J.C. McDonald, X. Jiang, P. LeDuc, M.-H. Wu, D.E. Ingber, G.M. Whitesides, *Adv. Mater.* **2001**, *13*, 570.
[298] B. Cortese, C. Piliego, I. Viola, S. D'Amone, R. Cingolani, G. Gigli, *Langmuir*, *Article ASAP*.
[299] M. Kim, Y.S. Kim, *J. Am. Chem. Soc.* **2007**, *129*, 11304.
[300] C. Sanchez, F. Verbakel, M.J. Escuti, C.W.M. Bastiaansen, D.J. Boer, *Adv. Mater.* **2008**, *20*, 74.
[301] X. Jiang, H. Zheng, S. Gourdin, P.T. Hammond, *Langmuir* **2002**, *18*, 2607.
[302] S. Ji, C.-C. Liu, G. Liu, P.F. Nealey, *ACS Nano* **2010**, *4*, 599.
[303] J. Park, P.T. Hammond, *Adv. Mater.* **2004**, *16*, 520.
[304] J.S. Park, S.M. Cho, G.Y. Han, S.J. Sim, J. Park, P.J. Yoo, *Langmuir* **2009**, *25*, 2575.
[305] K.T. Nam, R. Wartena, P.J. Yoo, F.W. Liau, Y.J. Lee, Y.-M. Chiang, P.T. Hammond, A.M. Belcher, *Proc. Natl. Acad. Sci. U.S.A.* **2008**, *105*, 17227.
[306] S. Schmidt, M. Nolte, A. Fery, *Phys. Chem. Phys.* **2007**, *9*, 4967.
[307] K. Nakamatsu, K. Tone, H. Namatsu, S. Matsui, *J. Vac. Sci. Technol. B* **2006**, *24*, 195.
[308] Y.S. Kim, S.J. Baek, P.T. Hammond, *Adv. Mater.* **2004**, *16*, 581.
[309] S.-M. Seo, J.-Y. Park, H.H. Lee, *Appl. Phys. Lett.* **2005**, *86*, 133114.
[310] J.-H. Choi, D. Kim, P.J. Yoo, H.H. Lee, *Adv. Mater.* **2005**, *17*, 166.
[311] J. Zhang, C.M. Li, M.B. Chan-Park, Q. Zhou, Y. Gan, F. Qin, B. Ong, T. Chen, *Appl. Phys. Lett.* **2007**, *90*, 243502.
[312] H. Kang, T.-I. Kim, H.H. Lee, *Appl. Phys. Lett.* **2008**, *93*, 203308.
[313] P. Pieranski, *Contemp. Phys.* **1983**, *24*, 25.
[314] A. vanBlaaderen, R. Ruel, P. Wiltzius, *Nature* **1997**, *385*, 321.
[315] J.D. Joannopoulos, P.R. Villeneuve, S. Fan, *Nature* **1997**, *386*, 143.
[316] J.E.G.J. Wijnhoven, W.L. Vos, *Science* **1998**, *281*, 802.
[317] S.-H. Kim, S.Y. Lee, S.-M. Yang, G.-R. Yi, *NPG Asia Mater.* **2011**, *3*, 25.
[318] M.D. Sacks, T.Y. Tseng, *J. Am. Ceram. Soc.* **1984**, *67*, 526.
[319] E. Kim, Y. Xia, G.M. Whitesides, *Adv. Mater.* **1996**, *8*, 245.
[320] Z.-Z. Gu, A. Fujishima, O. Sato, *Angew. Chem. Int. Ed.* **2002**, *41*, 2067.
[321] E. Kim, Y. Xia, G.M. Whitesides, *J. Am. Chem. Soc.* **1996**, *118*, 5722.

[322] P. Kim, K.W. Kwon, M.C. Park, S.H. Lee, S.M. Kim, K.Y. Suh, *Biochip J.* **2008**, *2*, 1.
[323] J. Yao, X. Yan, G. Lu, K. Zhang, X. Chen, L. Jiang, B. Yang, *Adv. Mater.* **2004**, *16*, 81.
[324] X. Yan, J. Yao, G. Lu, X. Li, J. Zhang, K. Han, B. Yang, *J. Am. Chem. Soc.* **2005**, *127*, 7688.
[325] X. Yan, J. Yao, G. Lu, X. Chen, K. Zhang, B. Yang, *J. Am. Chem. Soc.* **2004**, *126*, 10510.
[326] J.P. Hoogenboom, D.L.J. Vossen, C. Faivre-Moskalenko, M. Dogterom, A. van-Blaaderen, *Appl. Phys. Lett.* **2002**, *80*, 4828.
[327] T. Junno, K. Keeppert, L. Montelius, L. Samuelson, *Appl. Phys. Lett.* **1995**, *66*, 3627.
[328] B.H. Lee, H. Shin, M.M. Sung, *Chem. Mater.* **2007**, *19*, 5553.
[329] X.Y. Ling, I.Y. Phang, D.N. Reinhoudt, G.J. Vancso, J. Huskens, *ACS Appl. Mater. Interfaces* **2009**, *1*, 960.
[330] X.Y. Ling, I.Y. Phang, H. Schonherr, D.N. Reinhoudt, G.J. Vancso, J. Huskens, *Small* **2009**, *5*, 1428.
[331] N.R. Sieb, B.D. Gates, *Adv. Mater.* **2008**, *20*, 1376.
[332] B. Kowalczyk, M.M. Apodaca, H. Nakanishi, S.K. Smoukov, B.A. Grzybowski, *Small* **2009**, *5*, 1970.
[333] J.A. Wigenius, S. Fransson, F. vonPost, O. Inganas, *Biointerphases* **2008**, *3*, 75.
[334] D.J. Solis, S.R. Coyer, A.J. Garcia, E. Delamarche, *Adv. Mater.* **2010**, *22*, 111.
[335] C. Thibault, V. LeBerre, S. Casimirius, E. Trevisiol, J. Francois, C. Vieu, *J. Nanobiotechnology* **2005**, *3*, 7.
[336] S.A. Lange, V. Benes, D.P. Kern, J.K. Heinrich-Hörber, A. Bernard, *Anal. Chem.* **2004**, *76*, 1641.
[337] S.A. Ruiz, C.S. Chen, *Soft Matter* **2007**, *3*, 168.
[338] A. Cerf, C. Thibault, M. Genevieve, C. Vieu, *Microelectron. Eng.* **2009**, *86*, 1419.
[339] D.I. Rozkiewicz, W. Brugman, R.M. Kerkhoven, B.J. Ravoo, D.N. Reinhoudt, *J. Am. Chem. Soc.* **2007**, *129*, 11593.
[340] A.A. Yu, T.A. Savas, G.S. Taylor, A. Guiseppe-Elie, H.I. Smith, F. Stellacci, *Nano Lett.* **2005**, *5*, 1061.
[341] A.A. Yu, T. Savas, S. Cabrini, E. diFabrizio, H.I. Smith, F. Stellacci, *J. Am. Chem. Soc.* **2005**, *127*, 16774.
[342] S. Thevenet, H.-Y. Chen, J. Lahann, F. Stellacci, *Adv. Mater.* **2007**, *19*, 41333.
[343] A.A. Yu, F. Stellacci, *Adv. Mater.* **2007**, *19*, 4338.
[344] J.P. Renault, A. Bernard, D. Juncker, B. Michel, H.R. Bosshard, E. Delamarche, *Angew. Chem. Int. Ed.* **2002**, *41*, 2320.
[345] A. Bernard, D. Fitzli, P. Sonderegger, E. Delamarche, B. Michel, H.R. Bosshard, H. Biebuyck, *Nature Biotech.* **2001**, *19*, 866.
[346] H. Tan, S. Huang, K.-L. Yang, *Langmuir* **2007**, *23*, 8607.
[347] L.B. Thompson, N.H. Mack, R.G. Nuzzo, *Phys. Chem. Chem. Phys.* **2010**, *12*, 4301.
[348] K.Y. Suh, A. Khademhosseini, J.M. Yang, G. Eng, R. Langer, *Adv. Mater.* **2004**, *16*, 584.
[349] W. Senaratne, L. Andruzzi, C.K. Ober, *Biomacromolecules* **2005**, *6*, 2427.
[350] M. Morra, C. Cassineli, *J. Biomater. Sci. Polym. Ed.* **1999**, *10*, 1107.
[351] M. Morra, C. Cassinelli, A. Pavesio, D. Renier, *J. Colloid Interf. Sci.* **2003**, *259*, 236.
[352] D.B. Weibel, W.R. DiLuzio, G.M. Whitesides, *Nat. Rev. Microbiol.* **2007**, *5*, 209.
[353] M. Mayer, J. Yang, I. Gitlin, D.H. Gracias, G.M. Whitesides, *Proteomics* **2004**, *4*, 2366.
[354] D.B. Weibel, A. Lee, M. Mayer, S.F. Brady, D. Bruzewicz, J. Yang, W.R. DiLuzio, J. Clardy, G.M. Whitesides, *Langmuir* **2005**, *21*, 6436.

[355] H. Xu, X.Y. Ling, J. vanBennekom, X. Duan, M.J.W. Ludden, D.N. Reinhoudt, M. Wessling, R.G.H. Lammertink, J. Huskens, *J. Am. Chem. Soc.* **2009**, *131*, 797.
[356] C. Williams, Y. Tsuda, B.C. Isenberg, M. Yamato, T. Shimizu, T. Okano, J.Y. Wong, *Adv. Mater.* **2009**, *21*, 2161.
[357] S. Majd, M. Mayer, *J. Am. Chem. Soc.* **2008**, *130*, 16060.
[358] M.M. Stevens, M. Mayer, D.G. Anderson, D.B. Weibel, G.M. Whitesides, R. Langer, *Biomaterials* **2005**, *26*, 7636.
[359] J. Xiang, W. Lu, Y. Hu, Y. Wu, H. Yan, C. Lieber, *Nature* **2006**, *441*, 489.
[360] L. Sun, G. Qin, J.-H. Seo, G.K. Celler, W. Zhou, Z. Ma, *Small* **2010**, *6*, 2553.
[361] T. Takahashi, K. Takei, E. Adabi, Z. Fan, A.M. Niknejad, A. Javey, *ACS Nano* **2010**, *4*, 5855.
[362] C. Kocabas, H.-S. Kim, T. Banks, J.A. Rogers, A.A. Pesetski, J.E. Baumgardner, S.V. Krishnaswamy, H. Zhang, *Proc. Natl. Acad. Sci. U.S.A.* **2008**, *105*, 1405.
[363] L. Liao, J. Bai, Y. Qu, Y.-C. Lin, Y. Li, Y. Huang, X. Duan, *P. Natl. Acad. Sci. U.S.A.* **2010**, *107*, 6711.
[364] J. Valentine, S. Zhang, T. Zentgraf, E. Ulin-Avila, D.A. Genov, G. Bartai, X. Zhang, *Nature* **2008**, *455*, 376.
[365] R. Service, *Science* **2010**, *328*, 304.
[366] J.M. Nguyen, Y. Nagarah, Y. Qi, S.S. Nonnenmann, A.V. Morozov, S. Li, C.B. Arnold, M.C. McAlpine, *Nano Lett.* **2010**, *10*, 4595.
[367] Y. Qi, N.T. Jafferis, K. Lyons, C.M. Lee, H. Ahmad, M.C. McAlpine, *Nano Lett.* **2010**, *10*, 524.
[368] Y. Qi, M.C. McAlpine, *Energy Environ. Sci.* **2010**, *3*, 1275.
[369] Y. Qi, J. Kim, T.D. Nguyen, B. Lisko, P.K. Purohit, M.C. McAlpine, *Nano Lett.* **2011**, *11*, 1331.
[370] X. Feng, B.D. Yang, Y. Liu, Y. Wang, C. Dagdeviren, Z. Liu, A. Carlson, J. Li, Y. Huang, J.A. Rogers, *ACS Nano* **2011**, *4*, 3326.
[371] T.-H. Kim, K.-S. Cho, E.K. Lee, S.J. Lee, J. Chae, J.W. Kim, D.H. Kim, J.-Y. Kwon, G. Amaratunga, S.Y. Lee, B.L. Choi, Y. Kuk, J.M. Kim, K. Kim, *Nat. Photonics* **2011**, *5*, 176.
[372] K. Takei, T. Takahashi, J.C. Ho, H. Ko, A.G. Gillies, P.W. Leu, R.S. Fearing, A. Javey, *Nat. Mater.* **2010**, *9*, 821.
[373] J. Viventi, D.-H. Kim, J.D. Moss, Y.-S. Kim, J.A. Blanco, N. Annetta, A. Hicks, J. Xiao, Y. Huang, D.J. Callans, J.A. Rogers, B. Litt, *Sci. Transl. Med.* **2010**, *2*, 24ra22.
[374] J. Viventi, D.-H. Kim, L. Vigeland, E.S. Frechette, J.A. Blanco, Y.-S. Kim, A.E. Avrin, V.R. Tiruvadi, S.-W. Hwang, A.C. Vanleer, D.F. Wulsin, K. Davis, C.E. Gelber, L. Palmer, J.V.d. Spiegel, J. Wu, J. Xiao, Y. Huang, D. Contreras, J.A. Rogers, B. Litt, *Nat. Neurosci.* **2011**, *14*, 1599.
[375] D.-H. Kim, N. Lu, R. Ghaffari, Y.-S. Kim, S.P. Lee, L. Xu, J. Wu, R.-H. Kim, J. Song, Z. liu, J. Viventi, B.d. Graff, B. Elolampi, M. Mansour, M.J. Slepian, S. Hwang, J.D. Moss, S.-M. Won, Y. Huang, B. Litt, J.A. Rogers, *Nat. Mater.* **2011**, *10*, 316.
[376] M.J. Slepian, R. Ghaffari, J.A. Rogers, *Interv. Cardiol.* **2011**, *3*, 417.
[377] H.C. Ko, G. Shin, S. Wang, M.P. Stoykovich, J.W. Lee, D.-H. Kim, J.S. Ha, Y. Huang, K.-C. Hwang, J.A. Rogers, *Small* **2009**, *5*, 2703.
[378] G. Shin, I. Jung, V. Malyarchuk, J. Song, S. Wang, H.C. Ko, Y. Huang, J.S. Ha, J.A. Rogers, *Small* **2010**, *6*, 851.

[379] I. Jung, J. Xiao, V. Malyarchuk, C. Lub, M. Li, Z. Liu, J. Yoon, Y. Huang, J.A. Rogers, *Proc. Natl. Acad. Sci. U.S.A.* **2011**, *108*, 1788.
[380] S. Burroughs, R. Conner, B. Furman, E. Menard, A. Gray, M. Meitl, S. Bonafede, D. Kneeburg, K. Ghosal, R. Bukovnic, W. Wagner, S. Seel, M. Sullivan, *A new approach for a low cost CPV module design utilizing micro-transfer printing technology*, in *CPV-6*. 2010: Freiburg, Germany.

B13. Tables

Materials Class	Ink Structure	Common Transfer Protocols	Common Surface Modifications
Inorganic semiconductors *(Section 3)*	• Nanomembranes, nanoribbons, platelets and bars • Nanowires • Quantum Dots	• Additive transfer • Subtractive transfer • Deterministic assembly	• Heat • UV-Ozone or plasma modification • Adhesives
Metals *(Section 4)*	• Thin films in flat and structured forms • Nanowires • Nanoparticles	• Additive transfer • Subtractive transfer	• Heat • Pressure • Adhesives • Water • SAMs
Carbon *(Section 5)*	• Nanomembranes and thin films • Nanotubes	• Additive transfer • Subtractive transfer • Deterministic assembly	• Heat • Adhesives • Pressure
Organic materials *(Section 6)*	• Nanomembranes and thin films • Self-assembled microstructures and/or domains	• Additive transfer • Subtractive transfer	• UV-Ozone or plasma modification • Adhesives • SAMs
Colloids *(Section 7)*	• Nanomembranes and thin films • Self-assembled microstructures and/or domains • Nanoparticles/clusters	• Additive transfer • Subtractive transfer • Deterministic assembly	• Heat • Plasma modification • Adhesives • Water
Biological materials *(Section 8)*	• Nanomembranes and thin films • Self-assembled microstructures • Macromolecular configurations	• Additive transfer	• Adhesives • SAMs • Biocapture

Table B.1. Representative materials classes, structure geometries, transfer protocols and associated surface modifications that have been demonstrated in transfer printing.

B14. Figures

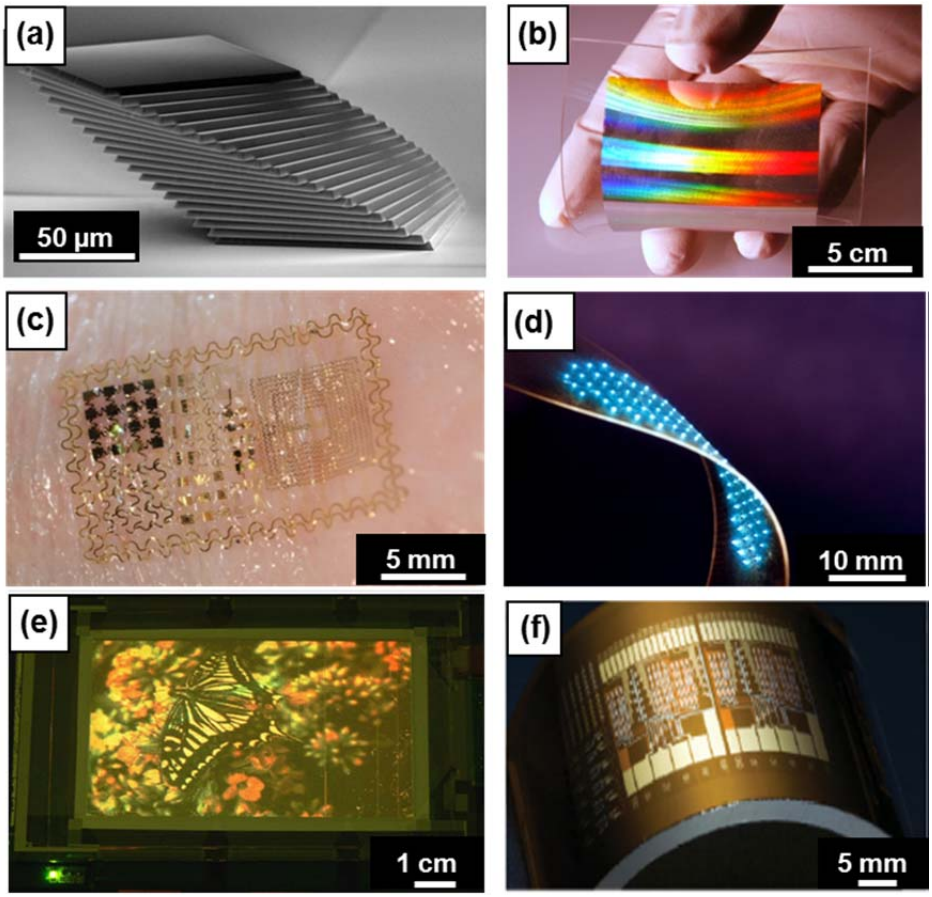

Figure B.1. Representative examples of unusual constructs, devices and integrated systems enabled by the techniques of transfer printing. (a) SEM image of a printed multilayer stack of silicon platelets. (b) Photograph of a large area (10 cm x 10 cm) negative index metamaterial (NIM) comprised of alternating layers of Ag and MgF_2 in a fishnet pattern printed onto flexible substrate. (c) Photograph of an 'epidermal' electronic device, conformally laminated onto the surface of the skin. The key components of the system, from radio frequency antennae, inductive coils, inductors, capacitors, silicon diodes, strain gauges, light emitting diodes (LEDs), temperature sensors, electrophysiological sensors and field effect transistors, are all fabricated by transfer printing. (d) Image of a mechanically flexed array of ultrathin, microscale, blue LEDs printed from a source wafer onto a thin strip of plastic. (e) Picture of a 4-inch, full-colour quantum dot (QD) LED display that uses printed collections of QDs in an active matrix configuration of 320× 240 pixels. (f) Photograph of a flexible integrated circuit (four-bit decoder composed of 88 transistors) that uses printed networks of single walled carbon nanotubes for the semiconductor.

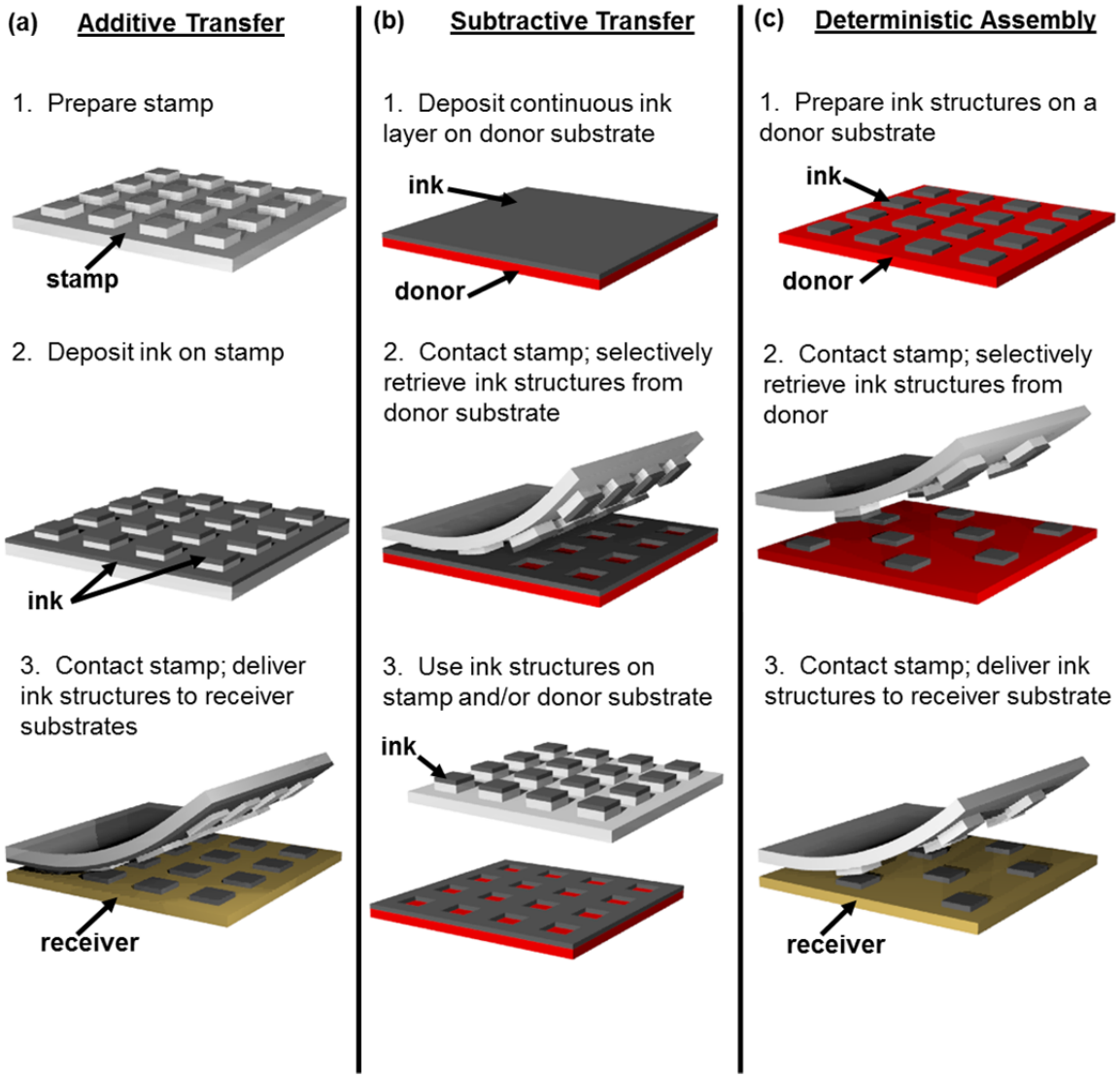

Figure B.2. Schematic illustrations of three basic modes for transfer printing. (a) Additive transfer exploits a stamp that is 'inked' with a material of interest, using processes such as physical vapor deposition, solution casting/assembly, or physical transfer. Contacting such an inked stamp to a target substrate followed by peel-back affects transfer of material. (b) Subtractive transfer starts with a continuous film of material deposited on a donor substrate. A stamp brought into contact with the film selectively removes material in the areas of contact, leaving behind a patterned film on the donor and transferred material on the stamp. A stamp inked in this manner can then be used for additive transfer, as in (a). Alternatively, the patterned material on the donor itself can be used in further device processing. (c) Deterministic assembly involves contact of a stamp with a donor substrate that supports pre-fabricated micro or nanostructures. Peeling the stamp away leads to removal of selected structures from the donor substrate. Printing onto a receiving substrate completes the process. In all three cases, chemical, thermal and/or mechanical strategies facilitate the inking and printing processes, to enable high yield, efficient operation.

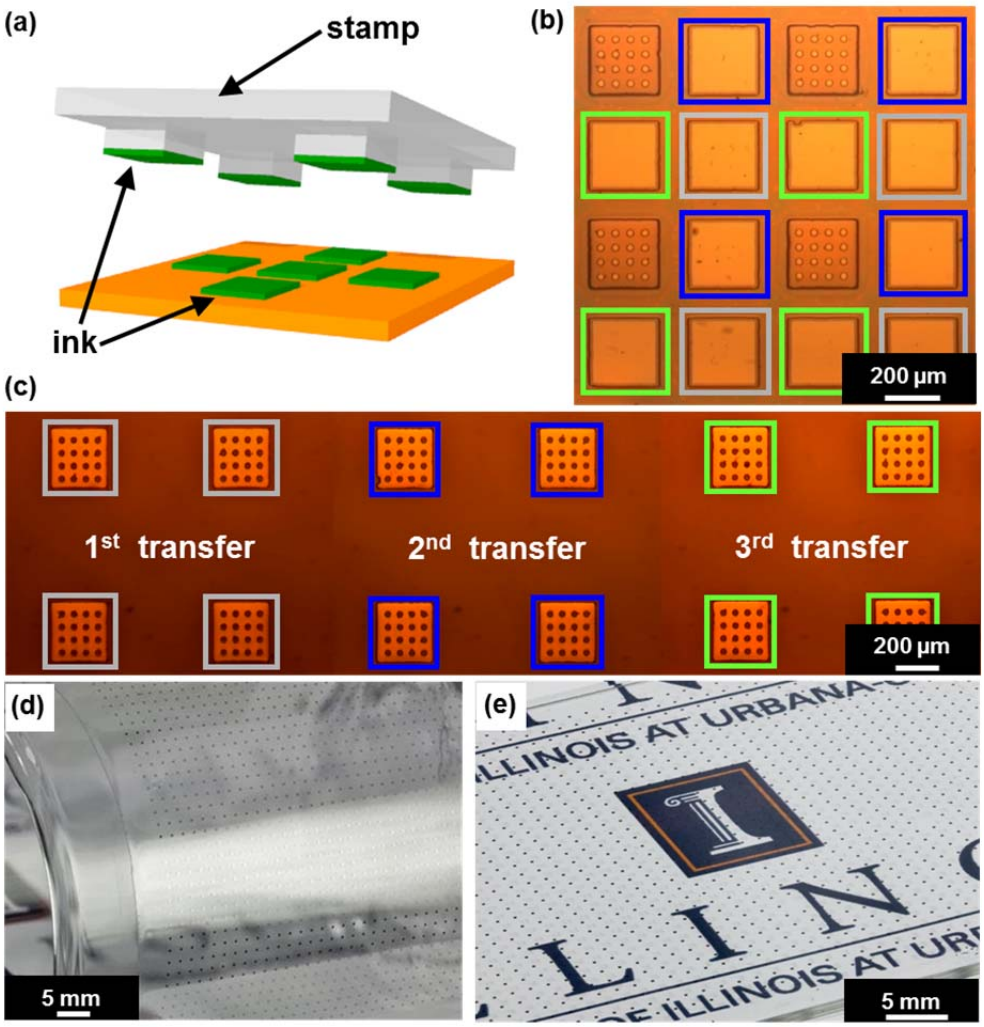

Figure B.3. (a) Schematic illustration of retrieving and printing selected sets of microstructures (platelets designed to yield AlInGaP LEDs) with a stamp. (b) Optical micrograph of a donor substrate after three cycles of printing. Each colored box (gray, blue, green) highlights different sets of platelets retrieved in sequential cycles of printing. (c) Micrograph of a receiving substrate after printing from the donor substrate of (b), illustrating the concept of area expansion, in which dense arrays of microstructures are distributed into sparse configurations. The gray, blue and green boxes show platelets that correspond to those highlighted in a similar manner in (b). (d) Large-scale collection of structures (~1600 in a square array with pitch of 1.4 mm) printed onto a thin, flexible sheet of plastic, shown here wrapped onto a cylindrical glass substrate. (e) Similar collection of structures printed onto a plate of glass.

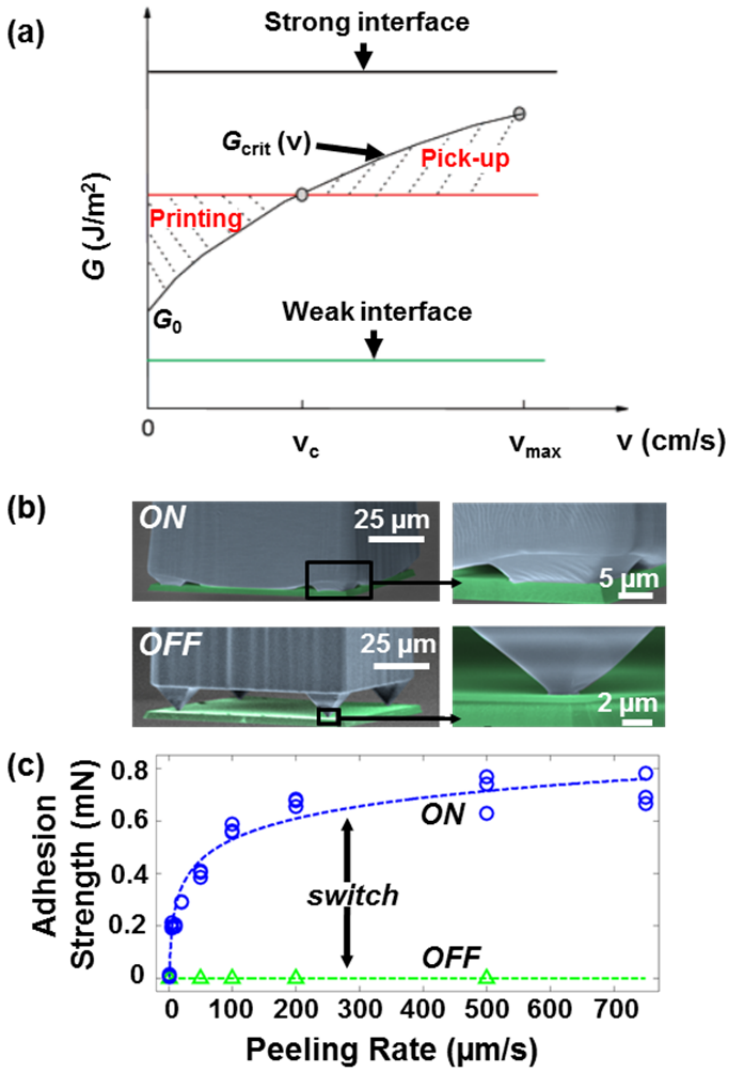

Figure B.4. (a) Schematic diagram of critical energy release rates for the stamp/ink and ink/substrate interfaces of a model printing experiment consisting of a stamp, continuous ink film, and receiver substrate. The intersection of the horizontal line in the middle with the monotonically increasing curve represents the critical peel velocity, v_c, for kinetically controlled transfer printing. The horizontal lines at the bottom and top represent very weak and very strong film/substrate interfaces, respectively, corresponding to retrieval only and printing only conditions. (b) Colored SEM micrographs of microstructured elastomeric surfaces bearing pyramidal microtips in the 'adhesion on' (top panel) and 'adhesion off' (bottom panel) states. Panels on the right show high magnification images of individual microtips in each state. The extreme differences in contact area provide high levels of adhesion switching between off and on states. (c) Pull-off force as a function of delamination velocity for microtipped stamps in the adhesion on and off states. When in full contact, the compressed stamp has a strong rate-dependent behavior due to the viscoelastic nature of the stamp. When only contacting at the microtips, adhesive forces are minimized.

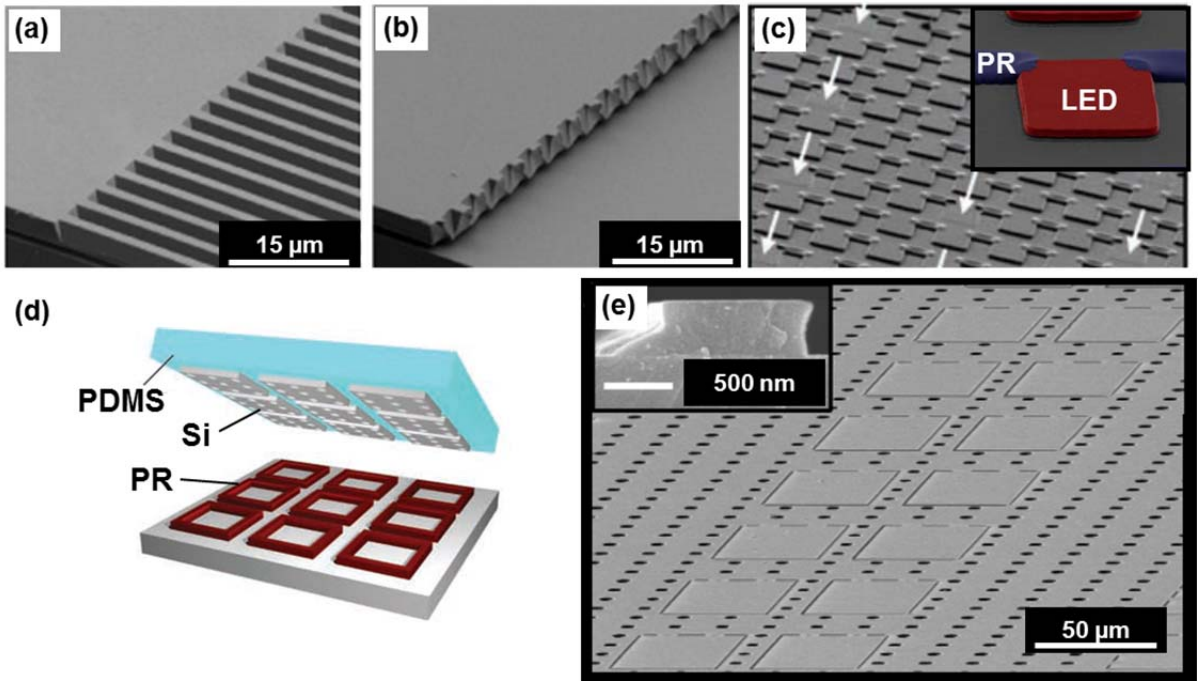

Figure B.5. (a) SEM image of silicon microbar, undercut etched but tethered via 'anchors' at their endpoints to the silicon wafer. (b) SEM image of the wafer after retrieving the microbars with a stamp. (c) SEM image of a GaAs wafer with an array of anchored, undercut etched set of ultrathin, microscale AlInGaP LEDs (indicated by white arrows) with a stamp. The inset shows a colorized angled-view SEM image of an individual LED. A pair of photoresist (PR) anchors (blue) at the two far corners hold the structure (red) above the GaAs wafer (grey) in the suspended configuration of a diving board, to facilitate retrieval with a stamp. (d) Schematic illustration of silicon structures retrieved from a substrate to which they were anchored with PR features around their perimeters. (e) SEM image of the PR structures in (d) after transfer printing. The inset shows cross-sectional view of one such structure.

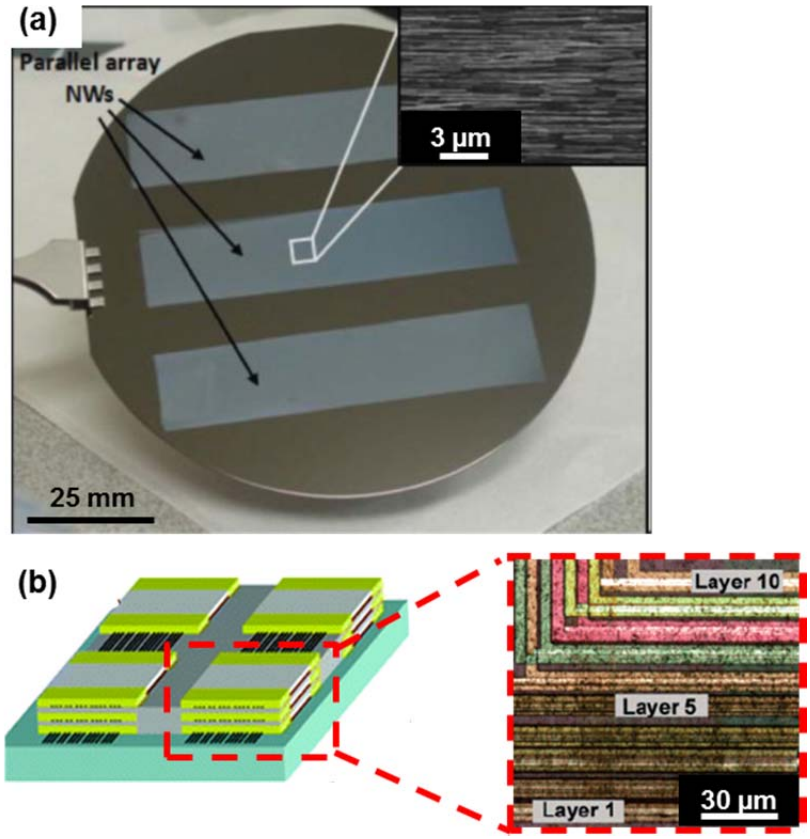

Figure B.6. (a) Photograph of parallel arrays of aligned Ge nanowires (NWs; diameters ~ 30 nm) assembled on a 4 inch diameter silicon wafer by contact printing. The inset provides an SEM image of a region of the printed NWs, showing a density of ~7 NW/μm. (b) Schematic illustration of a printing scheme that uses cylindrical growth substrates as a roller stamp. The SEM image in the inset shows that the grown Ge NWs are randomly oriented on the growth substrate. The printing process transfers these NWs in aligned forms to a receiver substrate through the action of directional shear forces. (c) Three-dimensional NW circuit fabricated by multiple cycles of printing, device fabrication, and interlayer deposition. Optical microscope image of 10 layers of Ge/Si NW field effect transistors. Each device is offset to facilitate imaging.

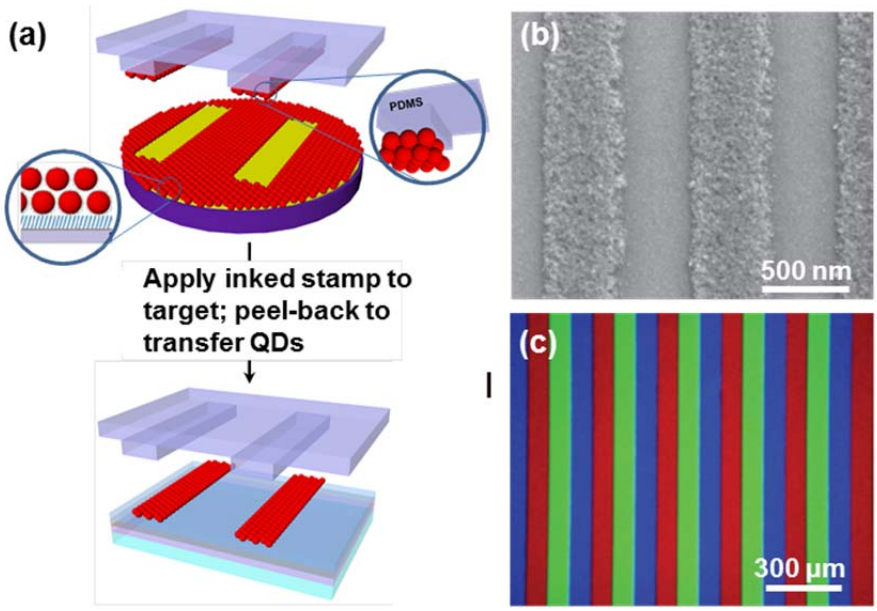

Figure B.7. (a) Schematic illustration of a transfer printing process for the patterning thin layers of quantum dots (QDs). Here, QD layers are retrieved from solution-cast assemblies on functionalize substrates. Red (R), green (G) and blue (B) emissive materials are printed in a sequential, aligned process. (b) SEM image of stripes of QDs printed onto a glass substrate. (c) Fluorescence micrograph of printed RGB stripes on a glass substrate.

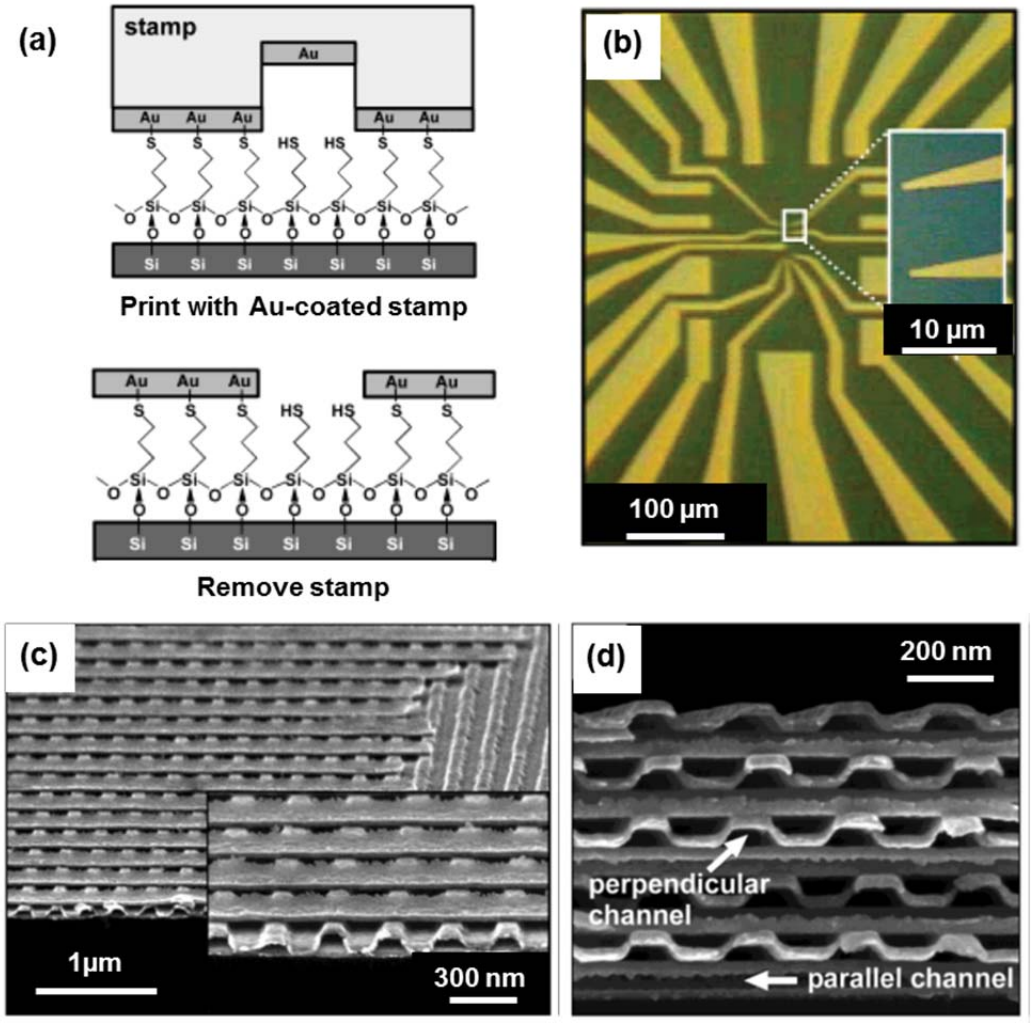

Figure B.8. (a) Schematic illustration of a process for printing thin layers of gold that uses a self-assembled monolayer of 3-mercaptopropyltrimethoxysilane on a silicon wafer. (b) Optical micrograph of a gold pattern printed in this way. (c) SEM image of three-dimensional structures formed by printing gold lines (20 nm thick, 300 nm wide) onto printed nanochannel structures of gold. (d) SEM cross sectional view of sample with 10 consecutively printed nanochannels of gold. Here, the stamps used for each printing step were rotated by 90° with respect to the direction of the channels of the underlying layer. In (c) and (d), the first structure of gold adheres to a GaAs substrate via covalent bonds to a dithiol monolayer. Cold welding bonds the subsequent gold layers to each other.

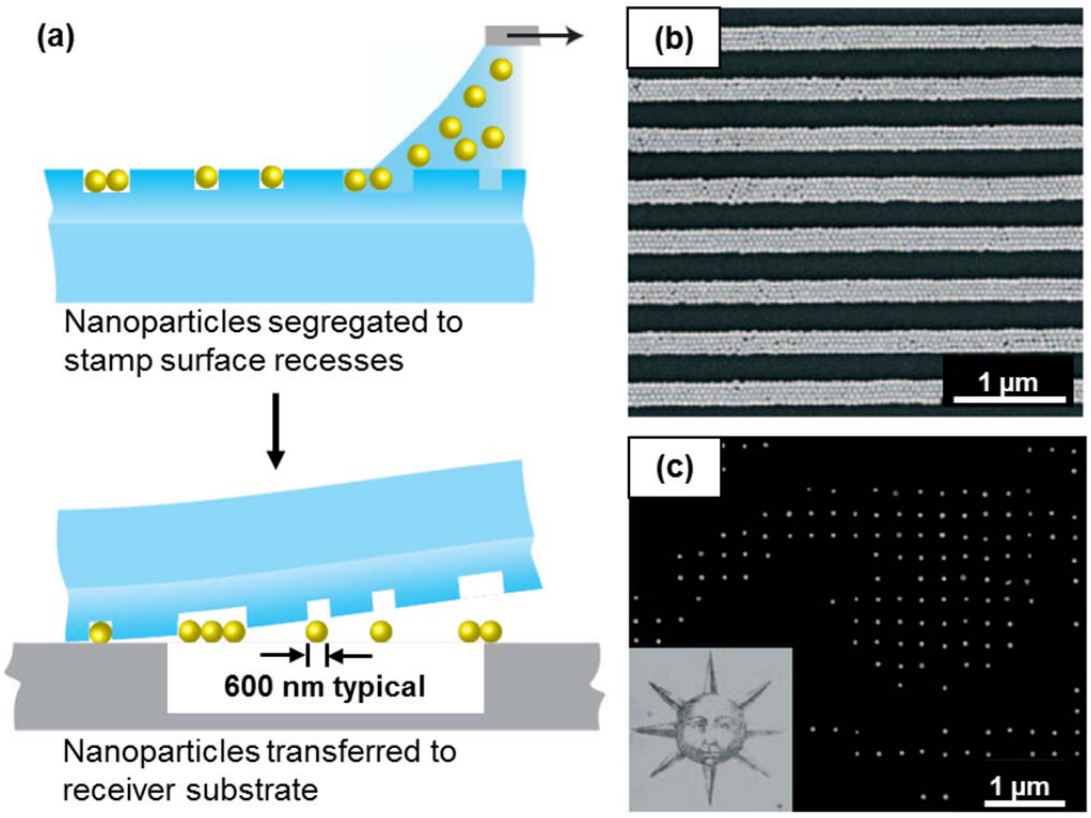

Figure B.9. (a) Schematic representation of transfer printing metallic nanoparticles, in a process that involves casting a solution suspension of the particles onto the surface of a stamp. Assemblies of particles in the recessed regions can be printed onto a receiver substrate. (c) SEM images of 200-nm-wide lines of close-packed 60-nm particles of gold (d) High magnification SEM image of a portion of a sparse (280 nm pitch) collection of 60-nm particles of gold in the layout of an illustration of the sun (inset).

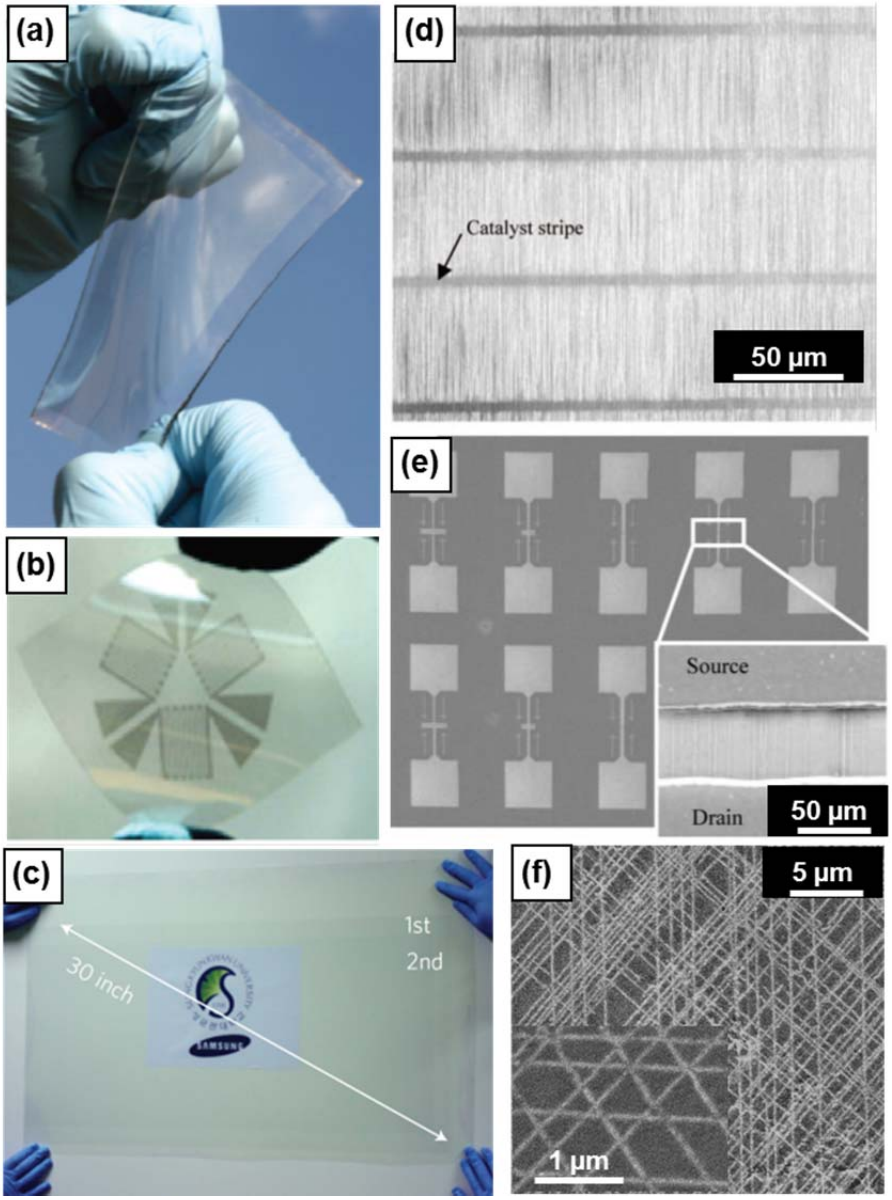

Figure B.10. Printed patterns of graphene and single walled carbon nanotubes (SWNTs). (a) Large area film of graphene film formed by chemical vapor deposition, printed onto a PDMS substrate (b) A three-element rosette strain gauge pattern formed out of graphene on a donor substrate and then printing, in a single step, onto a sheet of PDMS. (c) A transparent ultra-large area graphene film transferred from a copper foil donor substrate, onto a 35-inch sheet of PET, by a continuous, roll-to-roll process. (d) SEM image of aligned SWNTs grown on a quartz substrate and then printed onto a glass substrate coated with a thin layer of epoxy. (e) SEM image of an array of devices built with arrays of SWNTs printed onto a glass plate. The inset provides an SEM image of SWNTs bridging a pair of ITO electrodes in a representative device. (f) SEM image of overlapping, aligned arrays of SWNTs in a triangle lattice, formed by multiple cycles of printing. The inset gives a magnified view.

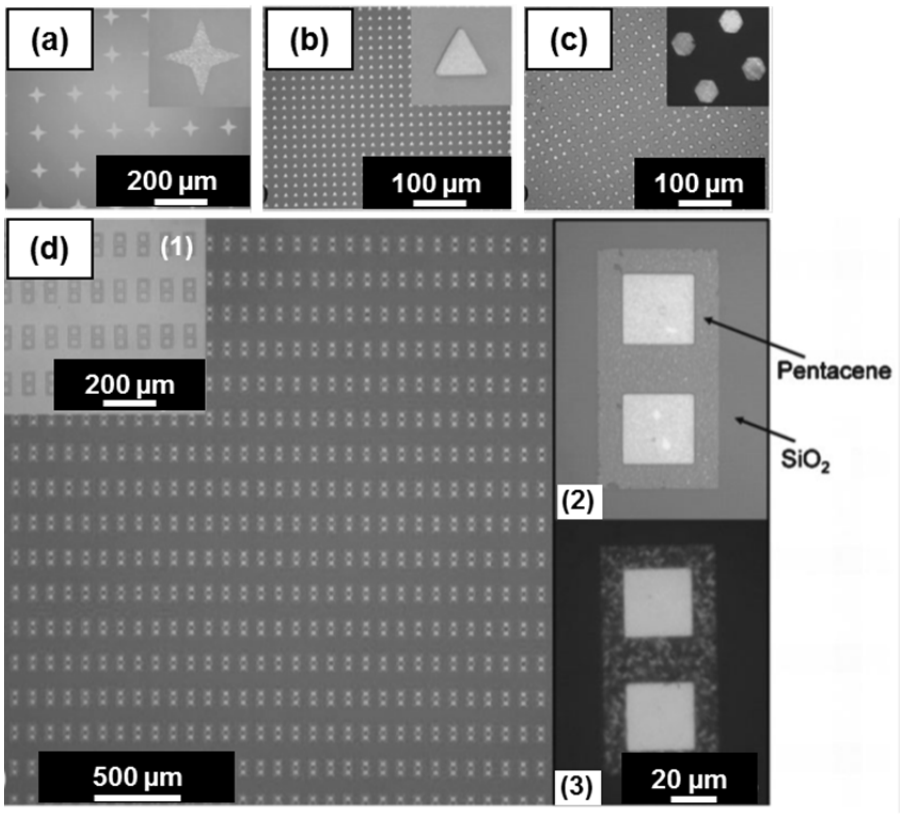

Figure B.11. Transfer printed patterns of solution- and vapor-deposited small-molecule organic semiconductors, and their use in bottom-contact thin film transistors with self-aligned electrodes. Optical micrographs of printed patterns of films of (a) pentacene and (b) hexathiopentacene (HTP)formed by vapor deposition. (c) Micrographs of 5,5'-bis(4-*tert*-butylphenyl)-2,2'-bithiophene (dtb-P2TP) deposited by dip-coating and then transfer printed. The inset is a view through crossed polarizers. (d) Micrographs showing printed bottom-contact pentacene transistors. Inset (1) Pentacene film on Au before transfer. Insets (2,3): Magnified (2) and cross-polarized (3) optical micrographs of the final devices.

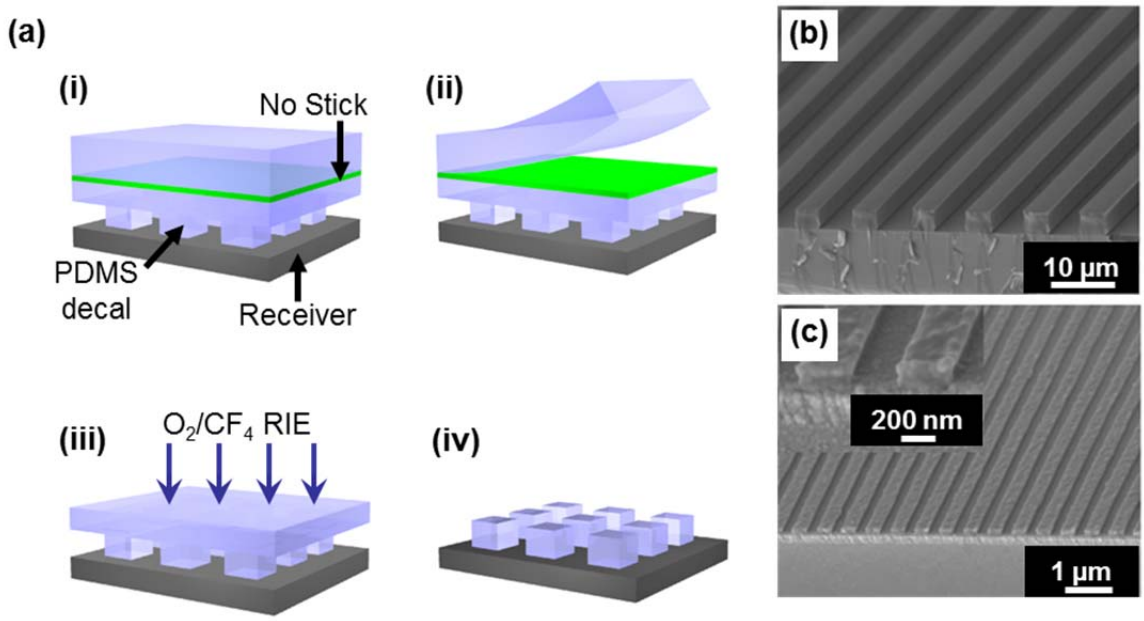

Figure B.12. (a) Schematic illustration for a form of selective pattern release (SPaR) decal transfer lithography to print structures of PDMS. (i) A selectively patterned stamp, which separates surface relief (stabilized by a thin membrane of PDMS) from the bulk of the stamp by an anti-adhesion layer('No Stick'), is permanently sealed to an oxide bearing receiver via UV-Ozone (UVO) treatment. (ii) The bulk PDMS is peeled away at the anti-adhesion interface, leaving behind a PDMS decal pattern on the receiver. (iii) Reactive ion etch (RIE) is used to etch through the stabilizing PDMS membrane, until discrete PDMS decals are revealed (iv). SEM images of (b) 5 □m and (c) 300 nm wide lines of PDMS printed as a closed form decal on an SiO_2/Al/Si substrate, after removal of the connecting top layer of PDMS by RIE. The inset of (c) gives a high resolution cross-sectional SEM image.

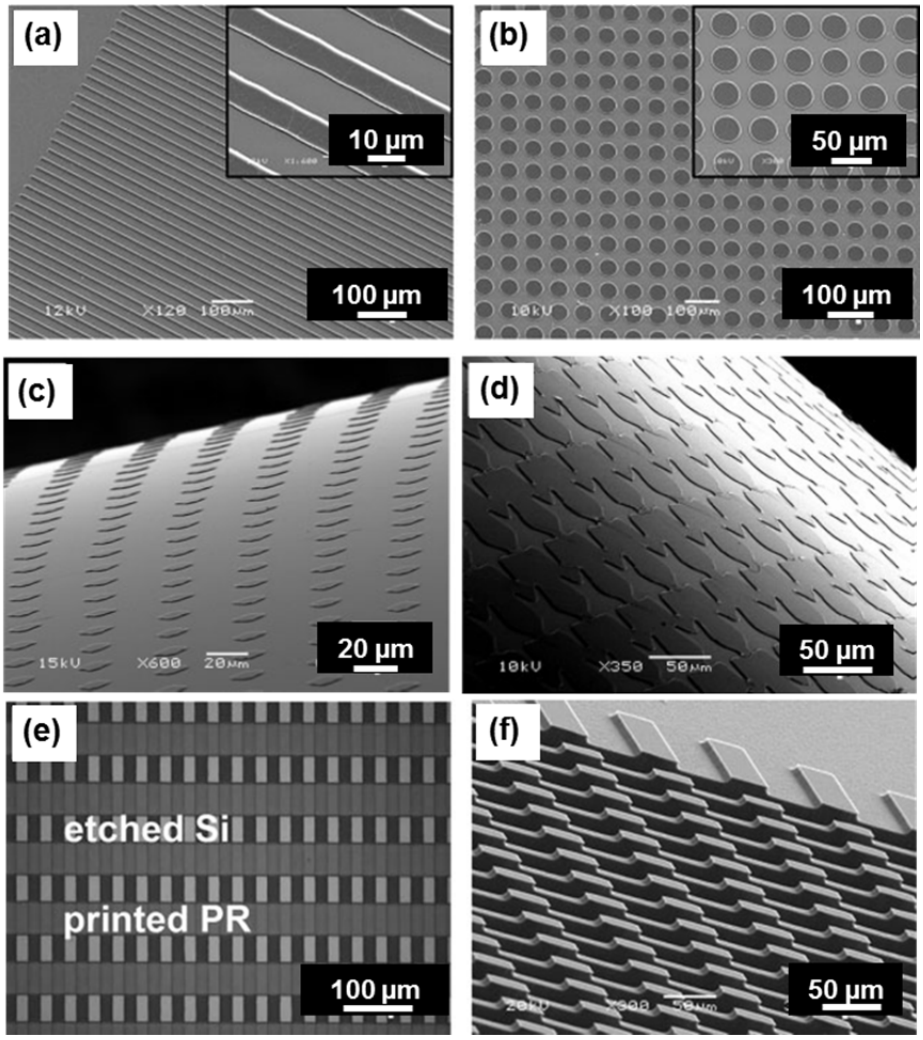

Figure B.13. Diverse patterns of photoresist (PR) transfer printed onto various substrates. SEM images of 0.85-µm-thick PR (S1805) in an array of (a) 10 µm lines separated by 20 µm and (b) 50 µm circles separated by 20 µm. The insets provided magnified views. Slowly rolling a heated cylinder across the stamp results in the PR patterns being picked up by the surface of the cylinder. SEM images of (c) an array of 10 µm x10 µm squares separated by 20 µm and (d) an array of 50-µm-wide star-shaped holes printed onto a glass cylinder with a diameter of 6 mm. (e) Optical micrograph of an array of 50-µm-wide lines PR (2.7 µm thick) on 200-µm wide trenches etched into the surface of a silicon wafer. (f) Multiple levels of relief formed in the silicon by etching the substrate in (e) using the PR as a mask.

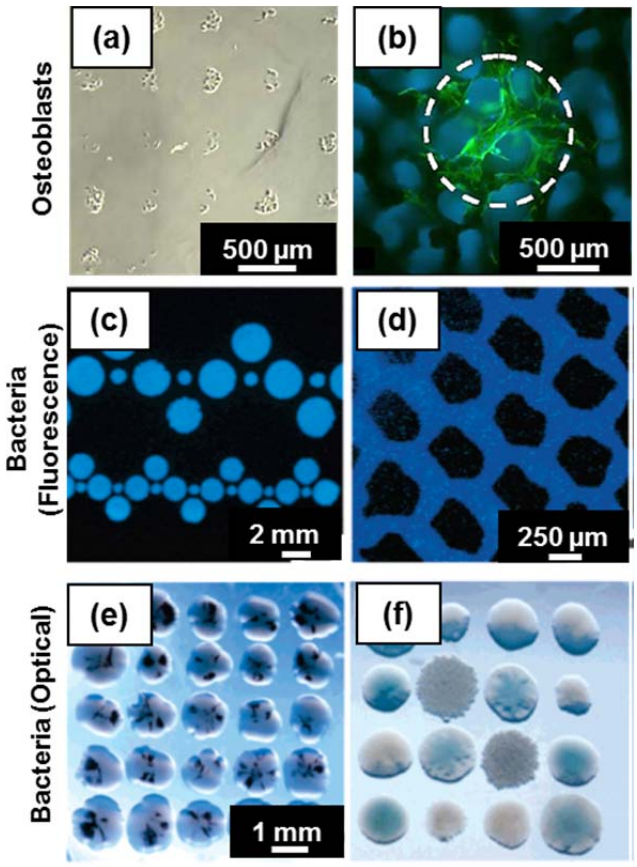

Figure B.14. (a) Fibronectin-coated glass slide patterns of printed cells formed using an agarose stamp with 200 µm features. (b) Scaffold with osteoblasts printed using an agarose stamp with 700 µm diameter circular features. Actin is stained green; phalloidin and DNA are stained blue. The white dashed circle denotes the area patterned with cells. The blue features in the background are artifacts of fluorescence microscopy, resulting from light reflected from the white hydroxyapatite scaffolds. (c)-(d) Images of patterns of V. fischeri printed onto a GVM−agar substrate using an agarose stamp. (e) Printed pattern of E. coli on LB−agar, with blue staining. (f) Array of 5 different printed colonies including E. coli clones that produce: N-acyl amino acid antibiotics (blue); violacein (purple), melanin (brown), and B. subtilis.

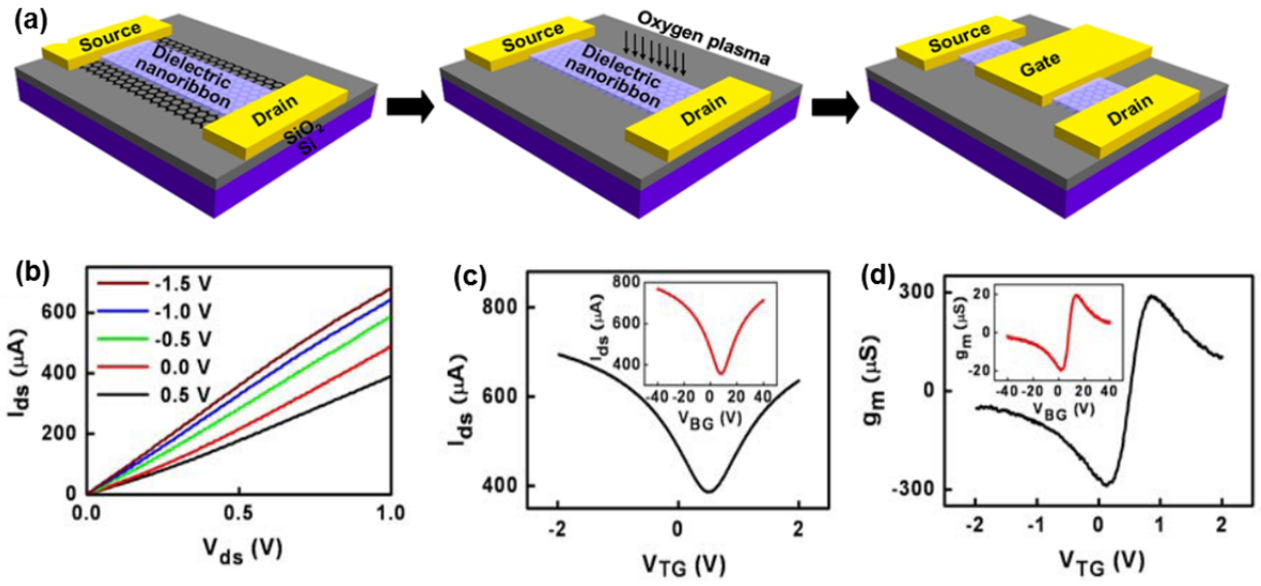

Figure B.15. (a) Process for fabricating top gated graphene transistors using transfer printing of ultrathin, nanoribbon dielectrics of Al_2O_3. Definition of source and drain electrodes is followed by oxygen plasma etching to remove excess graphene. The top gate electrode is defined through lithography and metallization. (b) Room temperature current-voltage characteristics of a typical device. (c) Transfer characteristics of top-gated and back-gated (inset) devices at V_{DS} = 1 V. (d) Transconductance, g_m, as a function of top-gate voltage V_{TG}. The inset plot shows g_m vs. V_{BG}, the voltage on the back-gate.

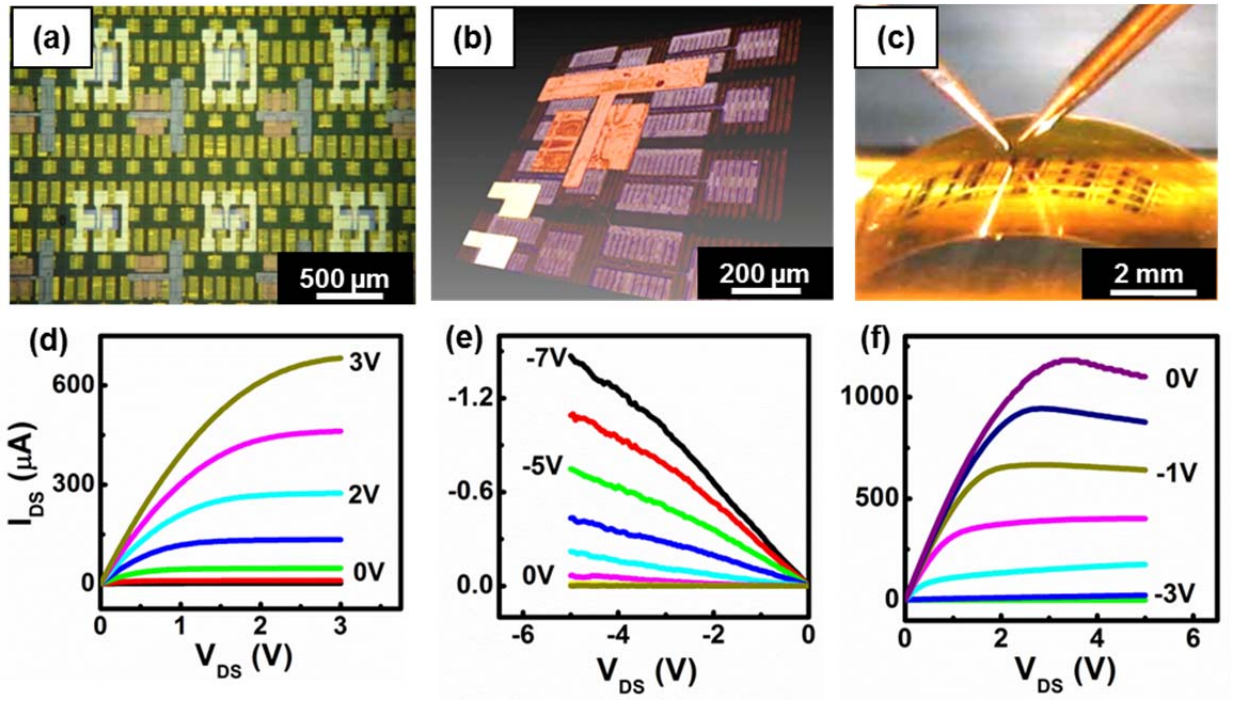

Figure B.16. (a) Optical micrograph of 3D, heterogeneously integrated electronic devices formed by printing, in a sequential fashion, GaN nanoribbons for HEMTs, Si nanoribbons MOSFETs, and SWNT networks for TFTs, in a three-layer stack. (b) 3D image collected by confocal microscopy. The layers are colorized (gold: top layer, Si MOSFETs; red: middle layer, SWNT TFTs; pink: bottom layer GaN HEMTs) for ease of viewing. (c) Image of the system in a bent configuration, during electrical probing. (d) Electrical characteristics of a GaN HEMT from the first layer (channel lengths, widths and gate widths of 20, 170, and 5 µm, respectively, and ribbon thicknesses, widths, and lengths of 1.2, 10, and 150 µm, respectively), (e) a SWNT TFT on the second layer (channel lengths and widths of 50 and 200 µm, respectively, and average tube diameters and lengths of 1.5 nm and 10 µm, respectively) and (f) a Si MOSFET on the third layer (channel lengths and widths of 19 and 200 µm, respectively).

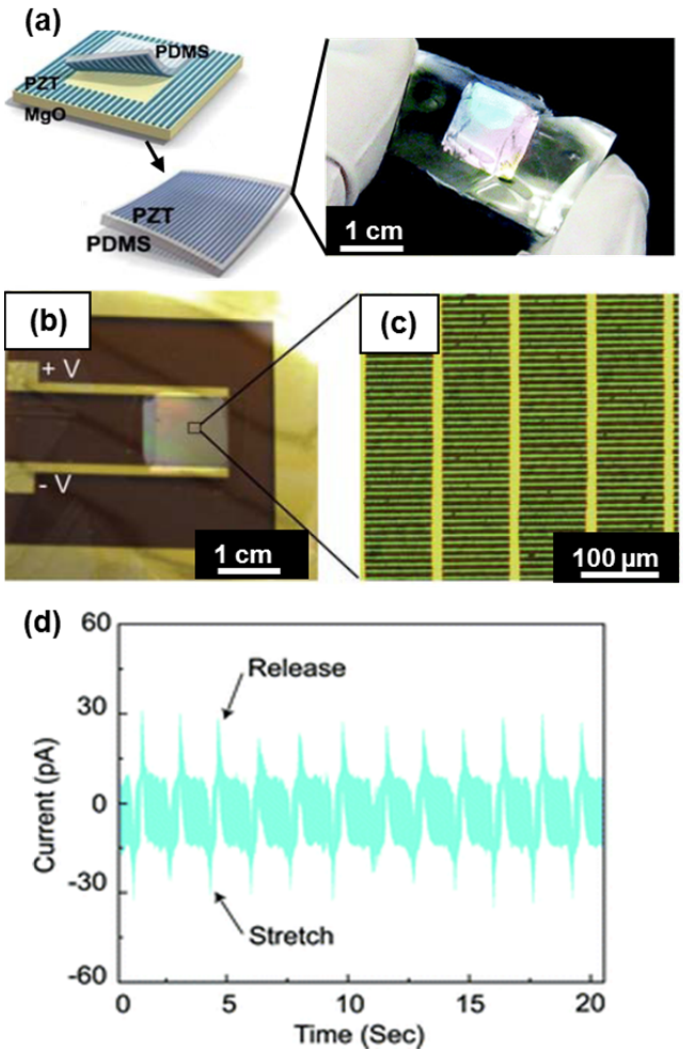

Figure B.17. Nanogenerator device made of PZT ribbons formed on a substrate of MgO and then printed onto a sheet of PDMS. (a) Schematic of the printing process, and photograph of a resulting device. (b) Optical micrograph of an interconnected array of PZT ribbons onto a thin sheet of polyimide and (c) magnified view. (d) Measured short-circuit current.

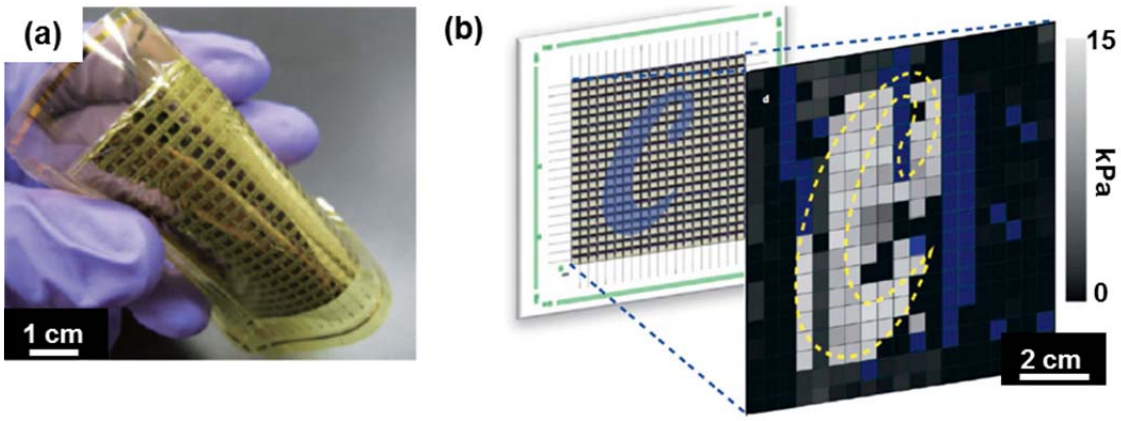

Figure B.18. (a) Array of pressure sensors on a flexible substrate, with active matrix addressing circuitry that incorporates printed arrays of semiconductor nanowires (7 x 7 cm^2 with a 19 x 18 pixel array). (b) Measured response of the device under compression in the geometry of a *'C'* character. The blue pixels are defective.

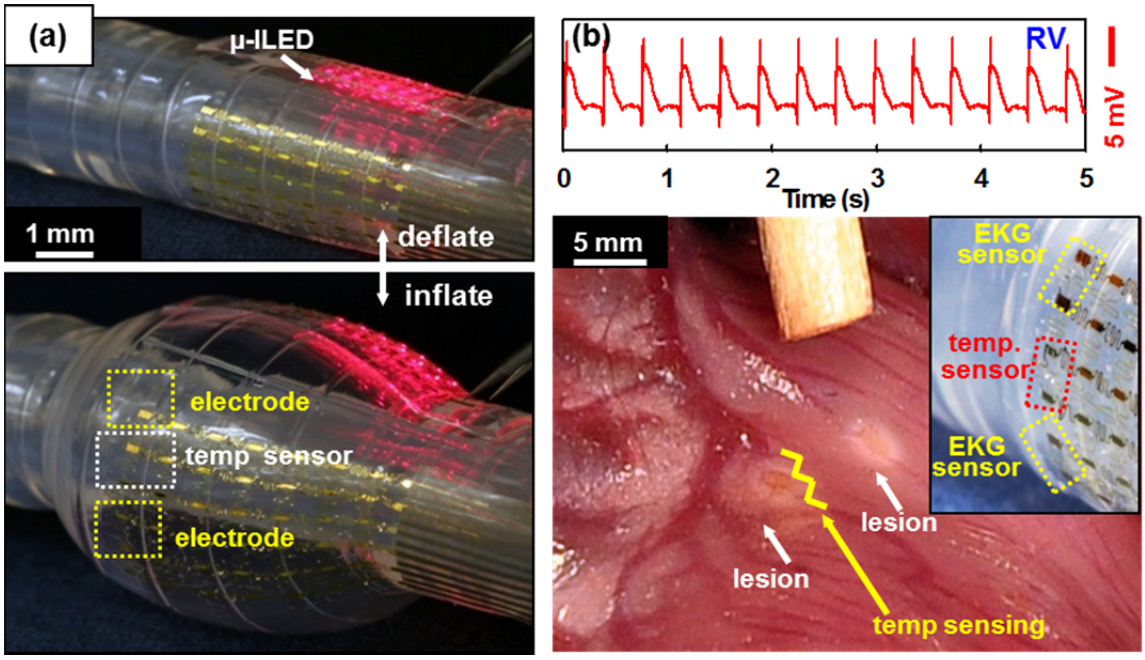

Figure B.19. (a) Optical image of a multifunctional, 'instrumented' balloon catheter in deflated (top panel) and inflated (bottom panel) states. The device includes interconnected arrays of printed components, including temperature sensors (anterior), microscale inorganic LEDs (μ-ILEDs) (posterior) and EP sensors (facing downward) (b) *In vivo* epicardial recordings of electrophysiological responses in a beating rabbit heart. Epicardial activation map of the right ventricle appears in the top panel. The bottom panel shows an optical image of epicardial lesions (white discoloration) created by two pairs of RF ablation electrodes. The yellow line denotes the region of temperature sensing. The inset shows an image of representative EKG sensors co-located with temperature sensors.

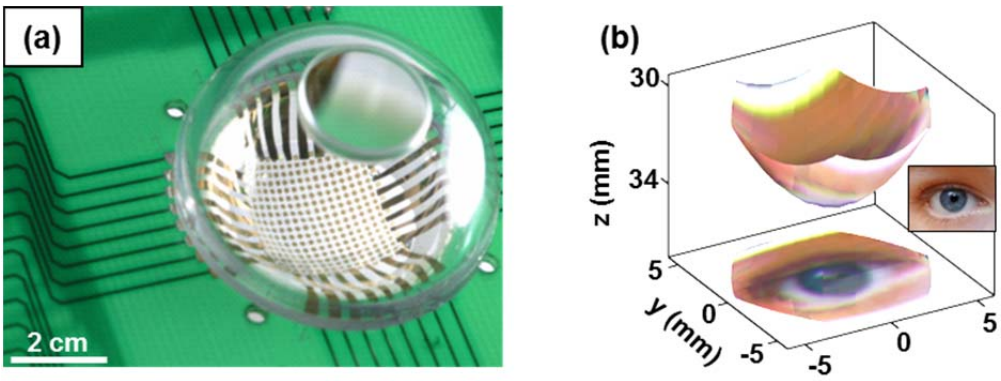

Figure B.20. (a) Photograph of an electronic eyeball camera, consisting of an array of silicon photodiodes printed onto the hemispherical surface of a glass substrate. A transparent hemispherical cap (for ease of viewing) supports a simple, single-component plano-convex imaging lens. (b) Example of a color picture collected with a camera similar to the one in (a) but with a paraboloid curvature. The top part of this frame corresponds to the image itself, while the bottom frame provides a planar projection. The inset at the right shows the object.

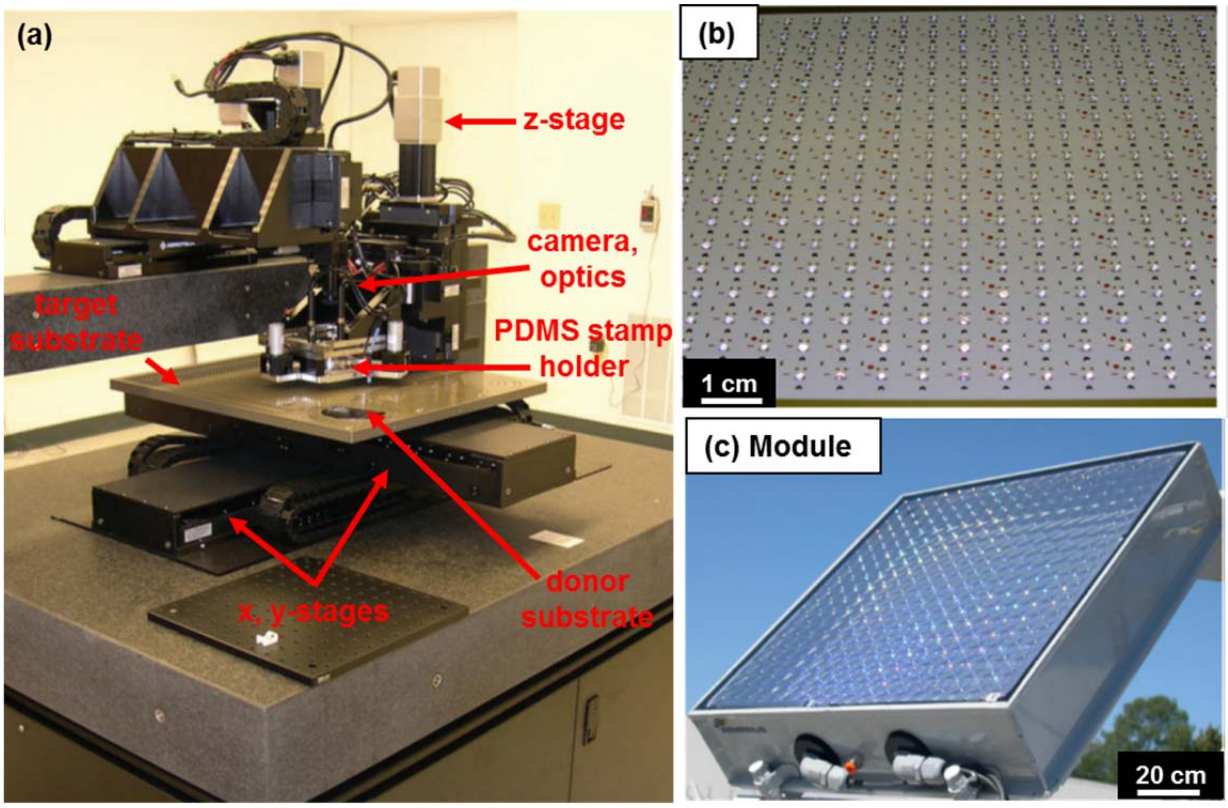

Figure B.21. (a) Picture of a high-throughput, automated tool for transfer printing, designed specifically for a type of high concentration, microscale photovoltaic technology. (b) Image of a backplane consisting of a large-area array of interconnected, microscale multijunction solar cells with glass spheres as focusing elements. (c) Image of a completed module.

APPENDIX C

MATERIALS ORIGINS OF RATE-DEPENDENT ADHESION

C1. Introduction

In Chapter 1, a general mechanics model was presented to describe the rate-dependent adhesive strength of elastomeric stamps that underlies transfer printing and many of the engineered protocols described in this dissertation. This appendix provides additional insight into the materials origins of this rate-dependence and discussion of how the general form of the energy release rate can be extended to the systems presented as well as other adhesiveless printing modalities under development.

C2. Critical Energy Release Rate

Chapter 1 presented an expression for the rate-dependent adhesion of elastomeric materials to rigid objects (substrates, inks, etc), through the energy release rate, G, in a form analogous to the initiation and propagation of an interfacial crack:[1-4]

$$G(v) = G_0[1 + \phi(v)] \tag{C1}$$

In this form, G assumes a minimum value, G_0, in the limit of zero or negligible peeling velocity, v, and ultimately increases proportionally with the peeling speed through the factor $\phi(v)$.[2, 3] $\phi(v)$, written more generally as $\phi(a_T V)$ where a_T is the Williams-Landel-Ferry (WLF)[5, 6] transformation shift factor and V is the extension rate of the crack tip, is typically an increasing function of velocity represented as a power law with exponent of approximately 0.6.[6] While

there are many aspects of the materials that determine both G_0 and $\phi(v)$, including cross-link density of the elastomer,[7] surface chemistry,[8] and contact electrification,[9] in most analyses of (C1) G_0 is identified processes that occur at the interface between the two contacted bodies while those pertaining to the bulk of the elastomer are encompassed in $\phi(v)$. [3, 9]

For simple, weakly-interacting elastomer systems, G_0 is determined by two main factors: the interfacial (Dupre) work of adhesion, w_0, and the number of polymeric chain segments between cross-links, N_0.[3, 7] To determine the work of adhesion between two surfaces *i* and *j*, a linear combination of both the polar and dispersion (nonpolar) components of the molecular forces can be obtained,[10-14]

$$w_0 = w_0^p + w_0^d \tag{C2}$$

The polar and dispersion components of the work of adhesion can be determined via contact angle measurements of probe liquids on a desired surface and have been described extensively in the literature.[11-13, 15] For the interfacial work of adhesion between two solid materials however, equation (C2) can be expressed using the harmonic mean approximation and the surface tensions γ_i and γ_j,[11, 13, 15, 16]

$$w_0 = \frac{4\gamma_i^d \gamma_j^d}{\gamma_i^d + \gamma_j^d} + \frac{4\gamma_i^p \gamma_j^p}{\gamma_i^p + \gamma_j^p} \tag{C3}$$

where *p* and *d* denote the polar and dispersive components, respectively. It has been shown by deGennes [7] and others [17, 18] that the energy required to extend and separate chains adhered to a solid surface is related to G_0 through a proportionality factor:

$$G_0 \propto N_0^{1/2} w_0 \tag{C4}$$

where N_0 is the number of segments between cross-link points. Thus, using expression (C4), we can estimate the interfacial effects on the energy release rate in (C1) through simple

determination of basic properties of system materials. An interesting result of equation (C4) is that for loosely cross-linked elastomer stamps (large N_0), more energy is required for separation compared to materials with dense cross-links (small N_0), a factor which may have bearing on comparison of the different PDMS formulations used for stamp elements in the preceding chapters.[6]

The origin of the rate-dependent term in (C1) lies in the viscoelastic relaxation of the elastomer bulk near the separation front. As a crack tip propagates, high strain-rates which develop around the separation front give rise to high-frequency, short-time mechanical responses.[3] As the distance from the crack tip increases, deformation also occurs, but at slower rates which are related to the radial distance from the separation front. The resulting strain-rate gradients established in the elastomer can be described by regions of high, intermediate, and low strain mechanical responses during peeling, qualitatively described as a "viscoelastic trumpet" and characterized by a single relaxation time, τ.[3, 8] In some regions of the elastomer bulk, the material responds to strain in a viscous manner which serves to amplify the energy required to separate the elastomer from a rigid surface. This amplification of separation energy is the dominant effect in the term $\phi(v)$ and the underlying materials origin for rate-dependent adhesives. In the case of a simple viscoelastic response (single relaxation time, etc) the complex modulus, $E(\omega)$ can be expressed as:[3, 7, 8]

$$E(\omega) = E_0 + (E_\infty - E_0)\frac{i\omega t}{1 + i\omega t} \tag{C5}$$

where E_0 is the low-frequency modulus, E_∞ is the high-frequency or glassy modulus, ω is the frequency, and τ the characteristic material relaxation time. The energy release rate can then be expressed analytically in terms of the velocity, relaxation time, and a ratio of the high and low-frequency moduli:[3]

$$G(v) = G_0[\lambda - 1][\arctan(\frac{\lambda v\tau}{l}) - \arctan(\frac{\lambda v\tau}{L})] \quad \text{(C6)}$$

Here l is the size of the adhesive zone at the crack tip (~1-10 nm) [3, 9] and L is the size of the elastomer. The modulus ratio, $\lambda = E_\infty / E_0$ can assume large values ($\lambda \geq 100$) for weakly cross-linked elastomers since E_0 tends to be small due to polymer networks in which only some chain ends are tethered while E_∞ can be large due to the effects of entangled free chains and dangling ends.[8] λ can be used to roughly approximate the boundaries delineating the different regimes of the viscoelastic trumpet, particularly the viscous regime in which energy amplification effects result in higher values of G. From (C6) it is evident that for arbitrarily large values of L ($> \lambda v\tau$), $G(v)$ increases without bound. The results show that a viscoelastic material with a modulus that grows with strain rate will exhibit adhesion strength to a solid surface that increases with separation speed.

C3. Dynamic Mechanical Analysis

Efforts to establish connections between the peel-rate dependent adhesive characteristics of elastomers discussed in this dissertation and the frequency dependence of the complex modulus are ongoing. Initial steps in this process require determination of the frequency response of the elastic moduli for the two variants of PDMS (Dow Corning Sylgard 184) most commonly used in adhesiveless printing modalities. To investigate the behaviors of these elastomers, dynamic mechanical analysis (DMA) was utilized to characterize the frequency and/or time-dependent response of the storage and loss moduli, E' and E", respectively.[19, 20] The two formulations of PDMS elastomer evaluated used the same commercial monomer and cross-linking agent, yet varied in the respective weight fractions, having mix ratios of 10:1

(wt.%) monomer:crosslinking agent (consistent with previous investigations in the literature[21-25]) and 5:1 (wt.%) monomer:crosslinking agent. The higher concentration of cross-linker can have interesting effects on the response of the PDMS possibly due to effects from a more densely cross-linked network (alteration of G_0) or stronger mechanical response (alteration of $\phi(v)$) as discussed previously. Experiments using a TA Instrument RS3A DMA measured across a range of frequencies and temperatures the tensile properties of the PDMS elastomers. For all tests, PDMS samples were configured in a dogbone geometry (gauge length 28 mm), the amplitude of oscillatory strain was fixed at 1%, the frequency varied from 0.1 Hz – 30 Hz (10 points per decade), and temperatures ranged from 50 ˚C to -110 ˚C. Across the measured range of frequencies, at a given temperature, the modulus of the material does not vary significantly. Figure C.1 shows representative storage and loss moduli across the limited range frequency sweep at room temperature (25 ˚C). Using the established Time-Temperature Superposition (TTS),[5, 19, 20] we transformed measurements taken across the range of temperatures to an equivalent rate at a reference temperature of 25 ˚C. The origins of this rate-temperature equivalence are the relation of the free-volume in the polymer to the relaxation time constants and the temperature dependence of the free-volume.[20, 26] In brief, tensile measurements gathered to describe the material modulus at reduced temperatures can probe the equivalent high or glassy frequency response of the material at the reference temperature (here approximately room temperature).

Figure C.2a shows the transformed data of the storage and loss moduli for 10:1 and 5:1 variants of PDMS as a function of frequency. Here we use a WLF transformation[5, 20] and extract the time-temperature shift factors, shown in Figure C.2b. As seen in Figure C.2, the moduli of both variants of PDMS grow from approximately 2 MPa at low frequencies up to

nearly 1 GPa at high frequencies (approaching the glassy regime). The application of the WLF transformation to measurements taken far from the glass transition temperature (T_g ~ -125 ˚C for PDMS) are imprecise, but the transformed data indicates that for high strain rates (> 10^3/sec), the PDMS exhibits storage and loss moduli that increase significantly with strain rate. These mechanical properties lead to strongly rate-dependent adhesion and validates our assumption for weakly cross-linked systems having λ>100.

To validate the low-frequency modulus values obtained from the Time-Temperature transformation method (Figure C.2a), tensile tests were performed on both variants of PDMS. Dogbone geometry samples having the same dimensions as those tested under frequency and temperature sweeps previously described were evaluated under static loading conditions in a TA Instrument RS3A DMA. Here, controlled extension of the gauge length of the samples at a strain rate $\dot{\varepsilon} = 0.1$ and measured normal loads on the sample enabled calculation of the normal stress and engineering strain in the deformed samples. Figure C.3 shows a representative stress-strain curve for both 10:1 and 5:1 PDMS under these loading conditions, extending to strains of approximately 50% in the gauge region. Typically, PDMS elastomers can support large strains prior to failure,[27, 28] however the strain range in Figure C.3 was chosen to highlight the extended linear behavior of the samples even under extreme deformations. As evident in stress-strain curves, the 5:1 PDMS exhibits a steeper slope with increasing strains than does the 10:1 PDMS. This corresponds, qualitatively, to a higher elastic modulus, consistent with the behavior over extended frequencies demonstrated in Figure C.2a. To quantify the modulus at these strain rates, small segments of each curve ranging from 0-10% strain were fitted with linear trend lines to extract slope (modulus values). For the 10:1 PDMS, the average modulus was estimated at 1.51 MPa while the 5:1 PDMS had an average elastic modulus of 1.84 MPa. Comparing these

values to the storage modulus values in Figure C.2a for low frequencies (ω~0.1 where loss modulus contributions to the total modulus are negligible), there is good agreement between the static and dynamically determined moduli. Small differences that arise between the two are likely due to errors in curve fitting for the estimated modulus values as well as small vertical shifts that occur during WLF transformation of the frequency- and temperature-dependent storage and loss moduli. Overall, the simple methods utilized to extract the dynamic and static moduli values provide critical insights into the material response under varying strain rates. These conditions are analogous to those experienced by the elastomer when undergoing peeling and can be exploited in ongoing analytical efforts to link explicitly the rate-dependent adhesive strength of PDMS to the complex modulus. These considerations, as well as others discussed throughout this dissertation, can be crucial for developing materials and methods to extend the utility of adhesiveless transfer printing modalities.

C4. References

[1] A.N. Gent, *Langmuir* **1996**, *12*, 4492.
[2] A.N. Gent, *J. Polym. Sci. B: Polym. Phys.* **1994**, *32*, 1543.
[3] F. Saulnier, T. Ondarcuhu, A. Aradian, E. Raphael, *Macromolecules* **2004**, *37*, 1067.
[4] X. Feng, M.A. Meitl, A.M. Bowen, Y. Huang, R.G. Nuzzo, J.A. Rogers, *Langmuir* **2007**, *23*, 12555.
[5] M.L. Williams, R.F. Landel, J.D. Ferry, *J. Am. Chem. Soc.* **1955**, *77*, 3701.
[6] Y. Sun, G.C. Walker, *Langmuir* **2005**, *21*, 8694.
[7] P.G.d. Gennes, *Comptes Rendus De L Academie Des Sciences II* **1995**, *320*, 193.
[8] P.G.d. Gennes, *Langmuir* **1996**, *12*, 4497.
[9] K. Shull, D. Ahn, W.-L. Chem, C.M. Flanigan, A. Crosby, *Macromol. Chem. Phys.* **1998**, *199*, 489.
[10] J.-H. Choi, D. Kim, P.J. Yoo, H.H. Lee, *Adv. Mater.* **2005**, *17*, 166.
[11] S. Wu, *Polymer interface and adhesion* 1982, New York: Marcel Dekker. 96-104.
[12] Z. Wang, J. Zhang, R. Xing, J. Yuan, D. Yan, Y. Han, *J. Am. Chem. Soc.* **2003**, *125*, 15278.
[13] J.A. Rogers, H.H. Lee, *Unconventional nanopatterning techniques and applications*. 2008, Hoboken: John Wiley & Sons, Inc. 598.
[14] S.-H. Hur, D.-Y. Khang, C. Kocabas, J.A. Rogers, *Appl. Phys. Lett.* **2004**, *85*, 5730.

[15] J.K. Kim, J.W. Park, H. Yang, M. Choi, J.H. Choi, K.Y. Suh, *Nanotechnology* **2006**, *17*, 940.
[16] S.-M. Seo, J.-Y. Park, H.H. Lee, *Appl. Phys. Lett.* **2005**, *86*, 133114.
[17] C.Y. Hui, D. Xu, K.J. Kramer, *J. Appl. Phys.* **1992**, *72*, 3294.
[18] D. Xu, C.Y. Hui, E.J. Kramer, *J. Appl. Phys.* **1992**, *72*, 3305.
[19] J. Israelachvili, *Intermolecular and Surface Forces*. 1991, Boston: Academic Press.
[20] I.M. Ward, J. Sweeney, *The Mechanical Properties of Solid Polymers*. 2nd ed. 2004, West Sussex: John Wiley & Sons, Ltd.
[21] T.-H. Kim, A. Carlson, J.-H. Ahn, S.M. Won, S. Wang, Y. Huang, J.A. Rogers, *Appl. Phys. Lett.* **2009**, *94*, 113502.
[22] M.A. Meitl, X. Feng, J. Dong, E. Menard, P.M. Ferreira, Y. Huang, J.A. Rogers, *Appl. Phys. Lett.* **2007**, *90*, 083110.
[23] J. Zaumseil, M.A. Meitl, J.W.P. Hsu, B.R. Acharya, K.W. Baldwin, Y.-L. Loo, J.A. Rogers, *Nano Lett.* **2003**, *3*, 1223.
[24] M.A. Meitl, Z.-T. Zhu, V. Kumar, K.J. Lee, X. Feng, Y.Y. Huang, I. Adesida, R.G. Nuzzo, J.A. Rogers, *Nat. Mater.* **2006**, *5*, 33.
[25] S. Bae, H. Kim, Y. Lee, X. Xu, J.-S. Park, Y. Zheng, J. Balakrishnan, T. Lei, H.R. Kim, Y.I. Song, Y.-J. Kim, K.S. Kim, B. Ozyilmaz, J.-H. Ahn, B.H. Hong, S. Iijima, *Nat. Nanotechnol.* **2010**, *5*, 574.
[26] J.D. Ferry, *Viscoelastic Properties of Polymers*. 3rd ed. 1980, New York: Wiley.
[27] D.-H. Kim, N. Lu, R. Ma, Y.-S. Kim, R.-H. Kim, S. Wang, J. Wu, S.M. Won, H. Tao, A. Islam, K.J. Yu, T.-I. Kim, R. Chowdhury, M. Ying, L. Xu, M. Li, H.-J. Chung, H. Keum, M. McCormick, P. Liu, Y.-W. Zhang, F.G. Omenetto, Y. Huang, T. Coleman, J.A. Rogers, *Science* **2011**, *333*, 838.
[28] D.H. Kim, J. Song, W.M. Choi, H.-S. Kim, R.-H. Kim, Z. Liu, Y.Y. Huang, K.-C. Hwang, Y.-W. Zhang, J.A. Rogers, *Proc. Natl. Acad. Sci. U.S.A.* **2008**, *105*, 18675.

C5. Figures

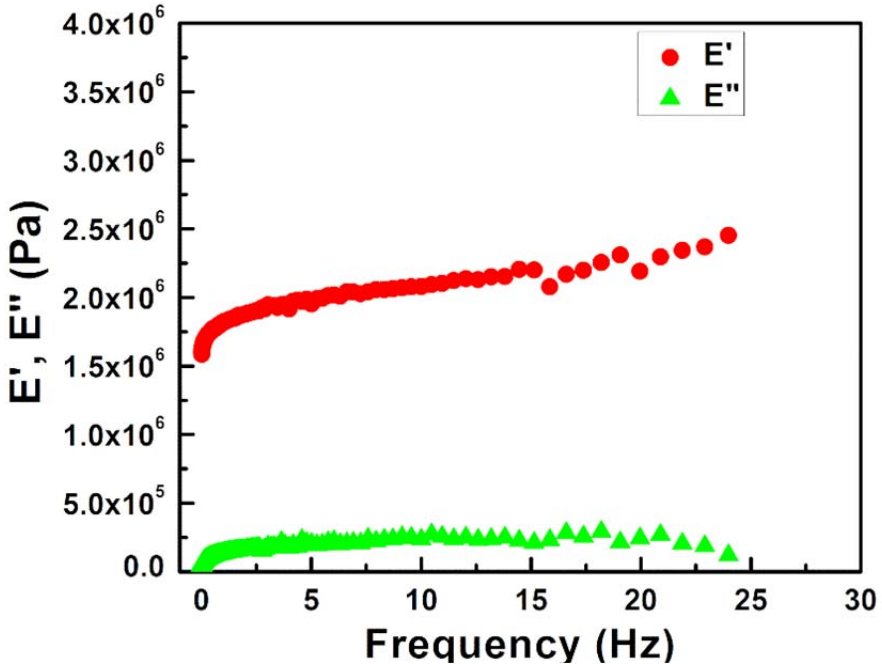

Figure C.1. Representative measurement of storage and loss moduli, E' and E", respectively for 10:1 PDMS at room temperature. The frequency of strain oscillation varied from 0.1 Hz to ~25 Hz and only small increases in moduli are evidenced in this narrow frequency window. Samples tested had a dogbone configuration.

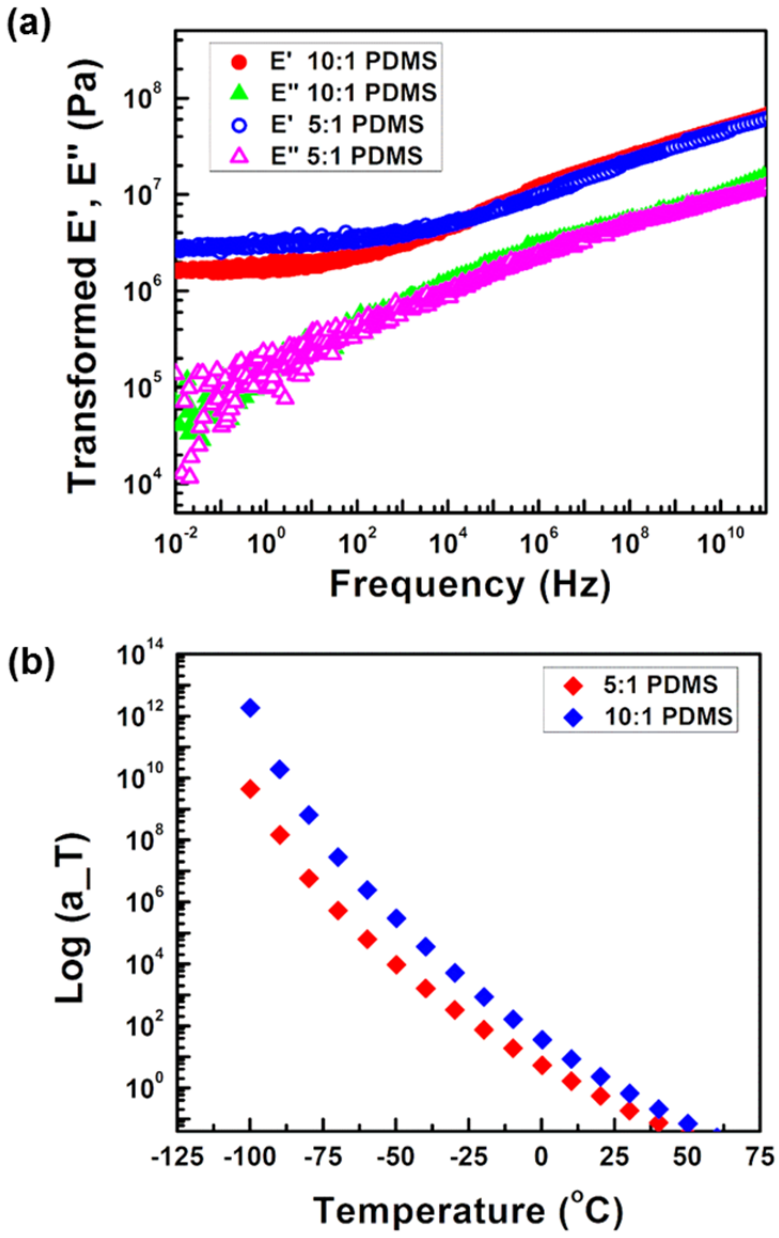

Figure C.2. (a) Transformed storage and loss modulus for both 10:1 and 5:1 PDMS samples. At low frequencies, the storage modulus for 5:1 PDMS is slightly larger than that for the 10:1 PDMS and both increase by several orders of magnitude with increasing frequency. A WLF model was used to exploit the time-temperature equivalence of the data. (b) The extracted temperature shift values a_T for the 5:1 and 10:1 PDMS.

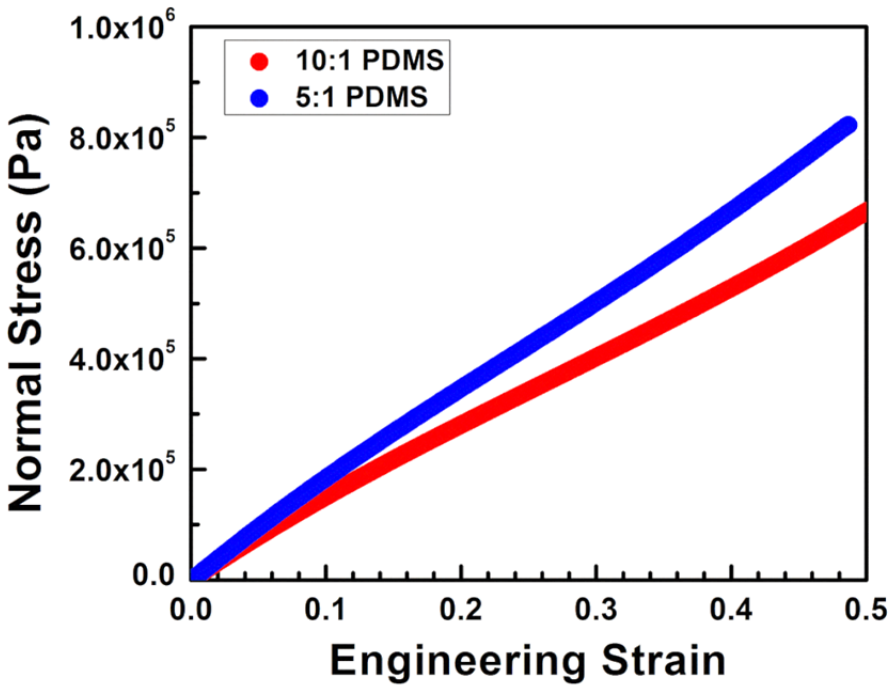

Figure C.3. Static stress-strain relationship for PDMS dogbone samples extended under a constant strain rate of 0.1. Moduli values can be determined by fitting low stress-strain regions to determine a slope. The 5:1 PDMS demonstrates a slightly stiffer material response than 10:1, consistent with transformed moduli data from previous figures.